POLITECNICO DI TORINO

Corso di Laurea Magistrale in INGEGNERIA BIOMEDICA
Sessione di Laurea Marzo/Aprile 2025

NUMERICAL MODELLING AND EXPERIMENTAL VALIDATION OF CANINE ENDOPROSTHESES WITH VARIABLE SHAPES

RELATORE:

Prof. De Pasquale Giorgio

CANDIDATA:

Vassia Rebecca

Anno Accademico 2024/2025

INDEX

ABSTRACT

The goal of this thesis is the static analysis of canine endoprostheses under a specific tensile load, replicating the forces acting during a dog's gait. This analysis is based on a finite element model (FEM) and subsequently validated through experimental laboratory tests. For this reason, it is crucial to investigate the behavior of the prosthesis and the prosthesis-bone complex under specific loading conditions to assess whether the prosthesis design and material are suitable for its intended function or prone to failure or hazardous deformations.

The introductory chapter examines the most prevalent skeletal disease affecting dogs, for which no standardized treatment has yet been established: osteosarcoma. This section provides an overview of current treatment approaches, including limb amputation, chemotherapy, and various limb-sparing surgical techniques. Among these techniques, particular attention is given to the use of endoprostheses, which are implanted following the surgical resection of the tumor. Three case studies have been analyzed in which researchers attempted to improve the design of canine endoprostheses for the radius.

The first chapter focuses on the anatomy of the canine limb and the biomechanical analysis of movement, highlighting the forces exerted during both walking and trotting. Special attention is given to the magnitude of these forces and the joints primarily involved in their transmission.

In the second chapter, finite element models (FEM) were created for each of the 11 provided canine prosthesis prototypes. Specifically, two models were developed for each prototype: a simpler model, referred to as Model 1, and a more detailed model, referred to as Model 2. Numerical simulations were performed for both models using the Ansys software. A tensile test was implemented to analyze the prosthesis's behavior under applied forces. The tests were conducted for two different force values in each case, allowing for the generation of a force-displacement graph based on the numerical simulation results.

The third chapter focuses on the experimental tests conducted in the laboratory, where physical models of the 11 prototypes were subjected to tensile testing using a dedicated testing machine. The results collected during these tests are presented. For each model, a force-displacement graph was plotted, and the breaking point of the specimen was recorded.

Finally, in the last chapter, a sensitivity analysis of both models was conducted and a critical comparison was performed between the numerical simulation results and the experimental laboratory results to validate the designed finite element model.

INTRODUCTION

OSTEOSARCOMA: THE MOST PREVALENT CANINE SKELETAL DISEASE

NATURE

Osteosarcoma is the most common primary bone neoplasia in dogs. It is a malignant mesenchymal tumour of primitive bone cells, with a high rate of metastasis, primarily to the lungs. The OS occurs mainly in the appendicular skeleton in specific sites of the forelimbs, such as the distal radius or proximal humerus, and rarely will cross a joint surface [1].

Primitive bone cells produce an extracellular osteoid matrix; the presence of tumour osteoid is fundamental for the histological diagnosis and differentiation of osteosarcoma from other bone sarcomas. The histologic pattern may vary between tumours or even within the same tumour, as a consequence, based on the type and amount of matrix, characteristics of the cells, and histologic pattern there is a histological subclassification of OS in osteoblastic, chondroblastic, fibroblastic, poorly differentiated, and telangiectatic osteosarcoma (a vascular subtype). If there is a difference in the biological behaviour of the different histologic subclassifications, it is not yet established; however, histologic grade, based on microscopic features, may be predictive of systemic behaviour such as the likelihood of metastasis [1].
Osteosarcoma has very aggressive local effects and causes lysis, production of bone, or both processes can occur concurrently; it is usually attended by soft tissue swelling and lameness but also pathological fracture of the affected bone can occur [1].

Metastasis is very common and typically arises early in the course of the disease, although it is often subclinical, without noticeable symptoms. The primary route is the hematogenous one, however, on rare occasions, the cancer may extend to regional lymph nodes.
While the lungs are the most frequent site for metastasis, the tumour can also spread to bones or other soft tissue sites with some frequency. Some differences in metastatic behaviour have been observed based on the anatomic location of the primary OS site: axial skeleton osteosarcomas are commonly less clinically aggressive than appendicular lesions, whereas those of the extra-skeletal tissues (e.g. mammary gland, subcutaneous tissue, gastrointestinal tract) are rarer but more aggressive [1].

MAIN RISK FACTORS

In order to better understand this type of neoplasia, many researchers deeply investigated every feature of affected dogs to perceive the main risk factors of osteosarcoma. Some of the outcomes turned out to be present in every single study, so they became the main risk factors, such as:

- **SIZE**: it is classically a cancer of large and giant breeds [6].

- **AGE**: it is largely a disease of middle-aged to older dogs and also a peak in age 1-2 years. Dogs aged 10 to < 12 years had 7.89 times the odds compared with dogs aged 4 to < 6 years according to William S. Dernell et al. [1].
  Another study confirms that the most common age of affected dogs is 7-10 years (36%) followed by 10-15 years (31,5%), both categories fell under the "Senior" classification, representing middle-aged to older dogs. [3]
  A further study found out that the oldest dogs (>14 years) were most at-risk whereas previous analyses identified a peak in risk at 9–12 years with reduced risk later in life. This study identifies a higher risk of osteosarcoma in older age groups as well as an early incidence peak in dogs of 2-3 years old. Although the biology associated with age and osteosarcoma risk requires further research in dogs, younger osteosarcoma patients may carry relatively higher heritable risk whereas older patients may reflect a greater contribution from age-related bone cancer risk. Unfortunately, osteosarcoma appears to be clinically aggressive in both old and young patients. [2]

- **BODYWEIGHT**: there is a specific connection between weight and OS; increasing the weight increases the tumour risk. In particular dogs with higher-than-average bodyweight for their breed showed increased risk [1].
  Interestingly, male dogs are typically heavier than their female counterparts; it may be that male dogs have previously been thought to be more at risk of osteosarcoma because of their sex, when it is their relatively higher bodyweight which may put them at higher risk than females.

- **BREED**: according to several scientific papers, the breeds most at risk for osteosarcoma are: Rottweiler, German Shepherd, Golden Retriever, and Great Dane, followed by Saint Bernard, Irish setter, and Doberman pinscher.
  In Y Dan G. O'Neill, Grace et all. work the most typical breeds among the osteosarcoma cases are Rottweiler (n=61, 18.43% of all cases), Labrador Retriever (38, 11.48%), Greyhound (34, 10.27%), German Shepherd Dog (11, 3.32%), Great Dane (11, 3.32%) and Staffordshire Bull Terrier (11, 3.32%), along with Crossbreed (62, 18.73%) [2].
  Another study finds evidence that there is an increased incidence of disease in certain breeds including Boxers, Great Danes, Rottweilers, Saint Bernards, Irish setters, Doberman pinschers, Greyhounds, German shepherds, Irish wolfhounds, and Leonbergers. In particular, in this study, 56 different breeds were represented by 598 dogs and 143 mixed-breed dogs (19.2%). The most common purebred dogs affected by OS are the Rottweiler (17.1%), Golden retriever (11.8%), Labrador retriever (10.9%), Doberman pinscher (5.7%), Greyhound (5.1%), German Shepherd

(4.7%), Saint Bernard (3.0%), Irish wolfhound (2.2%), Great Dane (1.9%), Great Pyrenees (1.3%), and Irish setter (1.3%). [3]

- **BODY CONFORMATION:** this factor is tied to the size and the breed, in particular, it is well-known that small-size dogs have less probability of achieving this disease so when considering leg length, chondrodystrophy is significantly associated with osteosarcoma protection compared with non-chondrodystrophic-breeds, supporting the conclusions from previous analyses that shorter leg length may be protective for osteosarcoma [6].

PRINCIPAL SITES OF OCCURRENCE

There are some specific body areas where Osteosarcoma can grow, in particular, it mainly occurs (about around 75%) in the appendicular skeleton, and it rarely (the remainder 25%) occurs in the axial skeleton [1].

The metaphyseal region of long bones is the most common primary site, with front limbs affected twice as often as rear limbs; specifically, the distal radius and proximal humerus are the two most typical locations while in the rear limbs, tumours are fairly evenly distributed between the distal femur and distal tibia. It is extremely rare for OS to be located in bones adjacent to the elbow, although there is one report of 12 cases located at the proximal radius or distal humerus, also proximal tibia and proximal femur, a slightly less common site than the distal femur and distal tibia. In addition, primary OS distal to the antebrachiocarpal and tarsocrural joints is relatively rare in dogs [1].

According to the research of Heyman SJ et all. in 116 cases of canine primary OS in the axial skeleton, it was reported that 27% were located in the mandible, 22% in the maxilla, 15% in the spine, 14% in the cranium, 10% in ribs, 9% in the nasal cavity or paranasal sinuses, and 6% in the pelvis. Single reports of OS development in the OS penis and the patella exist in the dog. Clinically documentable multicentric OS at the time of initial diagnosis occurs in less than 10% of all cases [4].

OVERVIEW OF ALL TREATMENT STRATEGIES FOR OSTEOSARCOMA

According to the fact that the leading region of tumour occurrence is the appendicular skeleton, in particular the forelimb, now we can discuss the current therapy directly at Osteosarcoma in this particular district. Below there is an overview of all treatment options.

AMPUTATION = The amputation of the affected limb is the standard local treatment for osteosarcoma because all kinds of dogs will usually function well after the amputation and have respectable mobility and quality of life [1]. There are rarely contraindications for this type of surgery, such as severe preexisting orthopaedic or neurological conditions. This is the most valid option also because the complete forequarter amputation for forelimb lesions assures complete local disease removal and also results in a more cosmetic and functional outcome.

RADIATION = Results of multiple studies have shown the analgesic benefits of palliative radiation therapy for OSA in dogs and other studies demonstrated histologic percent tumour necrosis post radiation as a predictor of local tumour control. Sometimes external beam radiation therapy is used in combination with limb-sparing techniques; but intraoperative radiation therapy protocols have shown radiation can achieve local tumour control but is associated with an unacceptable rate of complications [9]. In this manner, radiation is used in an effort to downstage the primary tumour to improve the success of local disease control following removal. At present, the role of radiation therapy used to replace surgery, with or without systemic chemotherapy, is unclear. Currently, the role of radiation therapy in dogs with appendicular OS is primarily reserved for palliation of bone pain.
Martin, Griffin, et al. tried a new method to evaluate the patient response: stereotactic body radiation therapy (SBRT), which involves the precise delivery of high doses of radiation to the tumour over a shortened period. They assessed survival time and fracture rate by evaluating patient response to SBRT as a first-line treatment using a uniform prescription of 36 Gy in three fractions of appendicular OSA sites. This study aims to assess the efficacy of SBRT as a treatment for appendicular OSA and evaluate the fracture risk following the treatment [10].

STEREOTACTIC RADIOSURGERY OR INTENSITY MODULATED RADIATION THERAPY (IMRT) = Is a means of precisely delivering radiation therapy to tumours while conformally avoiding normal tissues [1]. In a study, Stereotactic radiosurgery (gamma knife therapy) has been performed as a means of limb-salvage surgery in dogs. Dogs were treated using a frameless stereotactic radiosurgery system adapted from a system developed for the treatment of intracranial tumours in humans. The results of this study find out that acute effects to the skin were mild to moderate in most dogs and overall median survival was 363 days in this series [13]. Advantages of this technique include the normal tissue-sparing effects that stereotactic radiation potentially provides and the ability to avoid surgery. The disadvantage is that the technique involves equipment that is not typically available to veterinarians. These results suggest that stereotactic radiotherapy may provide a viable limb-sparing alternative, but further study is needed.

RADIOISOTOPES = The bone-seeking radioisotope, samarium ethylenediamine-tetramethylene phosphonate (samarium), has been used to treat osteosarcoma in dogs [1]. In high doses, samarium has been shown to locally deliver 20 to 200 Gy of radiation to normal bone and osteosarcoma tumours, respectively. Studies on samarium's efficacy for OS in dogs indicate that tumour doses equivalent to 20 Gy may be deposited in canine osteosarcomas using low to moderate doses of samarium, and the ratio between tumour dose and dose to surrounding tissues is favourable. The treatment provides pain relief in canine patients and, in some cases, tumour growth delay but is not curative [14].

CHEMOTHERAPY = This type of tumour has a high rate of metastases, in order to contain the metastasis, there are list of commonly reported adjuvant chemotherapy protocols for each adjuvant chemotherapy agent. Below is a list of the most common agents:

- **CISPLATIN** = Some authors indicate a significantly longer median survival time for dogs with appendicular OSA treated with cisplatin as an adjuvant therapy to amputation or limb-sparing surgery (322 days), than with surgery alone (138 days) [15]. However, in the treated group, 4 % of dogs were euthanatized because of the problem related to metastases, which was significantly higher than in the group of dogs with amputation alone. The results obtained indicate that cisplatin treatment is effective and improves survival in dogs with OS after amputation, but it does not inhibit metastases [16].
  The ideal timing of cisplatin delivery, concerning amputation, is currently unknown, but it seems reasonable to recommend the earliest possible administration of chemotherapy, which is usually at the time of amputation. However, no data exist to support a significant difference in survival for dogs treated preoperatively, immediately postoperatively, or after a delay. Most current protocols involve four treatments of cisplatin when it is used as a single agent; however, definitive studies in dogs have not been done to determine the most efficacious number of treatments.
  The recommended dose for cisplatin is 70 mg/m^2 body surface area because myelosuppression and renal toxicity become serious and life-threatening complications as the dose of cisplatin is increased [1].

- **CARBOPLATIN** = Carboplatin is a second-generation platinum compound that is less nephrotoxic than cisplatin with apparently similar antitumor effects [1]. Authors from the Veterinary Specialty Hospital of San Diego found out that dogs treated with adjunctive therapy had a prolonged median survival time (307 days) in comparison to those after surgery alone (approximately 138 days) and they also learned that dogs with adjuvant carboplatin-treated OSA using a similar protocol and showed that carboplatin administration is well tolerated and median survival time is similar to those treated with other chemotherapeutics (doxorubicin or cisplatin) [17].

One of the advantages of carboplatin is that it can be given without the saline diuresis necessary for cisplatin administration as it is not nephrotoxic like its predecessor, cisplatin; while it is not nephrotoxic, it is almost exclusively cleared by renal means, and if pre-existing renal function is compromised, significant myelosuppression can occur. The dose recommended for use in dogs is 300 mg/m^2 administered every 3 weeks for four treatments [9].

- **DOXURUBICIN** = Doxorubicin is also an effective agent for adjuvant chemotherapy in dogs with OS; however, it is not as efficacious as the platinum agents when used as a single agent. It is believed that doxorubicin used in OSA treatment is as effective as cisplatin or carboplatin [9]. From some studies, it is known that the median survival time for dogs receiving adjunctive therapy was 366 days, which was significantly longer than for the control group (138 days) [18]. The results obtained are similar to those with carboplatin as the adjunctive method of treatment, which indicates that both drugs may be used to prolong patients' lives, however, neither of them inhibits metastasis.

COMBINED CHEMOTHERAPY = Another attempt to improve chemotherapy's effectiveness was to compare the effects of two cytostatic drugs given in an alternating schedule. The efficiency of alternating the administration of cisplatin and doxorubicin after amputation was evaluated but the results of studies find that a disease-free interval and survival time are close to those reported for single-agent protocols. There is no clear evidence if combined chemotherapy is more efficient than single-agent therapy, however, it may reduce negative side effects, which might indicate that using multiple drugs in a long-lasting therapy increases the quality of patients' lives [9].

ISOLATED LIMB PERFUSION (ILP) = This method is an example of local adjuvant therapy that is used in concurrent limb salvage [1]. This technique consists of the isolation of limb circulation and perfusion with chemotherapy, which allows the delivery of high concentrations of chemotherapy as well as the delivery of compounds that are poorly tolerated systemically. ILP may be a method to facilitate therapeutic drug concentrations in primary tumours for preoperative downstaging before limb salvage [19].

LIMB-SPARING TECHNIQUES = Is preferred over amputation in dogs with severe preexisting orthopaedic or neurological disease and in dogs with osteosarcoma clinically and radiographically confined to the leg, where the primary tumour affects < 50% of the bone and dogs that are in otherwise good general health [1][9]. Consist in removing the primary tumour with marginal resection. In some cases, it can be preceded by a preoperative treatment such as radiotherapy or local chemotherapy and most dogs receive also therapy after surgery. After the tumour resection, the part of the bone lacking is replaced with something else which changes with the type of limb-sparing technique. The list of all these types of techniques is:

- **ALLOGRAFT LIMB-SPARING** = The procedure involves surgical resection of the tumour legion, which is then replaced with the allograft, typically frozen bone grafts from cadavers available from commercial bone banking facilities. In order to do that, the surgeon has to resect the tumour from the bone with a specific saw and a specific pattern, analyses both the tumour and the margin of the resection and only after that they can proceed with the operation. Typically, the radius is cut 3-5 cm proximal to the margins of the tumour; the most accurate imaging modality for determining the length of osteosarcoma tumours is Computed tomography [1]. The first step is to remove the articular cartilage, and then a fresh-frozen cortical allograft (thawed in 1 litre of an antibiotic in saline solution) is cut to fit, after that the medullary cavity is reamed to remove fat and cellular debris. Later the articular cartilage of the proximal carpal bones is removed, and the allograft is stabilized in compression using Association for the Study of Internal Fixation (ASIF/AO) principles. Afterwards, a dynamic compression plate is used to keep the graft in place with an attachment to the near bones. The plate extends proximally in the host radius and distally to a level just proximal to the metacarpophalangeal joint with a minimum of three screws proximal and four screws distal. The medullary canal of the allograft is filled with polymethyl methacrylate bone cement; this provides support for the screws during revascularization of the graft and acts as a reservoir for antibiotics. The healing of the allograft is not significantly impeded by the presence of the cement and has been shown to significantly decrease the incidence of orthopaedic failure, including allograft fracture and screw pullout [20].

  The advantages to allograft limb-sparing include the absence of external fixation and little owner involvement required in the postoperative period. The disadvantages are the high infection rate (approximately 40% and 50%) and the need for permanent internal hardware. Once an infection occurs, it may be controlled with long-term antibiotic therapy but is rarely, if ever, resolved. Revision surgeries are not uncommon and amputation for catastrophic implant failure or unmanageable infection is sometimes required [22].

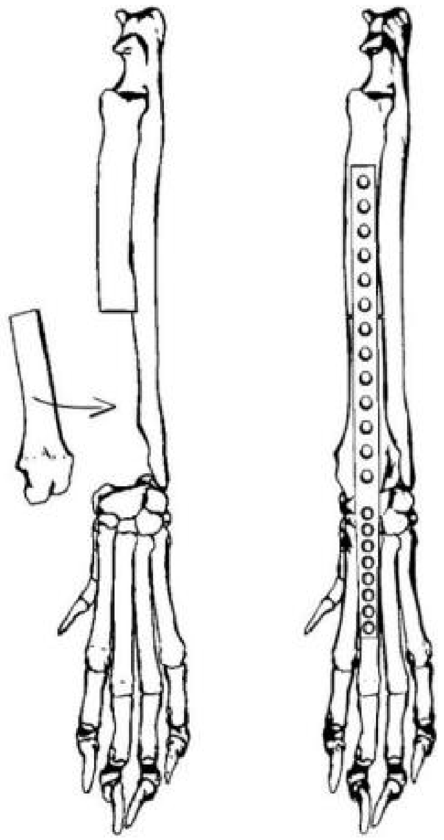

Figure 1: In the following figure we can see the main step of the allograft implantation. The allograft is seated where the radius was previously resected then a plate is applied to maintain the allograft in position.

- **ULNAR ROLL-OVER TRANSPOSITION (URT)** = This is the most common limb-sparing technique among the veterinary community when the ulna is not affected by osteosarcoma because in this technique the autogenous grafts have been obtained using adjacent bones such as the ulna (adjacent to the radius), or the fibula (adjacent to the tibia) [1].
  The vascularized ulna transposition technique uses the ipsilateral distal ulna as an autograft to reconstruct the distal radial defect by rotating the graft into position while preserving the caudal interosseous artery and vein and keeping intact the muscle attachments onto the periosteum of the distal aspect of the ulna. The procedure involves the following steps: the distal aspect of the radius is excised with appropriate margins; an ulnar osteotomy is performed at the level of the radial osteotomy while preserving its blood supply and muscle attachments. Then the ulnar graft is pivoted into the radial defect and a plate is applied to the cranial surface of the antebrachium and carpus/metacarpus in order to keep in place the autograft [23].
  This technique has several distinct advantages: it allows instantaneous transfer of a circumferentially complete autogenous bone column into the radial defect without causing morbidity at a different distant site, and its vascularity accelerates the process of union and allows hypertrophy of the graft and it avoids the time-consuming microvascular anastomosis, which may not be available at all facilities. The replacement bone is autologous, and the graft is

vascularized making it less likely to get infected and possibly speeding healing. The disadvantages to this technique are that the ulna transposition technique may be more prone to biomechanical complications in the postoperative period due to its smaller size relative to the radius and the need for permanent internal hardware [24].

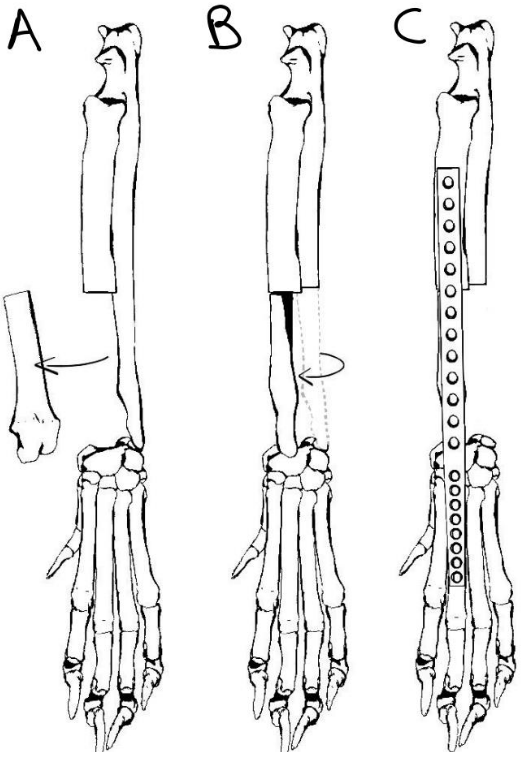

Figure 2: (A) The radius affected by the tumour is resected; (B) The ulnar allograft is positioned; (C) A plate is arranged to fixate the new bone.

- **LONGITUDINAL BONE TRANSPORT OSTEOGENESIS (BTO)** = This method is a modification of the original distraction osteogenesis technique developed to reconstruct large segmental bone defects caused by trauma or infection. Distraction osteogenesis refers to a tissue regeneration process whereby new bone is created between bony surfaces that are gradually pulled apart through prolonged, progressive, and gradual distraction that does not disrupt the blood supply and allows local tissues to accommodate slowly over time. The resultant new bone, known as regenerate bone, remodels into lamellar bone through a process similar to intramembranous ossification at a rate far exceeding that of normal fracture healing [24].
  Before surgery, a five- to six-ring circular fixator is constructed to allow one central ring (termed a transport ring) to move independently of the rest of the fixator. Following the procedure for removal of the tumour and preparation of the radiocarpal bone, the circular fixator is placed on the limb and attached to the remaining radius. Then a longitudinal section of normal bone (termed the transport segment) from the radius immediately proximal to the defect is

osteotomized and attached to the transport ring with wires; the transport segment is then moved slowly into the defect while new bone regenerates in the trailing distraction pathway. New bone continues to form longitudinally within the defect proximal to the transport segment for as long as the steady, slow distraction continues. When the transport segment reaches the radiocarpal bone (docking), the transport segment is compressed to the radiocarpal bone and heals to create an arthrodesis. After the transport period has ended, the fixator remains in place for a period of consolidation during which time the regenerated bone gains strength, and the transport segment heals to the adjacent bone. This technique is compatible with cisplatin, carboplatin, and combination chemotherapy [25].

The advantages to BTO limb sparing are the lack of internal hardware, the low risk of infection due to the autologous, vascularized nature of the replacement bone, and the ability of the new bone tissue to remodel over time. Patients are typically weight-bearing within the first 48 hours and once the incision is healed do not require exercise restriction. The disadvantages of the BTO procedure are the extensive client involvement needed to perform the daily distractions on the fixator and the extended amount of time the fixator remains on the limb [26].

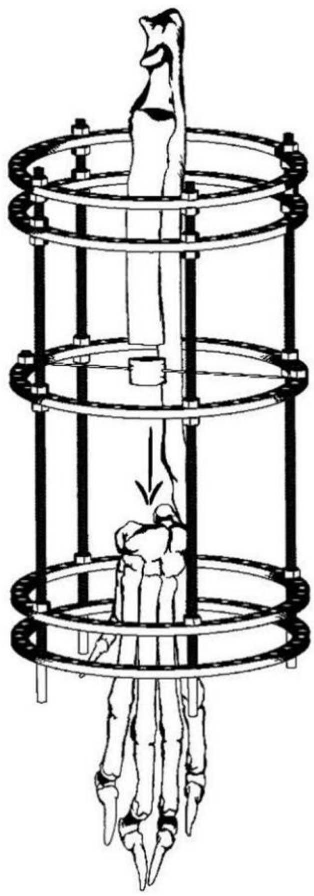

Figure 3: In this image, we can see the circular fixator used in this technique.

- **METAL ENDOPROSTHESIS LIMB SPARING** = In this technique the endoprosthesis is used to span the radial defect. An example is a limb-sparing technique using a commercially available metal endoprosthesis with a modified bone plate in a dog with distal radial and ulnar osteosarcoma; the limb-sparing plate spans the host radius and metacarpus, connecting to the implant, which abuts the host radius proximally and the radial carpal bone distally [24]. A negative suction drain has also been placed at the surgical site to decrease postoperative fluid accumulation.
  These are similar in appearance to limb-sparing constructs using cortical allograft, only a metallic spacer bridges the segmental defect; the surgical technique for placing this type of limb-sparing implant is similar to the technique used for the cortical allograft implants. A prospective comparison of complications between allograft limb sparing and metal endoprosthesis limb sparing has yet to be completed [22]. An advantage to the metal endoprosthesis technique is that large cortical allografts are not required, making limb-sparing available to more patients also treatment does not depend on special equipment, bone banking facilities, or external beam radiation machines. Known limitations to endoprostheses, however, include aseptic loosening, infection, joint or prosthetic instability, fatigue fracture, and wear or dissociation of modular components. Also, differences in the modulus of elasticity between the endoprosthesis and cortical bone can result in stress concentration at the endoprosthesis-bone interface and abnormal load transfer to the surrounding bone and these factors may lead to bone resorption at the endoprosthesis-bone/ bone-screw interface.
  Currently, there are 2 types of commercial endoprosthesis [28]. In particular, they are:

1. First-generation endoprosthesis (GEN1) → A 316L surgical stainless steel endoprosthesis that consists of a solid 122 mm segment of surgical steel with a flared distal end to abut the radial carpal bone, which is stabilized with a dedicated plate.

2. Second-generation endoprosthesis (GEN2) → it consists of a porous titanium radial defect spacer and has weight reduction through void regions, available in 2 lengths (98 and 122 mm); it is available with a hydroxyapatite coating.

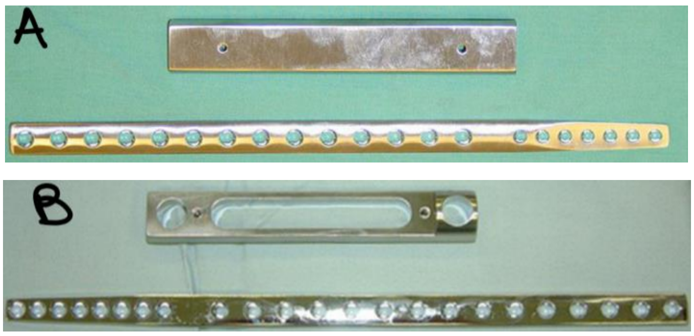

Figure 4: (A) Is the first generation endoprosthesis; (B) Is the second generation endoprosthesis.

However, they have not yet become a standard due to their high failure rates and the fact that they are only available in two different sizes. This limitation necessitates adapting the surgical situation to the prostheses only once in the operating room. With the ongoing advancements in additive manufacturing and 3D printing techniques, there is an effort to construct custom-made endoprostheses tailored to specific clinical cases [29]. However, the time required to transition from an X-ray to an actual custom-printed prosthesis is still prolonged, thus preventing this approach from becoming a definitive technique. Therefore, a viable strategy would be to optimize existing endoprosthesis models to enhance their versatility and ease of adaptation to various clinical situations and dimensions.

OVERVIEW OF THE RADIUS ENDOPROSTHESES MOST RECENT MODELS

FIRST MODEL UNDER REVIEW

We will now conduct a highly detailed analysis of the study on the endoprosthesis model proposed by Anatolie Timercan, Vladimir Brailovski, Yvan Petit, Bertrand Lussier, Bernard Séguin in the article "Personalized 3D-printed endoprostheses for limb sparing in dogs: modelling and in vitro testing" [30]. In this study they take into consideration the forelimb of a 70 kg Great Dane afflicted by osteosarcoma of the distal radius, which had been euthanized at the request of his owners; the limb was salvaged for the study and preserved at −25 °C after being covered with tissues soaked with saline solution. A custom-made endoprosthesis was made, following specific steps, and then it was tested.

The process, that has been made, for designing a custom-made prosthesis is as follows:

- Dogs were positioned in sternal recumbency with both thoracic limbs extended cranially and symmetrically aligned. The carpi were positioned at normal standing angles. The dogs were imaged using a multi-slice CT scanner; a helical scan of the region of interest was reconstructed.
- After that, the surgeon evaluated the tumour with a radiologist and determined the proximal extent of the tumour in the radius. The site of the radial osteotomy was determined by adding 4.5 to 5.0 cm proximal to the most proximal extent of the tumour [30].
- The DICOM images of the CT study were used to reconstruct the 3D bone models. The reconstructed bones were the radius, ulna, carpals, and metacarpals on the affected limb, and the radius on the contralateral limb.
- The unaffected contralateral radius model was mirrored and superimposed on the affected limb, following which the virtual osteotomy was performed using the prescribed cutting plane.
- A contoured bone plate was designed to correspond to the curvature of the bones and provide an antebrachiocarpal angle specific to the dog as measured preoperatively and from the CT. The plate covered ≥70% of the length of the remaining radius proximally and >80% of the length of the third and fourth metacarpals distally [30].
- Self-locking threaded holes and an intramedullary stem were then added to the implant. Ti 2.7 or 3.5 mm screws were used distally in the metacarpals and Ti 3.5 mm or 5.0 mm screws were used proximally in the radius [30].
- The endoprostheses were manufactured on an EOSINT M280 400 W Ytterbium fibre laser system (EOS GmbH, Munich, Germany) with Ti-6Al-4 V alloy (titanium alloy), (yield stress of 1000 MPa, Young's modulus of 110 GPa, and density of 4.41 g/m^3 [30].

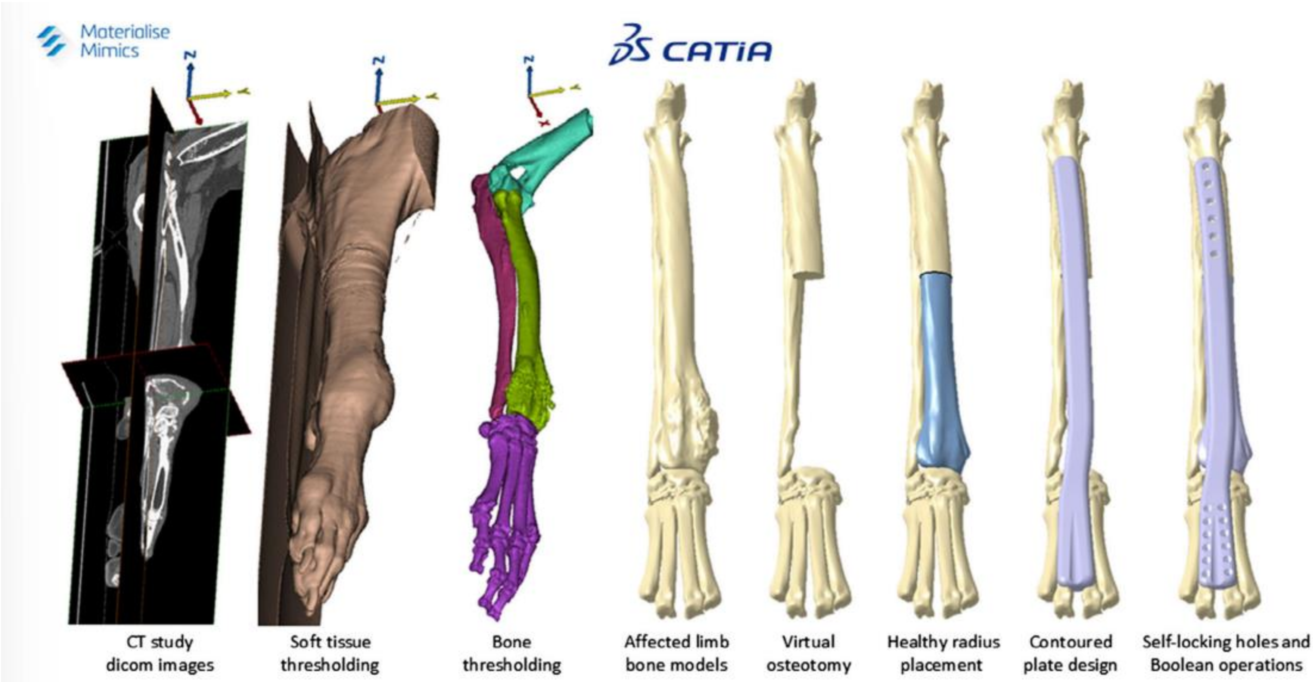

Figure 5: The previously listed steps are schematically illustrated in the image.

A similar methodology was applied for the design of the cutting guide. The distal portion of the guide was positioned around the ulnar styloid process, while the proximal portion was opposed to the cranial radius. The cutting slot was aligned with the osteotomy plane used on the radius. Cutting guides were printed with acrylonitrile butadiene styrene (ABS) plastic on a Fortus 250mc system.

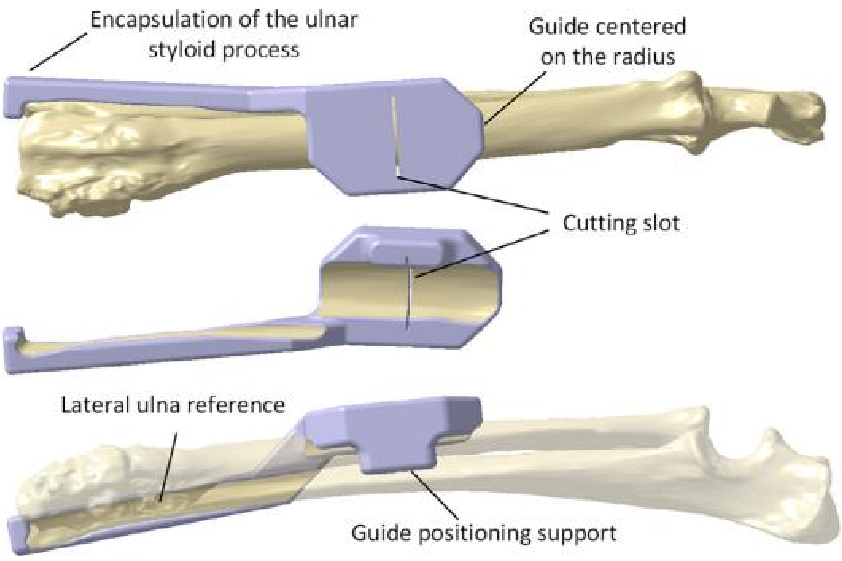

Figure 6: The cutting guide.

This study performs two different biomechanical testing of the forelimb with endoprostheses:

1) NON-LINEAR NUMERICAL ANALYSIS → The extremities of the humerus and phalanges were embedded in custom fixtures, and the elbow was positioned at angle 125, which is representative of normal limb positioning and allowing free longitudinal travel of the metacarpals, to avoid application of a flexural moment on the load cell [30].

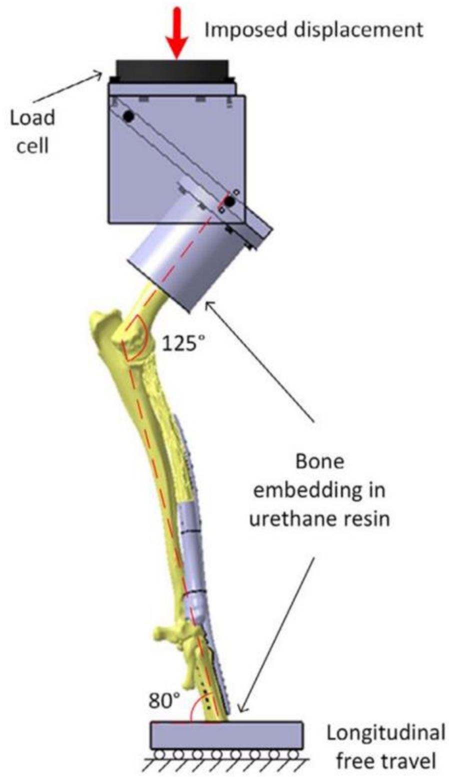

Figure 7: Testing configuration used in this specific study.

The reconstructed solid bone models and personalized endoprosthesis with screws were imported as STP files in Ansys Workbench. Only cortical bones were modelled, and screw threads were not designed. Resin embeddings were created around the humerus and metacarpals [30]. The material properties displayed in *Table 1* were applied to the various components (all the materials were assumed to have isotropic bilinear behaviour) and the boundary conditions were imposed as illustrated in *Figure. 8*.

Material	Properties				
	E (GPa)	ν	S_y (MPa)	UTS (MPa)	A (%)
Bone [37,38]	15	0.3	40	110	4
Ti-6Al-4 V (EOS datasheet)	110	0.33	945	1055	13
Urethane resin (Axson datasheet)	2.7	0.35	30	50	3

Table 1: The materials used in the model can be seen, along with their main properties such as Young's modulus (E), Poisson's coefficient (v), yield stress (Sy), ultimate tensile strength (UTS) and elongation to failure (A).

Figure 8: The boundary condition imposed.

To facilitate model solving, bones were represented as hollow tubes with outside diameters and wall thicknesses corresponding to the average values of the cortical bone structure. The personalized endoprosthesis was modelled as a straight plate extending from the salvaged part of the radius to the metacarpals [30]. The plate covered two metacarpals and was combined with a cylindrical part representing the removed part of the radius. The symmetry was exploited to reduce the mesh size, and the large deflections option was activated. The medial collateral, lateral collateral, and interosseous ligaments of the elbow joint were defined as spring elements on the surfaces corresponding to the attachment points determined from the CT scan. The contact conditions between the model components were defined as shown in *Figure 9*.
The Advanced Lagrangian contact formulation with a 0.5 stiffness coefficient was used to facilitate model solving and resulted in negligible contact penetration. A convergence study was conducted to obtain a mesh with 37,144 tetrahedral elements and 75,655 nodes [30].

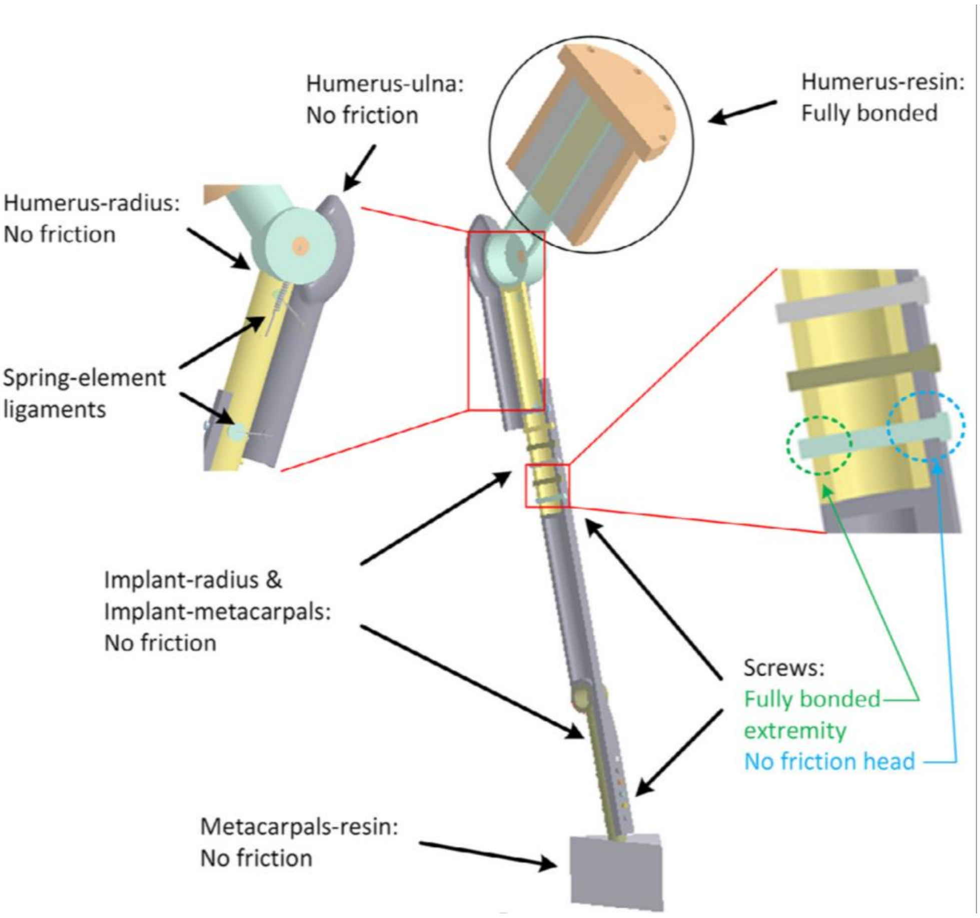

Figure 9: Contact condition between the model component.

2) EXPERIMENTAL TESTING → The cadaveric limb of the Great Dane was instrumented using the proposed personalized limb-sparing technique. In the proximal part of the construct, six 3.5 mm cortical screws were used, while twelve 2.7 mm cortical screws were used in its distal part to affix the endoprosthesis to the third and fourth metacarpals [30]. All screws were applied in neutralization mode. Muscles were stripped away from the humerus and metacarpals, with care taken to leave ligaments intact. Custom fixtures were used to embed the limb extremities in F100 polyurethane resin. A saline solution was used to keep the specimen moistened throughout dissection and testing.
Limb installation in an MTS 858 Bionix II with a 15 kN uniaxial load cell. The elbow was positioned at an angle of about 125°, and the metacarpal fixture was installed on a uniaxial translation table. Markers were placed on the endoprostheses and fixtures and tracked with an ARAMIS 5 M non-contact optical measurement system. The instrumented limb was then tested in compression with a crosshead speed of 0.5 mm/s. Forces and crosshead displacements were measured using a load cell and an LVDT of the MTS, respectively [30].

Next, they examined the results obtained using the two different testing methods:

- KINEMATICS ANALYSIS → This analysis compares the displacements of the upper part of the construct (of 10, 20, 30, and 40 mm) of the experimental markers and their numerical representation. As we can see in *Figure 10*, similar results are observed, indicating that the numerical model represents the actual kinematics of the limb-prosthesis construct well [30].

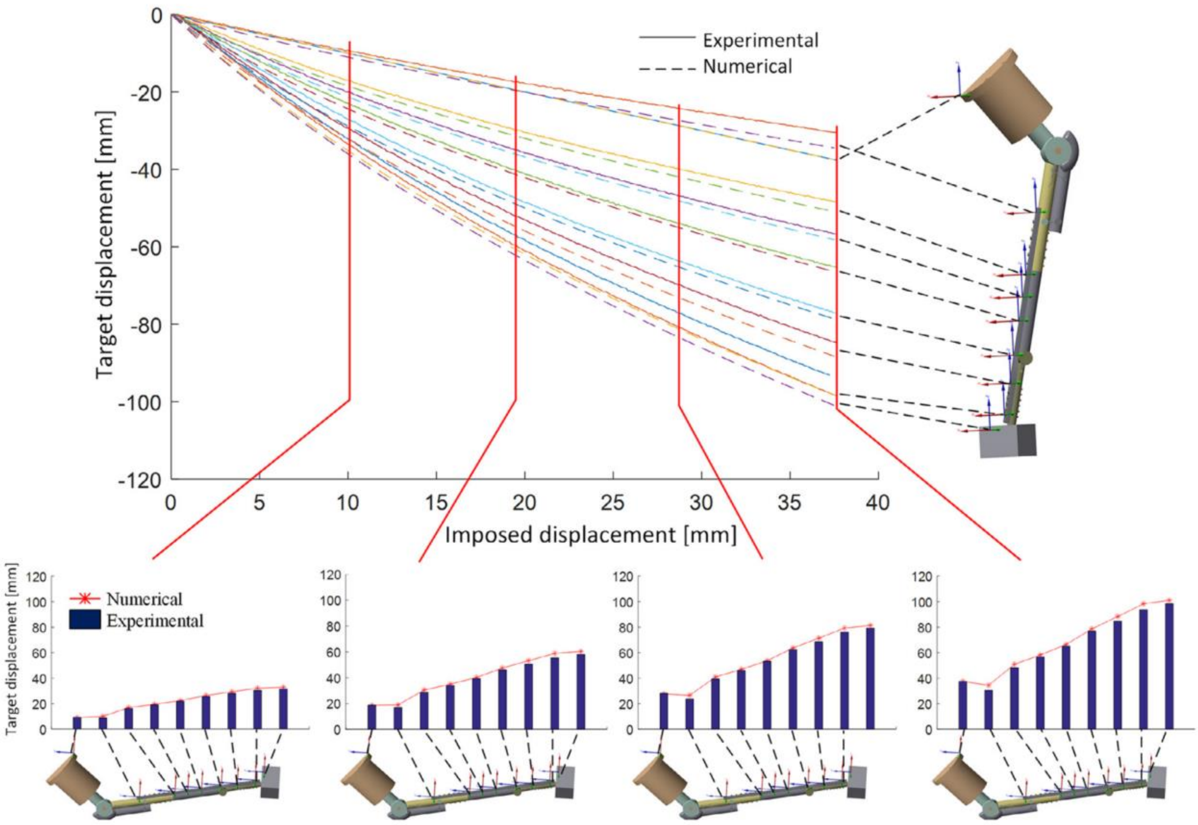

Figure 10: Displacement of both experimental marker and their numerical representation in specific positions.

- FORCE-DISPLACEMENT DIAGRAMS → The numerical model shows a slightly greater stiffness compared to the experimental construct, potentially due to model simplifications, such as the exclusion of cartilage layers within the joints. The limbs failed in the metacarpal region under a force of 230 N. This failure was attributed to bending moments caused by the increasing misalignment between the crosshead axis and the metacarpal embedding zone. The numerical model exhibited a similar phenomenon, with stress levels in the metacarpal bone (200 MPa) surpassing the ultimate strength of the bone reported in the literature (110 MPa) [30].

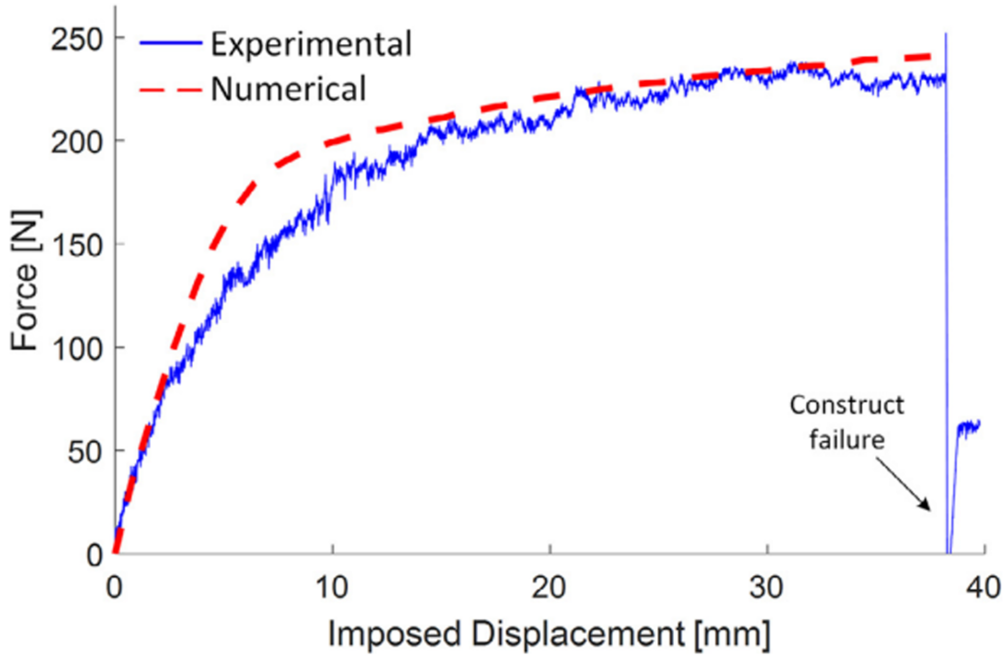

Figure 11: Force-displacement diagram comparing numerical model to experimental construct.

- STRESS ANALYSIS OF THE IMPLANT → The stress distributions within the endoprosthesis were analysed numerically and stress risers were identified in the region covering the carpal bones. The maximum calculated stress in the implant was ∼300 MPa, significantly lower than the yield stress of the additively manufactured Ti64 (Sy = 945 MPa). These calculations lead to the conclusion that under this particular loading configuration, the endoprosthesis could resist a threefold increase in load before yielding [30].

  The effect of varying the implant stiffness on the stress distribution in the implant and bone structure can be observed in F*igure 12a*. This analysis was realized to estimate the extent of stress sharing between the implant and the adjacent bones. The stress distribution is improved with a virtual implant material having a modulus of elasticity ranging from 25 to 50 GPa. In this case, stress concentration in the implant is reduced, and maximum stresses are evenly distributed over the area between the carpal stress riser and the distal screw fixation. In the metacarpal, bone stress concentration is unaffected, but maximum stresses are however slightly reduced [30].

  The model can also be used in experiments with various endoprosthesis designs. For example, *Figure 12b* shows that transversal pockets can be added in the radial part of the endoprosthesis, allowing a 30% mass reduction, without significantly affecting the maximal stresses in the implant [30]. Additionally, the endoprosthesis design can be modified to reinforce its carpal portion, thus attenuating the stress concentration in this zone and allowing for better stress distribution.

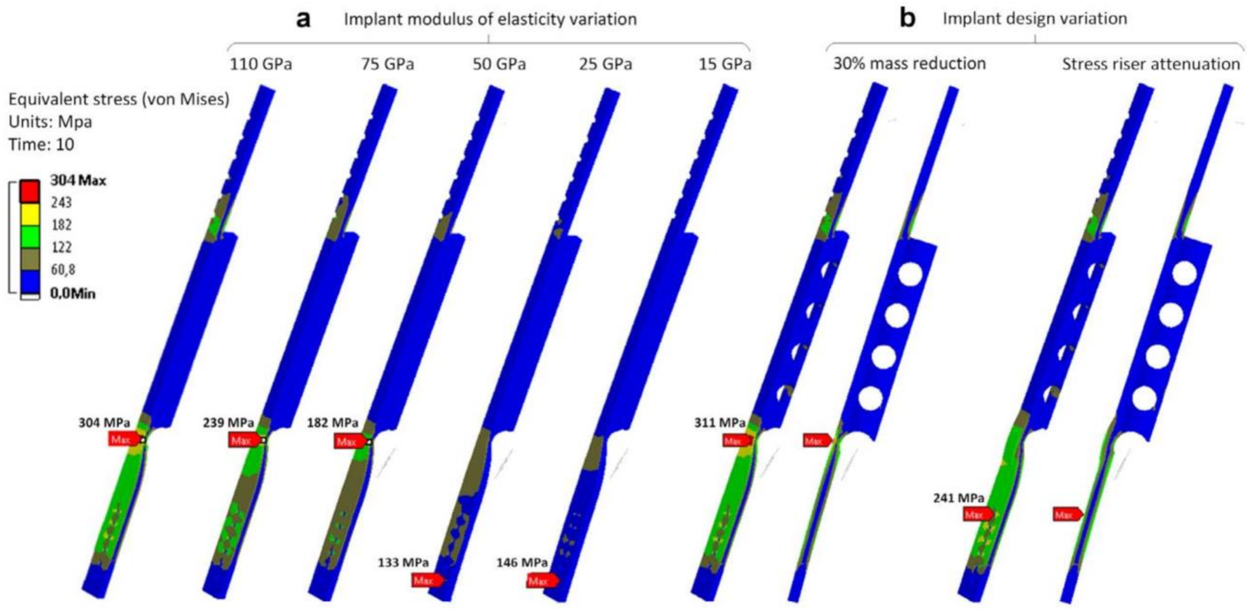

Figure 12: Stress distribution analysis of the costume-made endoprostheses for (a) stiffness variation and (b) design variation.

Due to experimental testing limitations, the numerical model was developed with free longitudinal translation of the lower extremity embedding. The fact that the metacarpals were not fixed changed the biomechanics of the constructs. However, since the model has been validated for a given set of boundary conditions, the latter could be modified to mimic the published setups and to compare the results obtained with those in the literature [30].

SECOND MODEL UNDER REVIEW

We will now conduct a highly detailed analysis of the study on the endoprosthesis model proposed by Timothy Joseph Horn in the article “Development and experimental evaluation of a novel, patient-specific implant for limb-sparing surgery” [24].
In this study, they started from the commercially available model and aimed to optimize it. In doing so, they developed a new type of prosthesis by attempting to eliminate failure points and make it as mechanically compatible as possible with bone by modifying the material's geometry while retaining the basic shape of the existing model. They produced a base model with different material geometries to assess the best one for use in the final model. Now there is a review of the various steps taken to achieve the production of the final model.

The first step was the experimental evaluation of key implant features of the proximal endoprosthesis in order to find the principal failure point given that canine limb sparing has been associated with a high failure rate. The most critical features are:

- The bone-implant interface is critical, as the prosthesis has a standardized shape that does not always perfectly fit the dog's bone. Therefore, during surgery, the surgeon must shape the limb bone to fit the prosthesis, but it is not always possible to achieve a perfect contact area between the two, which could eventually lead to failure. A possible solution is that patient-specific implants designed via 3D medical imaging data sets may provide a better anatomic fit and allow orthopaedic procedures to be carried out with little or no modification to the underlying bone structure thereby improving the bone-implant interface. Also additively manufactured bone plates do not require pre-bending and can significantly improve accuracy while reducing surgery times

- The screws, along with their positioning and orientation on the bone, are also a critical point. Those can also be optimized from CT data to avoid osteoporotic regions or facilitate multi-planar stabilization. A study by Kohles et al. (1994) showed improved stiffness using double-plate (orthogonally oriented) constructions over single-plate constructions.

- Another important point to consider is the load transferred to the bone and the material properties, which must be sufficiently compatible with those of the bone to ensure that the load is evenly distributed between the bone and the prosthesis. Finite element modeling of compressive loading in cylindrical structures populated with various unit cell geometries to demonstrate that porosity and geometry could be optimized to produce strains sufficient to stimulate bone healing while maintaining the mechanical integrity of the implant.

After that, a full factorial experiment of variants representing the proximal and segmental portions of limb-sparing implants was designed to elucidate the effects of plate contact area, plate orientation, and implant stiffness, on implant mechanical characteristics. To do that, five plate configurations were selected:

- three of these consisted of plates with a standard limb-sparing plate (commercially available from VOI, Veterinary Orthopedic Implants) cross-section including a cranial plate, a medial plate, and a cranial plate combined with a medial plate. Each plate was designed with six holes for fixation.

- a fourth group was a conformal cranial plate, this plate was designed to precisely match the surface contours of the bone subject to the area moment of inertia at any point along the longitudinal axis being equivalent to the standard plate at the same position. Each plate was designed with six holes for fixation.

- A fifth group was a cranial-medial configuration designed with a total of six holes (three per plate)

The cross-section of the cranial plate was designed from measurements of the commercial plate (3.84 mm thick, 11.94 mm wide, ventral radius 28.56 mm). The extrusion path for the contour profile was divided into 6 axially constrained parametric segments, spaced 11.99 mm apart, with nodes located at the midpoint between two screw holes such that the segments are free to rotate cranially and caudally about these points. The plate was not contoured medially or laterally. Cranial screw holes for 3.5 mm cortical bone screws with spherical countersinks were placed in the centre of each segment and normal to the plate surface [24].
The same method was used to define the contouring of the medial plates. The medial plate was designed with a second moment of inertia equivalent to that of the cranial limb sparing plate in the craniocaudal cantilever bending mode (3.81 mm thick, 11.94 mm wide, lateral radius 28.58 mm). The medial plate screw holes, located in between the cranio-caudal holes, lie along the neutral axis with minimal contribution to plate stiffness. The conformal cranial plate was designed by projecting the bounding geometry of the standard plate onto the surface of the radius model, this 11.94 mm wide surface was then offset 3.81 mm. The screw hole locations and angles are identical to those of the contoured plate design [24].
The VOI limb-sparing plate spans the segmental defect and is typically fixed to the graft with machine screws. The cross-section of the graft segment was designed as an ovoid in order to encompass the bounding geometry of the original (VOI) defect repair block and both the cranial and medial plate cross-sections. The ovoid consists of a circle ($R = 9.755$ mm) tangent to an ellipse with the same minor radius and a major radius, a, (in the mediolateral) of 12.253 mm [24].

Five graft segments, 165 mm in length, with an ovoid cross-section, were populated with rhombic dodecahedron unit cells with relative densities of 0.1, 0.2, 0.3, 0.4, and 1.0. The specimens were loaded to failure in four-point flexure with a crosshead speed of 1.5 mm/min. Loading was applied in the cranial-caudal direction (across the minor diameter). The major span was 139.7 mm, and the minor span was 50.8 mm. From these data, the 0.2 and 0.4 relative density meshes were selected for incorporation into the test implant designs. Based on the test results, the 0.2, 0.4, and 1.0 relative density sections were selected for incorporation into the test implant geometries [24].

These graft segments were combined with the five plate configurations and a dovetail boss was added to the distal end of the test implant to facilitate attachment to the test fixture. We can see the finite models in the image below (F*igure 13*).

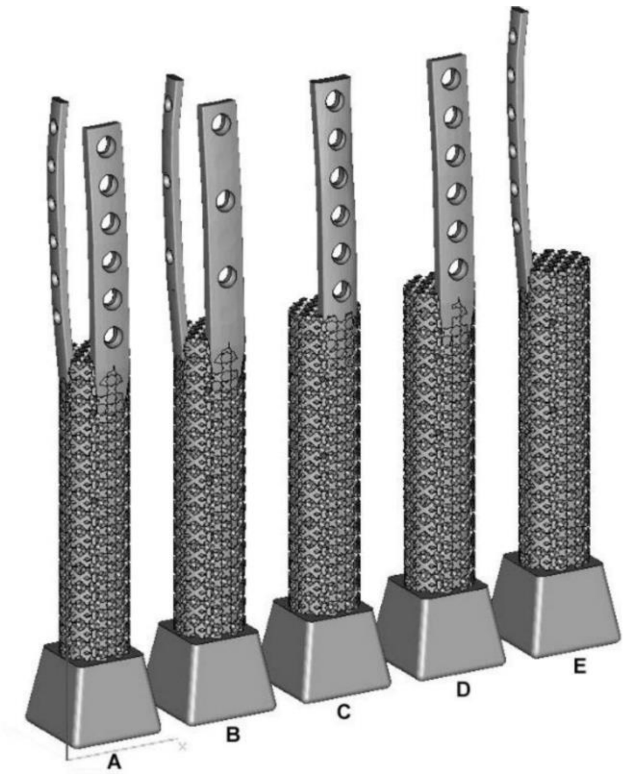

Figure 13: In this figure, we can see the five-plate configuration combined with the graft segment and a dovetail. The configurations are: (A) biplanar with 12 holes, (B) biplanar with 6 holes, (C) cranial-conformal, (D) cranial-contoured, and (E) medial.

These implants were fabricated in high-strength titanium alloy, Ti6Al4V, using the EBM process of direct metal additive manufacturing. The implants were then affixed to composite analogues of a patient-specific radius and subjected to non-destructive biomechanical testing in three modes: axial, cantilever, and torsional [24].

In order to affix the implants to the patient's radius they had to drill the bone too. For this purpose, cranial holes were drilled first, starting with the distal most hole using the cranial drill guide and a 2.5 mm bone drill at low speed: then the cranial drill guide was replaced by the cranial tap guide and cranial holes were taped with a 3.5 mm x 1.25 mm cortical bone screw tap. For the medial and biplanar scenarios, the same process was repeated [24]. We can see the results in the F*igure 14* below.

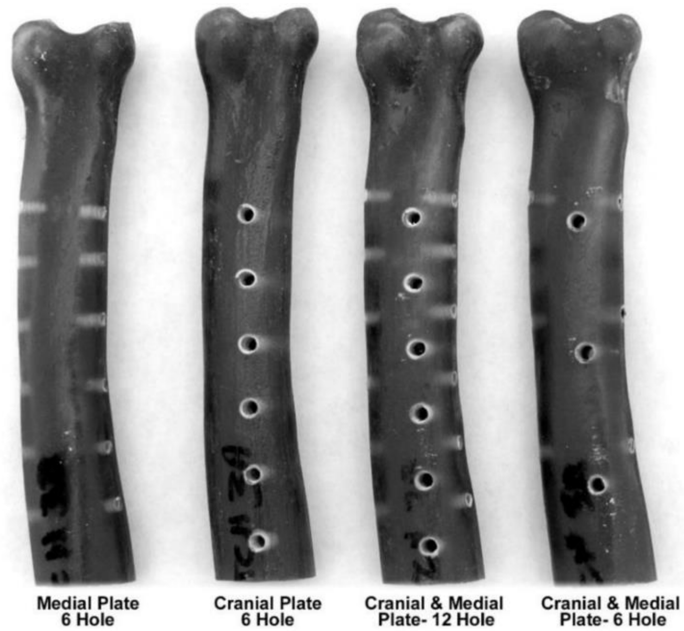

Figure 14: In this image, we can see the bone of the patient-specific radius with the holes corresponding to each implant configuration.

Once the complete bone-prosthesis model was obtained, to verify that the bone-implant contact area was adequate, they decided to measure the contact area and pressure on implants with a cranial contoured plate, the cranial conformal plate, and the cranial portion of the biplanar plate designs using pressure measurement film (Fujifilm Prescale). The method they adopted to achieve this is as shown in *Figure 15*:

Mono-sheet prescale film MS (10-50 MPa) and two-sheet LW (2.5-10 MPa) were cut to the exact width and length of the ventral surface of the bone plates. Hole diameters match the minor/root diameter of the 3.5 mm cortical bone screws. The prescale film was loaded between the cylinder and a ground and polished platen [24]. The distal-most screw was inserted through the plate and prescale film and lightly threaded into the analog radii. Alignment with the remaining proximal holes and plate edges was visually checked as the screw was tightened to a torque of 1.2 Nm with a 2.5 mm hexagonal driver [24]. The subsequent screws were inserted using the same technique, in sequence from the distal to proximal ends of the plate. Once all screws were placed, the torque was increased to 2.0 Nm in the same order [24]. Thirty seconds after the last screw was tightened to the specified torque, the construct was disassembled in reverse order. The prescale film was carefully loaded into a custom transparency holder.

Then, prescale films were converted to grayscale after all tests and these data were used in calculating other metrics such as total contact area, percent contact, and solidity (area/convex hull) [24].

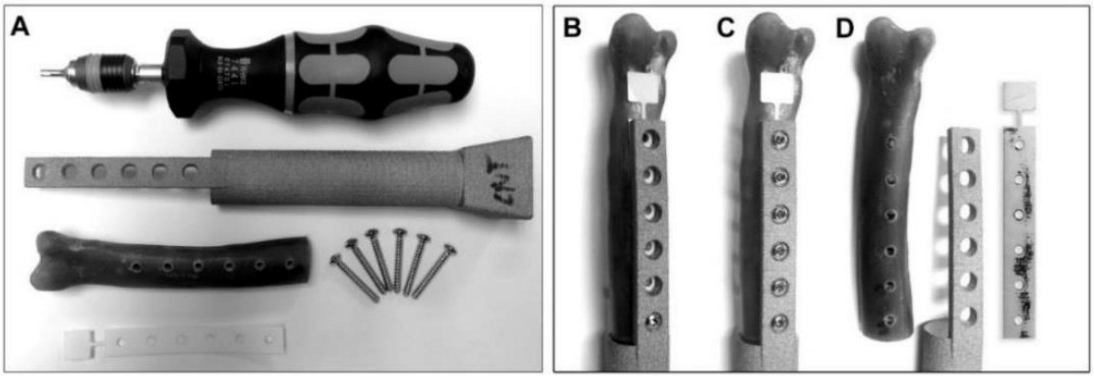

Figure 15: In this image, there are (A) the component of the prescale assembly, (B) the step where the prescale film is aligned with the distal screw, (C) the step where the prescale film is aligned with all the screws, (D) the disassembled construct and the stained prescale film.

Afterward, to prepare the complete bone-implant model for experimental testing, they applied strain gauges to the model. Specifically, the calibrated, preassembled, 350 Ω rosette strain gauges (Micro-Measurements, Raleigh NC) were applied to the cranial surface of the limb-sparing test plates between the first and second holes (distal) and the fifth and sixth holes (proximal) [24]. Cyanoacrylate adhesive was applied to both the plate and the underside of the strain gauge. Pressure was applied with a silicone rubber block for at least 15 minutes. After gluing, the gauges and leads were coated with RTV silicone for protection. A strain relief loop was loosely fixed to the proximal end of the segmental defect repair with a plastic tie. Each 3-wire cable was labeled according to channel number with a plastic marker and terminated in an RJ45 connection. Strain gauges were only applied to three replications of each implant design excluding the medial and six-hole biplanar constructs [24].

Figure 16: This image shows how were applied the strain gauge at the model.

MECHANICAL TESTING:

They evaluated three loading scenarios in this study: cantilever, torsion, and axial compression. All mechanical testing was carried out using an ATS 1620C testing machine.

- CANTIIVER TESTING → The position of the implant/analogue bone construct is rotated about the mediolateral plane (at the distal end of the device) 1.6 degrees from the horizontal to match the centre of rotation of the construct, which is necessary to account for the curvature of the radius. The crosshead loading fixture contacted the test implant at a distance of 158.68 mm from the base of the distal housing fixture. Loading was applied at a crosshead speed of 1.5 mm/min for each group to a maximum load of 110 N for all constructs with cranial plates. For the constructs consisting of only medial plating, a maximum load of 25 N was applied [24].

- TORSION TESTING → The torsional stiffness of the constructs was measured by placing an angular displacement of up to 10° at a rate of 6.5°/min. in external rotation. The torque transmission drive on the proximal end of the implant consisted of a split housing matching the epiphysis geometry [24].

- AXIAL TESTING → Axial loading to 450 N was applied to the limb-sparing test implants with a crosshead speed of 1.5 mm/min. The distal dovetail feature was oriented at an angle of 1.6° to the horizontal in the cranial-caudal direction [24].

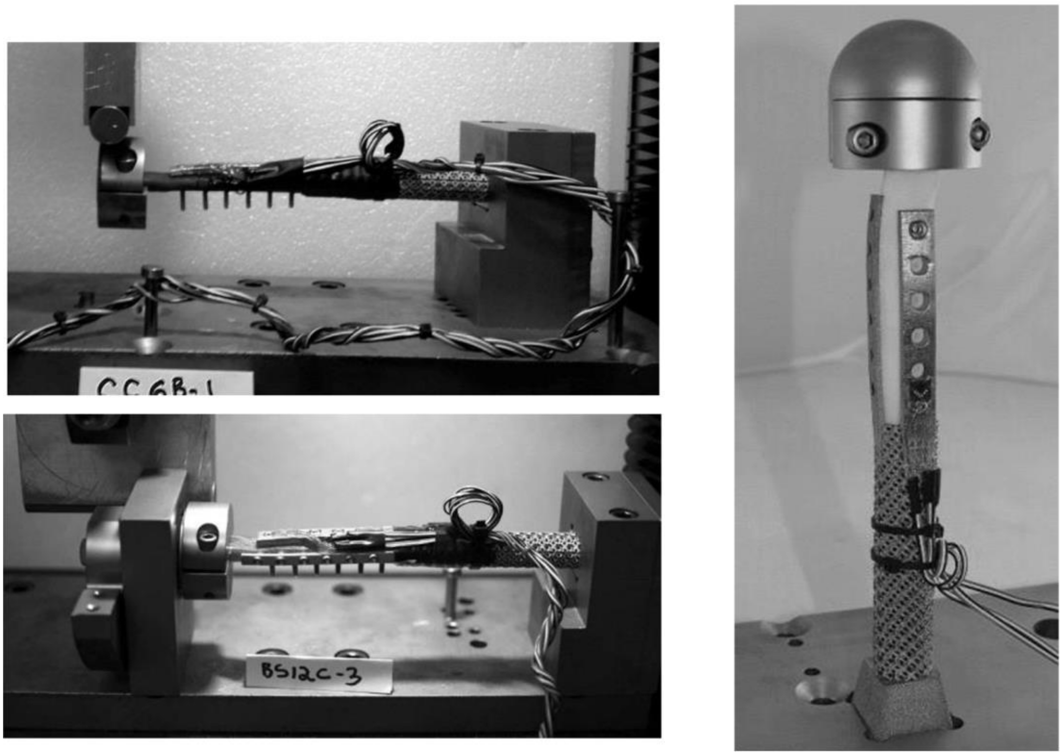

Figure 17: In this figure we can see: in the right the axial testing fixture, in the left on top the cantilever testing fixture and on the bottom the torsion testing fixture.

For each of the three testing modes, the stiffness was determined from the slope of the linear portion of the load-displacement plots. In addition, data were also recorded from strain gauges located distally and proximally on the cranial plates. One-way ANOVA was used to investigate the influence of the number of screws for the two biplanar configurations.

CANTILEVER TEST RESULTS → For cantilever stiffness they found out that the number of screws for the biplanar (medial-cranial) plate configurations (6 or 12) did not significantly influence construct stiffness ($p = 0.6656$), mesh relative density had a significant influence on the cantilever stiffness ($F < 0.0001$), the stiffness of the constructs with 1.0 relative density was significantly higher than both the 0.4 and 0.2 relative density which have no significant difference between them and also that the data do not support a significant difference between the cantilever stiffness of cranial conformal plates and cranial contoured plates ($F = 0.7598$) [24]. We can see these results in the image below (*Figure 18*):

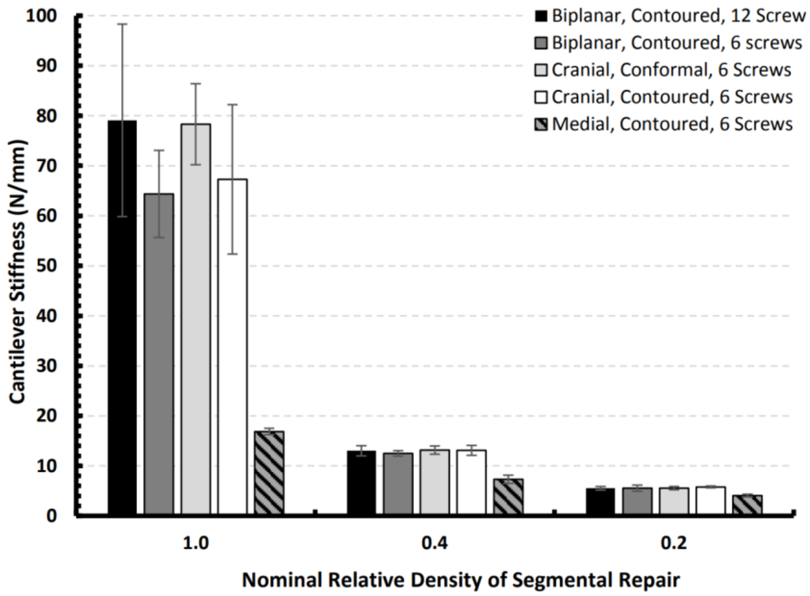

Figure 18: In this image, there is a chart showing cantilever stiffness for each configuration and for each relative density. Error bars indicate ±1 standard deviation.

Medial plate stiffness was significantly lower than cranial or biplanar stiffness, exceeding the ANOM lower control limits. The presence of the medial plate in the biplanar configuration did not increase the cantilever bending stiffness of constructs as compared to the constructs with only cranial plating [24].

AXIAL TEST RESULTS → For axial stiffness they found out that mesh relative density had a significant influence on the axial stiffness: the difference between the 0.4 and 0.2 relative density constructs was significant ($p = 0.0103$); no significant difference in axial stiffness associated with relative density for the medially plated constructs ($F = 0.1076$). When blocked by mesh types, ANOVA results show biplanar (medial-cranial) plate configurations with 12 screws have higher axial stiffness than those with six screws ($F = 0.0088$). The effect was most pronounced for constructs with 0.2 relative density mesh structures (F

= 0.0057). The data do not support a significant difference between the axial stiffness of cranial conformal plates and cranial contoured plates (F = 0.7598) [24].

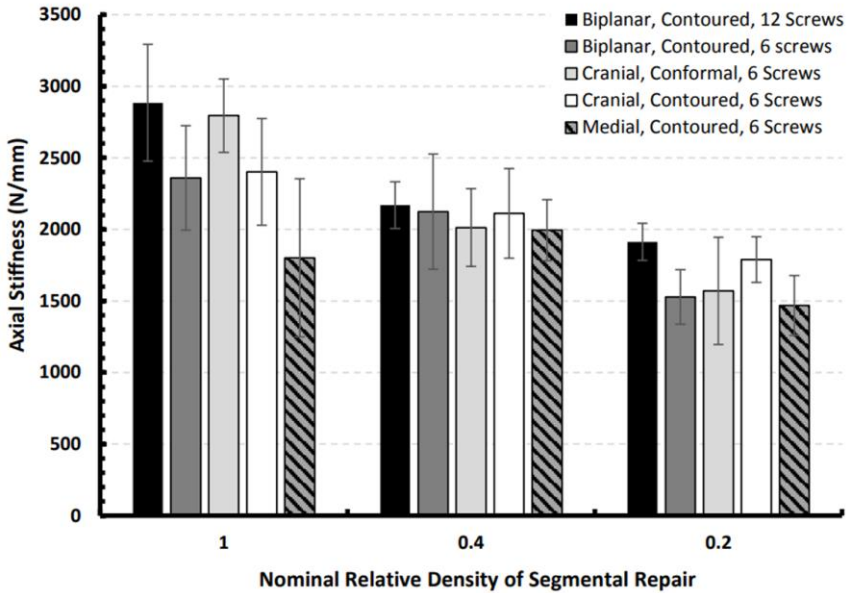

Figure 19: In this image, there is a chart showing axial stiffness for each configuration and for each relative density. Error bars indicate ±1 standard deviation.

For different contoured plate positions, (cranial, medial, biplanar), significant differences in the means were detected using ANOVA blocked by mesh relative density (F = 0.0002). Medial plate construct stiffness was significantly lower than biplanar or cranial plate stiffness (p < 0001 and p = 0.0078 respectively) [24].

TORSIONAL TEST RESULTS → For torsional stiffness they found out that mesh relative density had a significant influence on the torsional stiffness: there is no significant difference in torsional stiffness between 0.2 and 0.4 relative density meshes for the medially plated constructs (F = 0.1076); blocked by mesh relative density, ANOVA shows that torsional stiffness was higher for biplanar plate configurations with 12 screws than those with six screws (F = 0.0036). The data do not support a significant difference between the torsional stiffness of cranial conformal plates and cranial contoured plates (F = 0.7246) [24].

For different contoured plate positions, (cranial, medial, biplanar); significant differences in the means were detected using ANOVA blocked by mesh relative density (F = 0.0001). The medial plate construct's torsional stiffness was significantly lower than biplanar or cranial plate stiffness (p < 0001). Cranial plate torsional stiffness was significantly lower than the biplanar configuration (p = 0.0475) [24].

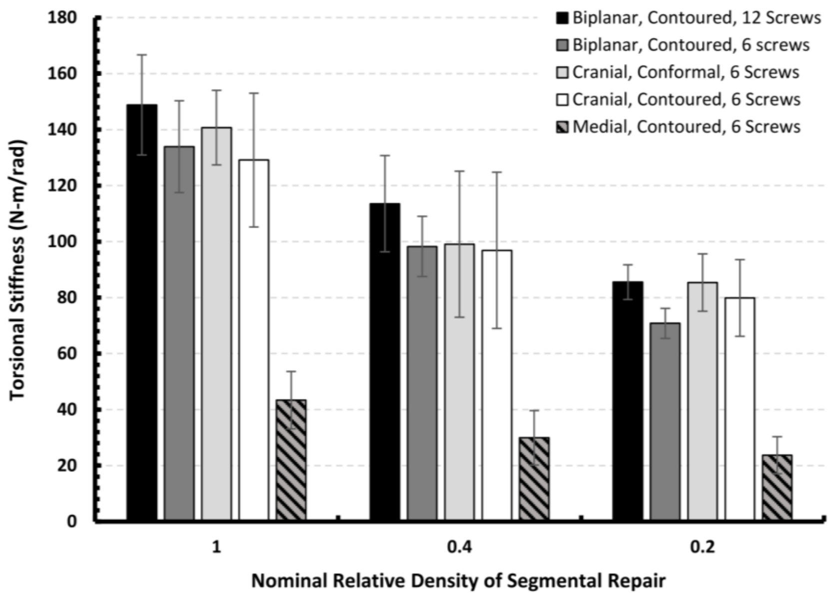

Figure 20: In this image, there is a chart showing torsional stiffness for each configuration and for each relative density. Error bars indicate ±1 standard deviation.

These results demonstrate that a significant reduction in implant stiffness is possible due to a decrease in the relative density of the EBM mesh segment and also to a specific plat conformation, the one designed with medial plating was the only significantly less than the other and this effect was most noticeable in the torsional and the cantilever modes of testing. From this study, we can also see that the influence of the number of screws in the biplanar configuration was significant in the axial and torsional bending modes when the graft segment stiffness was low (0.2 relative density). Another important feature is the contact area which this study showed is significantly greater in the conformal plates compared to contoured plates. It did not significantly affect the stiffness of the constructs in any of the testing modes. Still, the results show that while the interface contact pressure can be reduced by incorporating conformal plating, minute variations in geometry can result in localized pressure hot spots. The strain was recorded at two locations (distal and proximal) on the cranial surface of the limb-sparing plates, but the results show a relatively high variability that does not support strong conclusions. This variability may be due, in part, to the small sample size for each implant configuration and imperfections on the surface of the EBM-fabricated plates that resulted [24].

After they isolated and elucidated the influence of key design parameters on the performance of implants, they developed a patient-specific implant for limb sparing directly manufactured using electron beam melting technology (EBM). Their manufactured titanium endoprosthesis will exhibit lower stiffness than the commercially available alternative and a strain distribution similar to untreated limbs, as a result of the previous analysis. To demonstrate that also the complete custom endoprosthesis shows this property, they compared in vivo application of the two types of prosthesis the commercial one and the custom one. To achieve this purpose, they followed a precise sequence of steps. The main passages are the following:

1. **IMAGE ACQUISITION →** Five adult dogs were collected after euthanasia. Their thoracic limbs were disarticulated at the glenohumeral joint, and computed tomography imaging was performed using a helical CT with 512 x 512 resolution and 0° gantry tilt [24].

2. **PATIENT SPECIFIC IMPLANT DESIGN →** The limb receiving the custom implant was isolated and reconstruct as a three-dimensional model with the help of Mimics software.
   The external geometry of the graft segment was modelled after the geometry of the contralateral limb and was populated with 5.0 mm, 30% relative density unit cells of rhombic dodecahedra. The ventral surface of both the proximal (radial) and distal (metacarpal) plate sections were designed to conformal to the bone surface. In order to simplify the geometry, they used curvature analysis to identify and eliminate triangles with angles that deviate from those of nearest neighbours, a tangential fill strategy to repair the resulting holes [24].
   For securing the metacarpal bone they used six 2.7 mm cortical bone screw holes, evenly spaced between the proximal head of the 4th metacarpal and a locus 8 mm proximal to the distal end of the plate. Their orientation and location were modeled after the OrthoMed™ pancarpal arthrodesis plate namely on the 3rd metacarpal bone the screws were directed medially while on the 4th metacarpal were directed laterally following a specific pattern of orientation: the distal-most screw was angled by 30°, the middle screw was angled by 20° and the proximal-most screw was angled by 10°. In closing one 3.5 mm cortical bone screw was placed at the radial carpal bone [24].
   They also used six screws for the proximal end: three 3.5 mm cortical bone screws were located cranially and three 2.7 mm screws medially. The distance between the holes was evenly spaced and the distance between the distal-most hole on the proximal radius and the graft segment was 8 mm. The biplanar fixation was designed with 3 medially placed tabs connected to the edge of the cranial plate [24].

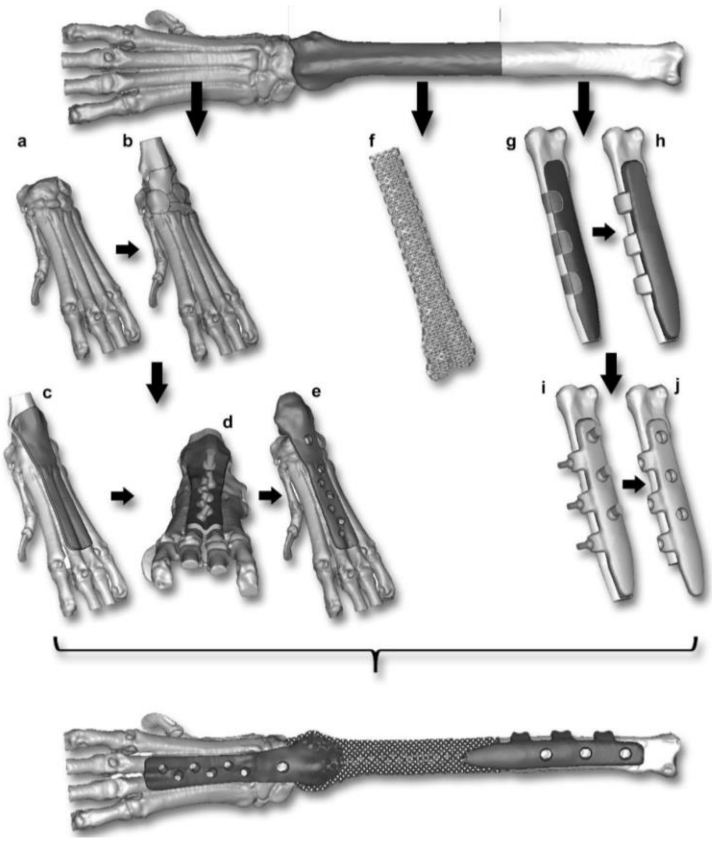

Figure 21: This image illustrate a summary of the major process steps.

3. **PATIENT SPECIFIC IMPLANT FABRICATION** → The machine used to fabricate the custom implant was an Arcam model A2 EBM machine and all processing parameters used were the standard and available from Arcam for Ti6Al4V. *Figure 22* shows the finished implants.

Figure 22: In this image, there are the five-custom models, one for each dog.

This study only evaluates one of these custom models; in particular in *Figure 23* we can see the two implant configurations, custom and commercial, examined in this study while in *Table 2* we can see some of the key differences between the two endoprosthesis groups.

Figure 23: Photograph of the two endoprosthesis configurations evaluated in this study: the custom endoprosthesis (top) and the commercial endoprosthesis (bottom).

	Commercial Endoprosthesis	**Custom Endoprosthesis**
Material	316 Stainless Steel	Grade 5 Titanium, Ti6Al4V
Osseous Defect Length	98 mm	95 mm
Distal Screw Number	6, 2.7 mm stainless steel	6, 2.7 mm titanium
Proximal Screw Number	6, 3.5 mm stainless steel	3, 3.5 mm titanium cranially placed 3, 2.7 mm titanium medially placed
Implant Mass	164.88 ± 0.21 g	54.87±3.03
Arthrodesis Angle	12º	12º

Table 2: This image shows the main implant measurements for the commercial and custom endoprosthesis.

4. **SPECIMEN PREPARATION →** For the purpose of potting the paw in the designated site, as shown in *Figure 24*, they had to prepare the limb. In order to do that they excised soft tissues surrounding the humerus up to approximately 35.0 mm proximal to the centre of the lateral epicondyle, leaving intact the ligaments of the elbow joint then the proximal head of the humerus was osteotomised at the surgical neck. They also excised the soft tissues of the paw and the digital pads, preserving ligamentous structures and the metacarpal pad [24].

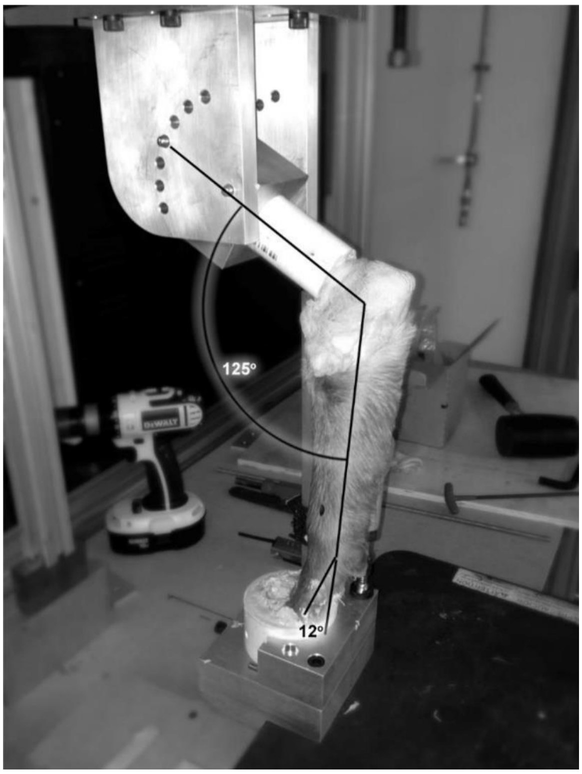

Figure 24: Figure showing the alignment of the limb during potting.

5. **SURGICAL PLACEMENT OF ENDOPROSTHESES** → Limb-sparing surgery was carried out over two periods. First, for the purpose of strain gauge placement, soft tissue incisions were made to expose the radius, then they applied a calibrated, preassembled, 350 Ω uniaxial strain gauges to the cranial surface of the radius at a location 3 mm proximal to the planned osteotomy and adjacent to the lateral side of the plate, as we can see in F*igure 25*.

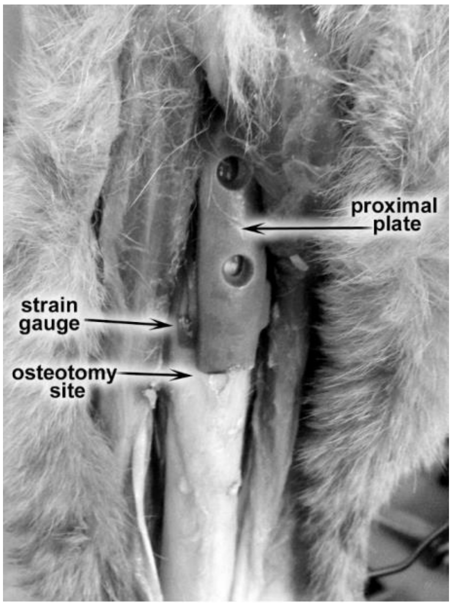

Figure 25: In this image, we can see where the strain gauge was placed.

After that the limbs were subjected to pre-surgical mechanical testing and lastly, succeeding the block removal of the distal portion of the radius, implants were placed with specific steps for each model. For both types of implants, the ulna was left intact and the cartilage was removed from the proximal surface of the radiocarpal bone.

For the commercial plates, the radial defect was filled with a 98 mm stainless steel spacer fixed to a limb-sparing plate (Veterinary Orthopedic Implants) with 2 machine screws. The plate was contoured to the bone surface with a plate-bending press (DePuy SynthesVet) and the distal portion of the arthrodesis plate was pre-bent to provide 12º of hyperextension. The proximal portion of the plate was applied to the cranial remnant of the radius and secured with six 3.5 mm stainless steel cortex screws (DePuy SynthesVet). The distal segment was then fixed with 2.7 mm stainless steel cortex screws (DePuy SynthesVet). A single 3.5 mm stainless steel cortex screw was placed in the radial carpal bone [24].

For the custom plate, the process is nearly identical to the commercial endoprosthesis except for the screws that were all in titanium.

In all cases, screw torque was limited to 2.0 Nm by using a calibrated precision torque screwdriver, adjustable in 0.1 Nm increments from 1.2-3.0 Nm, accurate to within ± 6 % (EN ISO 6789, Wera, Germany) [24]. *Figure 26* shows the two implant configurations after placement in a matched pair of forelimbs.

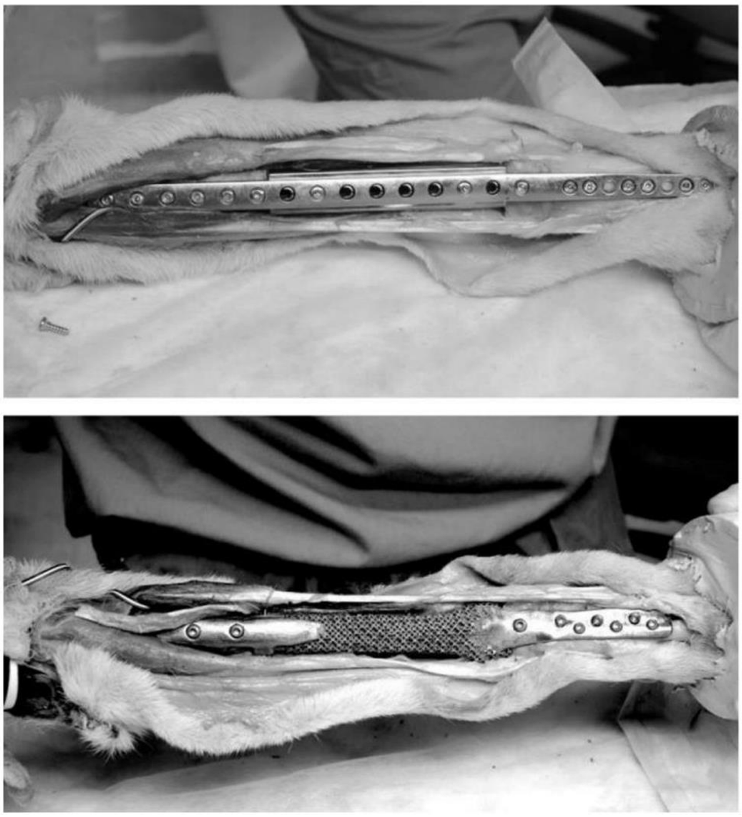

Figure 26: The image shows on the top the implant of commercial endoprosthesis and on the bottom the custom one.

6. **MECHANICAL TESTING OF LIMB SPARING CONSTRUCTS →** Mechanical testing was carried out before and after the surgical placement of implants using an ATS 1620C testing machine. For both pre-surgical and post-surgical tests, the loading was applied at a rate of 25.4 mm/min to a load of 260 N and unloaded to 12 N at a rate of 127 mm/min for ten cycles [24].

Figure 27: Those are photographs of the biomechanical testing, respectively before the surgical placement of the implant, after the surgical placement of the commercial endoprosthesis, and after the placement of the custom endoprosthesis.

For each limb pair, they recorded:

- the construct/limb stiffness, which was calculated as the slope of the linear portion of the load-displacement data and is shown in *Figure 28*:

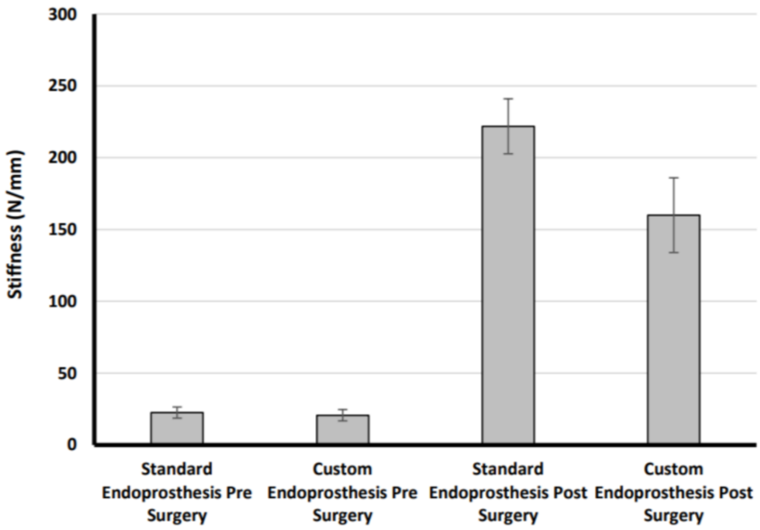

Figure 28: The graph shows the average stiffness for the limbs before and after surgery, for each configuration, with error bars indicating the 95% confidence interval.

Limbs reconstructed with the commercial and custom endoprostheses exhibited significantly higher stiffness after surgery than before surgery; in particular, commercial endoprostheses were significantly stiffer than custom endoprostheses (W=0.0313).

- The energy absorbed at 150 N, which was calculated from the area under the normalized load-displacement plot, it is shown in *Figure 29*:

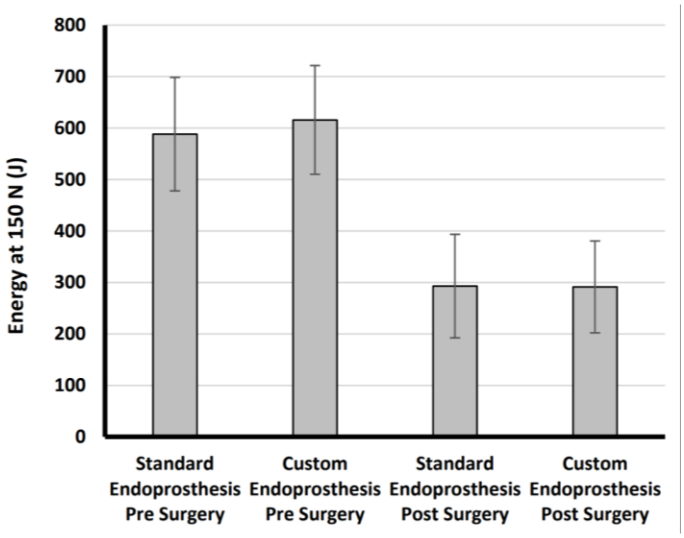

Figure 29: The graph shows the average energy (elastic potential energy) stored in the limbs before and after surgery, for each configuration at a load of 150 N (approximately 60% of the weight of the smallest dog), with the error bars that indicate the 95% confidence interval.

Limbs reconstructed with the commercial and custom endoprostheses exhibited significantly lower stored energy after surgery with no difference between Commercial endoprostheses and custom endoprostheses (W=0.500).

- The strain at 150 N that is shown in *Figure 30*:

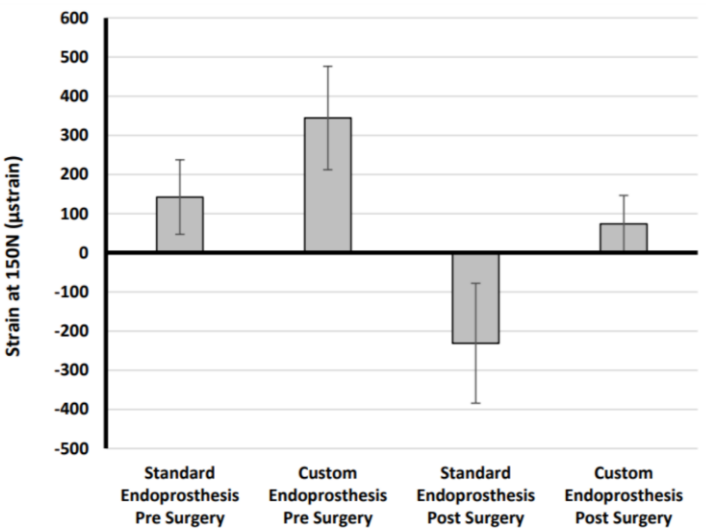

Figure 30: The graph shows the average measured strain at the distal portion of the radial remnant before and after surgery, for each implant configuration, at a load of 150 N.

Limbs treated with commercial endoprosthesis exhibited significantly different strains compared to presurgical strains: while presurgical strains tended to be tensile, post-surgical strains were compressive on the cranial surface of the distal portion of the radial remnant. Instead, limbs reconstructed with custom endoprostheses remained tensile, but they were significantly lower than untreated limbs (W = 0.0313).

The high stiffness of the stainless steel endoprosthesis leads to stress concentrations resulting in stress shielding and bone resorption at the bone implant interface. The results presented in this study suggest that the reductions in the relative density of the bulk Ti6Al4V material associated with the use of porous geometric lattice structures contribute to a loading profile that is similar to pre-surgical conditions compared to the significantly stiffer stainless steel endoprosthesis. However, this study could not isolate the effects of material stiffness from the geometric variations between the different implant designs.
In this study, limbs have been non-destructively tested in axial loading for ten cycles because clinical failures have not been reported to be acute, rather, they appear to be the result of cyclic loading and fatigue failure. The results showed no difference in the stiffness associated with each loading cycle [24].

THIRD MODEL UNDER REVIEW

We will now conduct a highly detailed analysis of the study on the endoprosthesis model proposed by James S.P., Santoni B.G., and Heyliger P.R in the article "Development of a novel endoprosthesis for canine limb-sparing using a finite element approach" [32].

In this study in order to evaluate the current endoprosthesis and facilitate novel designs for canine limb-sparing, a finite element model of the canine antebrachium was developed using computed tomography data. The following summarizes the steps taken to obtain the model and the results of the experimental tests conducted on it.

MODEL GENERATION:

- GEOMETRY
    - BONY GEOMETRY → The bony geometry for the canine forelimb finite element model was based on cadaveric CT image data, they used the forelimb of a 38 Kg Chesapeake Bay retriever. The model was limited to the antebrachial, carpal, and metacarpal regions. All voxels on the exterior with intensity values greater than 1000HU were deemed cortical bone while the remaining voxels within the metaphyseal regions of long bones were labelled as trabecular bone. Initially, all bones were meshed with tetrahedral elements using the automated mesh generator in AMIRA. Hence, a total of three models of increasing mesh resolution were generated to establish convergence [32].

    - ARTICULAR CARTILAGE → cartilage was extruded as a three-element thick layer from all osteochondral surfaces with a constant thickness (0.6 at the distal end of the radius, 0.5 on the carpal bone, 0.2 at all others) [32].

    - LIGAMENTS → were modelled as one-dimensional, non-linear spring elements.

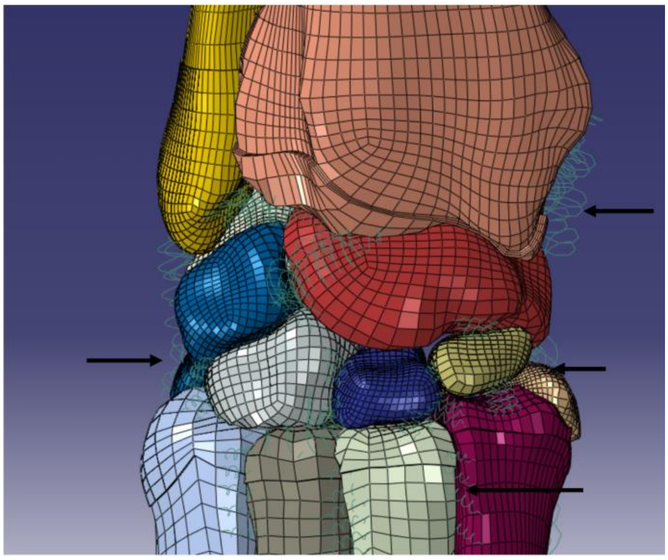

Figure 31: It represented all the geometry previously described.

- MATERIAL PROPERTIES

  - CORTICAL AND TRABECULAR BONE → Both the cortical and trabecular bones were modelled as linearly elastic and isotropic because the primary loading of all bones in the canine forelimb is in the axial direction. The Young's modulus of cortical bone was set at 15GPa with a Poisson's ratio of 0.3. The Young's modulus of trabecular bone was set at 4000MPa with a Poisson's ratio of 0.3. [32]

  - ARTICULAR CARTILAGE → Articular cartilage was modelled as a Mooney-Rivlin hyperelastic material, the values of the coefficients used in this study were: C_{01} = 0.22 MPa and C_{10} = 2.5 MPa defining the deviatoric response of the material and D = 0.06 defines the volumetric response of the material. The slope in the operating range of the nonlinear curve was approximated to be 15 MPa (Young's modulus of human knee cartilage). [32]

  - LIGAMENTS → For the six important stabilizing ligaments described, the data were obtained from uniaxial tensile tests. The interosseous ligament was modelled as a linear spring with a high stiffness coefficient (k=100000 N/mm) to represent the extremely stiff nature of this ligament. [32]

  - ENDOPROSTHESIS → The spacer, DCP, and cortical screws were made of stainless-steel grade 316L. The Young's modulus was set at 193 GPa and the Poisson's ratio was defined as 0.3 for all three parts. [32]

MODEL CONVERGENCE

A total of three models with increasing mesh resolution were created using TrueGrid and ABAQUS. Model convergence was examined throughout the complete load range. The parameters examined were bone strains of radius and ulna total area in contact within the radiocarpal joint and displacement of the radial carpal bone. The convergence threshold was set at 10%.

MODEL VALIDATION

- CADAVER EXPERIMENTS → For the purposes of model validation, eight forelimbs were obtained from the Colorado State University's Veterinary Teaching Hospital. All extraneous soft tissue was excised from the limbs to attain a clean surface for strain gauge attachment. The strain gauges were used to measure surface strain at three locations (proximal, mid-diaphyseal, distal) on the radius and the mid-diaphyseal region on the ulna, in *Figure 32* we can see their location.

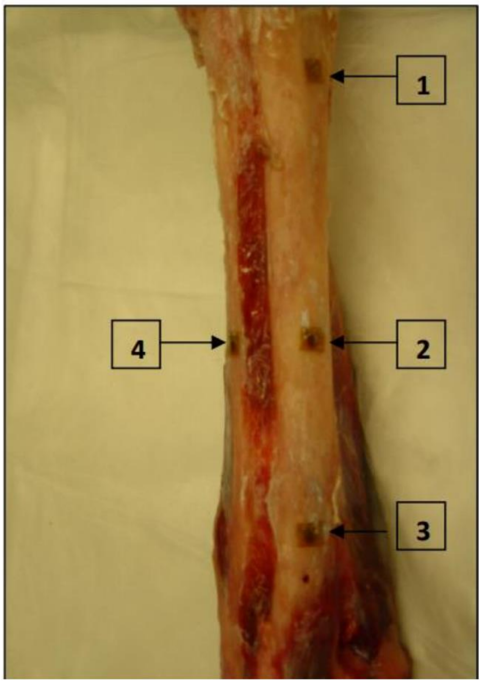

Figure 32: In this figure, there are indicated the location of the four strain gauges used.

The complete construct was fixed in a custom-designed apparatus for testing canine forelimbs where the distal ends of metacarpals II-IV were potted in polymethylmethacrylate and the angle between the antebrachial region and the humerus was set at 135 degrees while the angle between the metacarpal region and the antebrachial region was set at 10 degrees (from vertical) of extension. A single marker was attached to the caudal end of the radial carpal bone to measure its total displacement through the loading cycle. The limb was loaded to 110% BW, which is the load observed in the forelimb at trot [32].

The forelimb was first loaded with all extensor tendons intact then, in the second regime, all tendons supporting load under extension were resected since the finite element model did not include any of these tendons.

- VALIDATION RESULTS → The validation parameters investigated in this study were: bone surface strains and radial carpal bone motion. They analysed the approximate area where the experimental strain gauges were attached.

  Interestingly, a decreasing trend in the values of maximum principal strains was observed for the strain gauges on the radius, while the maximum principal strain values increased at the mid-diaphysis of the ulna, indicating a biomechanical change in the joint after tendon resection.

  The model predicted a displacement of 11.45mm and the average ± SD value obtained from the validation tests was 10.1±1.55mm [32].

After creating a finite element model of the limb, they used this model to test the currently available second-generation prosthesis with the aim of identifying failure points and all related issues.
For this purpose, first, they created a finite element model of the second-generation endoprosthesis, both the spacer and the dynamics compression plate, and the proximal radius, as we can see in *Figure 33.*

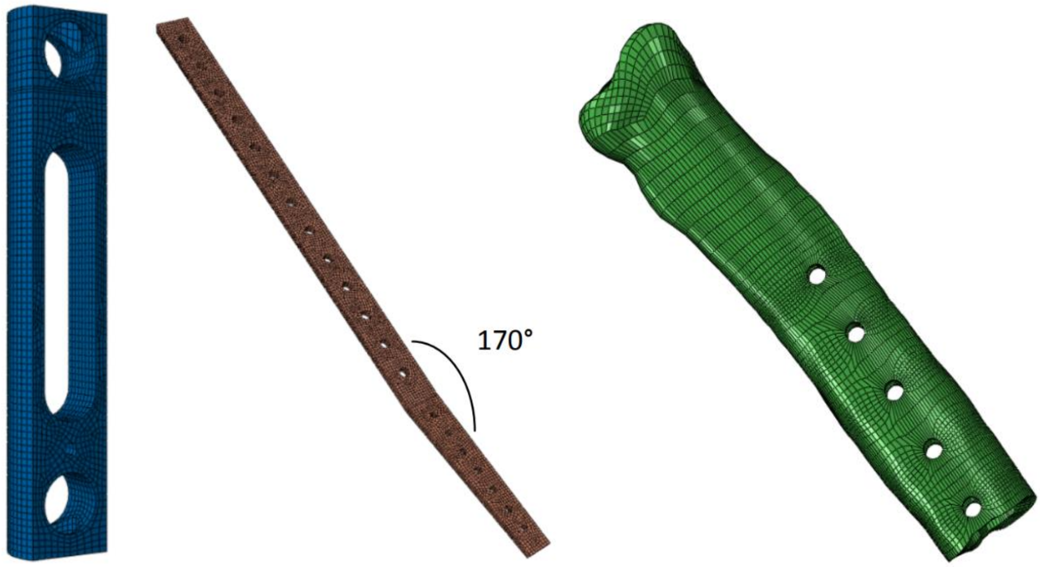

Figure 33: On the right, there is the proximal radius whit holes for the implant screws, on the centre there is the dynamic compression plate (DPC) and on the left, there is the endoprosthesis spacer.

After that they resected the radius by 50% from the distal end, and then the complete prostheses construct was imported into ABAQUS and incorporated with the intact canine forelimb model, in the end, potential areas of failure were investigated by evaluating the endoprosthesis spacer under a load of 400N in compression, was also examined the effect of distal support to the endoprosthesis. In *Figure 34* there is the final model.

Figure 34: This is the final model incorporating the current endoprosthesis and the bone model.

Other parameters were set in order to recreate the leg structure such as:

To simulate the fusion of all carpal bones, the ligaments connecting these carpal bones were given a high spring stiffness coefficient (k=10,000N/mm). To simulate a complete union between the screws inserted in the proximal radius a friction coefficient of 0.99 was established between the two contacting surfaces. The friction coefficient between the screw heads and the non-locking plate was set at 0.25: the effect of using a locking plate in place of the current non-locking plate was also investigated by using a tie-constraint between the screw heads and plate for simulated the locking mechanism. [32]
Support at the distal end of the spacer was simulated with a tie constraint between the spacer and the proximal surface of the radial carpal bone [32].

The results they found with the compression test are the following.
Regarding the screws in the proximal part of the model with a non-locking plate construct, they found a maximum von Mises stress of 405.3 MPa [32]. Additionally, ignoring stress concentrations arising from point contact between the screw head and the dynamic compression plate, a maximum average stress of 210 MPa was predicted at the third radial screw (*Figure 35*).

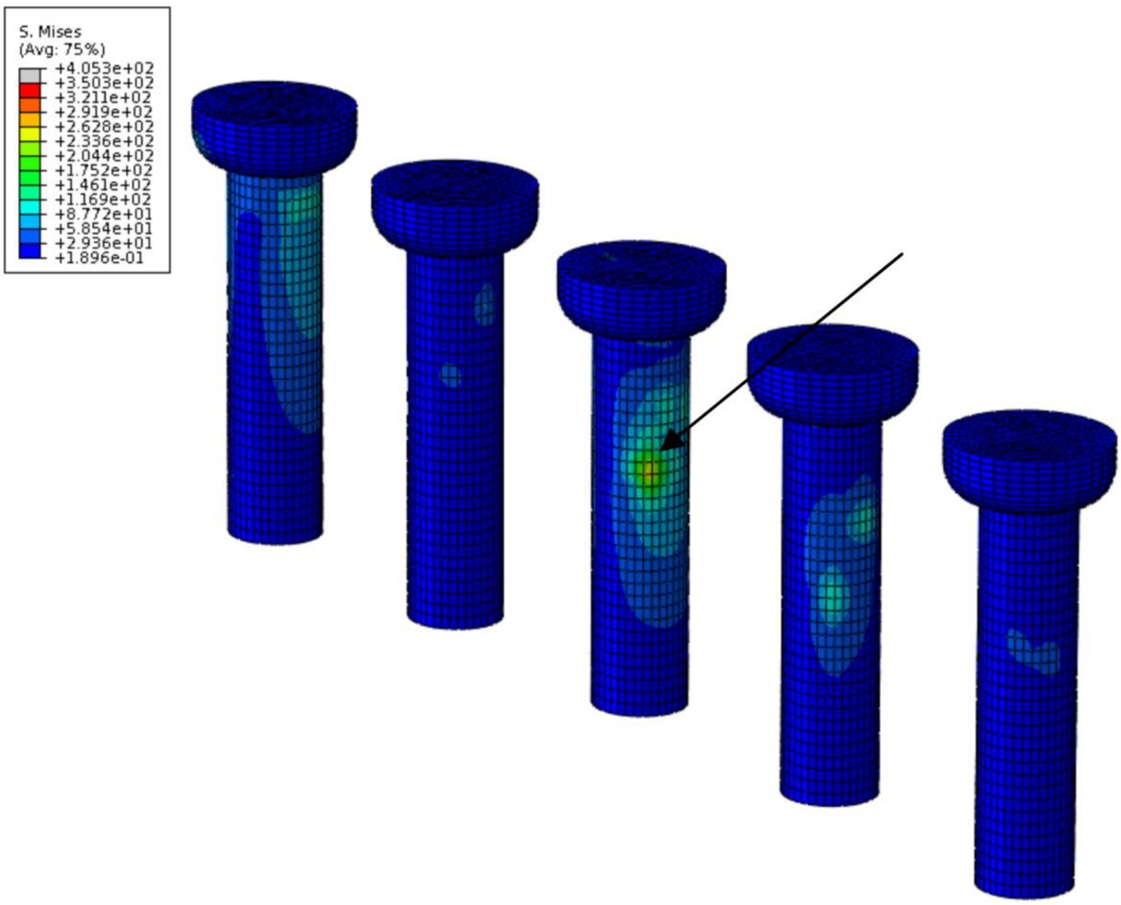

Figure 35: In this image, we can see the von Mises stress distribution for the proximal radial screw. The arrow indicates the location of the maximum stress of 405.3 MPa.

Concerning the radius, they found that the maximum stress predicted was 559MPa (*Figure 36*).

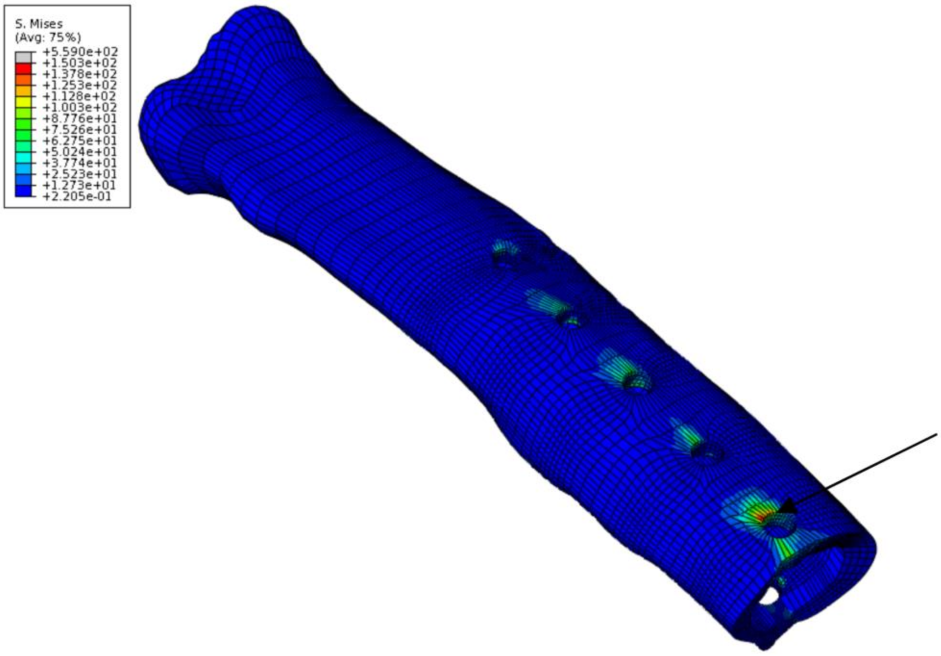

Figure 36: In this image, we can see the von Mises stress distribution of the radius. The arrow indicates the location of the maximum stress of 559 MPa.

For the distal part of the model they found that the maximum von Mises stress for the distal metacarpal screws was 128MPa (*Figure 37*) while for the bone of the 3rd metacarpal was 76MPa (*Figure 38*).

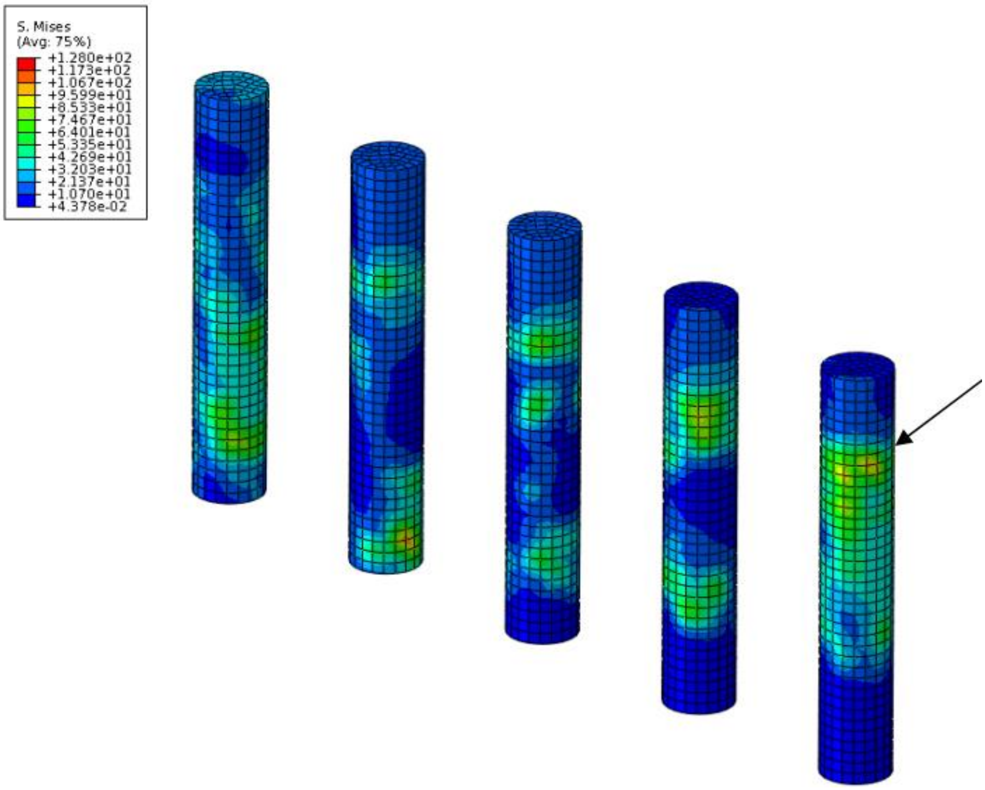

Figure 37: In this image, we can see the von Mises stress distribution for the distal metacarpal screw. The arrow indicates the location of maximum stress of 128 MPa.

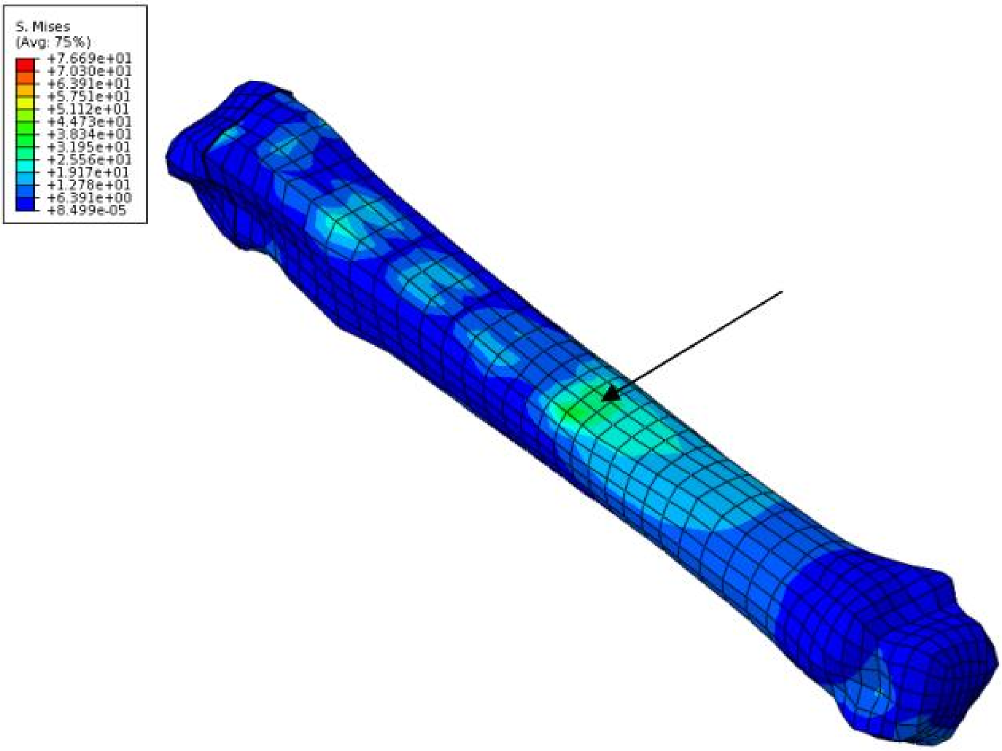

Figure 38: In this image, we can see the von Mises stress distribution of the 3rd metacarpal bone. The arrow indicates the location of the maximum stress of 76 MPa.

Regarding the screws connecting the metal endoprosthesis spacer to the dynamic compression plate, their maximum von Mises stress prediction was 340.7MPa (*Figure 39*).

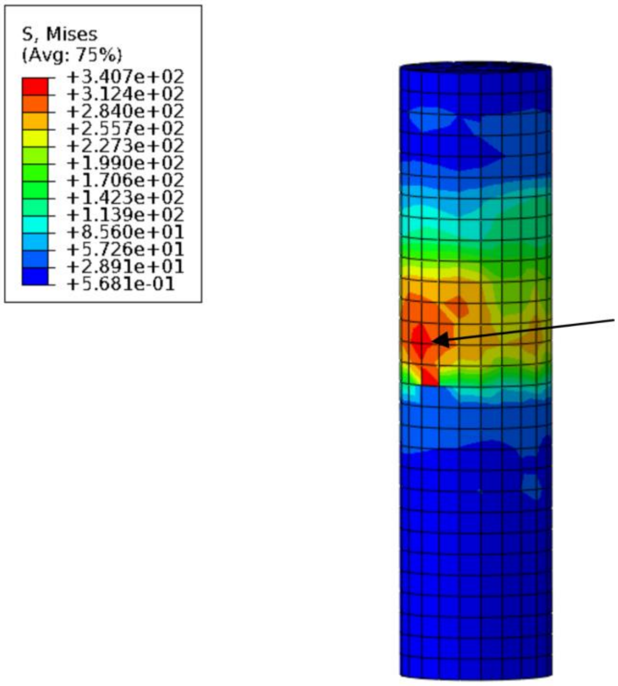

Figure 39: In this image, we can see the von Mises stress distribution of the endoprosthesis spacer screw. The arrow indicates the location of the maximum stress of 340.7 MPa.

The endoprosthesis spacer reported a maximum von Mises stress of 124.1MPa, as we can see in *Figure 40*.

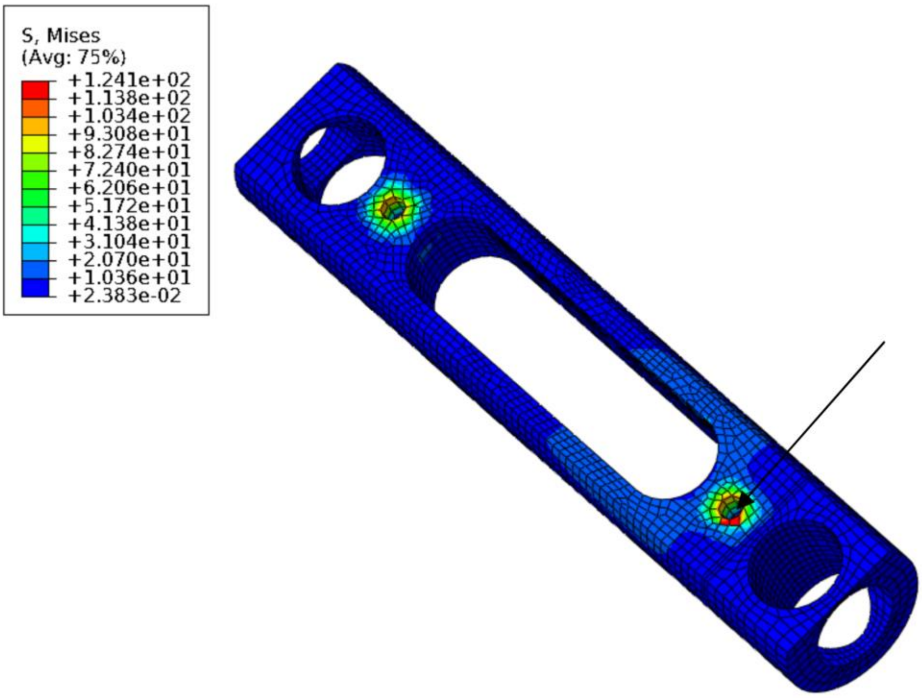

Figure 40: In this image, we can see the von Mises stress distribution of the endoprosthesis spacer. The arrow indicates the location of the maximum stress of 124.2 MPa.

The maximum von Mises stress within the dynamic compression plate was 126.2MPa as shown in *Figure 41*.

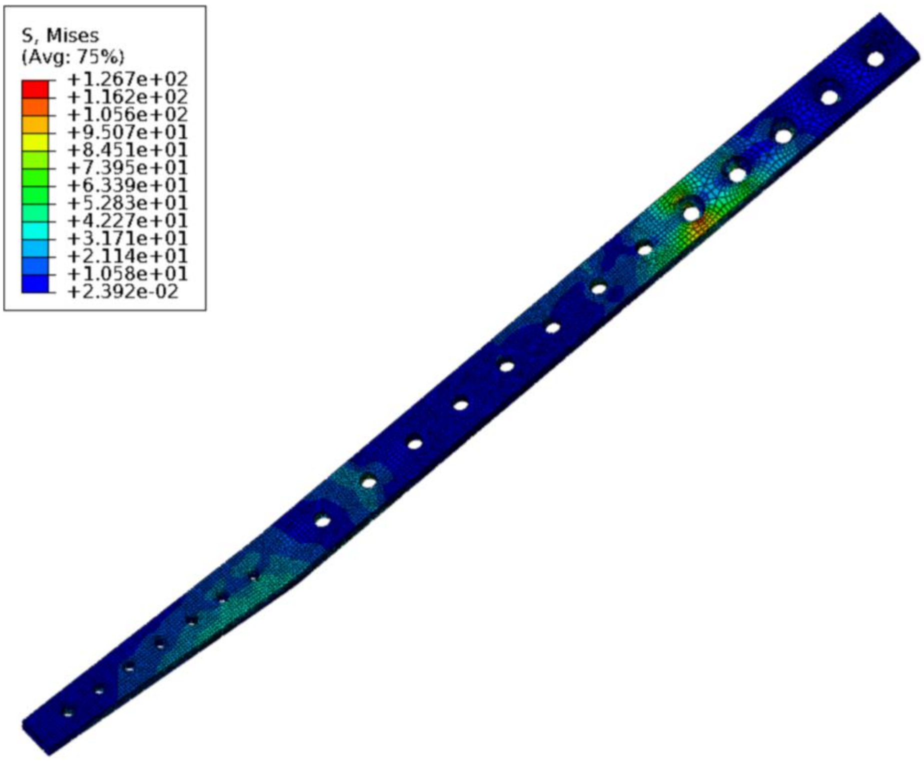

Figure 41: In this image, we can see the von Mises stress distribution of the dynamic compression plate.

Figure 42 shows a comparison of maximum stress predictions between the locking and non-locking plate constructs. As we can see for the model with the locking plate construct the maximum von Mises stress predicted within the proximal radial screws decreased slightly to 397MPa as compared to the non-locking construct. The maximum stress within the radius remained similar (574MPa). The maximum stresses within the distal metacarpal screws decreased by 20MPa to a value of 109.7MPa as compared to the non-locking plate construct. Stresses within the spacer screws decreased to 299.9MPa (340MPa). The maximum stresses within the endoprosthesis spacer were predicted to be 114.4MPa. [32]

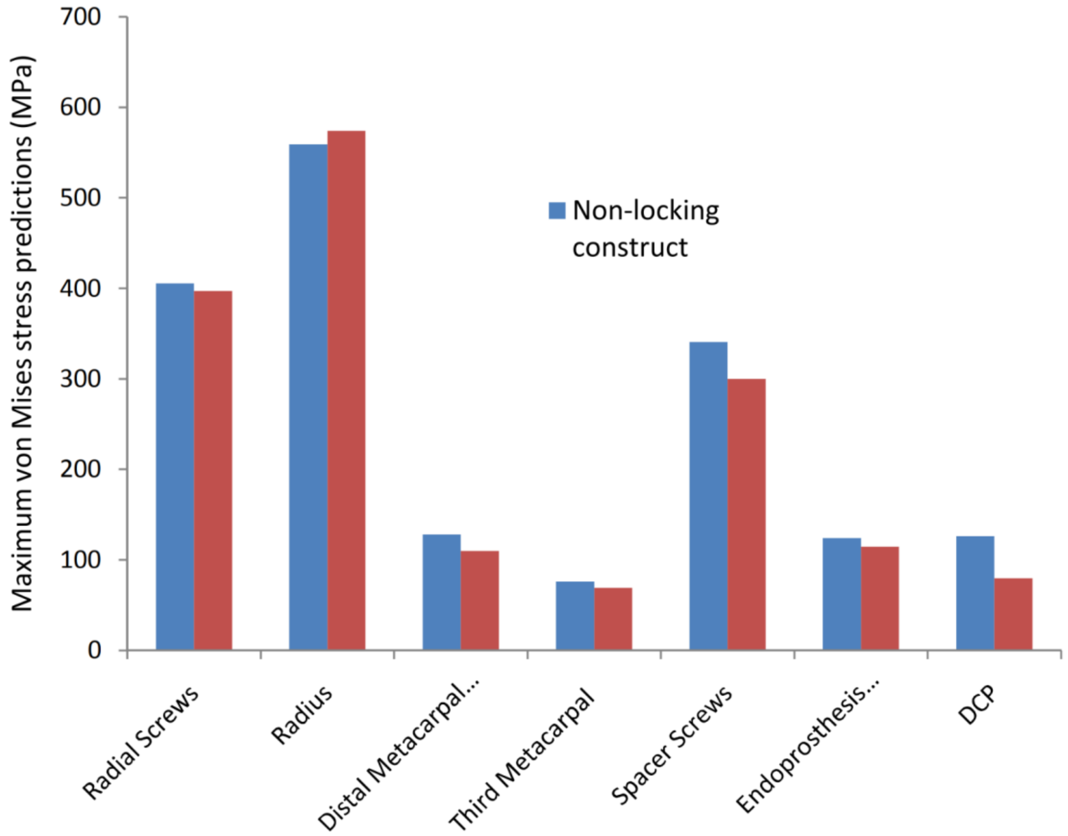

Figure 42: In this image, we can see the comparison of von Mises stress between the non-locking and the locking construct.

From the result we can see that the high stresses, for both the plate construct, were observed at the bone-screw interface in the proximal radius and also within the radial screws; considering the fatigue limit of 316L stainless in the body environment is 200MPa for 10 million cycles of loading the predicted stresses are too high for sustained performance of this endoprosthesis. So, the observed failure of the proximal screws in the clinical setting is congruent with the findings in this finite element study. [32]

In summary, the are no differences between the use of a locking plate or the non-locking plate concerning the stresses observed at the bone-screw interface (574MPa) or within the radial screws (404MPa); however, there is a great difference within the dissipation of stress observed in the proximal radius around the screw holes, as we can see in *Figure 43.*

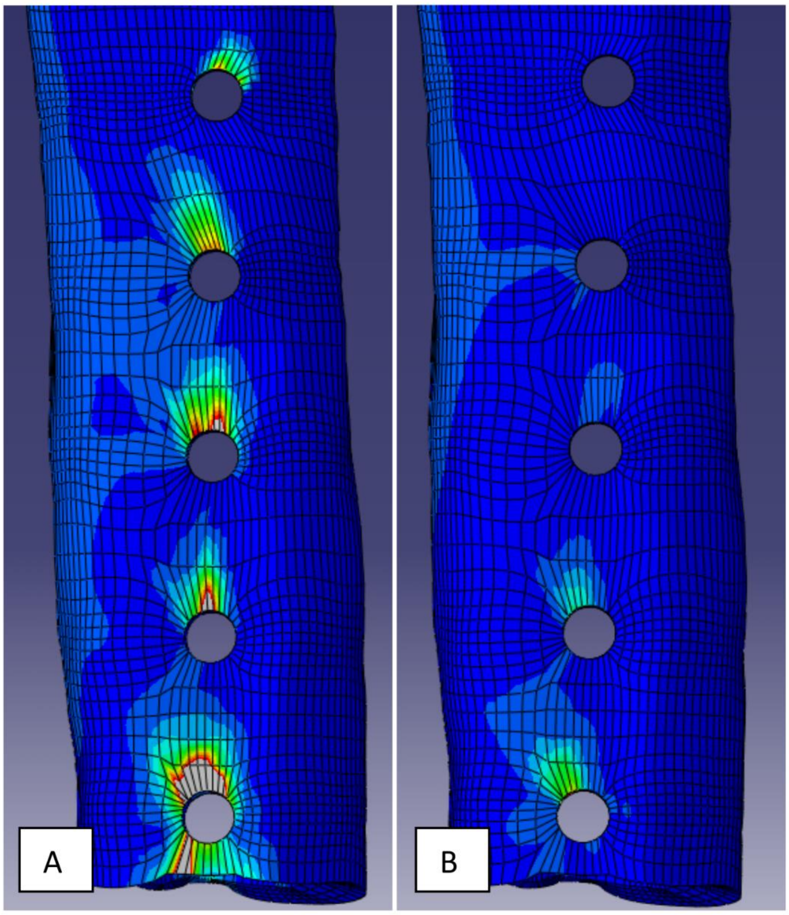

Figure 43: In this image, we can see the stress dissipation for the locking plate constructs (A) and the non-locking plate construct (A)

The high stresses predicted by the model in the proximal radius bone-screw interface are congruent with the screw loosening observed clinically.

Having identified the main problem of these second-generation endoprostheses, they attempted to design and test new models, using simplified models of idealized 3rd metacarpal and radius bones to reduce the computational time involved in testing. They proposed two different designs:

- DESIGN #1 → The intramedullary stem approach attempted to remove the off-axis loading observed in the earlier endoprosthesis by inserting an intramedullary stem which provides a higher area in contact with the native bone; while it retained the plate feature at the distal end of the implant, justified by the low stresses observed in this region during previously evaluation. It is shown in *Figure 44*. [32]

- DESIGN #2 → The collar approach attempted to reduce the load on the proximal radial screws by providing an additional plate on the opposing side, to eliminate excessive rotation of the radius and also provided support at the distal end of the radius. Also, this model retained the plate feature at the distal end of the implant, justified by the low stresses observed in this region during the previous evaluation [32]. It is shown in *Figure 45*.

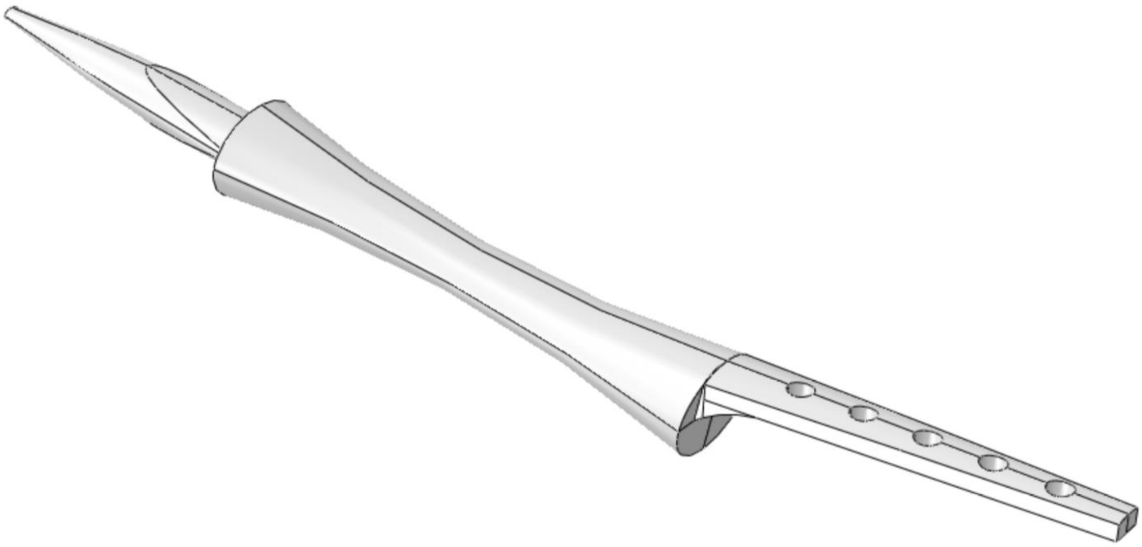

Figure 44: The initial design of model one of the endoprosthesis, called DESIGN #1.

Figure 45: The initial design of model two of the endoprosthesis, called DESIGN #2.

The two proposed designs were presented to the investigative team who noted some issues:

- For design #1 the main problems were its inability to achieve consistent orientation with the radius and the lack of a modular design, which is a problem due to the significant size variability of dog breeds.

- For design #2 the main problems were the lack of space between the radius and ulna for inserting the collar and also the lack of a modular design.

Also, the surgeons on the investigative team made specific requests such as the modular design, the ease of alignment between the proximal radius section and the carpus, and stress reduction within the radial screws.

After recommendations, the final model merged the two designs, as we can see in *Figure 46*, and incorporated a modular design whose primary components consisted of three independent parts, namely:

- The proximal endoprosthesis component (PEC): consisted of an intramedullary stem and a 180-degree wrap-around plate with locking screw holes at 45 degrees to the sagittal plane of the radius. It also included a lip to provide added stability to the proximal end of the resected radius.
- The mid-diaphyseal endoprosthesis component (MEC): it was designed to be simple for its geometry so there can be multiple sizes of the component and the surgeon can more accurately fit the endoprosthesis to the length of the patient's limb.
- The distal endoprosthesis component (DEC): it was designed with a 10-degree bend to mimic the physiological position of the canine radiocarpal joint at maximum extension and with six distal locking screw holes (2.7 mm cortical screws) for fixation with the 3rd metacarpal and a proximal screw hole (3.5 mm cortical screw) for radial carpal bone fixation.

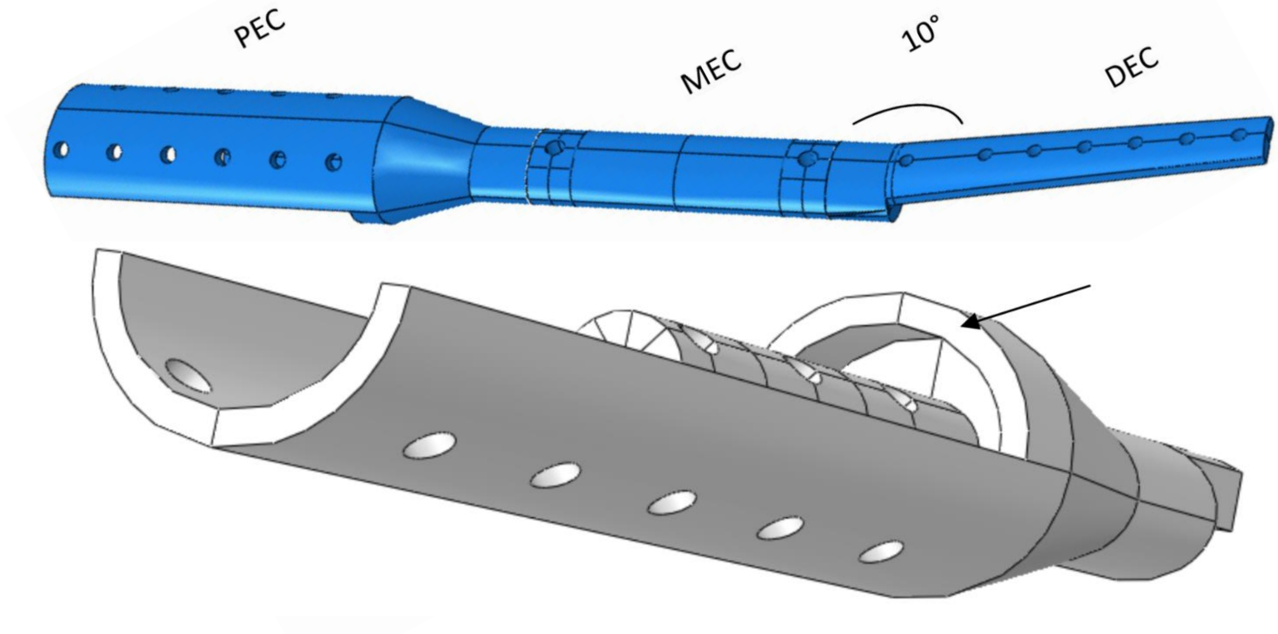

Figure 46: The design after the investigative team request and suggestion.

The complete construct, endoprosthesis, and idealized shape of the 3rd metacarpal and radius bones were evaluated at a load of 1000N with threaded interfaces simulated by a coefficient of friction of 0.99 signifying complete union. [32]

As a result of this first evaluation, they observed that the proposed design for the PEC was successful in eliminating high stresses within the proximal radial screws, the proposed design for the MEC was deemed acceptable for implantation, but they also observed that the 10-degree bend incorporated in the DEC was causing significant offset loading, resulting in unacceptably high bending stresses within the distal screws.

A second model of the DEC with zero degrees of extension was created and from its evaluation, they found that this model reduced the maximum stress prediction within the distal screws. So, the three final components of the model are the following as represented in *Figure 47*:

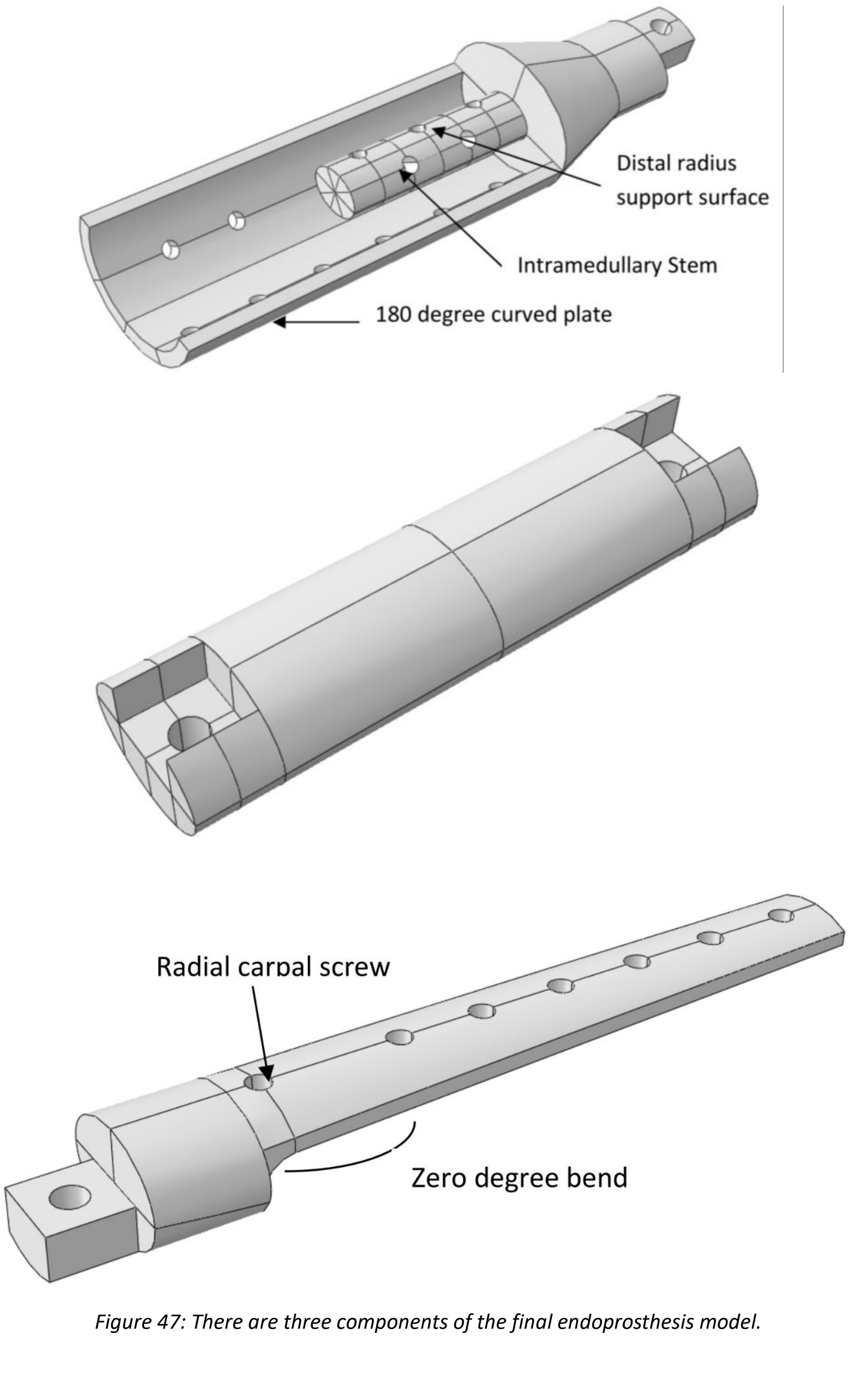

Figure 47: There are three components of the final endoprosthesis model.

The technical parameters they set were: the contact between all articulating surfaces of the implant was established with a coefficient of friction of 0.25, while between the distal radius surface and the PEC with a coefficient of friction of 0.1. All metallic components were made from 316L stainless steel with a Young's modulus of 193GPa and a Poisson's ratio of 0.3. All springs connecting the carpal bones were given a stiffness value of 110N/mm. The construct was implanted in the intact FE element model and loaded to 500N. [32]

There was one more clinically relevant problem: the intra-operative difficulty in obtaining proper alignment between the proximal radius and the carpus after tumor resection. To manage this issue an intra-operative apparatus was designed to aid the surgeons in aligning the proximal radius and carpus that is shown in *Figure 48*.

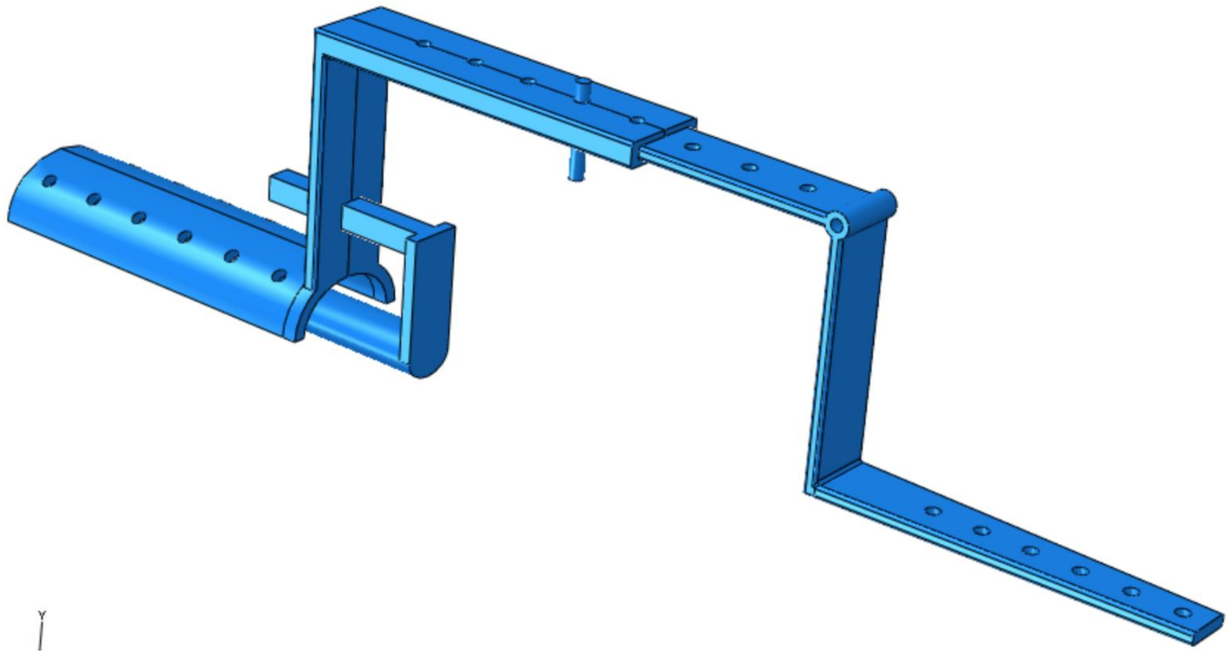

Figure 48: The intra-operative apparatus they create in order to facilitate the alignment of bones during the surgery.

Finally, after finding solutions to all the issues, they proceeded with the analysis of the new model, and the test results are reported below.

In *Figure 49* we can see the von Mises stress distribution for the metacarpal screws: a maximum von Mises stress of 216.9MPa was predicted at the most distal screw, and the average von Mises stress was 110MPa, located between the plate and bone interface. [32]

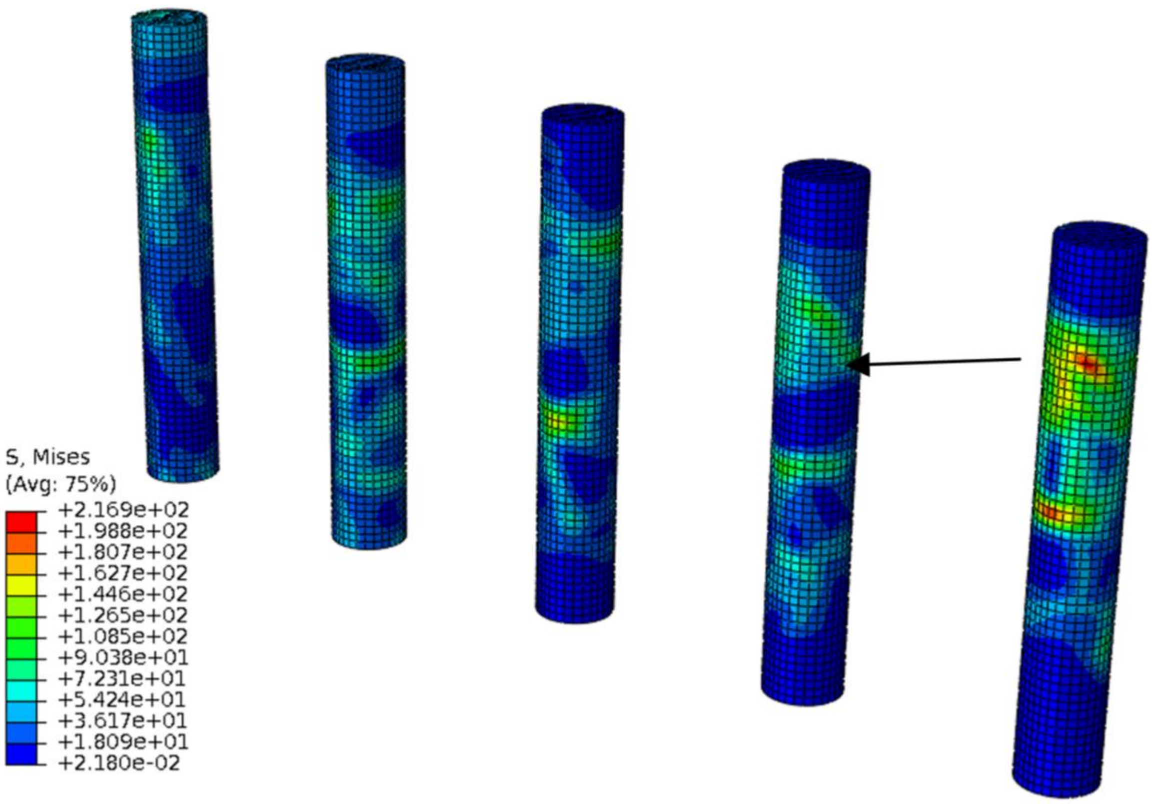

Figure 49: In this image, there is von Mises stress distribution for all the distal metacarpal screws.

In *Figure 50* we can see the von Mises stress distribution for the proximal radial screws: a maximum von Mises stress of 205.2MPa was observed, with an average von Mises stress of 95MPa.

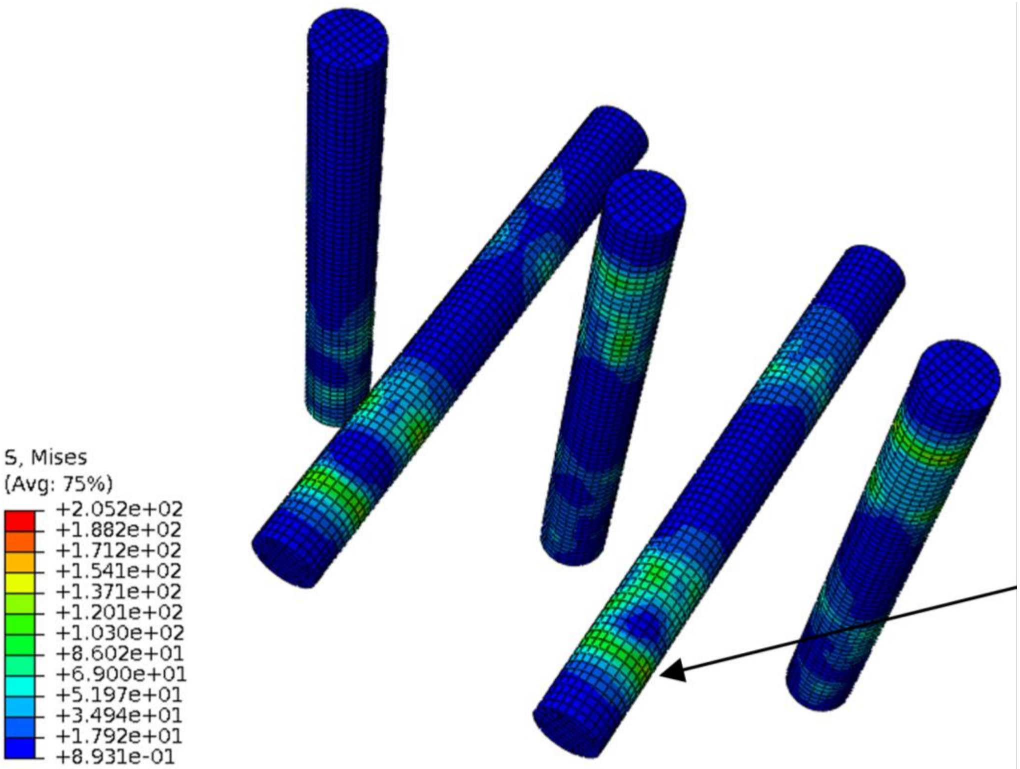

Figure 50: In this image, there is a von Mises stress distribution for all the proximal radial screws.

The results of von Mises' stress (*Figures 51, 52, 53, 54, 55*) are shown below.

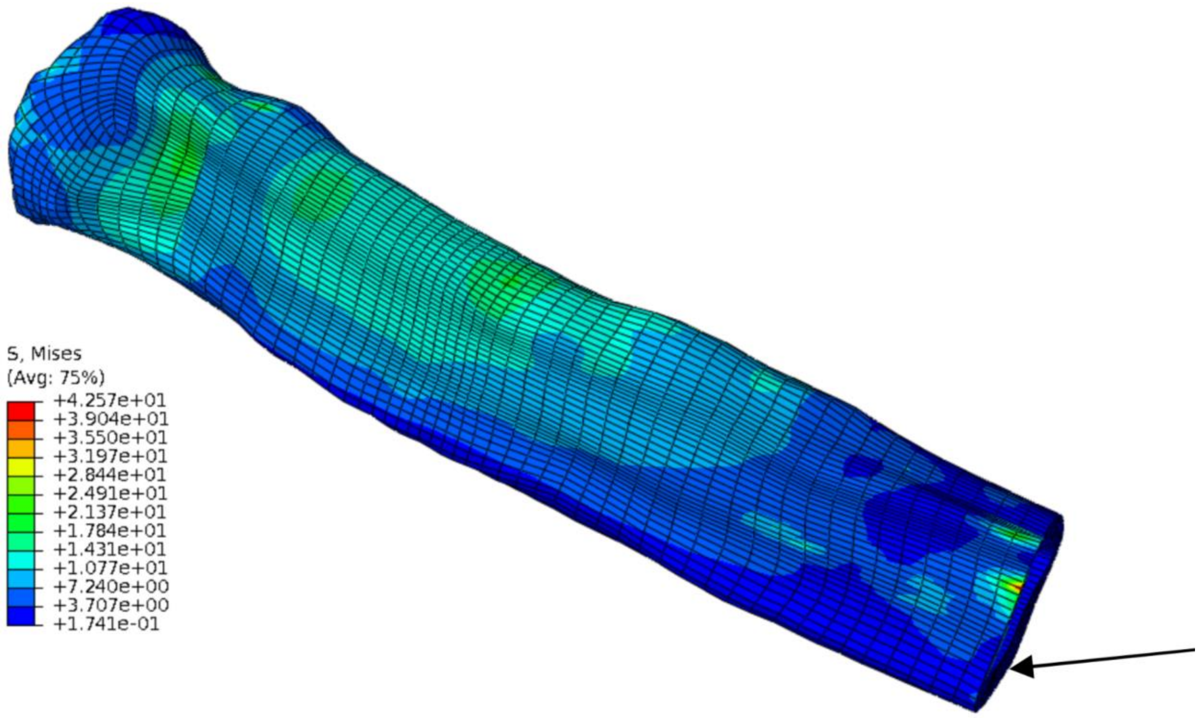

Figure 51: In this image, the von Mises stress distribution is in the radius: the maximum stress is 42.5 MPa.

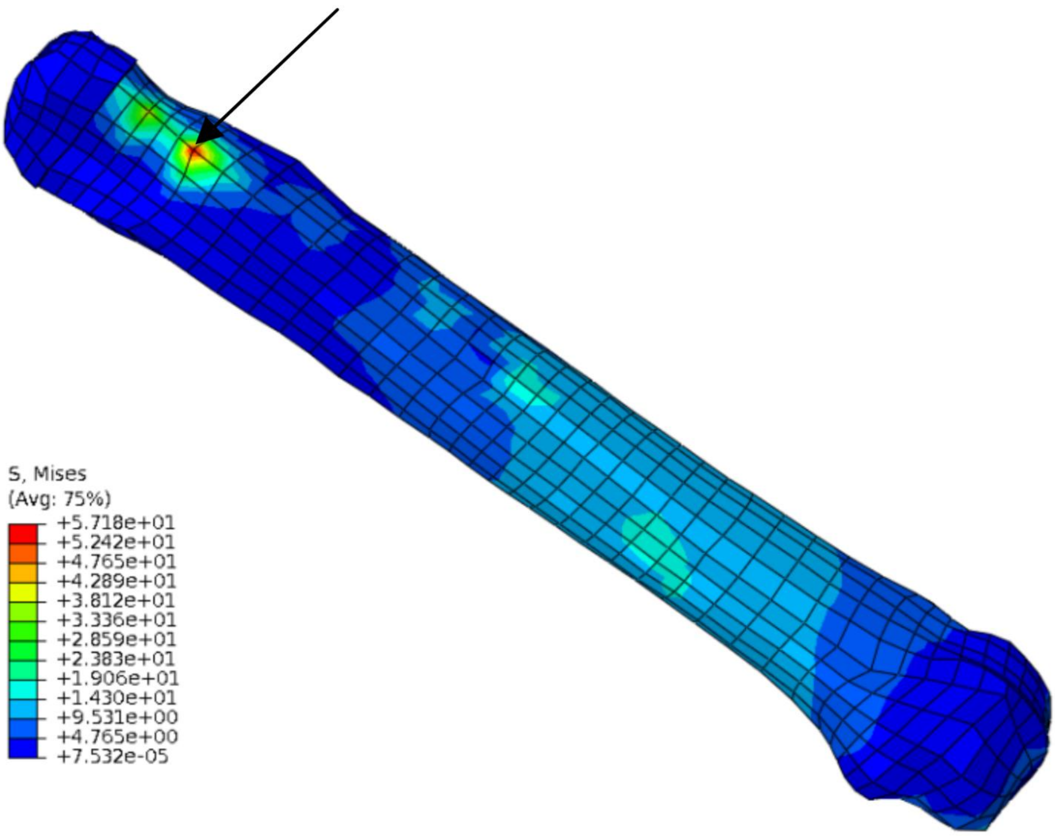

Figure 52: In this image, the von Mises stress distribution is in the third metacarpal bone: the maximum stress is 57.1MPa.

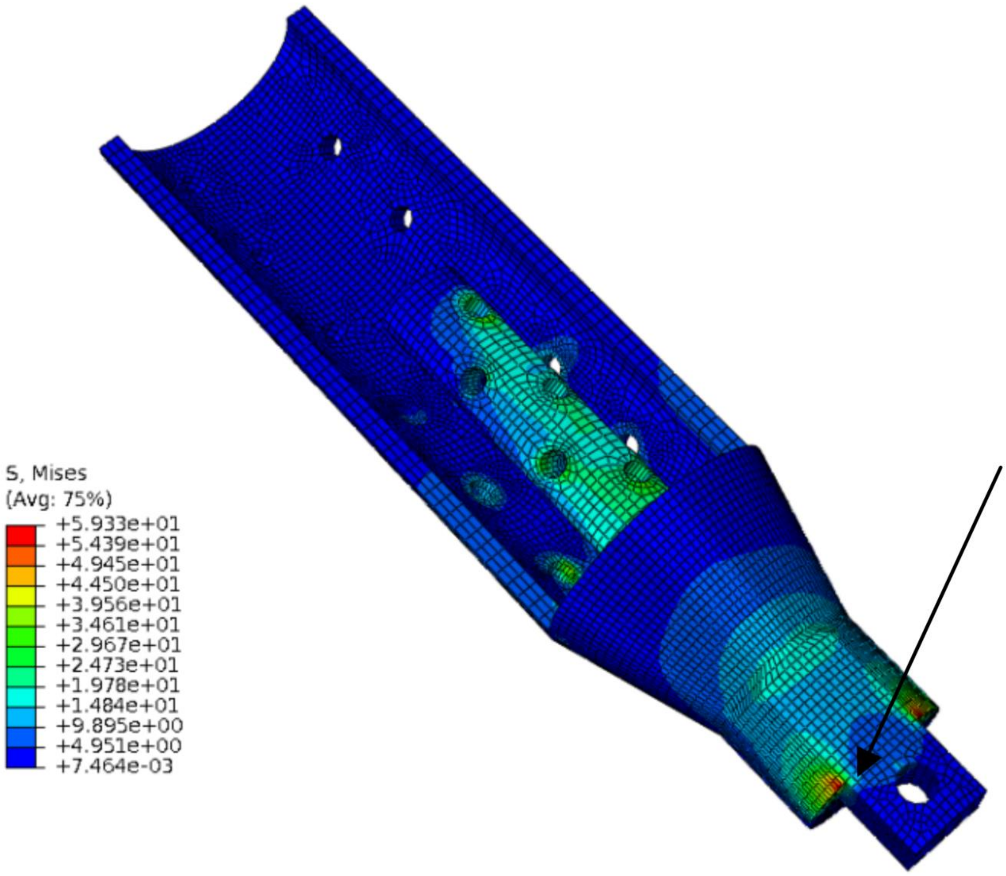

Figure 53: In this image, the von Mises stress distribution is in the PEC: the maximum stress is 59.33MPa.

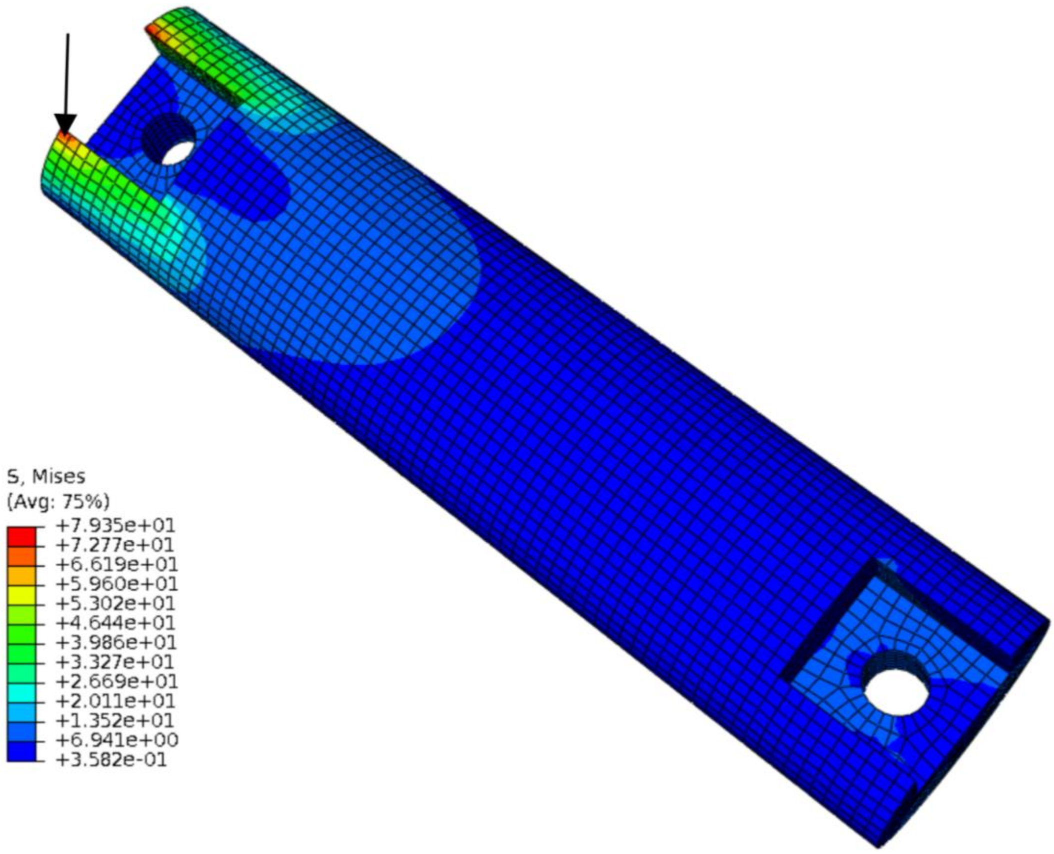

Figure 54: In this image, the von Mises stress distribution is in the MEC: the maximum stress is 79.3 MPa.

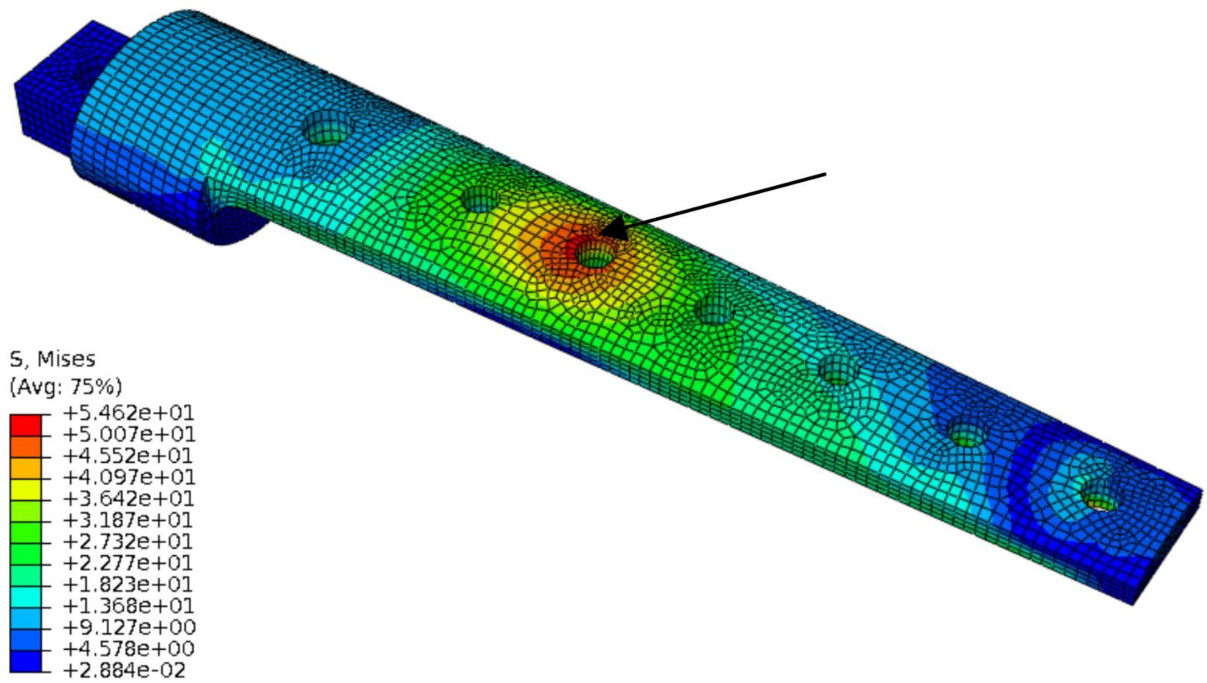

Figure 55: In this image, the von Mises stress distribution is in the DEC: the maximum stress is 54.62MPa. The 3.5 mm screws connecting the MEC to the PEC and DEC had a maximum von Mises stress of 46.01MPa.

In conclusion, the improvements introduced by this new model designed in this study were as follows: thanks to the new angle of the screws into the proximal radius bone, the bending force they were subjected to has significantly decreased. Moreover, this allowed for the replacement of 3.5 mm screws with 2.7 mm ones. With these adjustments, along with the use of locking screws instead of non-locking ones, they were able to reduce the von Mises stress peak by 50% for the screws inserted into the proximal radius [32].
The introduction of the intramedullary stem also contributed to reducing the von Mises stress on the proximal radius screws. By tying the distal surface with the radial carpal bone, they manage to reduce the stresses in the most proximal screw in the 3rd metacarpal.

An important point to highlight is the fact that the distal metacarpal screws are the weakest components of the entire implant. Therefore, when possible, meaning when the bone is thick enough, it is preferable to use 3.5 mm screws instead of 2.7 mm ones, as in the case of large-giant breed dogs [32].

As in all studies, there are biases to consider regarding the experimental measurements of stress. Specifically, in this study, the biases are due to the tie constraints employed in a node-to-surface approach for the coupling of bone and screw motion because the software only includes stress optimization algorithms with surface-to-surface tie constraints. The stress anomalies produced due to the contact tie constraints employed are a confounding factor, however, the use of the average stress value mitigates this effect when evaluating the peak stresses in the implant and screws.

CHAPTER 1: FORELIMB'S BIOMECHANICAL ANALYSIS

FORELIMB'S ANATOMY

Before proceeding with the creation of FEM models for our analyses, it is essential to analyse the biomechanics of the dog's limb. In particular, we will focus on studying the anatomy and biomechanics of the canine forelimb, which is the one most commonly affected by osteosarcoma according to data in the literature. The entire forelimb consists of the scapular, axillary, brachial, cubital, antebrachial, carpal, metacarpal, and phalangeal regions but only the antebrachial, carpal, and metacarpal regions are typically involved in limb-sparing procedures [24]. In *Figure 56,* it is represented the bony anatomy of these regions:

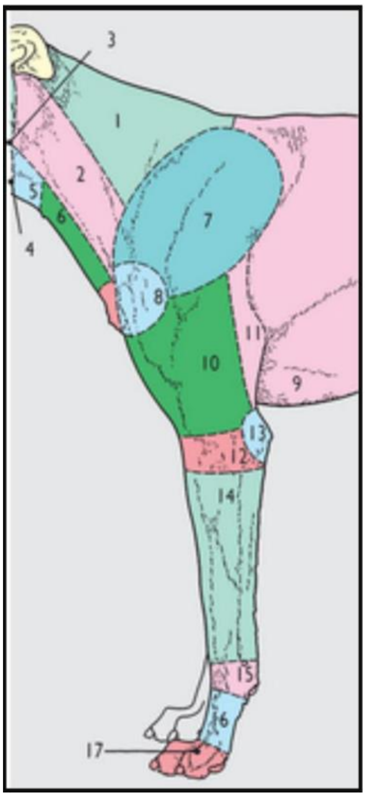

Figure 56: We can see the main anatomic regions: Scapular Region (7), Axillary Region (9), Brachial Region (10), Cubital Region (12), Antebrachial Region (14), Carpal Region (15), Metacarpal Region (16), Phalangeal (Digital) Region (17).

Delving further into detail, the three main regions of interest for limb-sparing surgery, along with the respective bones involved, are the following:

- The antebrachial region consists of the radius and ulna.
- The carpal region consists of a total of seven bones divided into two transverse layers: the proximal one consists of the radial carpal, ulnar carpal, and accessory carpal bones and the distal one consists of the numbered carpal bones I-IV.
- The metacarpal region consists of the numbered metacarpal bones I-V.

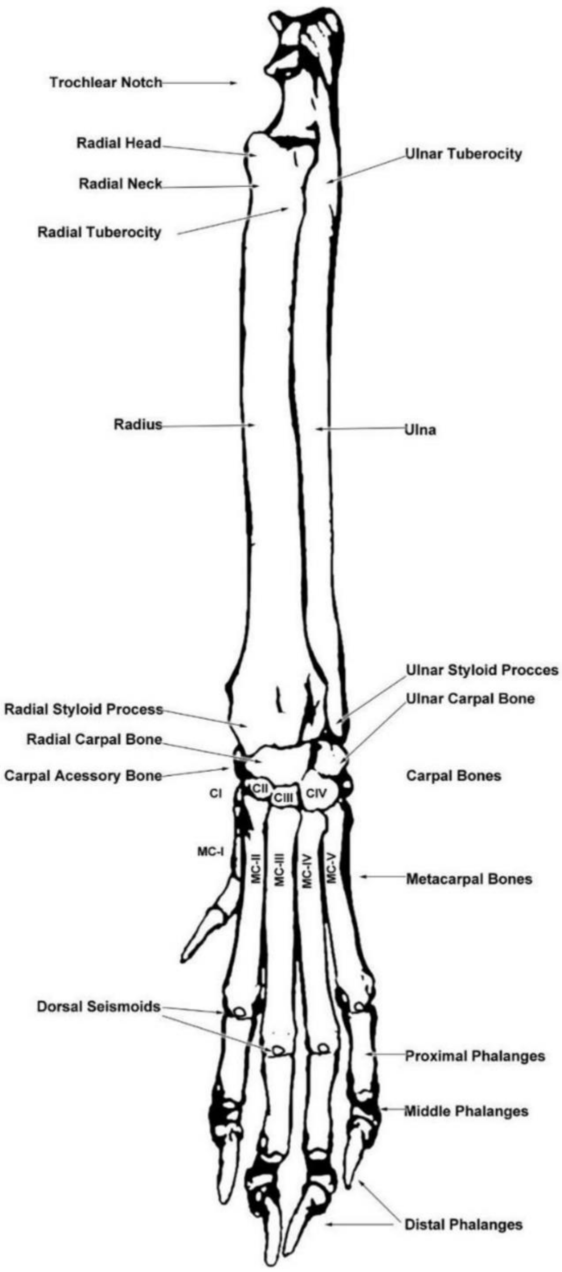

Figure 57: This image illustrates the bony anatomy of the antebrachial, carpal, and metacarpal region of the forelimb.

From previous studies it is known that the radius and ulna are the main load-bearing structures of the antebrachium limb; they both articulate proximally with the humerus and the load transferred through it is shared equally at the proximal end of both bones [33].

The radius is the bone of interest, it articulates proximally with the humerus bone forming the elbow joint, and distally with the radial carpal bone, it also articulates with the ulna: proximally by its caudal surface and distally by its lateral border. The ulna extends from the elbow to the carpus, it proximally articulates with the humerus and distally with the ulnar carpal, the accessory carpal bones, and also with the ulnar notch of the radius [36].

The carpus represents the region between the forearm and the metacarpus, it consists of the radial carpal bone and the ulnar carpal bone, in particular:

- The radial carpal bone is the largest of all the carpal bones: it articulates proximally with the radius, distally with the four numbered carpal bones, and laterally with the ulnar carpal bone.

- The ulnar carpal bone, which is smaller than the radial carpal bone, articulates proximally with the radius and ulna, distally with the fourth and fifth metacarpal, medially with the radial carpal and on the palmar side with the accessory carpal.

Lastly, the metacarpal bones II-V are the primary load-bearing bones of the metacarpus, where the III and IV bear the most load while the Metacarpal I bone is quite small and slender and does not bear any load [32].
All these bones make up the following joint interfaces: The proximal and distal radioulnar synovial joints joined together the radius and the ulna, the antebrachiocarpal joint exists between the distal part of the radius and ulna and the proximal row of carpal bones, the middle carpal joint is defined between the two rows of carpal bones and the carpometacarpal joint is located between the distal row of the carpal bones and the metacarpus.

There are numerous ligaments in the carpal joint that exist to ensure stability and allow flexion and extension with limited lateral movement. The intermetacarpal joints are close-fitting joints between the proximal ends of the metacarpal bones, the bones are joined together by fibrous tissues called the interosseous metacarpal ligaments [34].
The flexor retinaculum and the palmar carpal fibrocartilage are two primary structures that ensure the integrity of the carpal joint. The palmar carpal fibrocartilage covers the palmar aspect of all carpal bones and the proximal parts of metacarpals III, IV, and V smoothing the irregularities at the carpo-metacarpal joint and prevents hyperextension of the carpal joint [35]. Also, the palmar radiocarpal (PR, which connects the radius with the radial carpal bone) and the palmar ulnocarpal (PU, that connects the ulna with the radial carpal bone) intra-articular ligaments prevent hyper-extension of the carpal joint [36].
The medial and lateral collateral ligaments (MC, LC) of the carpus are stabilizing ligaments; they limit valgus and varus movement of the carpal joint, respectively. The medial collateral ligament originates from a tubercle above the styloid process of the radius and terminates at the most medial part of the radial carpal bone while the lateral collateral ligament originates at the styloid process of the ulna and inserts at the most lateral aspect of the ulnar carpal bone [36].
Those are the main ligaments, but numerous other short ligaments unite the carpal bones transversely, holding them together in the two rows. Many published papers have investigated the canine carpal joint anatomically using different methods such as radiographs and gross dissection [37], magnetic resonance imaging [38], and computed tomography arthroscopy [39].

TYPES OF ANALYSES FOR FORELIMB'S BIOMECHANICS

To fully understand the biomechanics of the dog's forelimb, and therefore to know the geometries and forces acting during its motion, it is necessary to perform objective gait analysis techniques. The main techniques used for this purpose are kinetics and kinematics analysis, which, when performed together, can provide a more complete depiction of limb function.

KINETIC ANALYSIS

The kinetic analysis involves the collection of ground reaction forces (GRF), which are the forces transmitted between each limb and the ground during gait. This provides an indirect measure of overall limb function and a direct measure of weight-bearing in the limb [40].

Kinetic gait analysis can be performed using a force plate (which consists of sensing elements covered by a top plate) to obtain a non-invasive, objective, and quantitative assessment of the forces. During data collection, the dog is led across the force plate by a handler, who must not interfere in any way while the dog is in contact with the plate, as we can see in *Figure 58*. When the subject steps on the force plate, the magnitude of the force is measured by the deflection of the sensing elements within the plate; three orthogonal ground-reaction forces are measured: mediolateral (Fx), craniocaudal or braking/propulsion (Fy), and vertical (Fz) [41].

The mechanism used to measure force operates as follows: the displacement of the sensing elements (they can be strain gauges or piezoelectric quartz crystal) is proportional to the force applied to the plate and creates an electric signal, which is amplified and recorded by the computer. In most cases, data are collected for the entire stance phase of the ipsilateral forelimbs and hind limbs. Force data are collected at the designated frequency, and a force-versus-time curve is generated by a computer, which is a graphic representation of the ground-reaction forces generated during the stance phase of the stride [41].

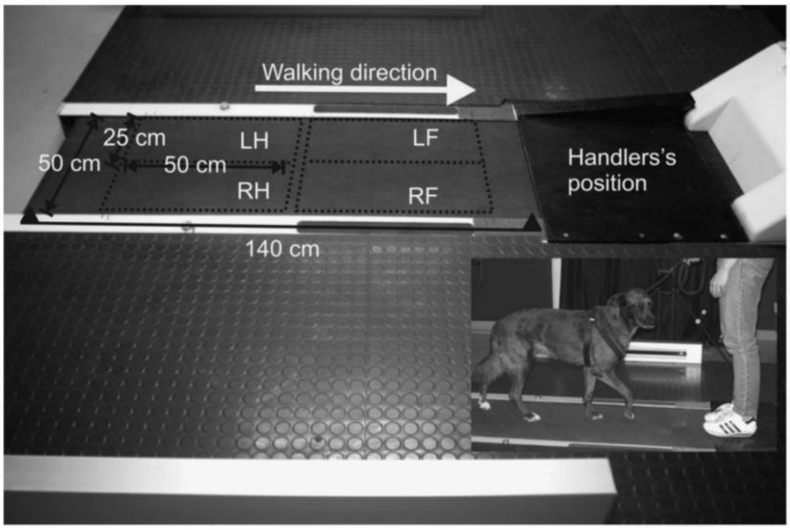

Figure 58: In this figure, we can see a force plate that can be used for ground reaction force measurements.

KINEMATIC ANALYSIS

Kinematic analysis is the study of motion without forces and allows for the evaluation of the range of motion, angular velocities, segmental velocities of each portion of the limb, stride frequency, and length. This can be performed in two-dimensions (2D) or three-dimensions (3D) and there are differences between these two methods including equipment as well as mathematical modelling techniques.

The most common method for acquiring kinematic data in dogs is using a video motion capture (MoCap) system that includes cameras and all associated equipment, and it is referred to as a kinematic analysis system. Three-dimensional kinematic MoCap systems require multiple synchronized cameras and extensive calibration techniques, while 2D kinematic analysis uses a single camera and simple calibration techniques [40]. As the dog is walked or trotted through the testing space, the video cameras record the movement of the retroreflective targets, then the computer analyzes the data from all cameras by direct linear transformation to determine the relative positions of each target in three-dimensional space [41]. Both of these methods require the use of specific markers, which vary depending on the technique being used: high-contrast markers are used for 2D systems in conjunction with standard video cameras, while retroreflective markers are used for 3D systems together with specialized video and optical cameras. These markers must be placed on the animal's limb at points relevant to the analysis, ensuring that they are positioned in such a way as to minimize the effect of skin motion artifacts. For this reason, they are usually placed on palpable anatomic bony landmarks and also on anatomic landmarks associated with the location of a joint centre. The locations and patterns of markers establish what is commonly referred to as the kinematic model.

Two-dimensional kinematic models focus on a single plane of motion, most frequently the sagittal plane, because of this, these models are often referred to as planar models. Three-dimensional kinematic models use groups of markers to compare segment motion across multiple planes; these models provide more detailed information, specifically in describing motion in more than just the sagittal plane [40].

Figure 59: In this figure, there is a picture of a dog trotting along a gait path on the force plate and with the marker on his body.

There have been several other kinematic analysis systems developed in the past few years such as radio-stereometric analysis (RSA), dynamic magnetic resonance imaging (MRI), dynamic computed tomography (CT), and accelerometer systems but many of these systems are still in their infancy and the most common is the 3D system [42].

OVERVIEW OF FORELIMB'S BIOMECHANICAL STUDY

Some researchers have utilized these kinematic and kinetic measurement systems, previously described, to analyse the canine forelimb, which is of particular interest for this thesis, for various purposes and under different circumstances to better understand the dynamic of the motion and the forces. We will now present a brief analysis of the results they obtained.

INVERSE DYNAMIC APPROACH FOR 2D FORELIMB MODEL

In this study, Nielsen et al. [45] used the inverse dynamics approach: from morphometric, positional, and force data they calculated net joint moments such as joint angular position, intersegmental forces, joint moment of force, and mechanical power at the elbow, antebrachiocarpal, and metacarpophalangeal joints of dogs at a walk. With this aim, they used six clinically normal adult mixed-breed dogs in good body condition and not overtly obese, and kinetic and kinematic data were collected simultaneously from walking dogs. In detail: Kinetic data were collected at 1,000 Hz from a force platform mounted flush with the surface of a 15 m walkway while kinematic data were collected at 200 Hz from 3 synchronized video cameras [45]. They applied reflective markers to shaved skin overlying the approximate centres of the left shoulder, elbow, antebrachiocarpal, and metacarpophalangeal joints, and over the most proximolateral aspect of the 4th middle phalanx (*Figure 60*).

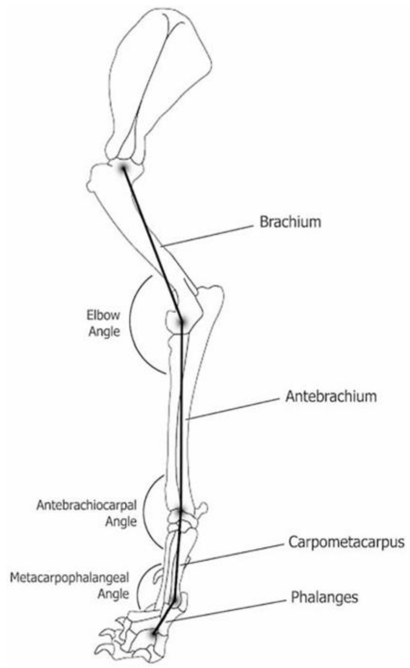

Figure 60: In this image is the anatomic location of body segments, joint angles, and kinematics markers used in the analysis.

Each dog was led at a walk on the force platform with a forward velocity between 0.8 and 1.0 m/s. Ten valid trials were collected for each dog and only three from each dog were selected for analysis of stance duration, peak force, and contour of the vertical and craniocaudal components of the ground reaction force data [45]. A trial was valid when a strike of only the left paw occurred completely on the force platform, all reflective markers were visible in the test space by at least 2 cameras, and no tension on the lead nor other observed irregularity of straight-forward motion was observed. [45]
After the walking measurements were taken, euthanasia was performed on the dogs and the forelimb segments were isolated for the purpose of measuring morphologic parameters; these parameters were recorded for all six dogs in the study and subsequently averaged. The results are presented in T*able 3*:

Measurements	Segments			
	Phalangeal	Carpometacarpal	Antebrachial	Brachial
Mass (%)*	0.32 ± 0.04	0.38 ± 0.04	1.26 ± 0.12	2.99 ± 0.35
Length (cm)	5.2 ± 0.5	8.4 ± 0.6	18.2 ± 0.7	17.8 ± 0.5
Center of mass (%)†	50.0 ± 2.8	52.9 ± 3.7	59.0 ± 2.3	53.1 ± 2.7
Mass moment of inertia (kg•cm^2)	0.8 ± 0.3	1.4 ± 0.3	14 ± 2.0	55 ± 11

*Percentage of total body mass. †Percentage of total length as measured from the distal end of segment.

Table 3: The location of the center of mass was determined for each segment by use of a balanced technique. Limb segment masses and lengths were measured directly. Lengths were measured between approximate joint centers corresponding to the skin markers placed for kinematic data acquisition. Mass moments of inertia were determined by the use of a pendulum technique.

In *Table 4* we can see their results, in particular, there are:
Mean (± SD) temporal variables, peak ground reaction forces, and peak vertical intersegmental force of 6 dogs with a mean (± SD) body mass of 25.3 ± 2.5 kg [45].

Measurements	Dogs						Overall
	1	2	3	4	5	6	
Temporal variables	—	—	—	—	—	—	—
Forward velocity (m/s)	0.94 ± 0.01	0.78 ± 0.10	0.96 ± 0.02	0.92 ± 0.01	0.78 ± 0.02	0.84 ± 0.09	0.84 ± 0.09
Stance duration (s)	0.53 ± 0.05	0.50 ± 0.06	0.47 ± 0.04	0.54 ± 0.02	0.55 ± 0.04	0.55 ± 0.06	0.52 ± 0.05
PGRF	—	—	—	—	—	—	—
Vertical (% BW)	53.02 ± 2.29	63.82 ± 3.11	64.95 ± 0.93	63.93 ± 0.56	59.83 ± 2.15	66.82 ± 1.64	62.60 ± 4.53
Craniocaudal (% BW)	11.99 ± 0.46	9.10 ± 1.83	13.40 ± 2.77	13.99 ± 1.45	10.47 ± 0.47	10.52 ± 1.69	11.55 ± 2.31
PVIF	—	—	—	—	—	—	—
MCP joint (% BW)	52.73 ± 2.29	63.27 ± 3.25	NA	63.55 ± 0.57	59.53 ± 2.15	66.49 ± 1.64	61.71 ± 4.83
ABC joint (% BW)	52.35 ± 2.29	62.93 ± 3.26	NA	63.15 ± 0.56	59.20 ± 2.15	66.10 ± 1.65	61.35 ± 4.81
Elbow joint (% BW)	51.09 ± 2.29	61.66 ± 3.27	NA	62.03 ± 0.56	57.92 ± 2.15	64.81 ± 1.65	60.10 ± 4.83
Shoulder joint (% BW)	47.90 ± 2.29	58.78 ± 3.32	NA	58.95 ± 0.56	55.18 ± 2.17	62.12 ± 1.66	57.21 ± 4.94

PGRF = Peak ground reaction force. PVIF = Peak vertical intersegmental force. MCP = Metacarpophalangeal. ABC = Antebrachiocarpal. BW = Body weight. NA = Not available.

Table 4: There are summarised the results of the study. Vertical and craniocaudal ground reaction forces were normalized by the dog's body weight and reported as a percentage of body weight. Vertical ground reaction force data were used to determine the initiation and termination of the stance phase of the left forelimb in the gait cycle. Time data were normalized by the duration of the stance phase for each trial and reported in 2% intervals as a percentage of the total stance phase. Position data for the joint centres were used to obtain angles between each segment and the horizontal plane over time for the duration of the stance phase. A cubic spline was fit to the angular position versus time data. Angular velocities and accelerations were determined by calculating the first and second derivatives, respectively, of the cubic spline functions.

In *Figure 61* we can see the two components of the averaged forelimb ground reaction forces (% body weight [BW]) versus the percentage of stance phase in 6 dogs:

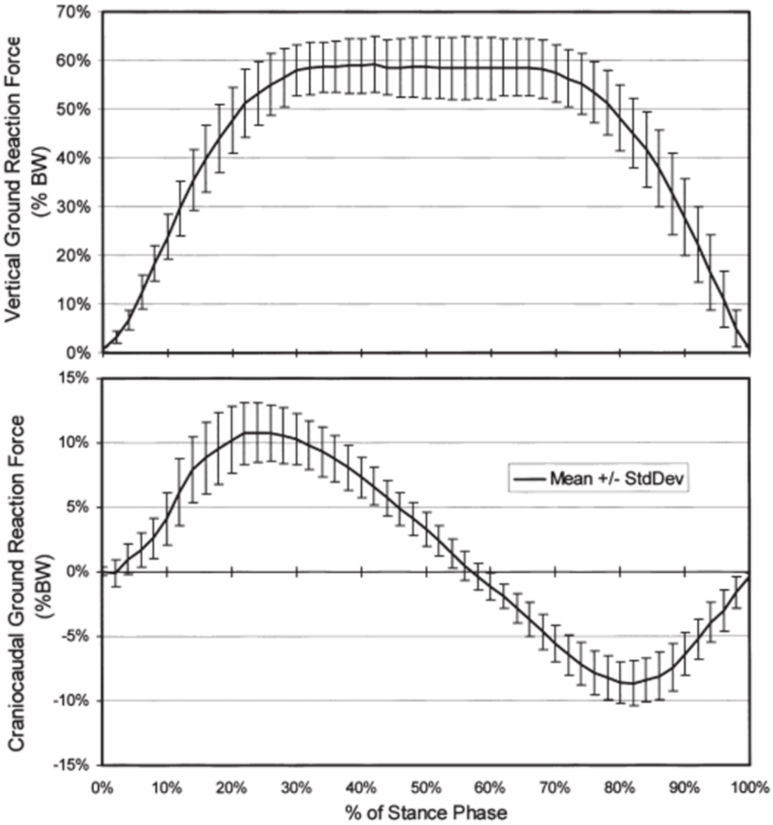

Figure 61: The mean peak vertical force was 62.6 ± 4.5% of body weight, and the mean peak craniocaudal force was 11.6 ± 2.3% of body weight. The craniocaudal force curve was nearly symmetric so that the peak propulsive force was similar to the peak braking force during stance.

The sum of the joint moments was calculated across the shoulder, elbow, antebrachiocarpal, and metacarpophalangeal joints and resulted in a net extensor moment throughout the stance phase for support of the forelimb; its value is shown in *Figure 62*.

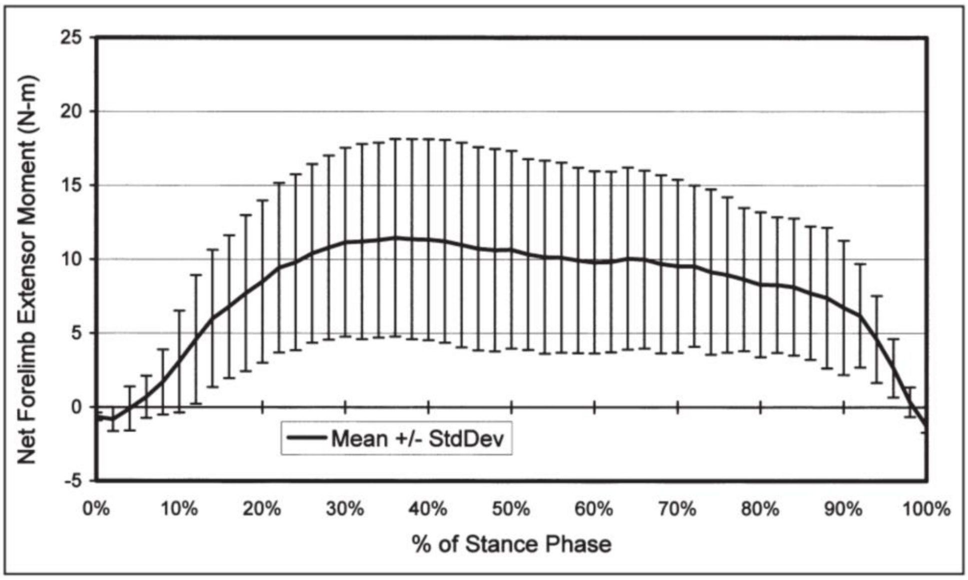

Figure 62: Mean (± SD) net forelimb extensor moment versus the percentage of stance phase in 5 dogs.

In *Figure 63* we can see the averaged measure in 5 dogs of joint angle, a moment of force, and mechanical power for all the forelimb joints such as the metacarpophalangeal joint (MCP), antebrachiocarpal joint (ABC) and elbow joint and also the averaged measure in 5 dogs of the moment of force for the shoulder joint.

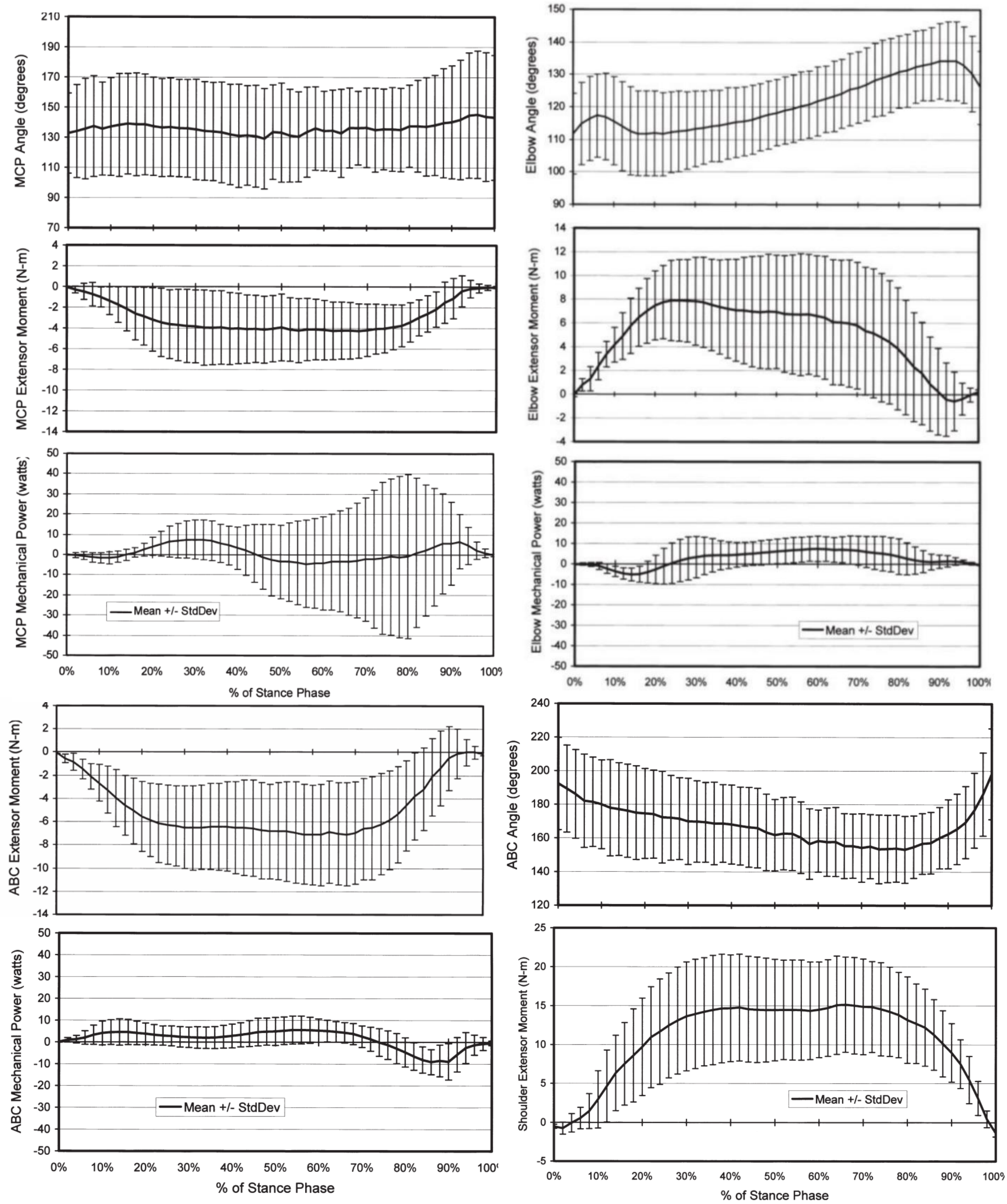

Figure 63: Mean (± SD) joint angle, moment of force, and mechanical power versus the percentage of stance phase in 5 dogs in ABC joint, elbow joint and MCP joint and the mean (± SD) moment of force at the shoulder joint versus the percentage of stance phase in 5 dogs.

At a walking gait, intersegmental forces were found to be similar in form to the measured ground reaction forces, with an overall small decrease in magnitude the more proximal the location of each joint. A net flexor moment was observed at the metacarpophalangeal and antebrachiocarpal joints, and a net extensor moment was observed at the elbow and shoulder joints; together, they provide a net extensor support moment for the forelimb throughout the stance.

MEASUREMENT OF THE GROUND REACTION FORCE

Bockstahler, Skalicky et al. [43] measured the ground reaction force for ten orthopaedically healthy dogs of different breeds, on a treadmill system with four biomechanical platforms (specially developed by them for this study). The dogs were walked by their owners on the treadmill at an operating speed of 1.22 m/s, for a walking time of 35 to 120s, three times per day for three consecutive days. Five distinct steps were analysed from each measurement, the analysed step was the clear one, namely the step where each force plate had been hit exclusively by its corresponding limb. [43]
For each limb and every step, they calculated, from the vertical force curves, the peak vertical force (PFz), vertical impulse (IFz), and the duration of the stance phase (ST). The vertical forces were normalised by the individual body weight of the dog and peak vertical force and impulse were expressed as a percentage of body weight (%BW). The results from this study are summarised in *Table 5* [43]:

Force	Leg	Mean (%BW) $N = 90$	SD	CI	CV
Peak vertical force (%BW)	LF	63.33	2.08	62.89–63.76	3.28
	RF	63.65	2.02	63.23–64.08	3.18
	LH	39.63	2.60	39.09–40.18	6.57
	RH	39.11	2.68	38.55–39.67	6.86
Vertical impulse (%BWs)	LF	30.39	3.02	29.76–31.02	9.94
	RF	30.02	2.47	29.50–30.55	8.24
	LH	18.40	1.88	18.01–18.79	10.23
	RH	18.10	2.01	17.67–18.51	11.09
Stance time (s)	LF	0.65	0.06	0.64–0.67	9.2
	RF	0.64	0.05	0.63–0.65	7.8
	LH	0.62	0.05	0.61–0.63	8.0
	RH	0.62	0.05	0.61–0.63	8.0

Table 5: The table's data are: LF, left forelimb; RF, right forelimb; LH, left hindlimb; RH, right hindlimb; SD, standard deviation; CI = 95% confidence interval; CV, coefficient of variation.

COMPARISON OF GROUND REACTION FORCES OF TWO DIFFERENT BREEDS

The purpose of the study by Bertram, Lee et al. [44] was to determine whether differences in trotting gait between Labrador Retrievers and Greyhounds are attributable to differences in the way these breeds move or to differences in their body form or size. Labrador Retrievers and Greyhounds were chosen for this study because they are commonly perceived as having different body shapes and styles of movement.
In order to do that, they use a series of 4 force platforms to simultaneously, but independently, record

ground reaction forces from forelimbs and hind limbs of trotting dogs in 3 consecutive steps. They used eight 5-month-old clinically normal Greyhounds and 5 clinically normal Labrador Retrievers between 6 and 18 months old. Dogs were allowed to trot along the tracks and over the force platforms at their preferred speeds and each run was recorded on videotape for later reference.

A total of 47 successful runs were obtained from the Greyhounds, and 42 successful runs were obtained from the Labrador Retrievers. An individual run was considered successful if the dog maintained a trotting gait throughout the run and contacted each force platform.

Concerning the forelimbs, the results they found out were: the vertical component of the ground reaction force is similar in the two breeds while the forelimb duty factor for Greyhounds was significantly less than the forelimb duty factor for Labrador Retrievers as we can see in *Table 6*. [43]

Variable	Labrador Retrievers (n = 5)	Greyhounds (n = 8)
Absolute values* (mean ± 95% confidence interval)		
Stride period (s)	0.43 ± 0.003†	0.46 ± 0.006
Stride frequency (s^{-1})	2.32 ± 0.016†	2.17 ± 0.028
Stride length (m)	1.05 ± 0.008†	1.13 ± 0.013
Normalized values‡ (mean ± 95% confidence interval)		
Relative stride period	2.28 ± 0.019	2.29 ± 0.043
Relative stride length	2.95 ± 0.026	2.96 ± 0.055
Mean vertical force§ (mean ± SD)		
Diagonal pair	1.00 ± 0.06	0.98 ± 0.08
Forelimb	0.66 ± 0.05	0.67 ± 0.06
Hind limb	0.43 ± 0.04†	0.57 ± 0.07
Maximum vertical force§ (mean ± SD)		
Diagonal pair	1.91 ± 0.13	1.89 ± 0.21
Forelimb	1.17 ± 0.07	1.17 ± 0.11
Hind limb	0.76 ± 0.08†	1.07 ± 0.13
Duty factorII (mean ± SD)		
Diagonal pair	0.507 ± 0.023	0.513 ± 0.045
Forelimb	0.505 ± 0.023†	0.426 ± 0.027
Hind limb	0.401 ± 0.028	0.377 ± 0.039

*Table 6: These are the results of this study. Legend: *Predicted absolute values at a standard relative velocity of 1.3, determined by use of linear regression. †Significantly (P < 0.05) different from the value for Greyhounds. ‡Absolute values were normalized for limb length, and values at a standard relative velocity of 1.3 were then determined by use of linear regression. §Expressed as a proportion of body weight. II Fraction of the total stride period that the foot was in contact with the ground.*

KINEMATIC GAIT ANALYSES IN GOLDEN RETRIEVERS

Silva, Cardoso et al. [46] in their study analyse the kinematic gait analysis in healthy Golden Retrievers dogs. For their purpose, they used seven female golden retriever dogs, aged between 2 and 4 years, with weights varying from 21 to 28 kg, that were submitted for physical and radiological evaluation and

resulted clean from disease. For the analysis, they established a 2-dimensional space using a digital camera placed in the sagittal plane in the cranium-caudal direction of the right side of each animal and 3M adhesive reflexive markers, which were placed on the animals using the correct adhesive glue. The markers were positioned at the level of the principal joint: shoulder, elbow, carpal, metacarpal phalanges for the forelimb and iliac crest, hip, knee, tarsal joint, metatarsal phalanges for the hindlimb.
First of all, they measured the principal biometric data of each dog, then they averaged this data and obtained the following measures summarized in *Table 7*:

Variáble	Unity	Mean	Standard deviation	*p value*
Humeral	[cm]	18,710	0,756	*0,150*
Ulna	[cm]	18,860	0,945	*0,150*
Carpus	[cm]	5,786	0,393	*0,150*
Femur	[cm]	19,710	0,906	*0,150*
Tibia	[cm]	19,070	1,272	*0,150*
Tarsus	[cm]	11,140	0,627	*0,150*
Chest	[cm]	70,430	2,457	*0,150*
Height	[cm]	55,210	0,951	*0,150*
Weight	[Kg]	23,260	1,919	*0,150*

Table 7:There are the averaged main biometric data that has been measured for this study.

From the kinematics analysis, they found out that the joints angles of the main joints, during the gait, are:

Variable	Unity	Mean	Standard deviation	*p value*
Carpal – swing phase	[degrees]	97,990	9,435	*0,093*
Carpal – propulsion phase	[degrees]	203,800	5,966	*0,150*
Carpal – stance phase	[degrees]	204,500	6,676	*0,150*
Elbow – swing phase	[degrees]	77,670	9,704	*0,068*
Elbow – propulsion phase	[degrees]	127,900	6,976	*0,150*
Elbow – stance phase	[degrees]	116,600	8,136	*0,029*
Shoulder – swing phase	[degrees]	107,800	12,170	*0,150*
Shoulder – propulsion phase	[degrees]	122,000	14,060	*0,104*
Shoulder – stance phase	[degrees]	133,100	12,400	*0,060*

Table 8: There are the mean of the values of the joint angles of seven studied dogs.

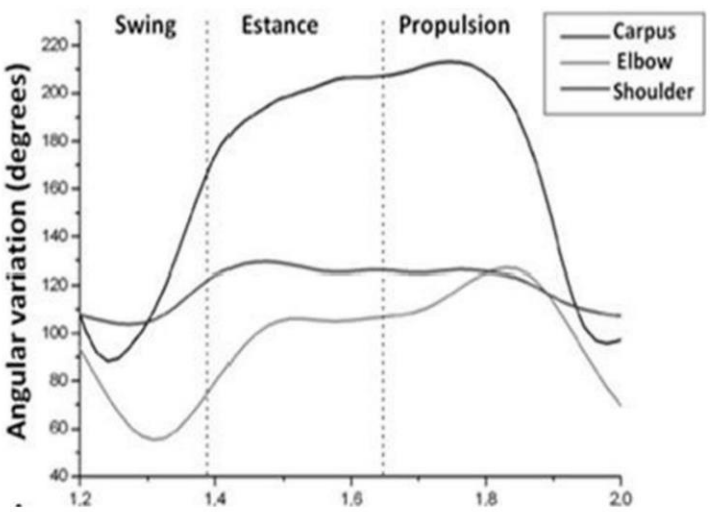

Figure 64: We can see the articular behaviour of forelimbs during periods of swing, stance, and propulsion during a stride.

In conclusion, as we can learn from the data previously reported, the forces acting on the dog's forelimb, expressed as a percentage of the dog's body weight (%BW), have been estimated as follows:

- 63% of BW during a simple walk
- 110% of BW during trot

Therefore, we can use these force values as reference values for our analyses and tests.

CHAPTER 2: NUMERICAL MODELING OF CANINE ENDOPROSTHESES

After reviewing the literature on canine prosthetics and the biomechanics of the canine limb, we will now focus on a detailed analysis of specific types of veterinary prostheses. The prostheses considered in this thesis are fracture fixation prostheses, designed to hold together two fractured bone segments. Starting with a physical prosthesis model, a finite element model (FEM) was created, on which a static numerical analysis under a specific tensile load was conducted using the Ansys APDL software.

This analysis aims to investigate the prosthesis's elastic deformation subjected to specific tensile loads, identify the most stressed areas, and assess whether the geometry and materials used in these models are suitable for their intended function.

Two numerical analyses were conducted. The first analysis considered only the prosthesis, while the second analysis examined the combined prosthesis-bone system, where the bone was modeled as a rectangular specimen made of a specific bone-mimicking material. The key variables in this study are the elastic moduli of both the prosthesis materials and the bone-mimicking specimen, while the calculated variables include the deformation of the model, its stiffness, and the stresses to which it is subjected.

Let us now examine in detail the steps taken to develop the FEM model and perform the analyses.

GEOMETRY DESIGN WITH SOLIDWORKS

The study subjects of this thesis are canine endoprosthesis specimens designed for fracture fixation. The prototypes considered in this study amount to 11 and consist of four main components: the plate, the screws, the screw housing, and the bone-mimicking specimen.

The distinctive feature of these prototypes lies in the tilting screw housing, which allows the screws to be inserted at specific angles rather than being strictly perpendicular to the bone during prosthesis implantation. This design feature facilitates the fixation process during surgery by providing a certain degree of mobility to the screws instead of a rigid attachment.

The plates and screws of these models vary in size. The screws are threaded and share the same structural design across all prototypes and are always made of the same material, which is Grade 5 titanium; which has an elastic modulus of 110 GPa and a Poisson's ratio of 0.33. Conversely, the plates differ in the number of screws they accommodate, the inclination of the screws, the plate geometry, its dimensions, and the materials used. More specifically, these prototypes can be categorized into two groups based on plate and screw dimensions as well as materials: mini endoprostheses and micro endoprostheses.

The plates belonging to these groups share specific characteristics:

- MINI ENDOPROSTHESES: The first four prototypes belong to this group. The common characteristics among all prototypes in this category are as follows: the plate thickness is 2 mm, the inner and outer diameters of the screw housing are 4.3 mm and 8 mm, respectively, and the screws have a diameter of 3 mm and a length of 20 mm. The plates in this group are made of grade 5 titanium, which has an elastic modulus of 110 GPa and a Poisson's ratio of 0.33
- MICRO ENDOPROSTHESES: The remaining prototypes belong to this group. Their shared characteristics are as follows: the plate thickness is 1.3 mm, the inner and outer diameters of the screw housing are 3.8 mm and 6.5 mm, respectively, and the screws have a diameter of 2 mm and a length of 18 mm. The plates in this group are made of grade 4 titanium, which has an elastic modulus of 105 GPa and a Poisson's ratio of 0.34.

The bone-mimicking specimens provided for prosthesis fixation, allowing the study of the prosthesis-bone system, have a parallelepiped shape. The rectangular surface where the prosthesis is attached measures 20 mm in width and 50 mm in height, with a total depth of 55 mm. These specimens are composed of two materials: the first material, 50 PFC, occupies the top 3 mm of the depth and represents the cortical bone, directly interfacing with the prosthesis. The second material, 15 PFC, occupies the remaining volume and simulates the cancellous bone. The PCF, the material used for constructing these blocks, is a solid rigid polyurethane foam commonly employed in experimental tests for orthopedic devices. It is used as a bone substitute since it optimally simulates many of the bone's properties and characteristics. There are different types of PCF, varying based on density; the ones used in our analysis are 50 PCF and 15 PCF, which have an elastic modulus of 1.469 GPa and 173 MPa, respectively, and a Poisson’s ratio of 0.3.

Based on the physical dimensions of the prototype models, a 3D design was developed using SolidWorks CAD software. To simplify the model, the tilting housing was not included in the CAD representation. We began by creating a preliminary model (Model 1) that included only the prosthesis and screws, enabling accurate modeling of the contact surfaces between these two components. Subsequently, a complete structural model (Model 2) was developed, incorporating the prosthesis, screws, and the bone-mimicking material, allowing the simulation of prosthesis attachment to the bone.
These two models were generated for each of the 11 endoprosthesis prototypes.

3D CAD OF MODEL 1

For the design of Model 1 of the prototypes, the realistic shape of the plate was modeled, while the screws were simplified as plain cylinders, and their threading was not considered.

The following images show the model 1 of all 11 prototypes:

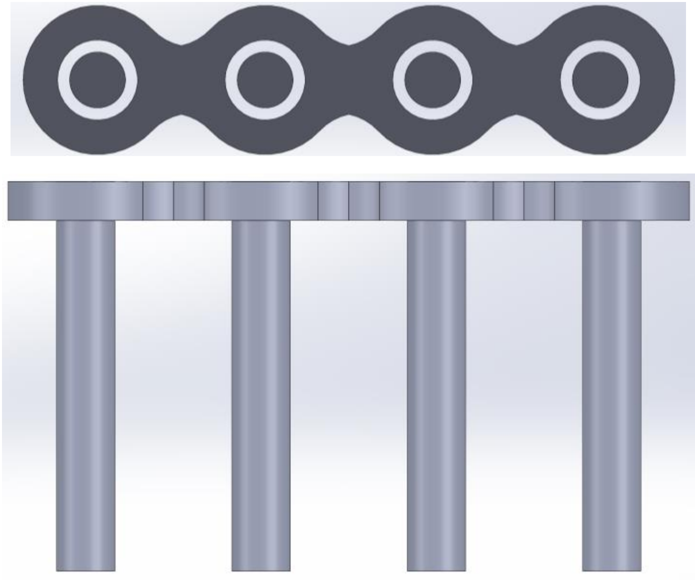

Figure 65: This is the model 1 of the prosthesis number 1. All the screws are perpendicular to the plate.

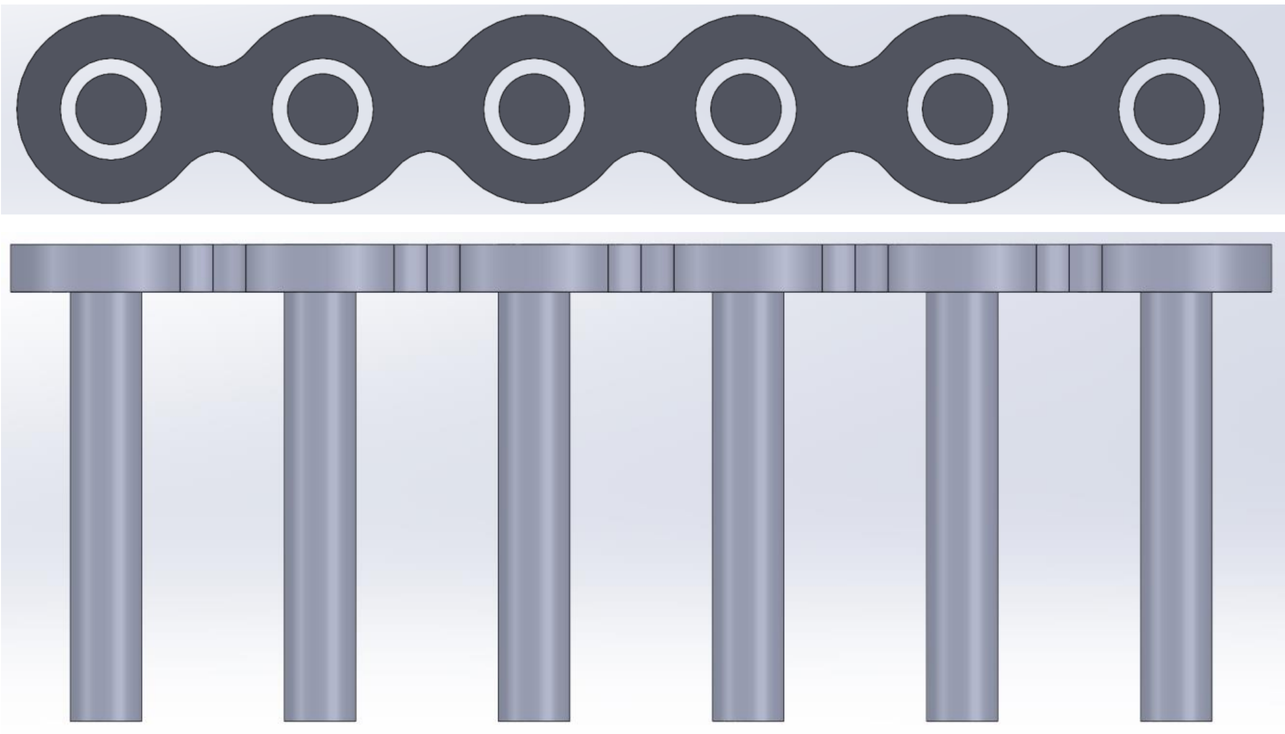

Figure 66: This is the model 1 of the prosthesis number 2. All the screws are perpendicular to the plate.

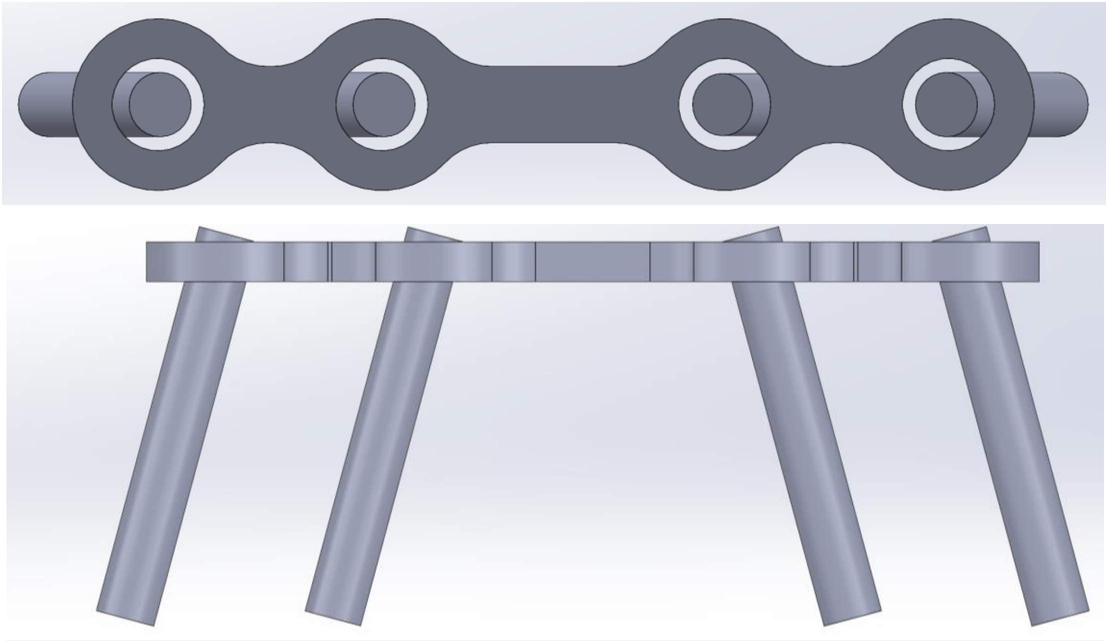

Figure 67: This is the model 1 of the prosthesis number 3. As we can see from the image, the screws are no longer perpendicular but have an inclination of 15 degrees to the normal surface of the plate, one half in a clockwise direction, while the other half in a counterclockwise direction.

.

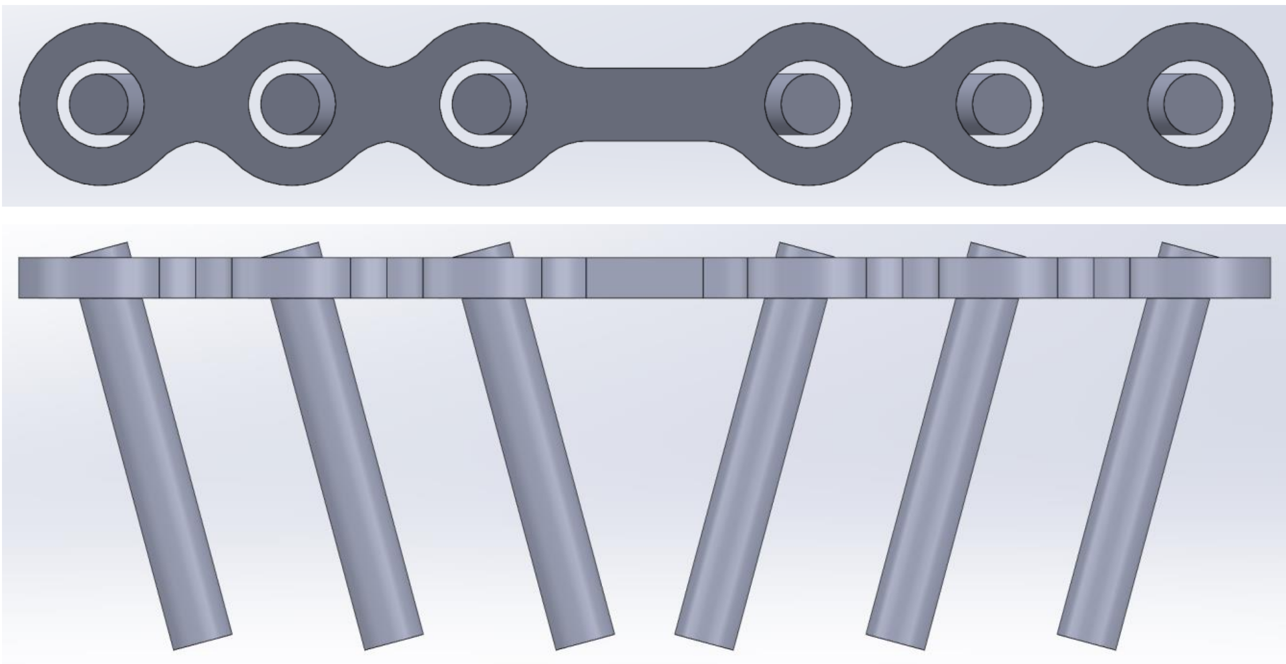

Figure 68: This is the model 1 of the prosthesis number 4. As we can see from the image, the screws are no longer perpendicular but have an inclination of 15 degrees to the normal surface of the plate, one half in a clockwise direction, while the other half in a counterclockwise direction.

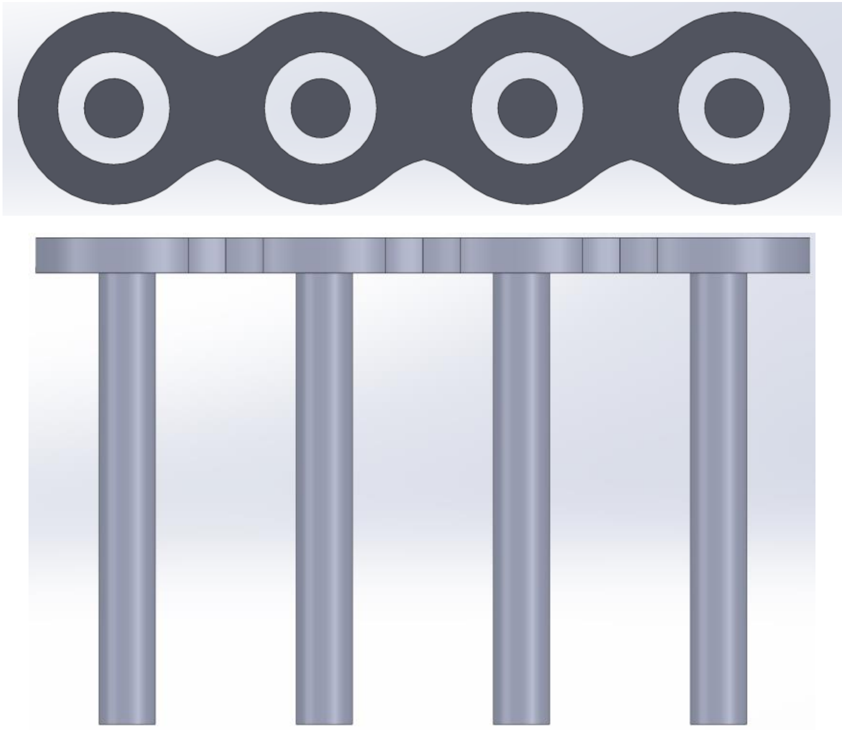

Figure 69: This is the model 1 of the prosthesis number 5. All the screws are perpendicular to the plate.

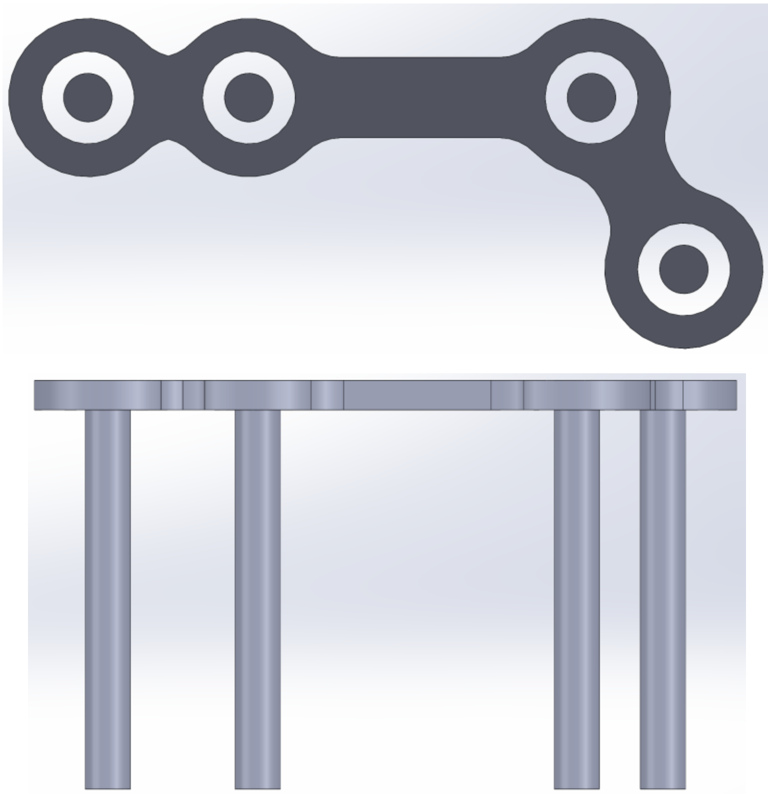

Figure 70: This is the model 1 of the prosthesis number 6. All the screws are perpendicular to the plate.

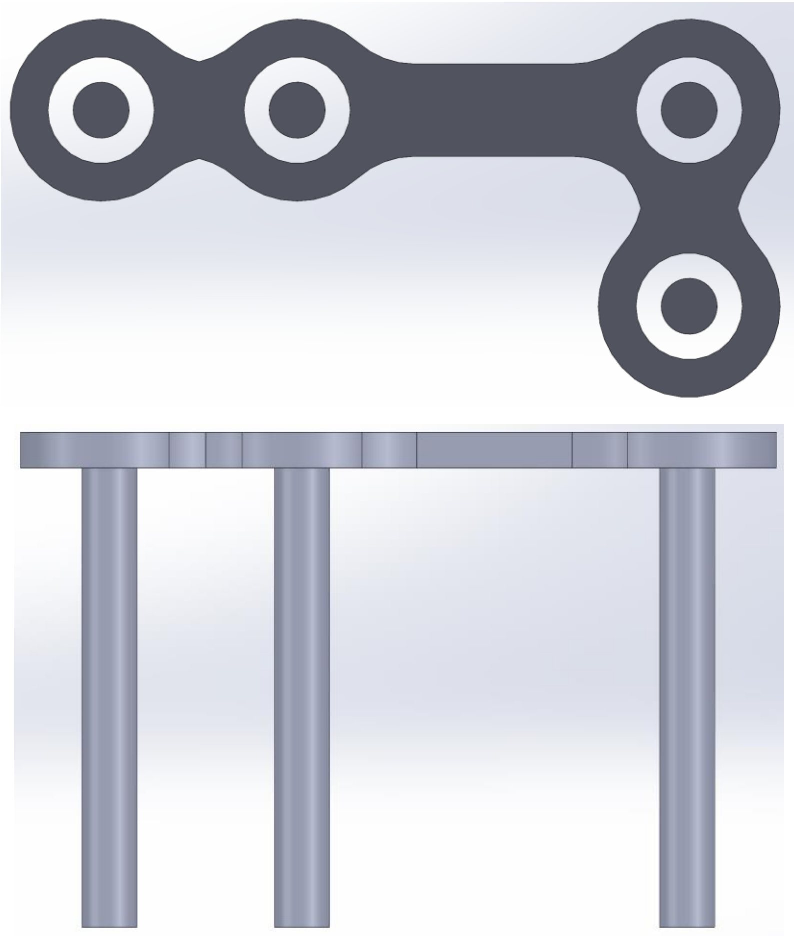

Figure 71: This is the model 1 of the prosthesis number 7. All the screws are perpendicular to the plate.

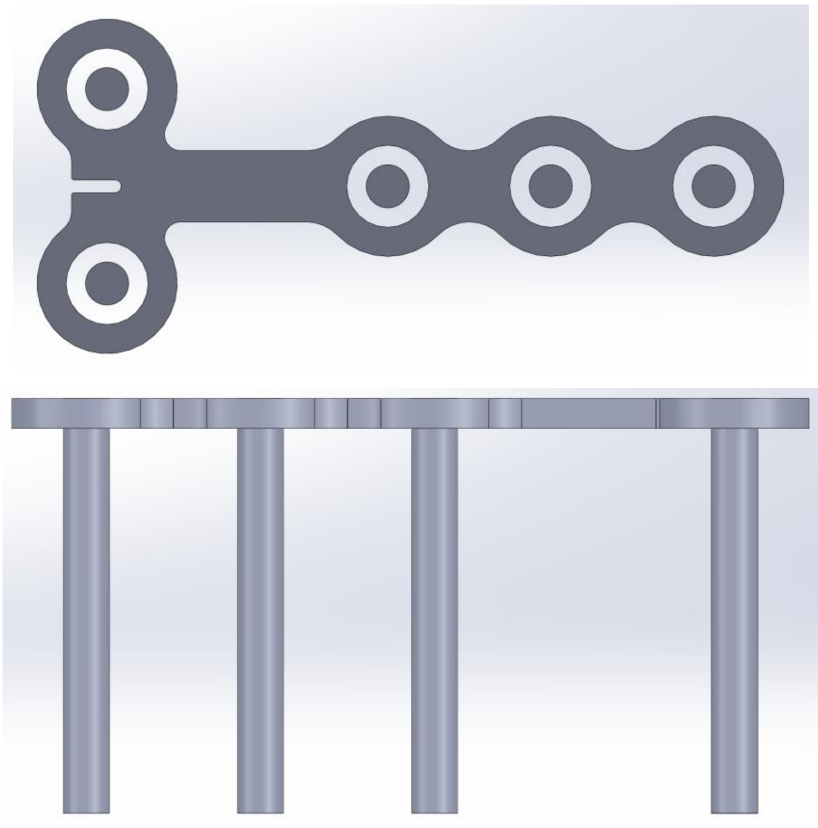

Figure 72: This is the model 1 of the prosthesis number 8. All the screws are perpendicular to the plate.

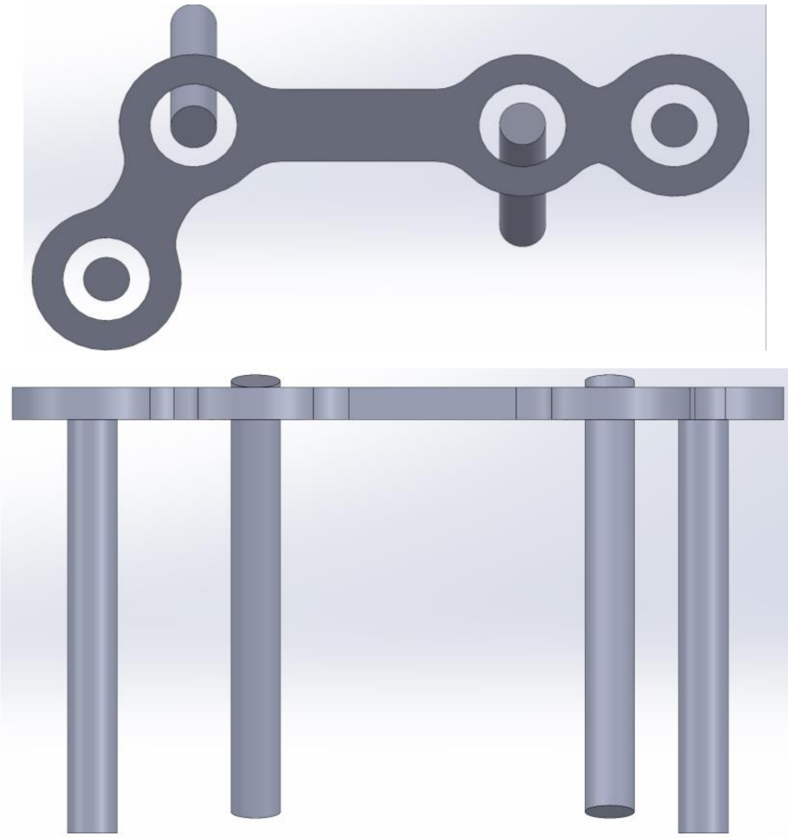

Figure 73: This is the model 1 of the prosthesis number 9. Two screws are perpendicular to the plate while the other two have an inclination of 15 degrees to the normal surface of the plate.

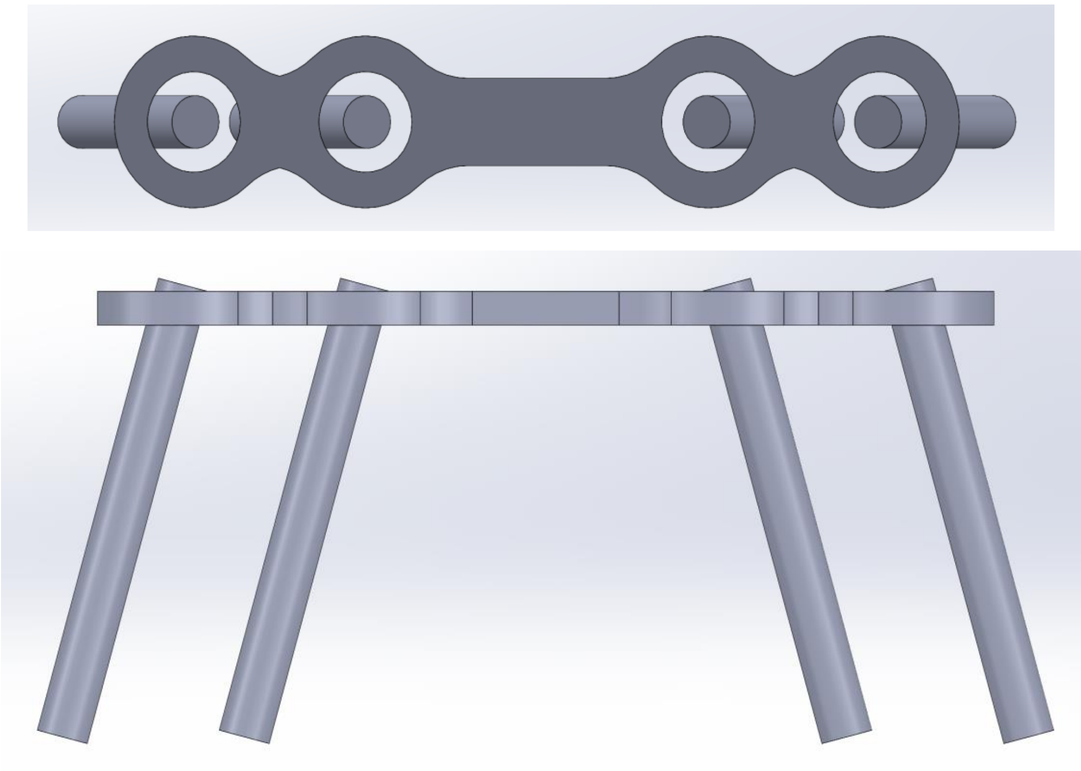

Figure 74: This is the model 1 of the prosthesis number 10. As we can see from the image, the screws are no longer perpendicular but have an inclination of 15 degrees to the normal surface of the plate, one half in a clockwise direction, while the other half in a counterclockwise direction.

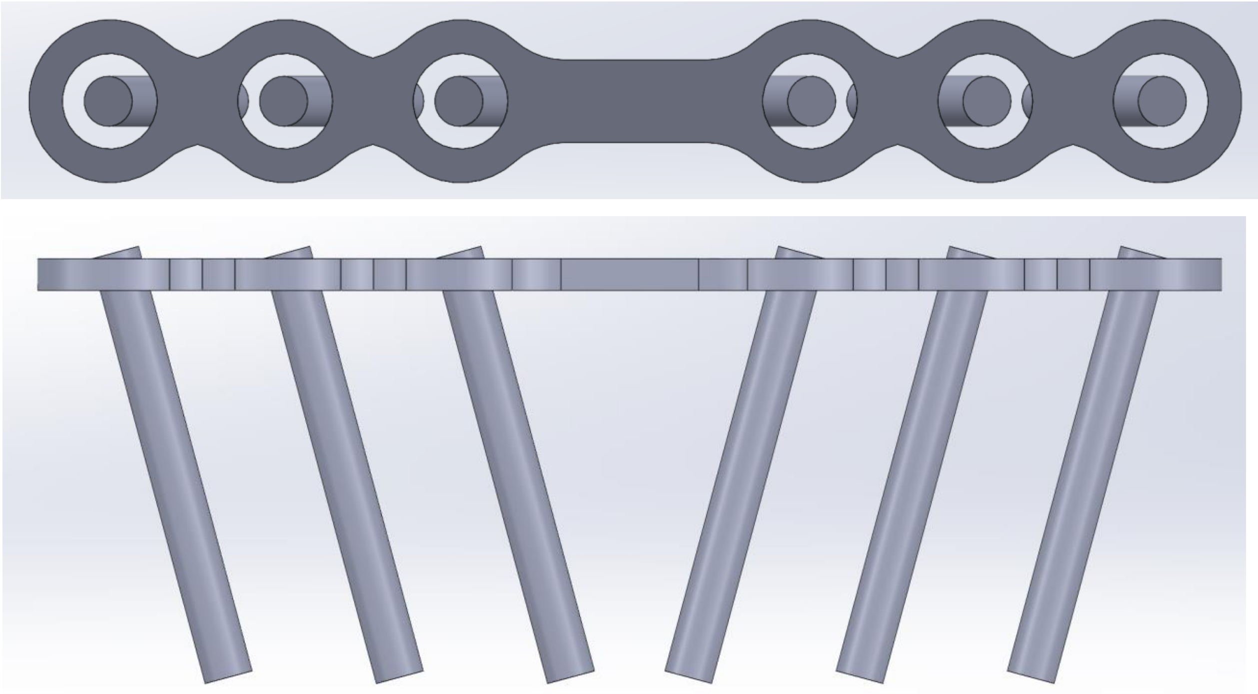

Figure 75: This is the model 1 of the prosthesis number 11. As we can see from the image, the screws are no longer perpendicular but have an inclination of 15 degrees to the normal surface of the plate, one half in a clockwise direction, while the other half in a counterclockwise direction.

As observed in the Model 1 drawings of the various prototypes, some prototypes exhibit similarities:

- Prototypes 6 and 9 share the same plate geometry, differing only in the inclination of the screws.
- Prototypes 6 and 7 have the same number and inclination of screws but differ in their geometry.
- Prototypes 1 and 5 have the same geometry and screw inclination but differ in size.
- Prototypes 3 and 10 have the same geometry and screw inclination but differ in size.
- Prototypes 4 and 11 have the same geometry and screw inclination but differ in size.

3D CAD OD MODEL 2

For the design of Model 2 of the prototypes, the Model 1 design was used with the addition of the two previously described foam blocks, one attached to one half of the prosthesis and the other connected to the other half, simulating two fractured bone segments that the prosthesis must hold together.

The following images show the model 2 of all 11 prototypes:

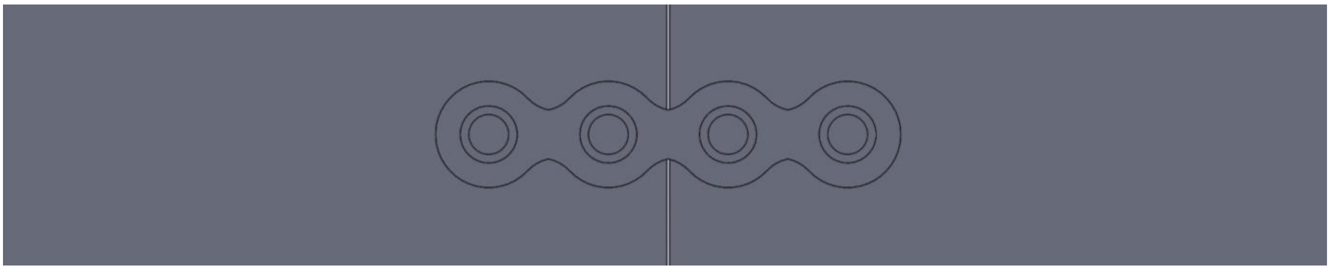

Figure 76: This is the model 2 of the prosthesis number 1.

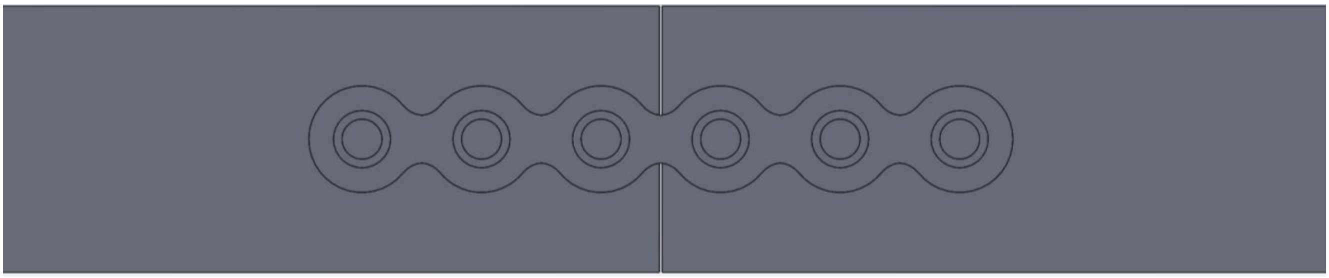

Figure 77: This is the model 2 of the prosthesis number 2.

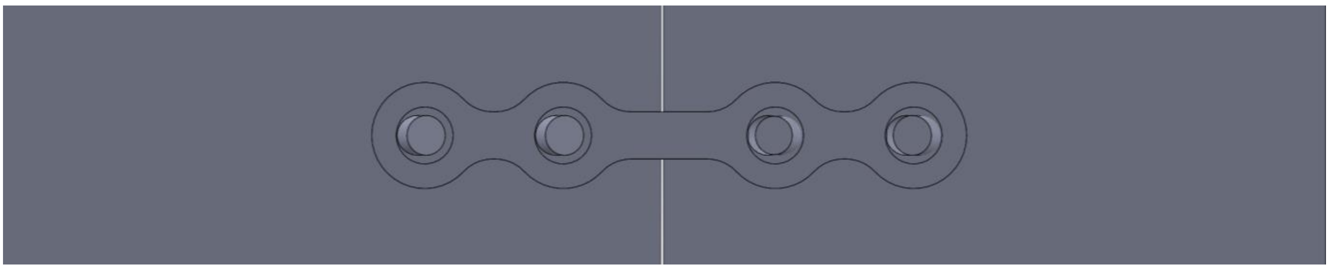

Figure 78: This is the model 2 of the prosthesis number 3.

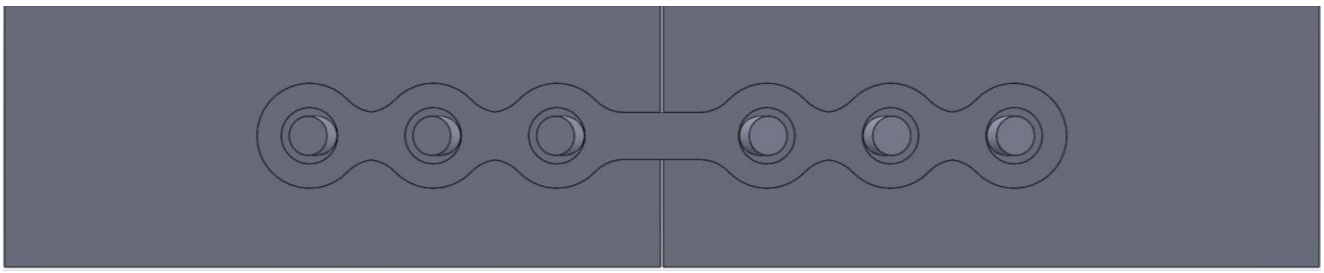

Figure 79: This is the model 2 of the prosthesis number 4.

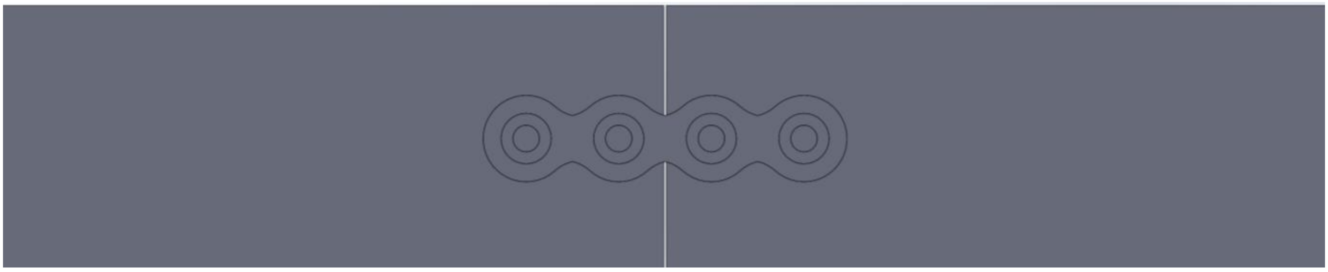

Figure 80: This is the model 2 of the prosthesis number 5.

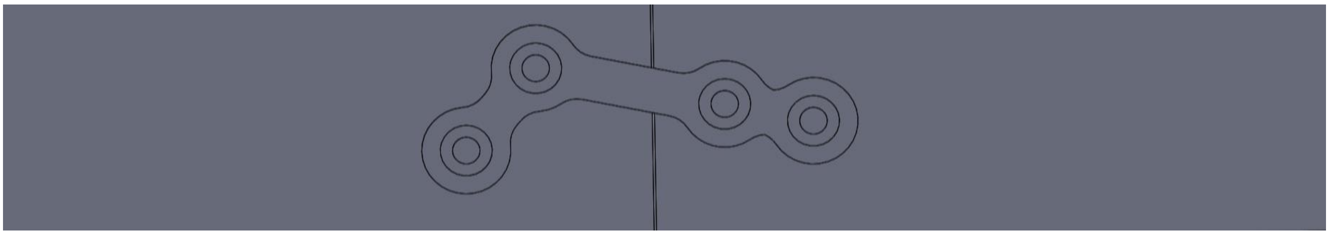

Figure 81: This is the model 2 of the prosthesis number 6.

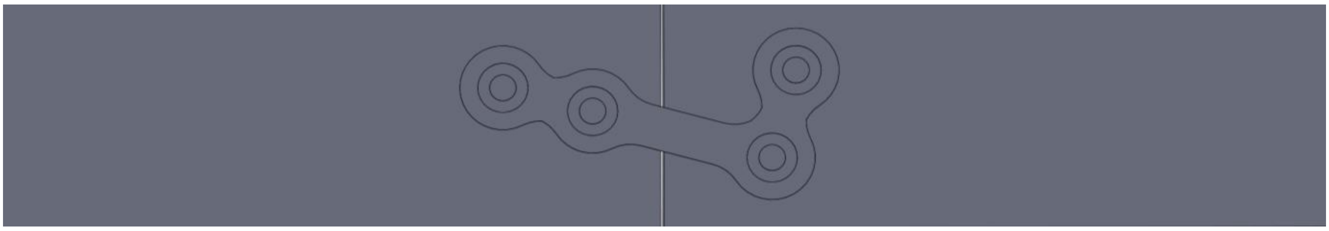

Figure 82: This is the model 2 of the prosthesis number 7.

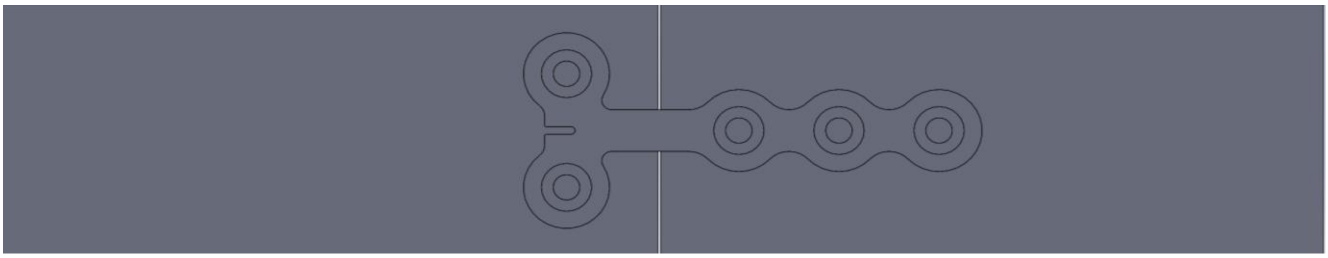

Figure 83: This is the model 2 of the prosthesis number 8.

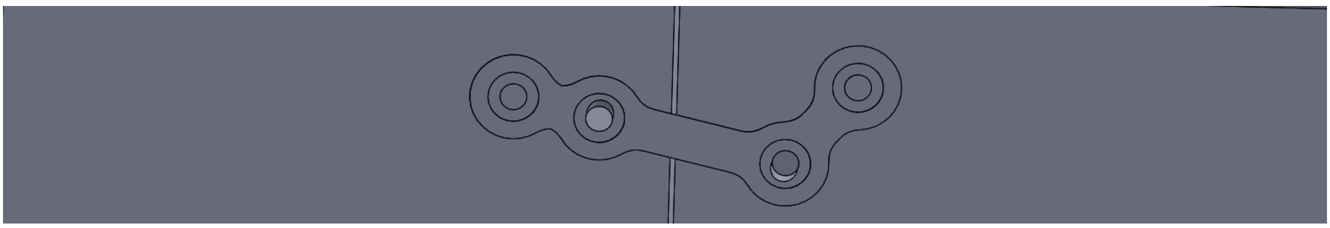

Figure 84: This is the model 2 of the prosthesis number 9.

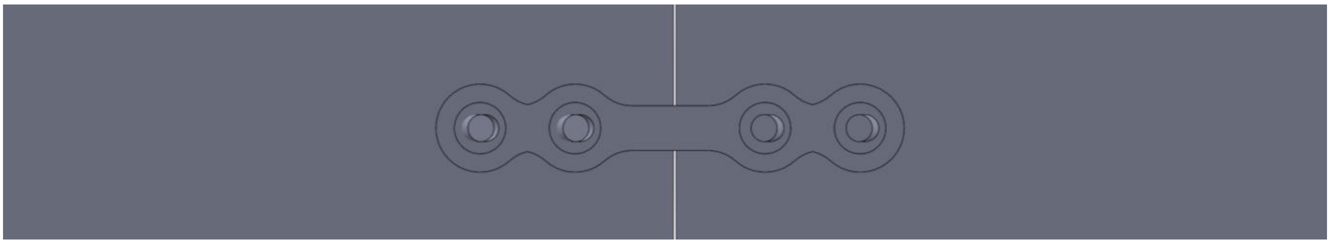

Figure 85: This is the model 2 of the prosthesis number 10.

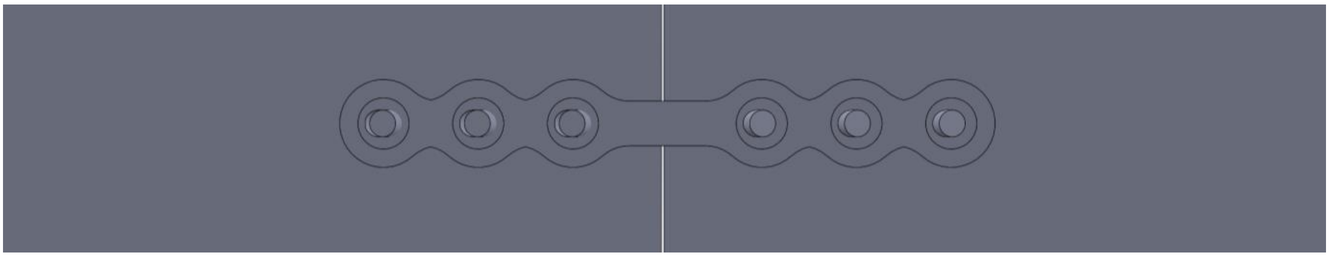

Figure 86: This is the model 2 of the prosthesis number 11.

STATIC TENSILE ANALYSIS WITH ANSYS

Once the 3D design of each of the 11 prototypes was obtained, it was imported into the ANSYS APDL software to perform specific numerical analyses in order to study the model thoroughly. The numerical analysis of the FEM model of the endoprosthesis prototypes conducted in this thesis was a static tension analysis.

This tension analysis involves fixing one part of the model using a constraint, while the other part is free and subjected to a tensile load, meaning a force that pulls the model toward the opposite side of the constrained section. This was done to replicate the experimental tensile test, which involves inserting the prototype—i.e., the prosthesis screwed to two bone-like material specimens—into a gripping system. This setup simulates fracture fixation, as one part of the prosthesis is screwed to one specimen while the other part is fixed to another specimen. Within the gripping system, one of the two specimens is held stationary, while the other is pulled along the prosthesis axis by an applied tensile load.

A pure tension analysis was chosen because it generates the most significant forces, causing the specimen to undergo more critical deformations. These deformations allow us to determine if the prosthesis design is suitable for the loads it will experience during use. By simulating pure tensile force, other types of stress, such as compression, rotation, and bending forces, were not considered. These are secondary stresses since their intensity is much lower compared to the tensile force. Therefore, the tensile force was chosen as it represents the most critical condition.

To conduct the tensile tests as accurately as possible, the process began with Model 1 of the various prosthetic prototypes, followed by the final Model 2. For simplicity, both analyses will be reviewed individually.

COMPARISON BETWEEN MODEL 1 AND MODEL 2

Through the static analysis in ANSYS, the aim is to replicate the linear behavior of the prosthesis-bone system observed in the initial phase of the experimental tensile tests. During the tensile test, the specimen initially exhibits a linear elastic behavior, where it deforms elastically before transitioning to a plastic behavior, in which it undergoes plastic deformation until yielding and potentially reaching fracture.

The 11 endoprosthesis specimens analyzed in this study were modeled using two different approaches. The first model, referred to as Model 1, is a simplified model in which only the plate and screws are explicitly analyzed, while other components of the specimen, such as the two bone-like material volumes and the tilting screw housing, are represented through boundary conditions applied to the specimen. The second model, referred to as Model 2, is more comprehensive than the first one and considers the entire prosthesis-bone system, including the plate, screws, and the two bone volumes. The only component not explicitly included but represented through boundary conditions is the tilting screw housing.

The main difference between the two models lies in the fact that, in the first model, the volume of the bone specimen is not explicitly considered. Instead, its presence is accounted for only through constraints applied to the screws. Specifically, to simulate the presence of bone between the screws—preventing them from moving freely and ensuring interaction with the bone-like material—springs have been applied between adjacent screw nodes. These springs have an elastic coefficient that reflects the characteristics of the bone-like material. However, this approach represents a significant approximation, as it does not consider the entire bone volume but rather approximates it using springs only between adjacent screws. In Model 1, due to the constraints imposed on the screws to simulate the presence of bone, the focus is placed on the behavior of the prosthetic plate during tensile loading. The attention is therefore directed toward the deformation occurring in the plate, allowing for the evaluation of its stiffness under these conditions. While this model does not accurately predict the overall system's behavior, it effectively predicts the real behavior of the prosthetic plate.

Moreover, in Model 1, due to both the exclusion of bone-like material volumes and the choice of constraints used to simulate the traction test performed in the laboratory, it is not possible to observe the effect of different screw inclinations. Instead, only the impact of variations in geometry and material can be appreciated. Conversely, in Model 2, which is more comprehensive, the effect of different screw inclinations can be observed, along with the influence of the plate geometry and material.

Another difference between the two models is that in Model 1, the screws are considered as cylinders with infinite stiffness to simulate their fixation within the bone volume. In contrast, in Model 2, they are also represented as cylinders—thus not reflecting the actual screw shape—but they have the true stiffness value of the material they are made of.

Conversely, in Model 2, the explicit inclusion of the bone-like material volumes enhances the model's capability to predict the overall behavior of the specimen. This model focuses on the bone-like material, enabling a more detailed analysis of its deformation during tensile testing. However, the accuracy of the prosthesis plate deformation is slightly lower compared to Model 1.

In conclusion, Model 1 provides a better prediction of the real behavior of the prosthesis plate, while Model 2 offers a more accurate representation of the overall behavior of the bone-like material specimens.

ANALYSIS OF MODEL 1

Once the geometry created in SolidWorks was imported into Ansys, the following steps were performed to conduct the tensile test on Model 1 of all prototypes:

1) The materials for the plate and screws were assigned, specifically the elastic modulus and Poisson's ratio corresponding to the materials used in their construction. For prototypes 1 to 4, mini endoprostheses, the plate material is Grade 5 titanium, while for prototypes 5 to 11, micro endoprostheses, the material is Grade 4 titanium. Additionally, the screws were modeled as infinitely rigid cylinders, meaning their elastic modulus was set as 1000 times that of their material, grade 5 titanium. The material properties used in the analysis are listed in *Table 9* below.

ELEMENT	MATERIAL	ELASTIC MODULUS [Gpa]	POISSON'S RATIO
PLATE MINI	Grade 5 Titanium	110	0,33
PLATE MICRO	Grade 4 Titanium	105	0,34
SCREW	Grade 5 Titanium	1,10E+05	0,33

Table 9: This table lists the two materials used for the construction of the prosthetic model plates: Grade 4 titanium and Grade 5 titanium and the material used for the screws. Depending on the prototype, one material or the other was used.

2) A mesh was created for the volumes using the SOLID185 tetrahedron element with a free structure. The mesh size used for the analysis of this model was selected based on the results obtained from the sensitivity studies, which are described in the following chapters. A mesh size of

0.25 mm was employed for the first four prototypes, whereas a mesh size of 0.325 mm was used for the remaining ones.

3) The contacts between the plate and screws were modeled as rigid contact, meaning all degrees of freedom for the nodes in the hole area were matched with those of the nodes in the screw area that passed through the hole. This approach aims to replicate the behavior observed in the experimental tests, specifically the pivoting housing of the screw that connects the plate to the screw.

4) To account for the presence of bone-like material between the screws and the existence of two separate blocks connected to the prosthesis, the following constraint strategy was implemented: springs were introduced between adjacent screw nodes using the COMBINE14 element. These springs were not applied between all screws; instead, they were used only to connect the screws belonging to the right half and those belonging to the left half. The two central screws were not connected to each other, thereby simulating the presence of two distinct bone volumes to which the screws are anchored.
   The screw element was assigned the material properties of the bone-like specimen, specifically 15 PCF material, which has an elastic modulus of 173 MPa and a Poisson's ratio of 0.30. Furthermore, for calculating the elastic constant of the spring—defined as the product of the elastic modulus of the spring material and its cross-sectional area, divided by the spring length—a square cross-section was assumed, with a side length equal to the mesh size. The length of the spring was experimentally measured as the distance between the screws.

5) Finally, loads and constraints were applied. The screw at the rightmost end was constrained through a fixed support, meaning that all nodes within the screw volume protruding from the plate hole were assigned zero displacements along the three axes (x, y, and z). This setup replicates the experimental test condition in which one of the two bone-like material specimens is clamped in the gripping system and remains stationary.
   For the screw at the leftmost end, all degrees of freedom of the nodes within the screw volume (excluding the regions in contact with the plate) were coupled, ensuring that they moved together as a single unit. A force was then applied in the negative x-direction (toward the left). This configuration simulates the experimental condition where the screws are fixed to the bone-like specimen, causing them to move under the applied load, which acts in the opposite direction to the fixed specimen.

Figure 87 below provides an example of how the constraints and loads were applied, as previously described.

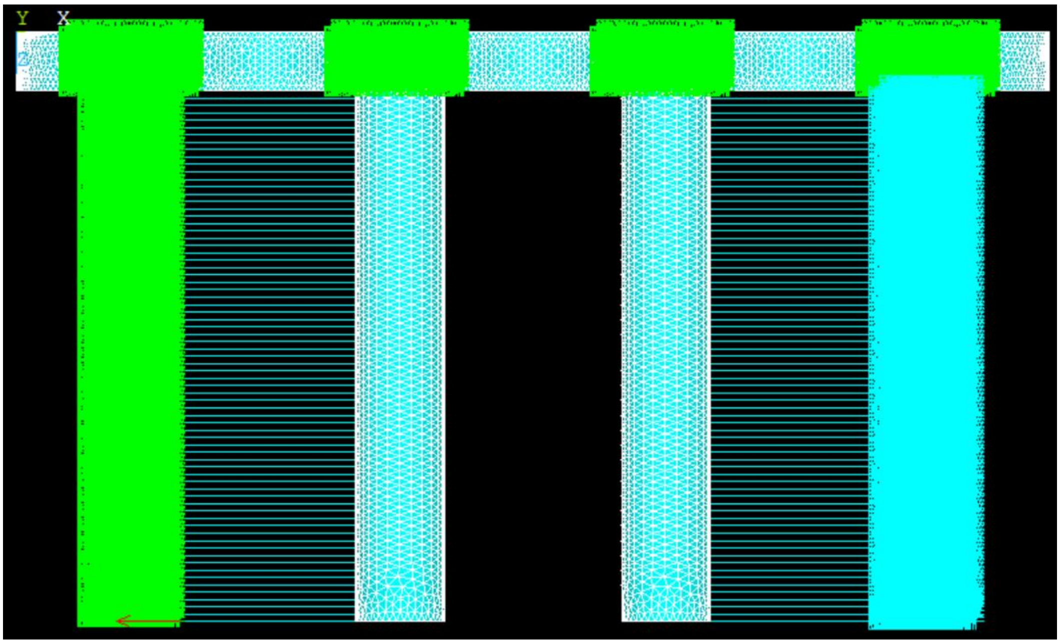

Figure 87: The constraints applied to Model 1 of prototype 1 are shown in the figure. The fixed constraints are indicated in light blue, the degrees of freedom constraints are shown in green, and the applied forces are depicted in red.

The forces selected for the static analysis of this specimen, later used to derive the force-displacement graph, were chosen based on the results of the experimental test. During the experimental test, it was observed that the specimen exhibited an initial phase of elastic deformation before undergoing plastic deformation, during which the force-deformation curve followed a linear trend. Therefore, the forces used in our numerical analysis were selected within the elastic deformation range of the specimen.

As a result, the force values chosen to represent the linear elastic behavior of the prosthesis prototypes were 80 N and 100 N.

Once all these steps were completed, the tensile test solution was launched. Finally, using the post-processor, it was possible to display the results of the test, where both the initial and the deformed geometries are shown. The deformation along each individual axis can also be observed, as well as the Von Mises stress.

In the following images, we can observe the deformation of the prosthesis prototypes along the x-axis, which is the axis along which the tensile test is performed. This deformation is shown for both force values chosen as the applied load, which were then used to calculate the model's stiffness. The deformations are expressed in meters.

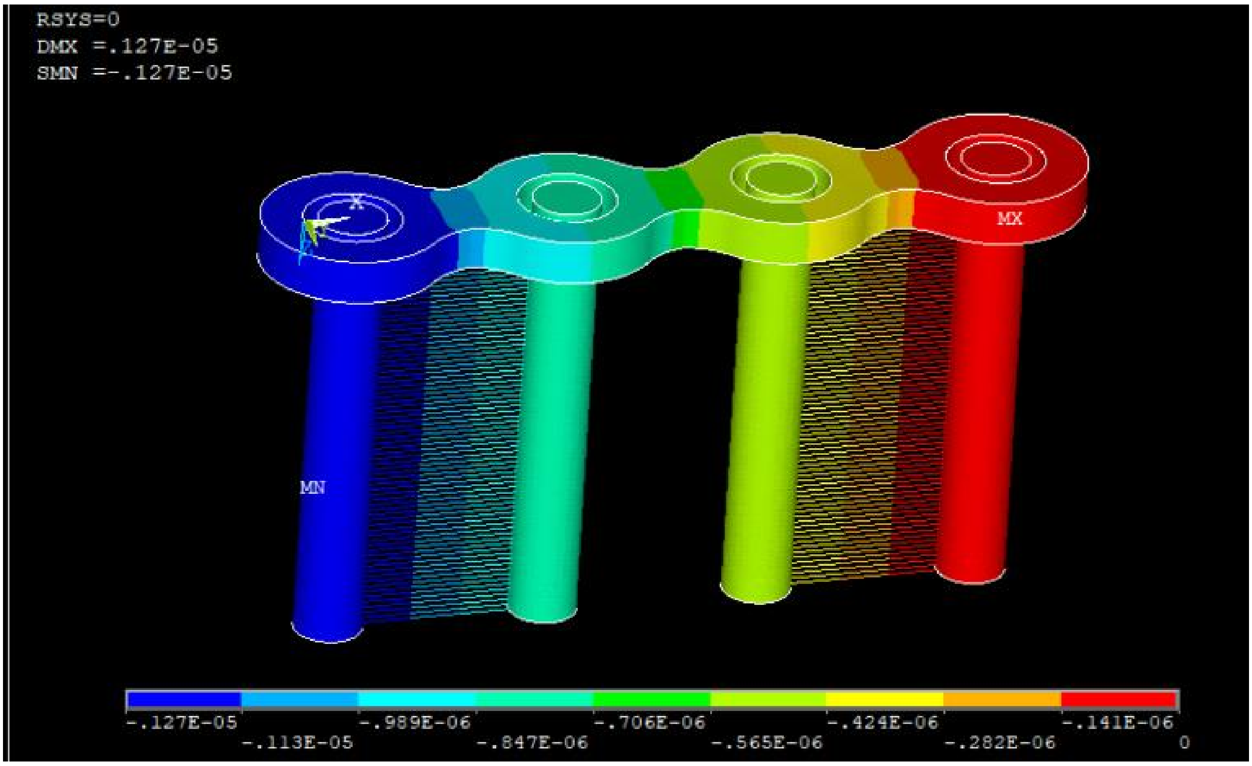

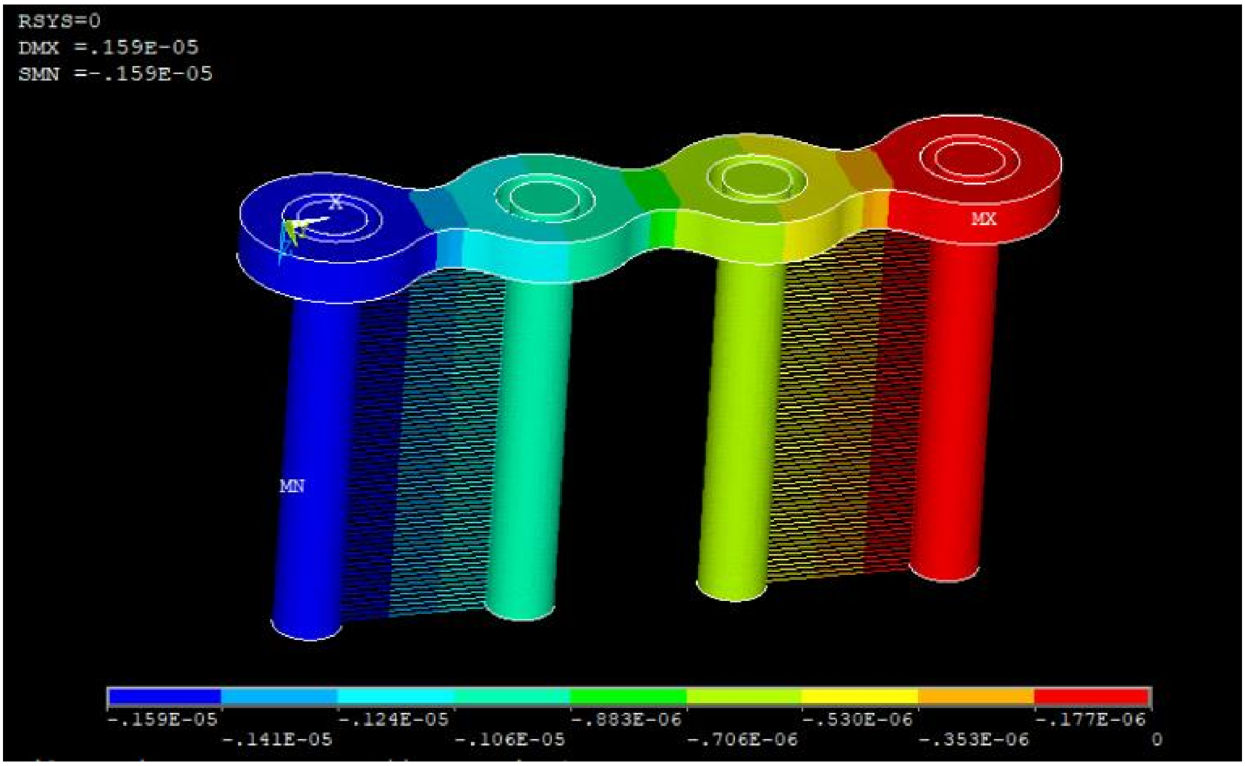

Figure 88: Prototype 1. In the image above, the deformation of the specimen is shown for a force of 80 N, while in the image below, the deformation is shown for a force of 100 N.

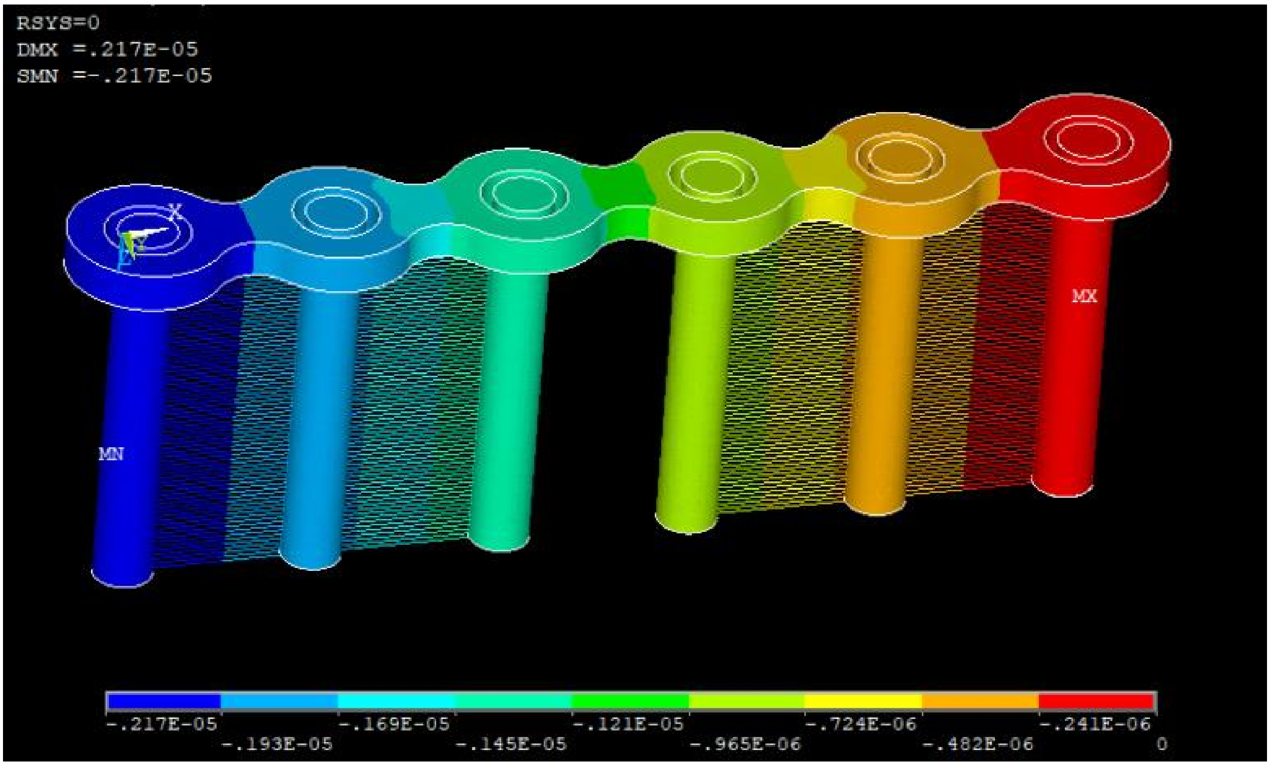

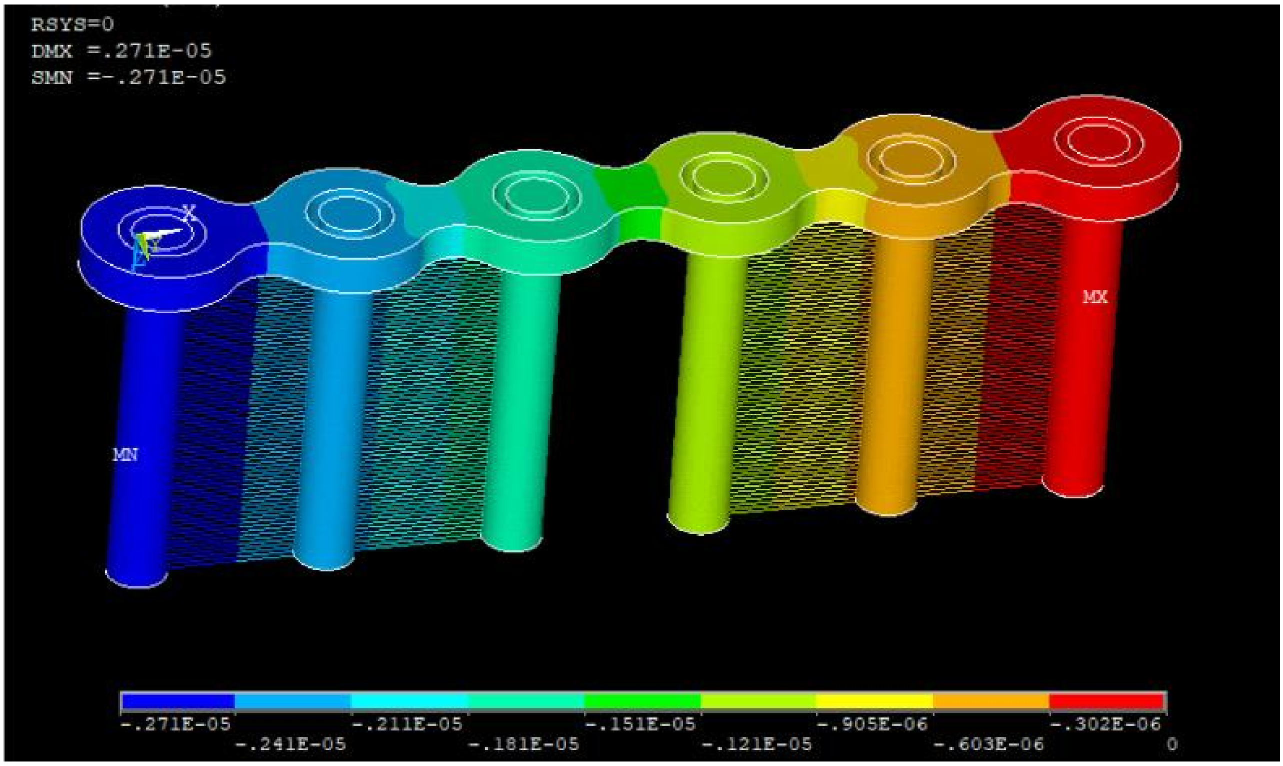

Figure 89: Prototype 2. In the image above, the deformation of the specimen is shown for a force of 80 N, while in the image below, the deformation is shown for a force of 100 N.

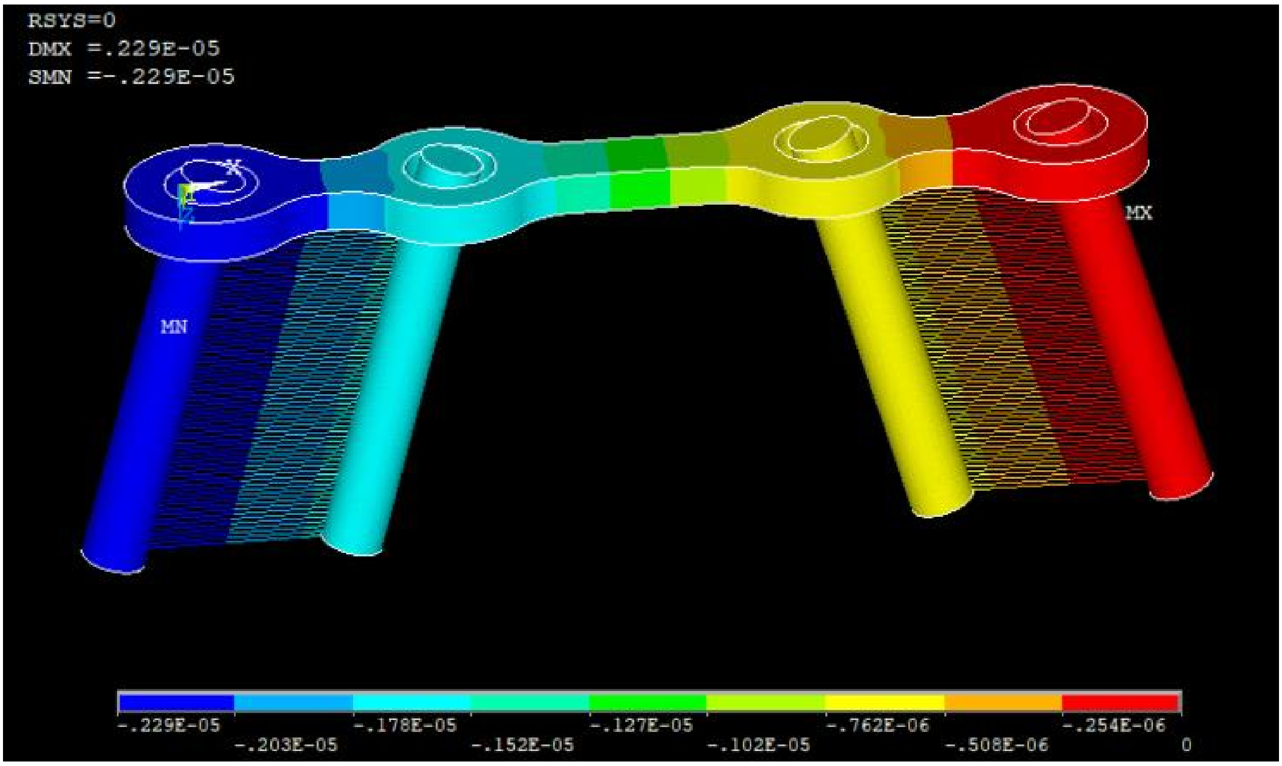

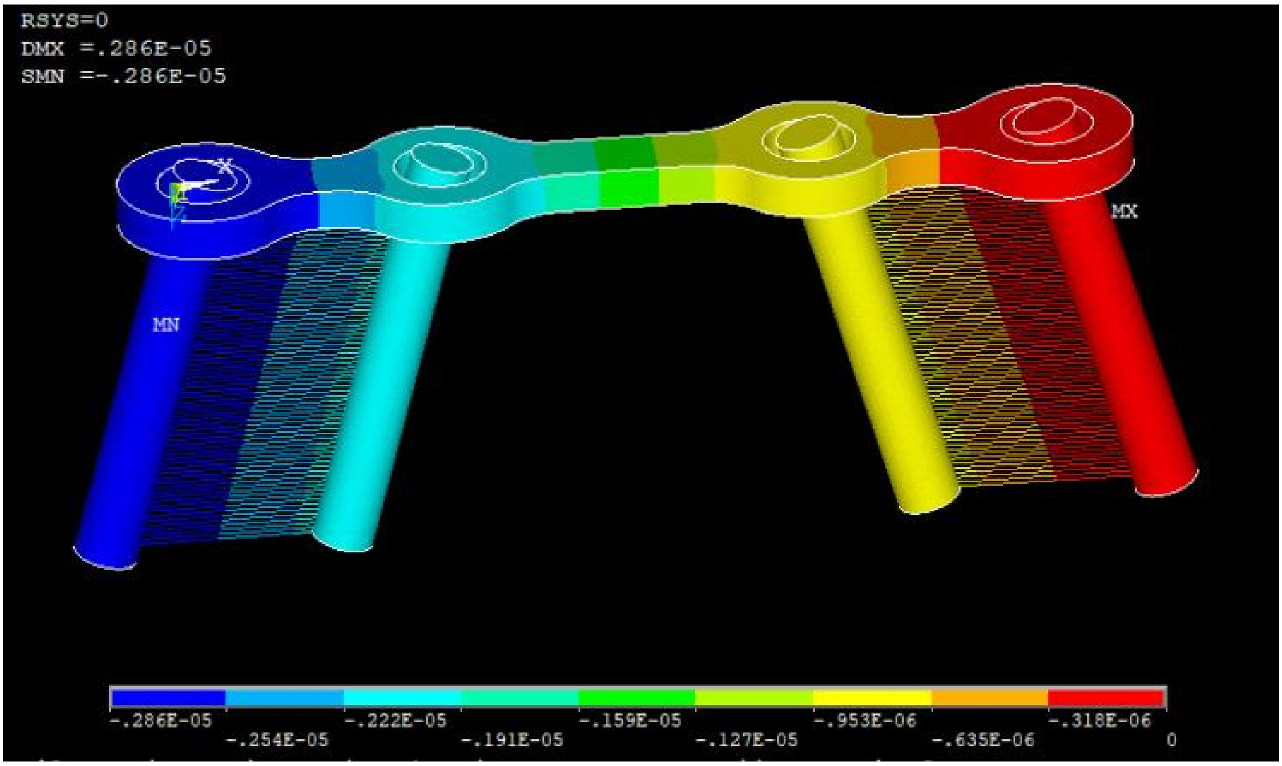

Figure 90: Prototype 3. In the image above, the deformation of the specimen is shown for a force of 80 N, while in the image below, the deformation is shown for a force of 100 N.

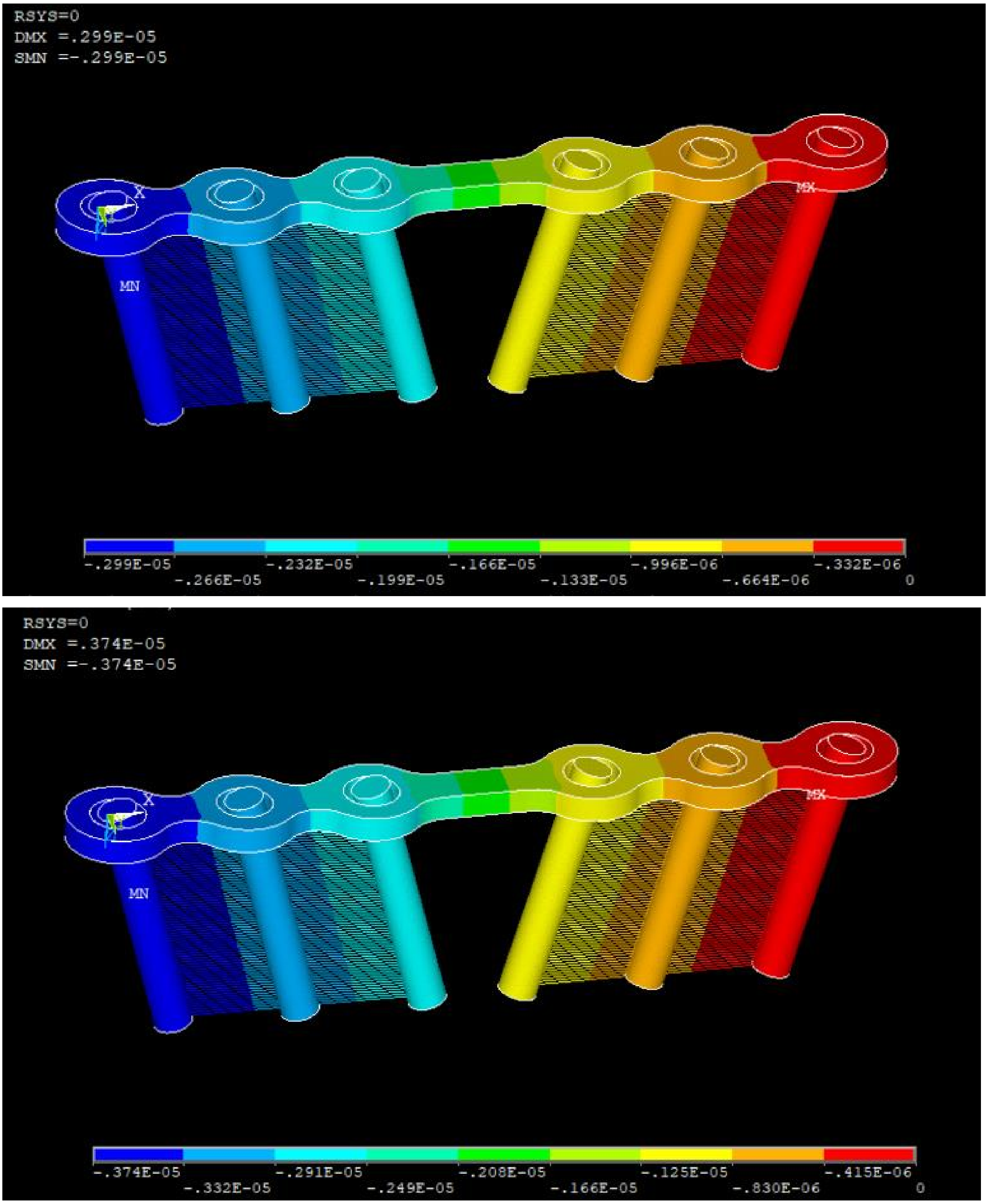

Figure 91: Prototype 4. In the image above, the deformation of the specimen is shown for a force of 80 N, while in the image below, the deformation is shown for a force of 100 N.

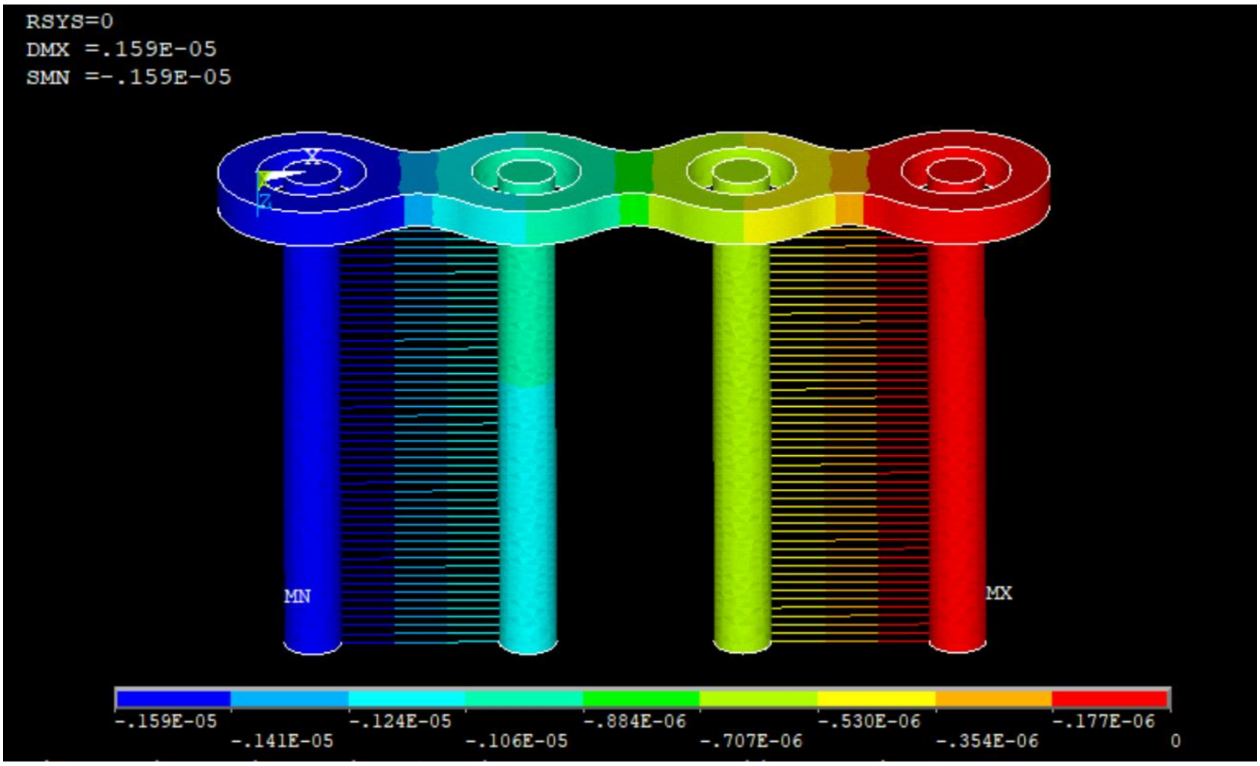

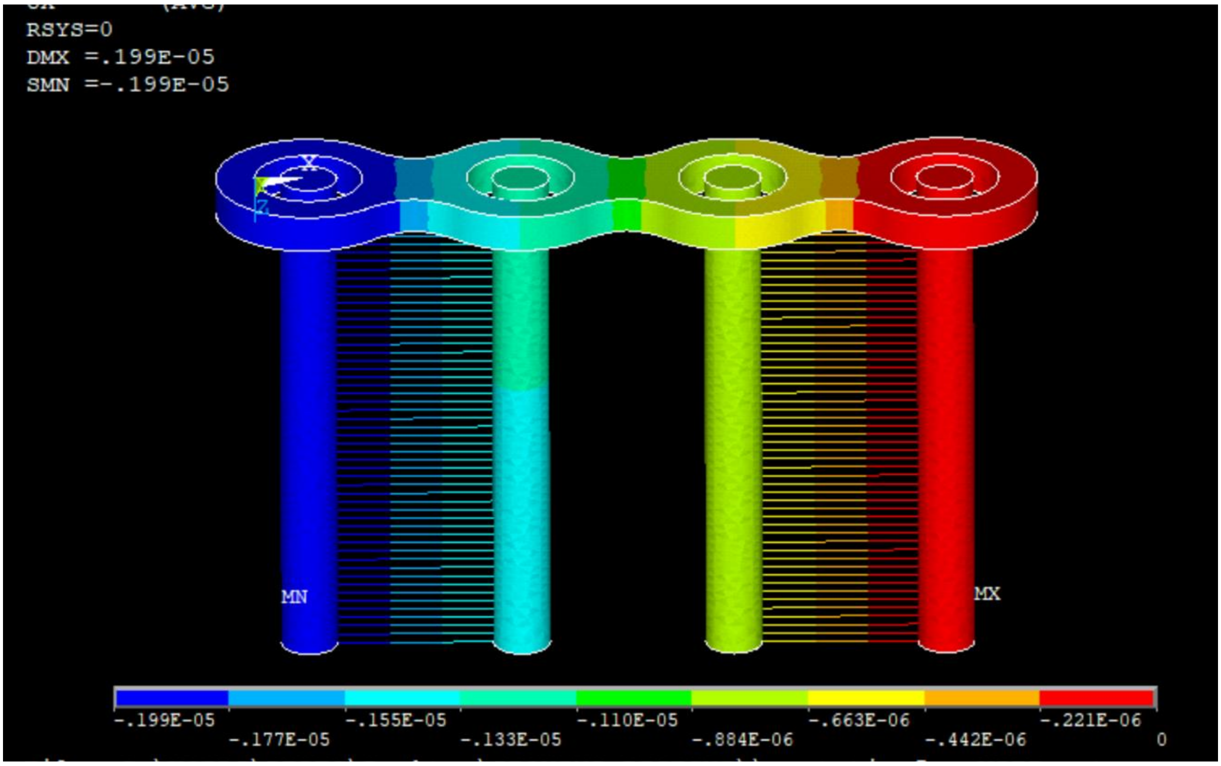

Figure 92: Prototype 5. In the image above, the deformation of the specimen is shown for a force of 80 N, while in the image below, the deformation is shown for a force of 100 N.

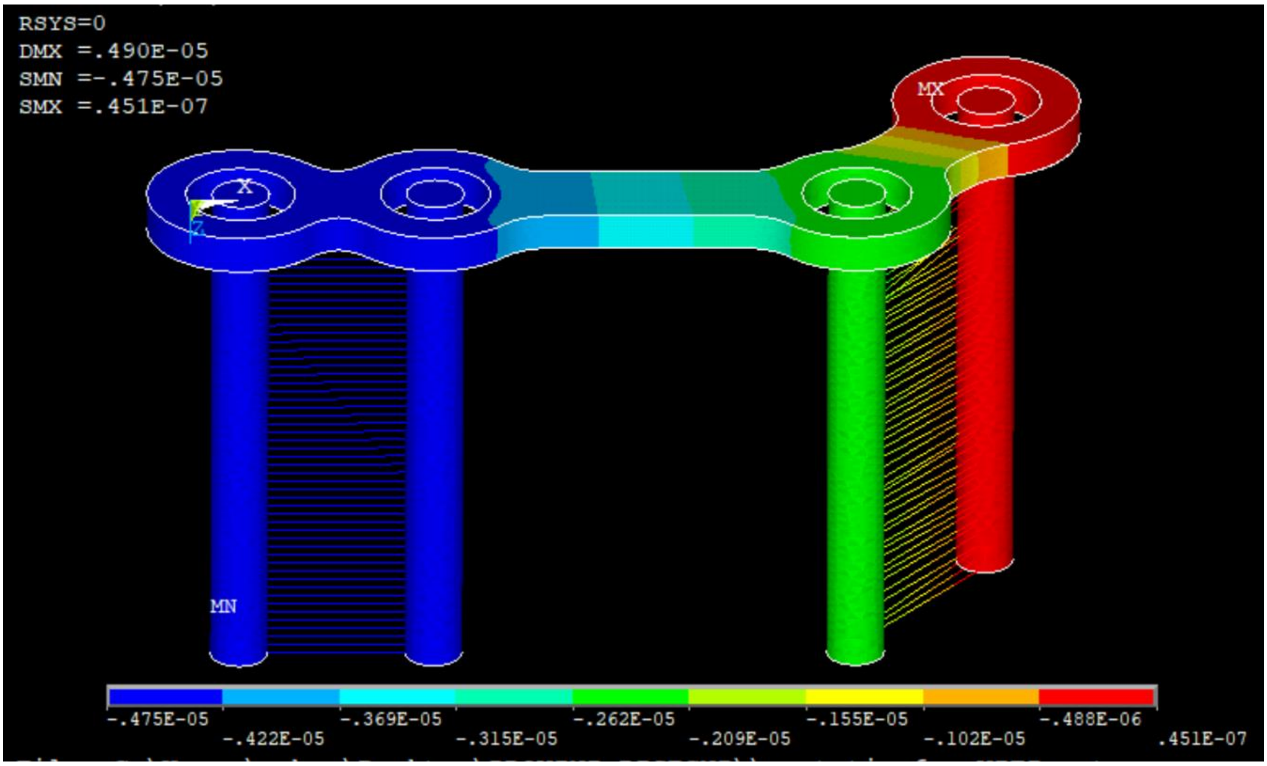

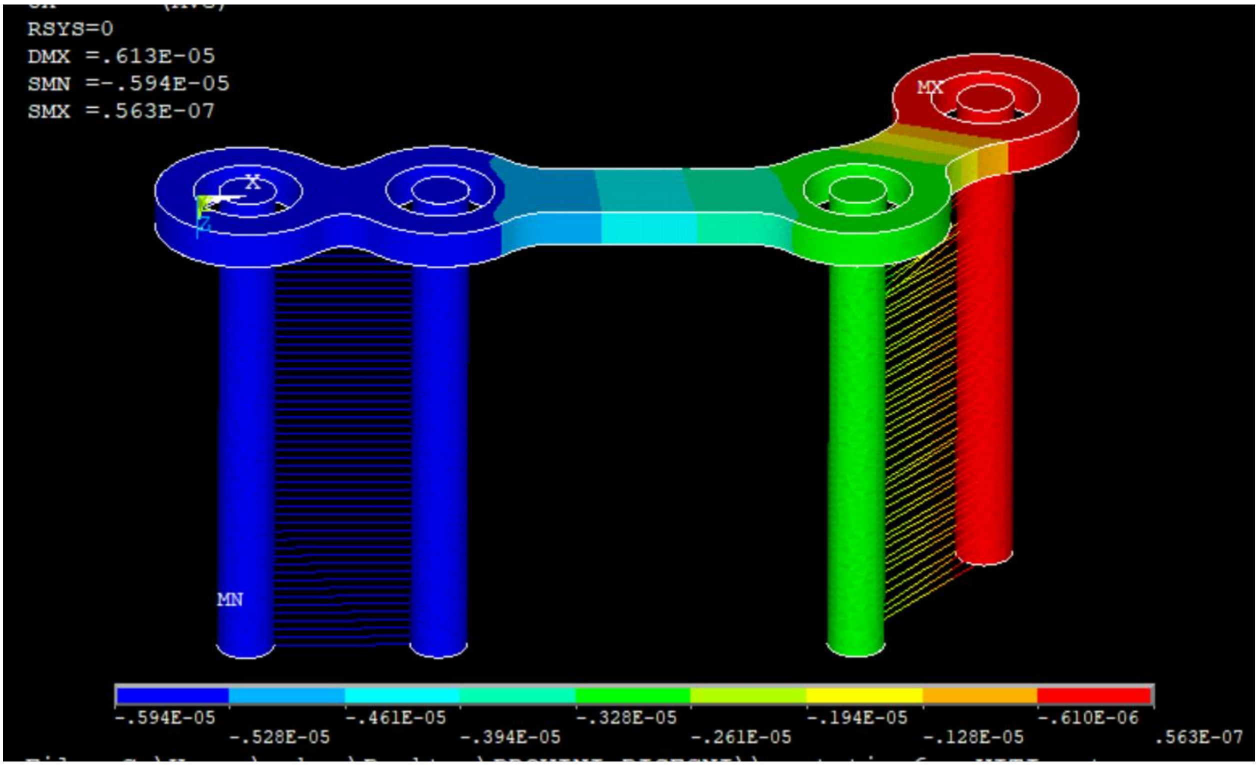

Figure 93: Prototype 6. In the image above, the deformation of the specimen is shown for a force of 80 N, while in the image below, the deformation is shown for a force of 100 N.

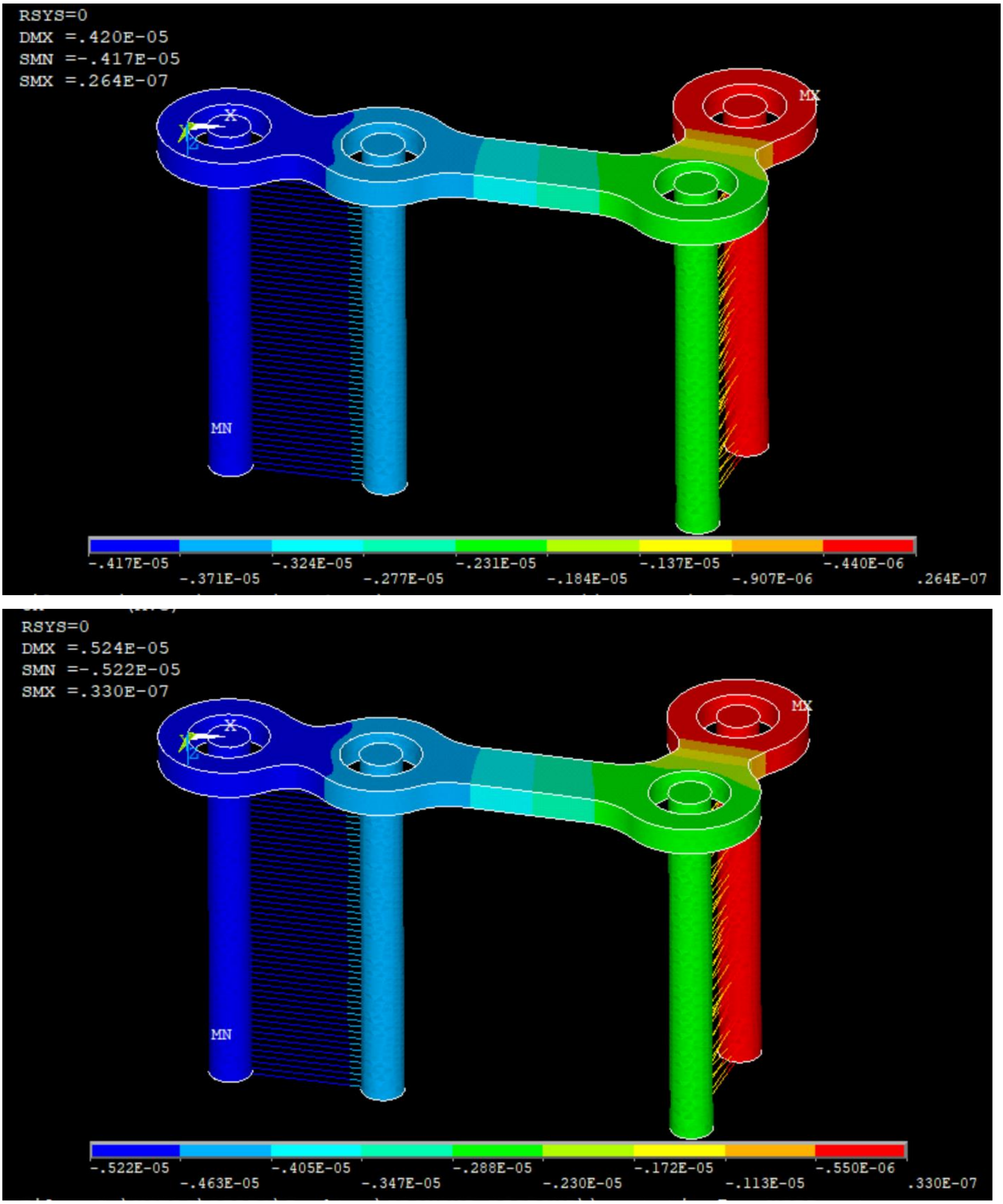

Figure 94: Prototype 7. In the image above, the deformation of the specimen is shown for a force of 80 N, while in the image below, the deformation is shown for a force of 100 N.

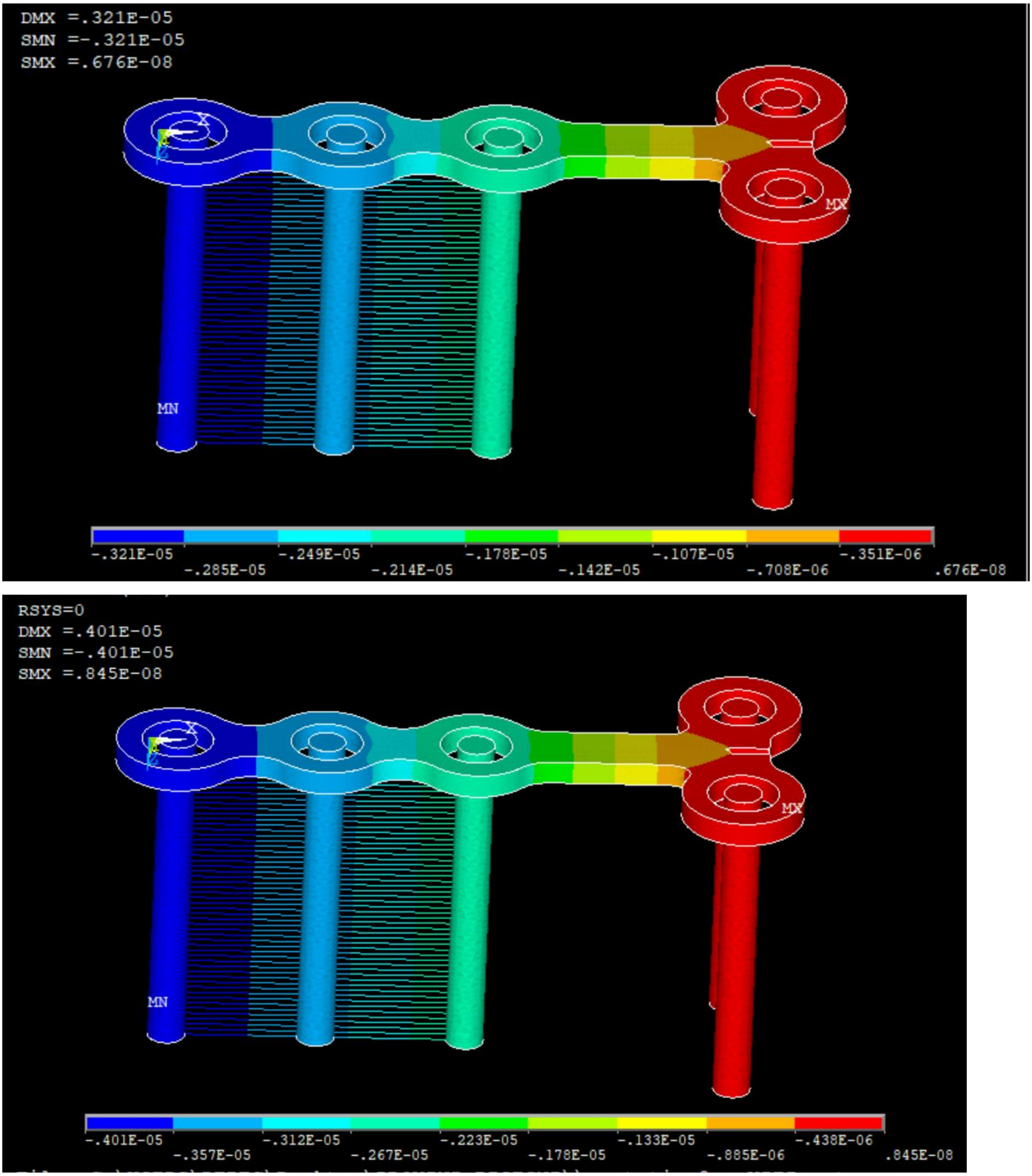

Figure 95: Prototype 8. In the image above, the deformation of the specimen is shown for a force of 80 N, while in the image below, the deformation is shown for a force of 100 N.

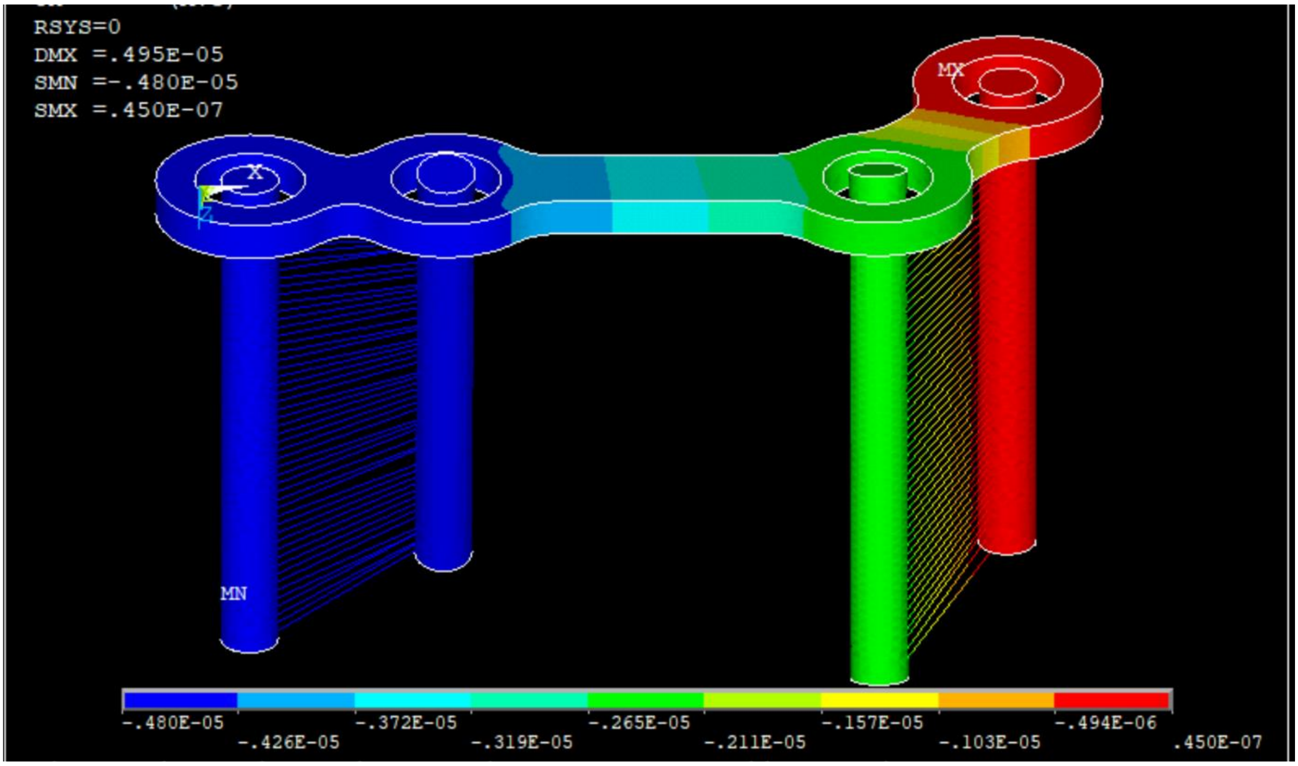

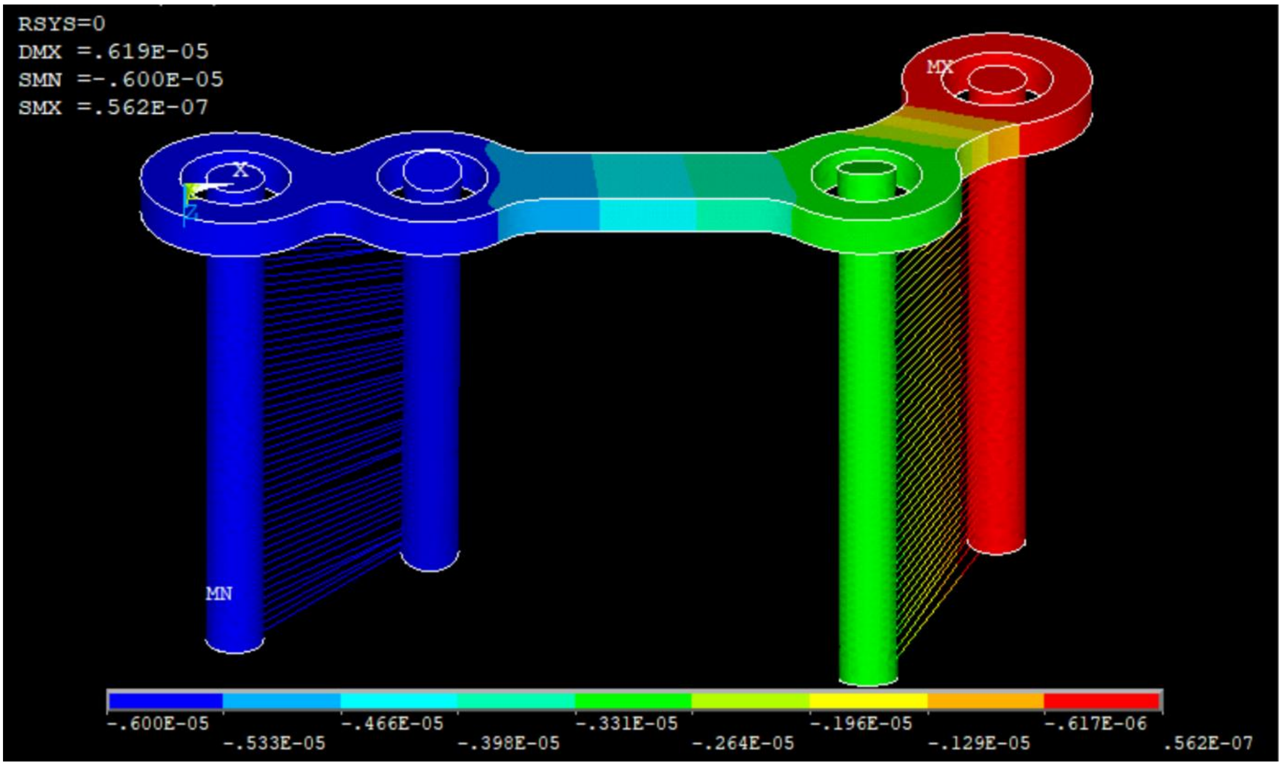

Figure 96: Prototype 9. In the image above, the deformation of the specimen is shown for a force of 80 N, while in the image below, the deformation is shown for a force of 100 N.

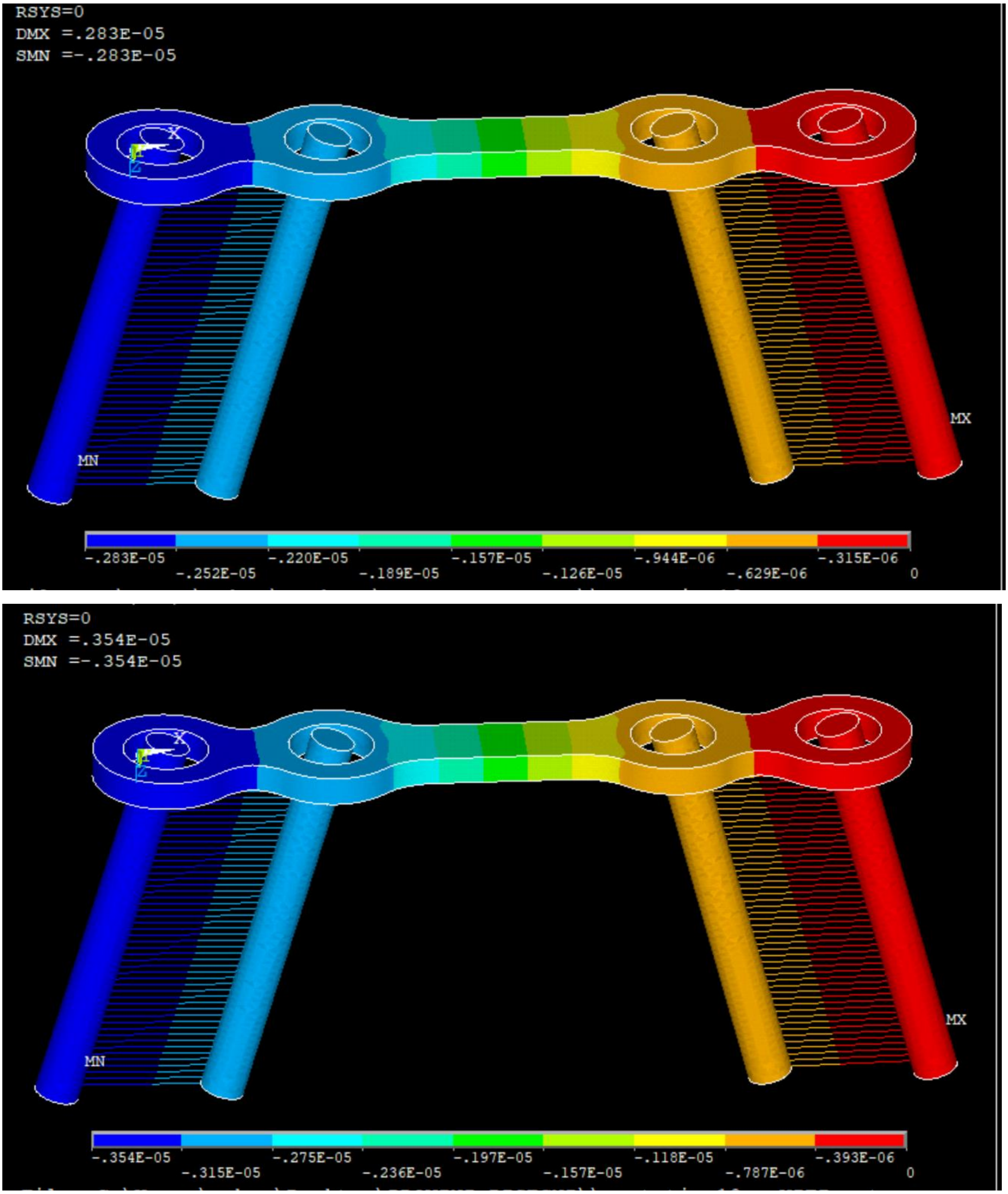

Figure 97: Prototype 10. In the image above, the deformation of the specimen is shown for a force of 80 N, while in the image below, the deformation is shown for a force of 100 N.

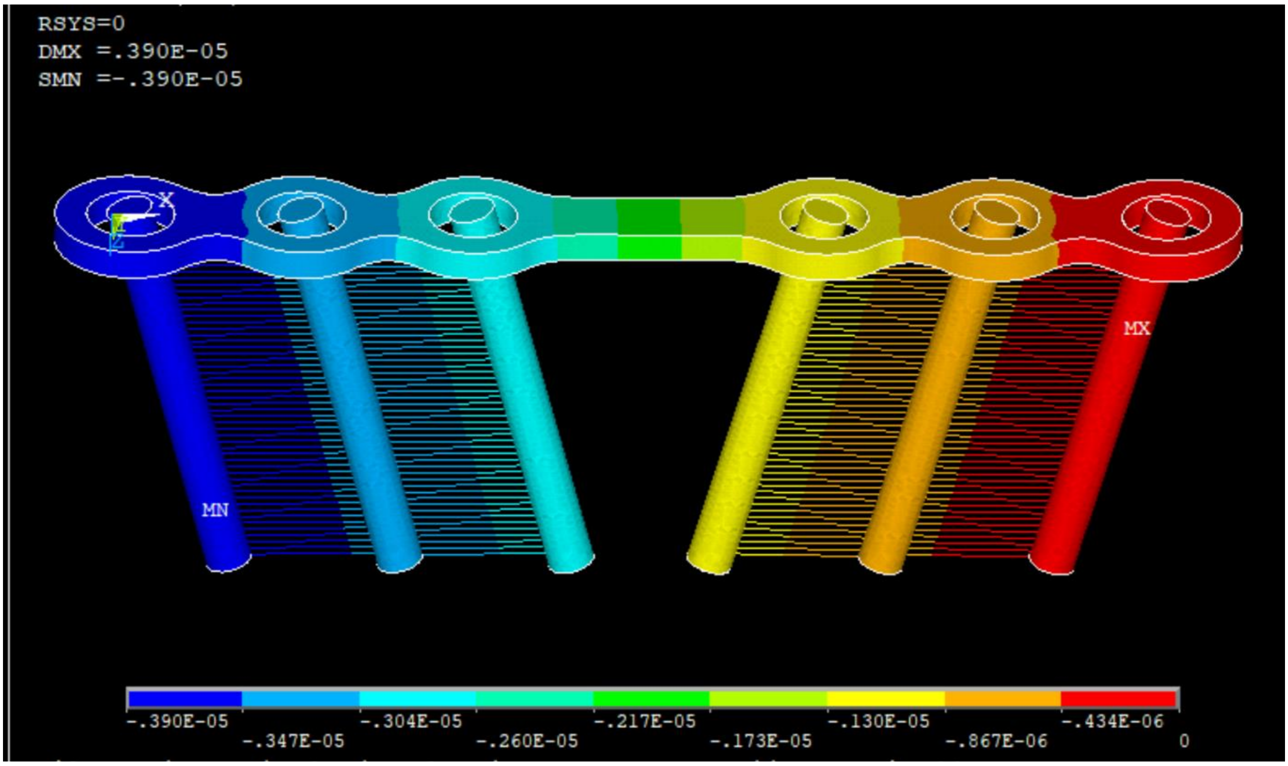

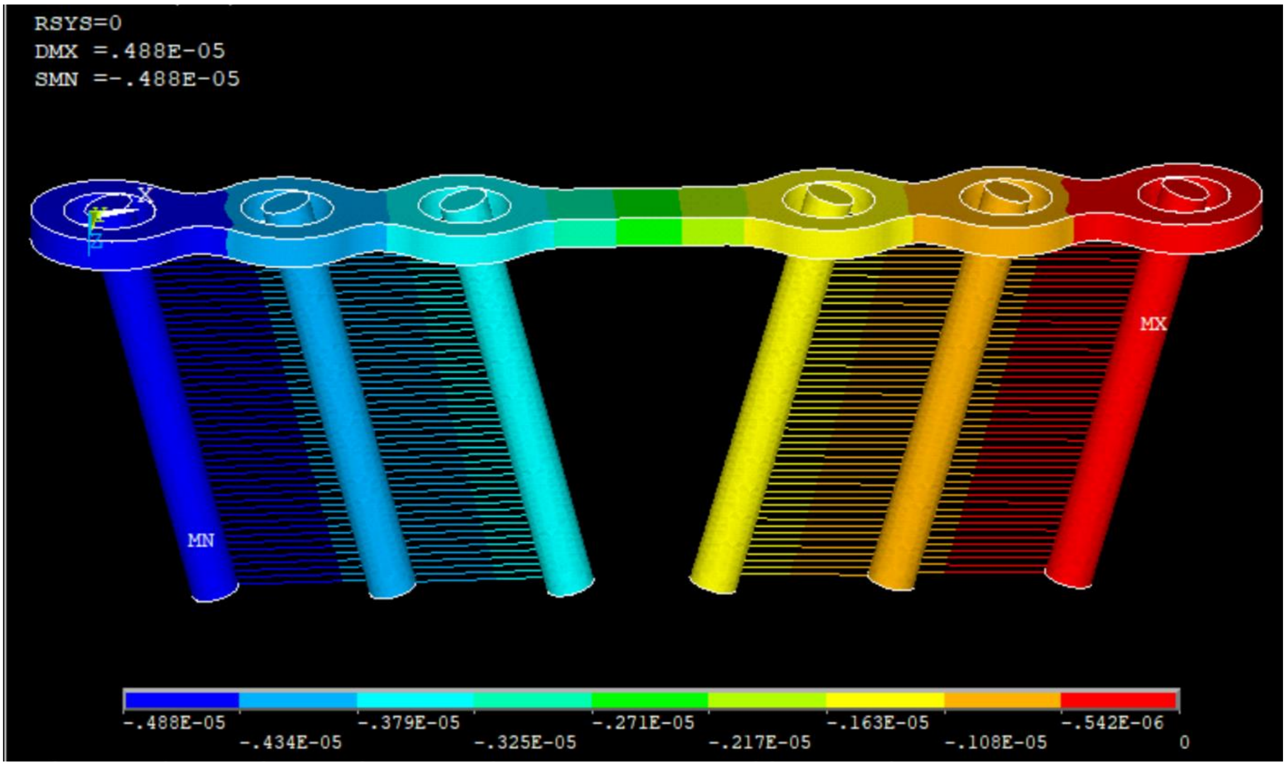

Figure 98: Prototype 11. In the image above, the deformation of the specimen is shown for a force of 80 N, while in the image below, the deformation is shown for a force of 100 N.

For each prototype, two tensile analyses were conducted using different force values to obtain the Force-Displacement curve associated with the test. In *Tables 10, 11, and 12*, we can see a summary of the displacement data calculated numerically and the corresponding stiffness values calculated based on these displacements for each of the 11 endoprosthesis prototypes along each of the three directions: x, y, and z.

In this tables, the first column indicates the number of the considered prototype, the second column shows the maximum deformation corresponding to a force of 80 N, the third column presents the maximum deformation corresponding to a force of 100 N, and finally, the fourth column displays the stiffness value calculated from the force-displacement graph of each prototype using the forces of 80 N and 100 N along with their associated deformations. The deformation is expressed in millimeters (mm), while the stiffness is measured in kilonewtons per millimeter (kN/mm).

PROTOTYPE NUMBER	X1 [mm]	X2 [mm]	STIFFNESS [kN/mm]
1	1,27E-03	1,59E-03	62,5
2	2,17E-03	2,71E-03	37,037
3	2,29E-03	2,86E-03	35,088
4	2,99E-03	3,74E-03	26,667
5	1,59E-03	1,99E-03	50
6	4,75E-03	5,94E-03	16,807
7	4,17E-03	5,22E-03	19,048
8	3,21E-03	4,01E-03	25
9	4,80E-03	6,00E-03	16,667
10	2,83E-03	3,54E-03	28,169
11	3,90E-03	4,88E-03	20,408

Table 10: In this table, we can see a summary of the displacement data calculated from the static tension analysis along the x-axis and the stiffness values for each of the endoprosthesis prototypes.

PROTOTYPE NUMBER	Y1 [mm]	Y2 [mm]	STIFFNESS [kN/mm]
1	1,09E-04	1,36E-04	735,294
2	1,09E-04	1,12E-04	6000
3	1,20E-04	1,50E-04	666,667
4	1,20E-04	1,50E-04	666,667
5	1,66E-04	2,07E-04	487,805
6	1,42E-03	1,79E-03	54,201
7	8,79E-04	1,10E-03	90,909
8	2,01E-04	2,51E-04	400
9	1,43E-03	1,79E-03	56,338
10	1,99E-04	2,49E-04	402,414
11	1,99E-04	2,49E-04	399,202

Table 11: In this table, we can see a summary of the displacement data calculated from the static tension analysis along the y-axis and the stiffness values for each of the endoprosthesis prototypes.

PROTOTYPE NUMBER	Z1 [mm]	Z2 [mm]	STIFFNESS [kN/mm]
1	8,84E-05	1,11E-04	904,977
2	8,97E-05	1,36E-04	432,9
3	8,35E-05	1,04E-04	961,538
4	8,84E-05	1,11E-04	904,977
5	9,36E-05	1,17E-04	854,701
6	1,85E-04	2,31E-04	433,839
7	1,52E-04	1,90E-04	526,316
8	1,41E-04	1,76E-04	566,572
9	1,90E-04	2,38E-04	419,287
10	9,45E-05	1,18E-04	847,458
11	9,21E-05	1,15E-04	869,565

Table 12: In this table, we can see a summary of the displacement data calculated from the static tension analysis along the z-axis and the stiffness values for each of the endoprosthesis prototypes.

In *Table 13*, the summarized data of the maximum Von Mises stress for each prototype is presented. Specifically, the first column indicates the prototype number, the second column shows the maximum Von Mises stress associated with the applied force of 80 N during tension analysis, and the third column displays the maximum Von Mises stress associated with the applied force of 100 N during tension analysis. The Von Mises stresses are given in megapascals (MPa).

PROTOTYPE NUMBER	VON MISES STRESS 1 [MPa]	VON MISES STRESS 2 [MPa]
1	18,4	23
2	18,4	23
3	16,1	20,1
4	16,9	21,2
5	24,7	30,9
6	48,7	60,9
7	42,2	52,7
8	36,1	45,2
9	48,8	60,9
10	23,6	29,6
11	24,6	30,8

Table 13: In this table, we can see a summary of the Von Mises stress data calculated from the static tension analysis.

DISCUSSION OF MODEL 1 RESULTS

As we can observe from the images representing the prosthesis deformation, the plate deforms following the deformation of the screws. This occurs because, in this model, the screws have been represented as cylinders with infinite stiffness. Additionally, the constraints imposed on the screws ensure that the regions of the plate through which the screws pass exhibit the same deformations as the screws themselves. This is because the degrees of freedom of the nodes in the hole areas of the plate have been constrained to those of the nodes in the corresponding areas of the screws passing through the holes. Consequently, in these regions, the plate behaves similarly to the screws.

The deformation values of the prostheses are significantly small, which is consistent with the elastic modulus of the materials used for the plate, as these materials are relatively rigid. Furthermore, the screws are considered infinitely rigid cylinders. In this model, the focus is placed on the deformation of the prosthesis, and the behavior within the bone specimen is not considered, as the bone material in this model is regarded solely as a constraint between the screws.

The stiffness values derived from the force-deformation graph, obtained from the displacement resulting from numerical analysis, are very high, in the order of tens of kN/mm, as shown in the tables summarizing all the data. This is because, in this model, the calculated stiffness corresponds only to that of the prosthesis, without taking into account the contribution of the bone. From the tables, it can be observed that for all prototypes, the lowest stiffness is along the x-axis, which corresponds to the direction of traction. Indeed, the prosthesis is expected to deform more along the traction axis compared to the other directions.

Since some prototypes exhibit similar geometries, it is possible to analyze how the model's stiffness varies by changing the material, geometric dimensions, and screw inclination. Regarding the stiffness along the x-axis, which is the direction of traction, it can be observed that:

- Prototypes 1 and 5 have similar geometries, both featuring four screws that are perpendicular to the plate. The main differences between them lie in their dimensions and materials. Prototype 1 is made of Grade 5 titanium and is thicker, whereas Prototype 5 is made of Grade 4 titanium and is thinner. The tables show that Prototype 1 has higher stiffness values compared to Prototype 5, which is consistent with the fact that Grade 5 titanium has a higher elastic modulus. Therefore, given the same shape, it is expected that Prototype 1 exhibits greater stiffness.

- Prototypes 3 and 10 have similar geometries, both incorporating four screws inclined at 15 degrees toward the prosthesis extremity. Prototype 3 is made of Grade 5 titanium and is thicker, while Prototype 10 is made of Grade 4 titanium and is thinner. The tables indicate that Prototype 3 has higher stiffness values than Prototype 10, aligning with the higher elastic modulus of

Grade 5 titanium. Consequently, for the same shape, it is reasonable for Prototype 3 to have greater stiffness.

- Prototypes 4 and 11 share similar geometries, each containing six screws inclined at 15 degrees toward the center of the prosthesis. Prototype 4 is made of Grade 5 titanium and is thicker, whereas Prototype 11 is made of Grade 4 titanium and is thinner. The tables show that Prototype 4 has higher stiffness values compared to Prototype 11, which is consistent with the higher elastic modulus of Grade 5 titanium. Therefore, maintaining the same shape, Prototype 4 is expected to have greater stiffness.
- Prototypes 1, 3, 5, and 10 all feature four screws, but with different inclinations. Prototypes 1 and 5 have screws perpendicular to the plate, while Prototypes 3 and 10 have screws inclined at 15 degrees relative to the perpendicular, toward the extremity of the prosthesis. It can be observed that Prototypes 3 and 10 exhibit lower stiffness compared to Prototypes 1 and 5. Since, due to the imposed constraints, the screw inclination does not affect the model's behavior, the stiffness difference in this case is associated with the prosthesis length. Longer prostheses undergo greater deformation and, consequently, have lower stiffness.
- Prototypes 6 and 9 are made of the same material and share the same plate geometry but differ in screw inclination. Prototype 6 has all screws perpendicular to the plate, whereas Prototype 9 has two screws perpendicular to the plate and two screws inclined at 15 degrees relative to the vertical, toward the prosthesis side. As observed in the tables, these two prototypes exhibit very similar stiffness values. This result is as expected: given that their geometries are nearly identical and the screw inclination does not influence deformation due to the imposed constraints, it is reasonable for these two models to have similar stiffness.
- Prototypes 10 and 11 are made of the same material and have similar shapes. In particular, Prototype 10 has two screws per side, while Prototype 11 has three screws per side, making Prototype 11 longer than Prototype 10. The data show that the model's stiffness in this case is related to the prosthesis length. Since Prototype 11 is longer than Prototype 10, it deforms more and, consequently, has lower stiffness.
- Prototypes 3 and 4 are made of the same material and have similar shapes. Specifically, Prototype 3 has two screws per side, while Prototype 4 has three screws per side, making Prototype 4 longer than Prototype 3. The data indicate that the model's stiffness in this case is dependent on prosthesis length. Since Prototype 4 is longer than Prototype 3, it undergoes greater deformation and, therefore, has lower stiffness.

- Prototypes 2 and 4 are made of the same material, have similar shapes, and feature the same number of screws (three per side). However, Prototype 4 has a greater overall length compared to Prototype 2. The table shows that Prototype 2 exhibits significantly higher stiffness than Prototype 4.
- Prototypes 6 and 7 both have four screws positioned perpendicularly to the plate and share similar shapes, specifically an L-shape. However, while Prototype 7 has a 90-degree angle between the two arms, Prototype 6 features an angle of 118.25 degrees. The tables indicate that Prototype 7 is stiffer than Prototype 6, demonstrating that the geometry of this model significantly influences the prosthesis stiffness.

Therefore, for this model, deformation along the x-axis depends on the prosthesis length. Longer prostheses experience greater deformation and consequently have lower stiffness.

Regarding stiffness along the y-axis, we can observe that the first four prototypes exhibit higher stiffness values compared to the others, which is consistent with the fact that the material used in the first four prototypes has a higher elastic modulus than that of the remaining ones. Additionally, most prototypes have stiffness values in the range of hundreds of kN/mm, except for Prototypes 6, 7, and 9, which exhibit stiffness values in the range of tens of kN/mm. This is because, in these specimens, the plate geometry extends along the y-axis as well, unlike the other models, which develop only along the x-axis. This structural difference makes these prototypes more deformable along the y-axis.

Finally, examining stiffness along the z-axis in detail, we can observe that the first four specimens exhibit greater stiffness compared to the others. Between the two groups of prostheses, mini and micro, there is a notable difference; however, within each group, the stiffness values are relatively similar to one another.

Regarding the Von Mises stress*, Table 13* shows that the prototypes subjected to the highest stress are numbers 6, 7, 8, and 9, which have non-linear shapes and geometries that extend not only along the x-axis but also along the y-axis. The stress values experienced by the prosthesis are lower than the yield strength of titanium—795 MPa for grade 5 titanium (used in the first four specimens) and 485 MPa for grade 4 titanium (used in the remaining specimens).

The appendix contains figures illustrating the Von Mises stress distribution along the prosthesis for each prototype.

ANALYSIS OF MODEL 2

Once the geometry created in SolidWorks was imported into Ansys, the following steps were performed to conduct the tensile test on Model 2 of all prototypes:

1) The materials for the plate and screws were assigned, specifically the elastic modulus and Poisson's ratio corresponding to the materials used in their construction. For prototypes 1 to 4, mini endoprostheses, the plate material is Grade 5 titanium, while for prototypes 5 to 11, micro endoprostheses, the material is Grade 4 titanium. Additionally, the material for the screws were assigned, their material is grade 5 titanium. The material for the bone-like volume was also assigned, whose elastic modulus was calculated by taking a weighted average of the elastic moduli of the two materials that composed the bone specimen, namely 50 PCF and 15 PCF, which have elastic moduli of 1.469 GPa and 173 MPa, respectively. The material properties used in the analysis are listed in *Table 14* below.

ELEMENT	MATERIAL	ELASTIC MODULUS [GPa]	POISSON'S RATIO
PLATE MINI	Grade 5 Titanium	110	0,33
PLATE MICRO	Grade 4 Titanium	105	0,34
SCREW	Grade 5 Titanium	110	0,33
BONE	weighted average PCF	3,94E-01	0,3

Table 14: This table lists the two materials used for the construction of the prosthetic model plates: Grade 4 titanium and Grade 5 titanium -depending on the prototype, one material or the other was used as previously indicated. The material of the screw and the material for the bone-like volume.

2) A mesh was created for the volumes using the SOLID185 tetrahedron element with a free structure. The mesh size used for the analysis of this model was selected based on the results obtained from the sensitivity studies, which are described in the following chapters. A mesh size of 0.5 mm was employed for the first four prototypes, whereas a mesh size of 0.65 mm was used for the remaining ones.

3) The contacts between the plate and screws were modeled as rigid contact, meaning all degrees of freedom for the nodes in the hole area were matched with those of the nodes in the screw area that passed through the hole. This approach aims to replicate the behavior observed in the experimental tests, specifically the pivoting housing of the screw that connects the plate to the screw.

4) The contact between the screws and the bone section into which they are threaded was represented by merging the nodes of the two contacting surfaces, namely the surface of the screw and the bone surface into which the screw is inserted.

5) Finally, the loads and constraints were applied. One of the two bone-like material volumes was constrained with a fixed support to simulate the experimental test, where a bone sample was placed inside a holding clamp that held it in place. Specifically, the holding clamp used in the experimental test did not contain the entire volume of the sample, but only a part of it; the sample was inserted into the fixture for only 2.5 cm. To precisely replicate this, the fixed support was applied only to the last 2.5 cm of the bone-like material volume. This constraint involved selecting all the nodes of this volume and imposing a displacement of zero along the x, y, and z axes. For the other volume, to simulate the experimental test where the second volume was placed in a different holding clamp and pulled, all the nodes of the last 2.5 cm of the volume were selected, and all their degrees of freedom were set equal using the CP command, so that they moved together, just as during the experimental test. Finally, the desired force was applied to this set of nodes.

Figure 99 below provides an example of how the constraints and loads were applied, as previously described.

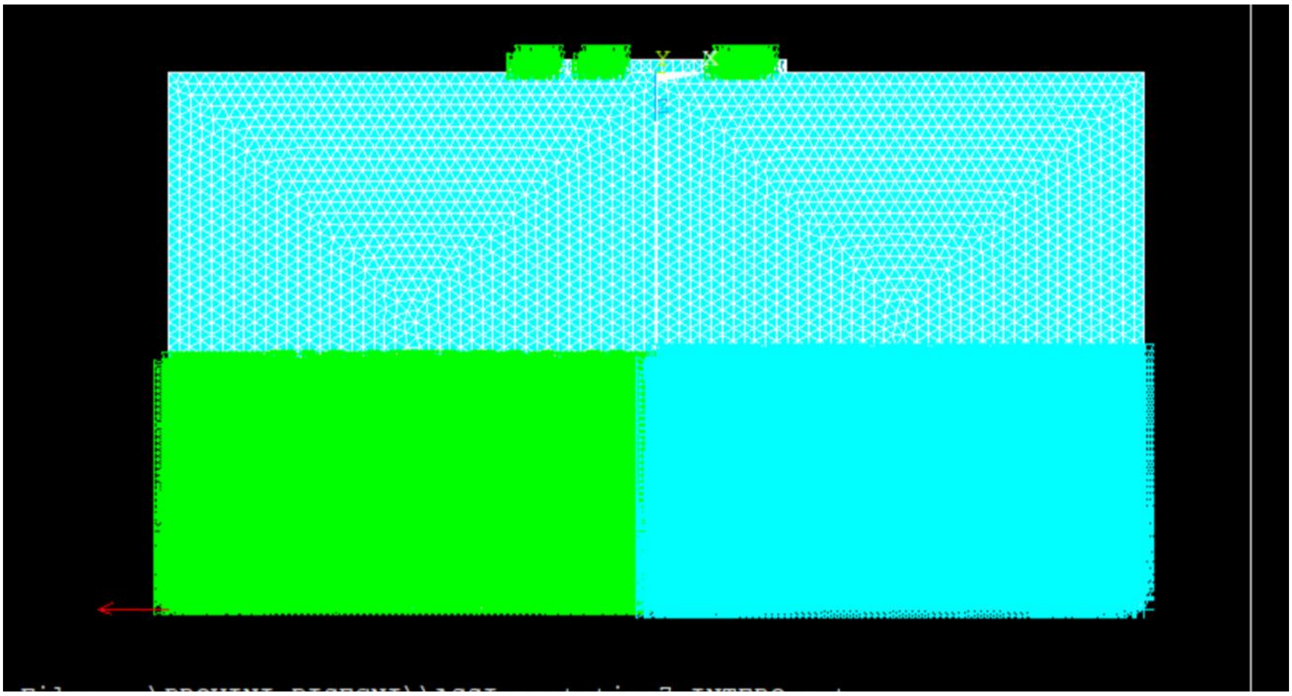

Figure 99: In the figure, the constraints applied to Model 2 of prototype 6 are shown. The fixed constraints are indicated in light blue, the degrees of freedom constraints are shown in green, and the applied forces are depicted in red.

The forces selected for the static analysis of this specimen, later used to derive the force-displacement graph, were chosen based on the results of the experimental test. During the experimental test, it was observed that the specimen exhibited an initial phase of elastic deformation before undergoing plastic deformation, during which the force-deformation curve followed a linear trend. Therefore, the forces used in our numerical analysis were selected within the elastic deformation range of the specimen.

As a result, the force values chosen to represent the linear elastic behavior of the prosthesis prototypes were 80 N and 100 N.

Once all these steps were completed, the tensile test solution was launched. Finally, using the post-processor, it was possible to display the results of the test, where both the initial and the deformed geometries are shown. The deformation along each individual axis can also be observed. In the following images, we can observe the deformation of the prosthesis prototypes along the x-axis, which is the axis along which the tensile test is performed. This deformation is shown for both force values chosen as the applied load, which were then used to calculate the model's stiffness.

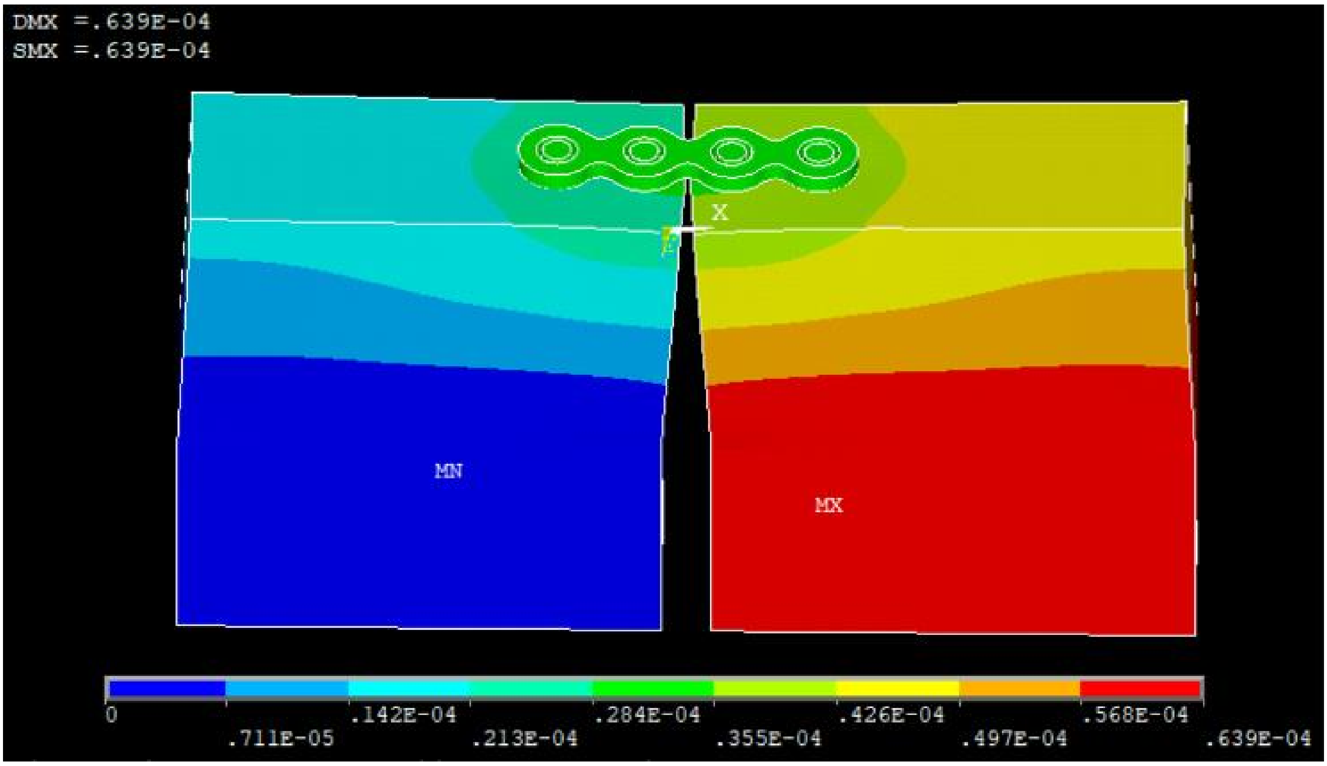

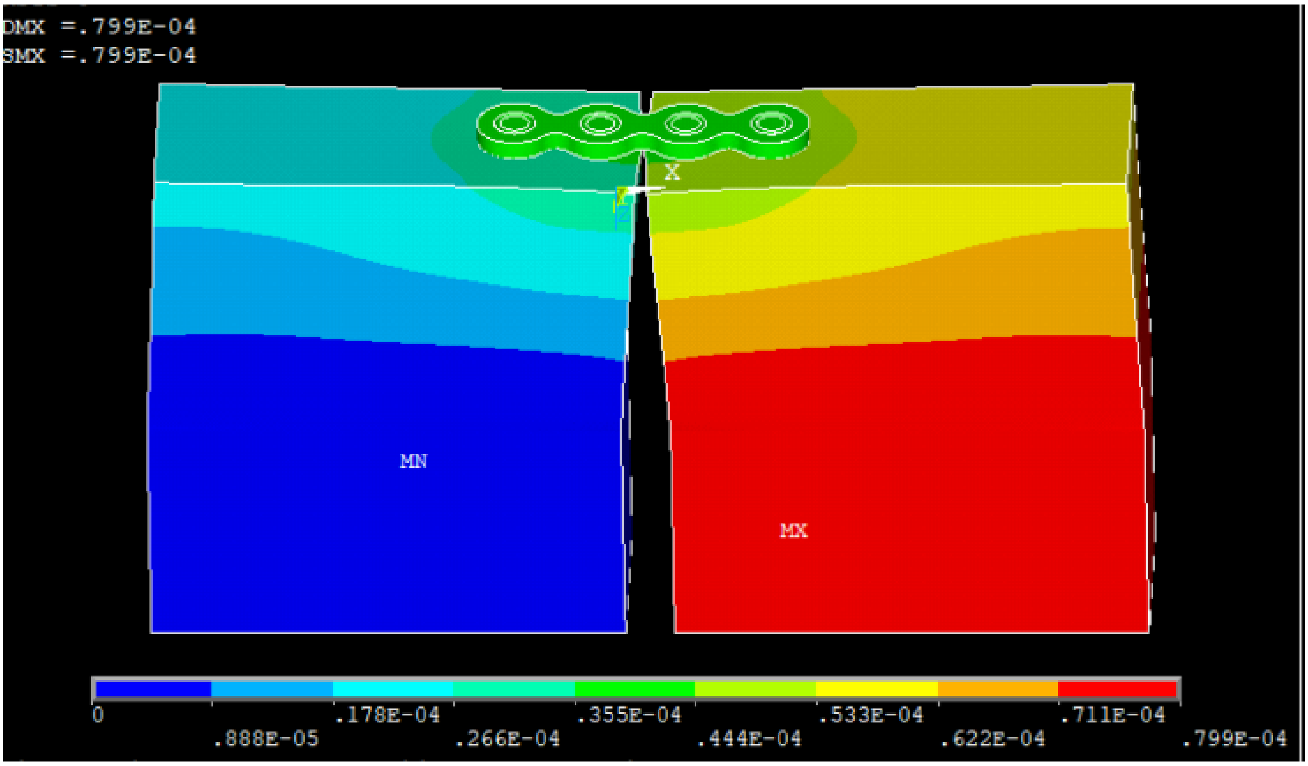

Figure 100: Prototype 1. In the image above, the deformation of the specimen is shown for a force of 80 N, while in the image below, the deformation is shown for a force of 100 N.

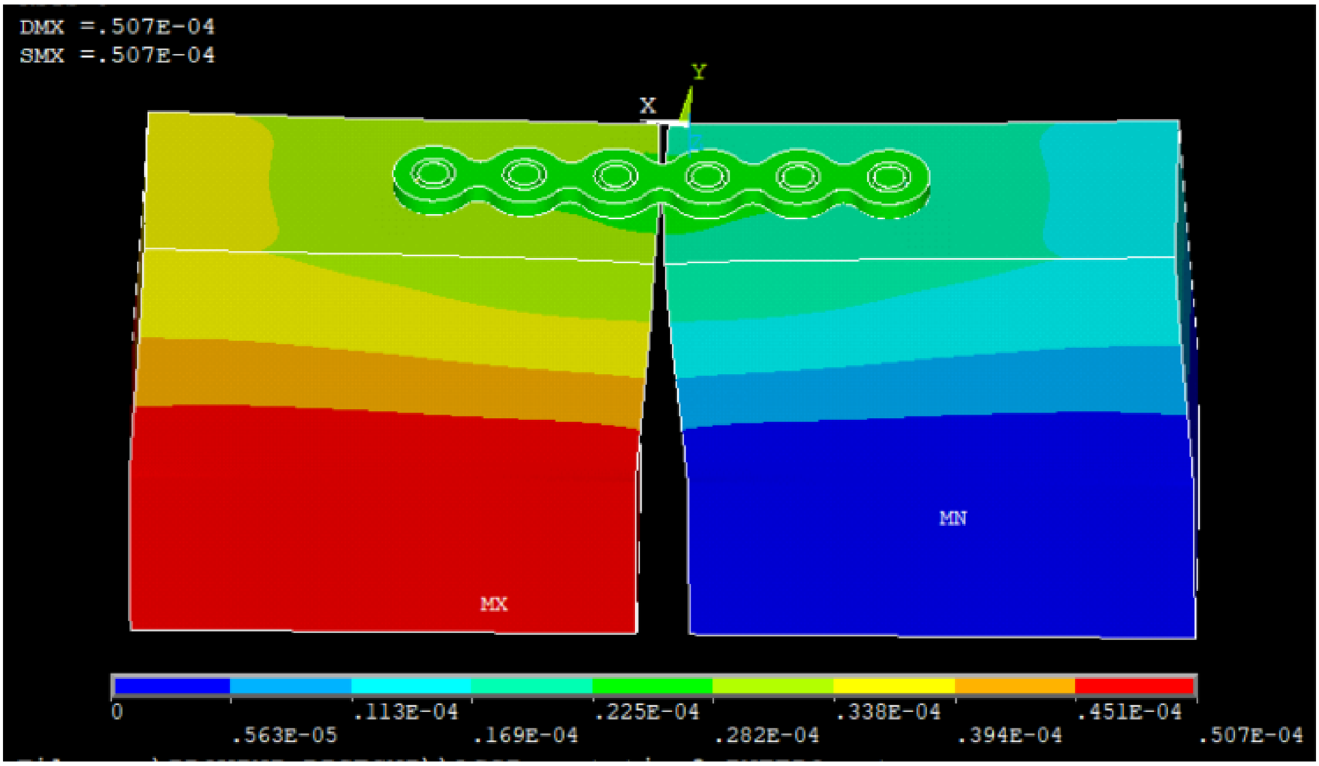

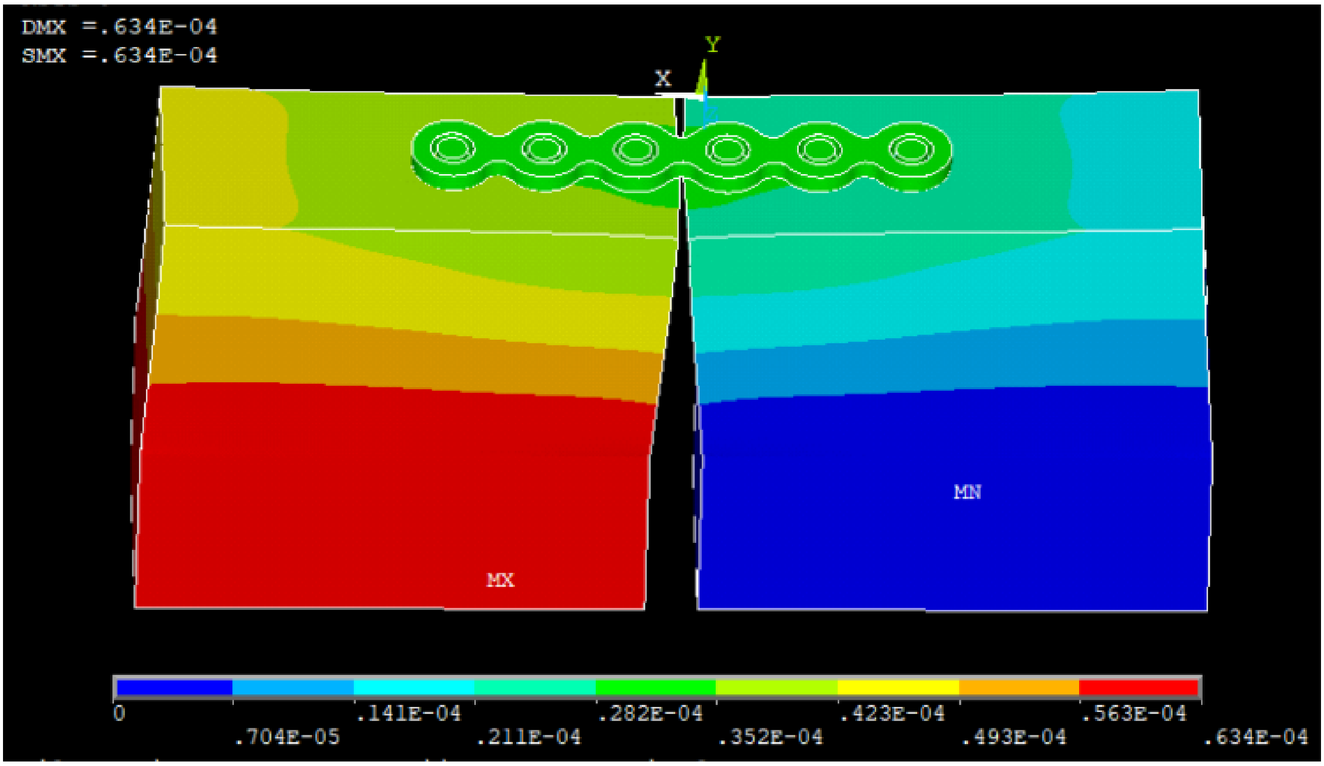

Figure 101: Prototype 2. In the image above, the deformation of the specimen is shown for a force of 80 N, while in the image below, the deformation is shown for a force of 100 N.

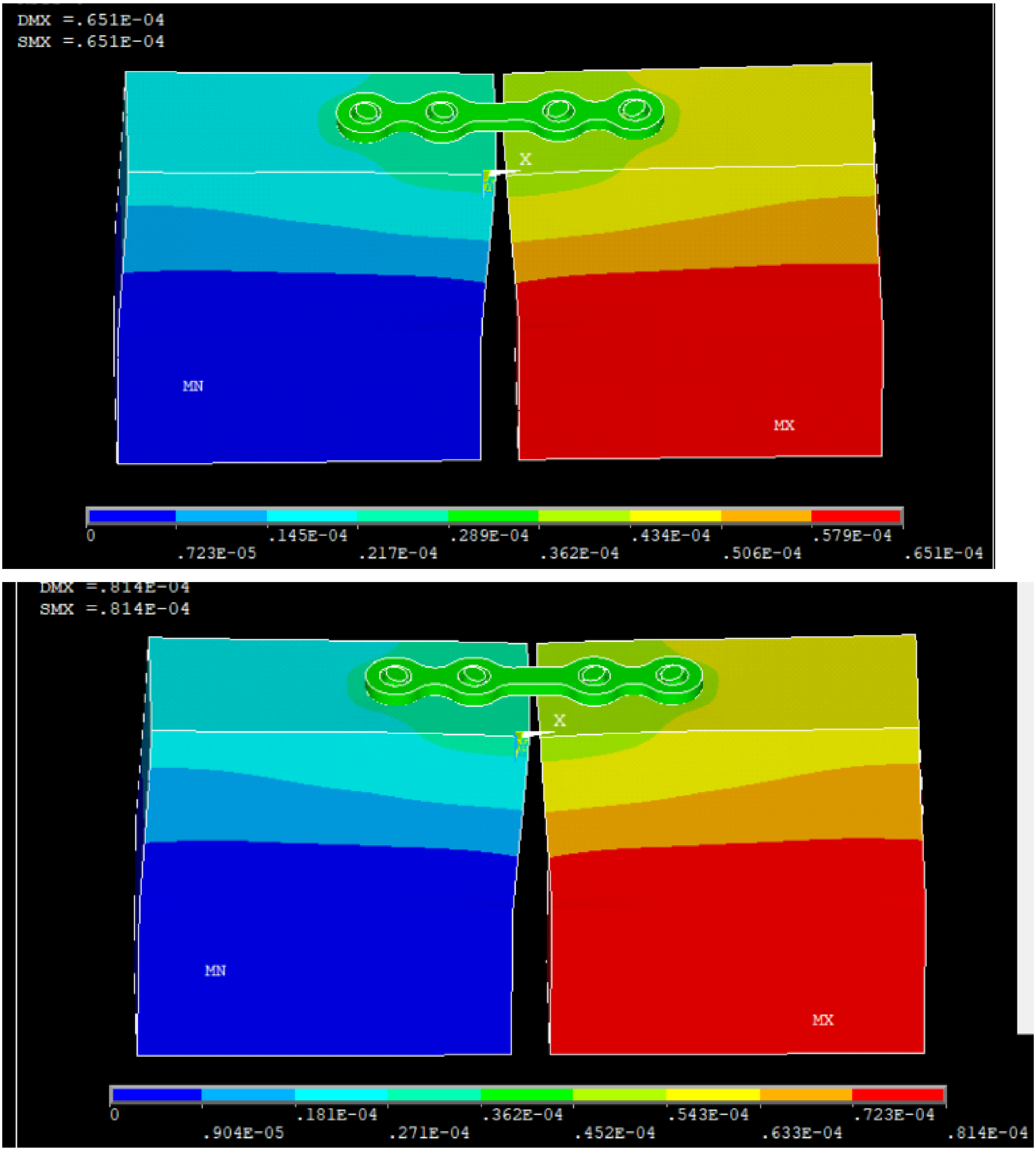

Figure 102: Prototype 3. In the image above, the deformation of the specimen is shown for a force of 80 N, while in the image below, the deformation is shown for a force of 100 N.

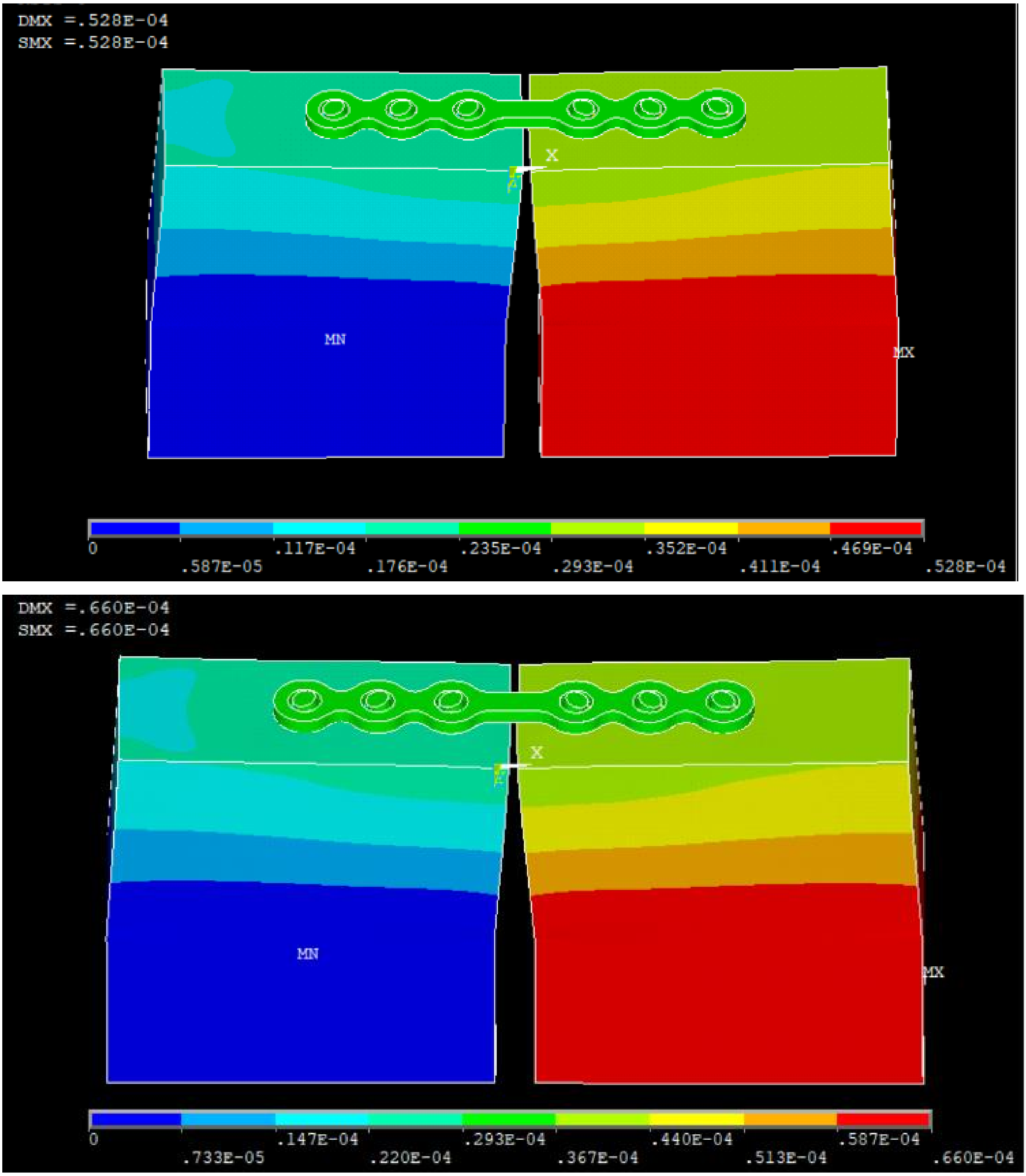

Figure 103: Prototype 4. In the image above, the deformation of the specimen is shown for a force of 80 N, while in the image below, the deformation is shown for a force of 100 N.

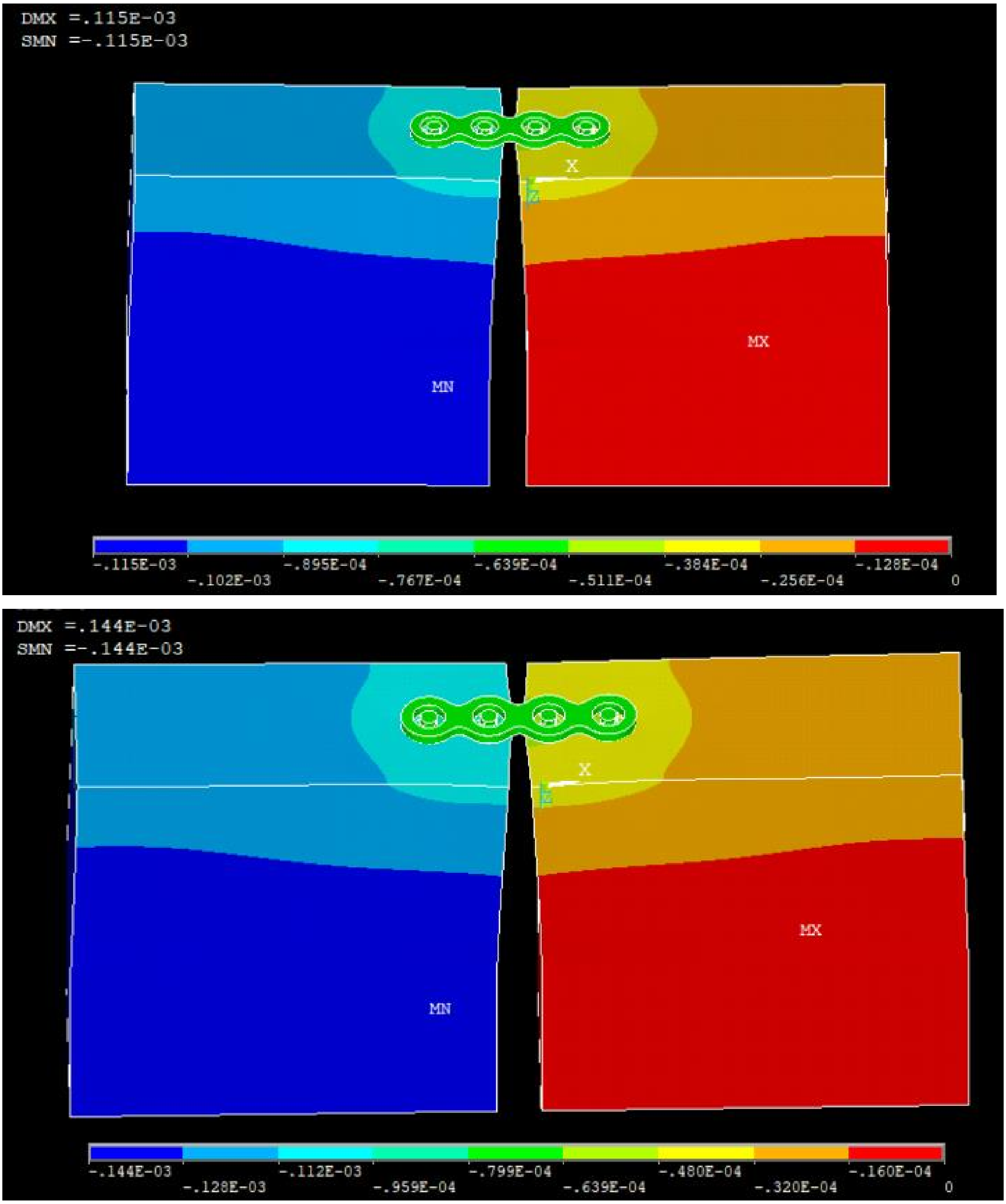

*Figure 104: Prototype 5***.** *In the image above, the deformation of the specimen is shown for a force of 80 N, while in the image below, the deformation is shown for a force of 100 N.*

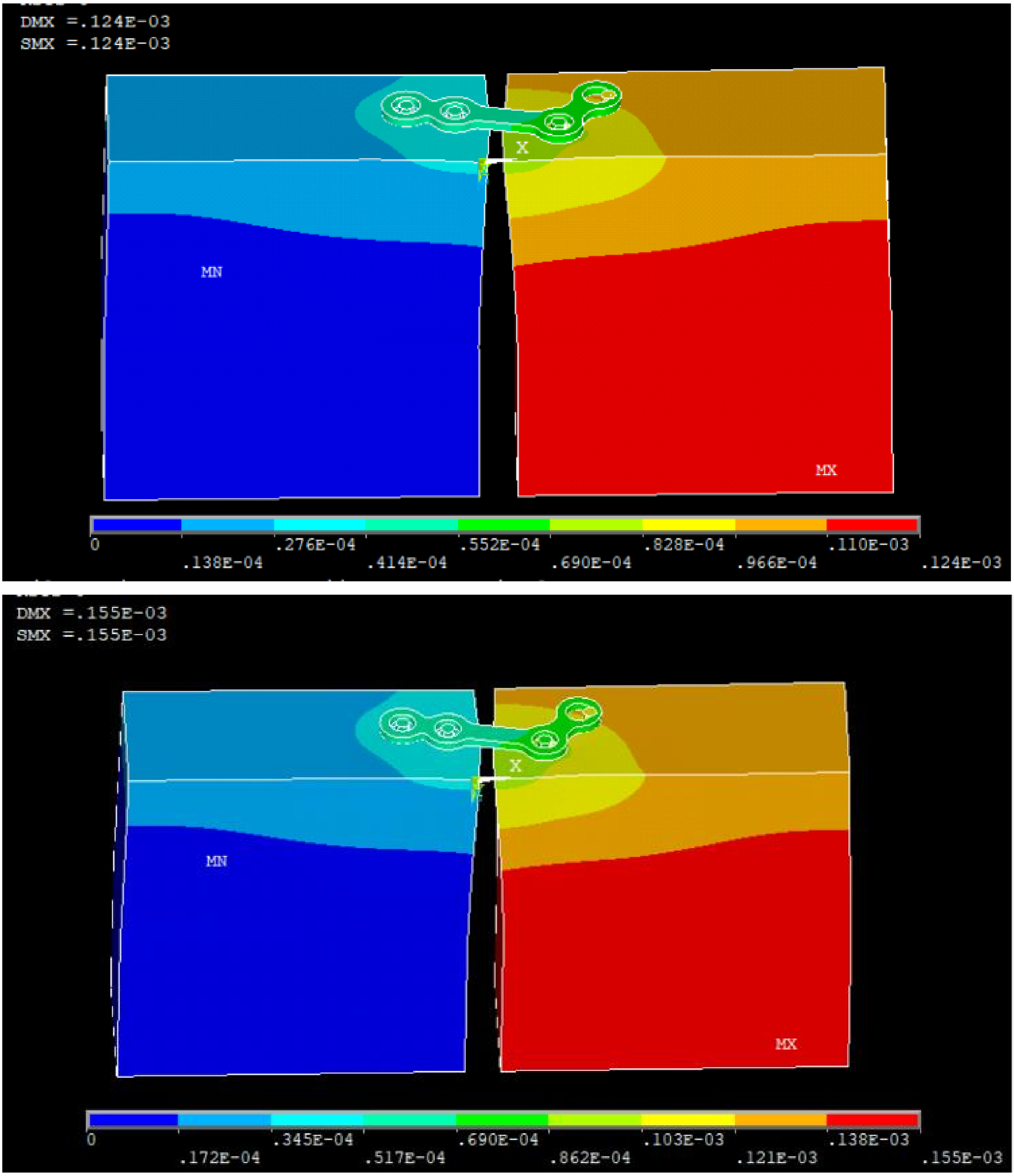

Figure 105: Prototype 6. In the image above, the deformation of the specimen is shown for a force of 80 N, while in the image below, the deformation is shown for a force of 100 N.

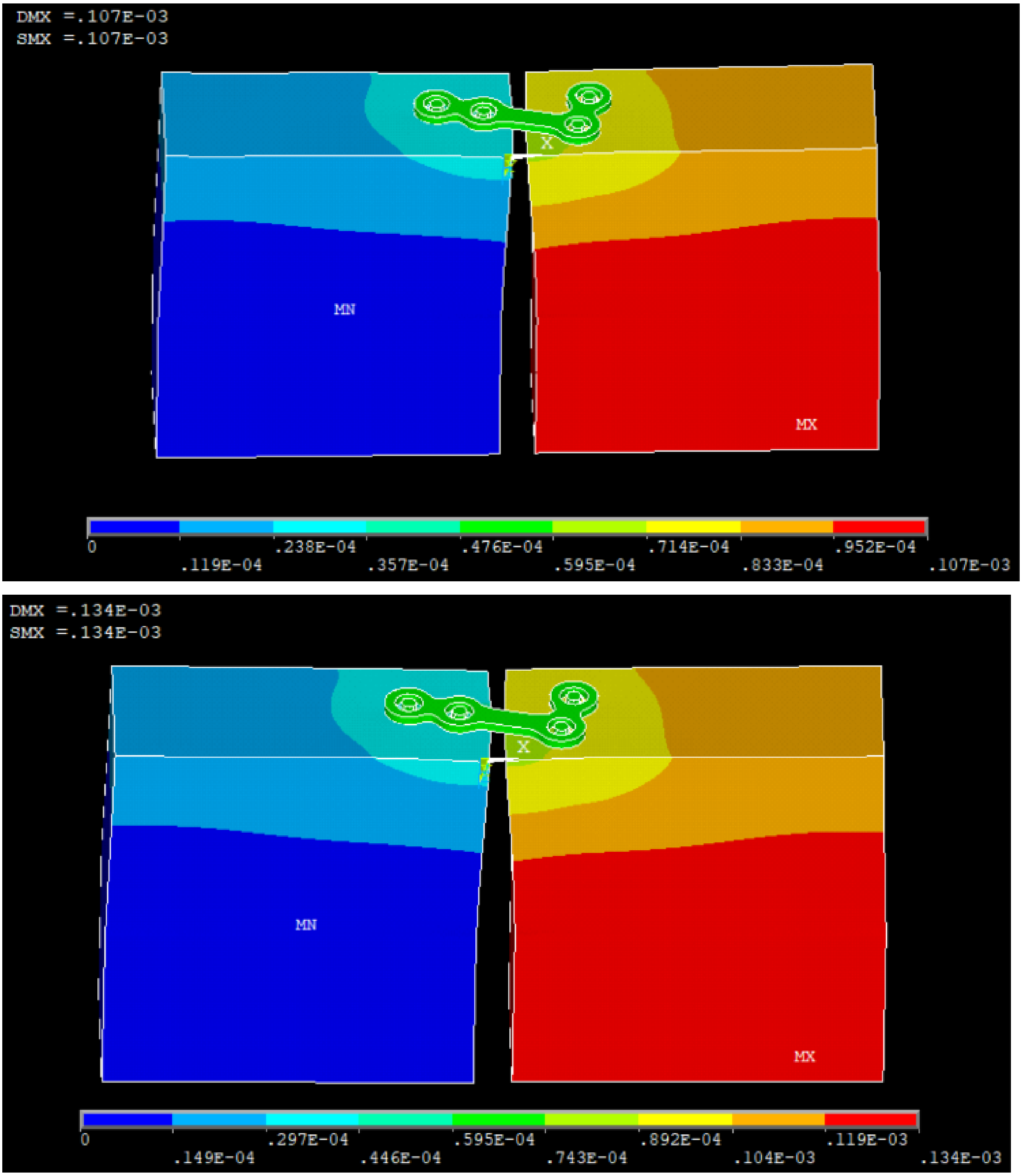

Figure 106: Prototype 7. In the image above, the deformation of the specimen is shown for a force of 80 N, while in the image below, the deformation is shown for a force of 100 N.

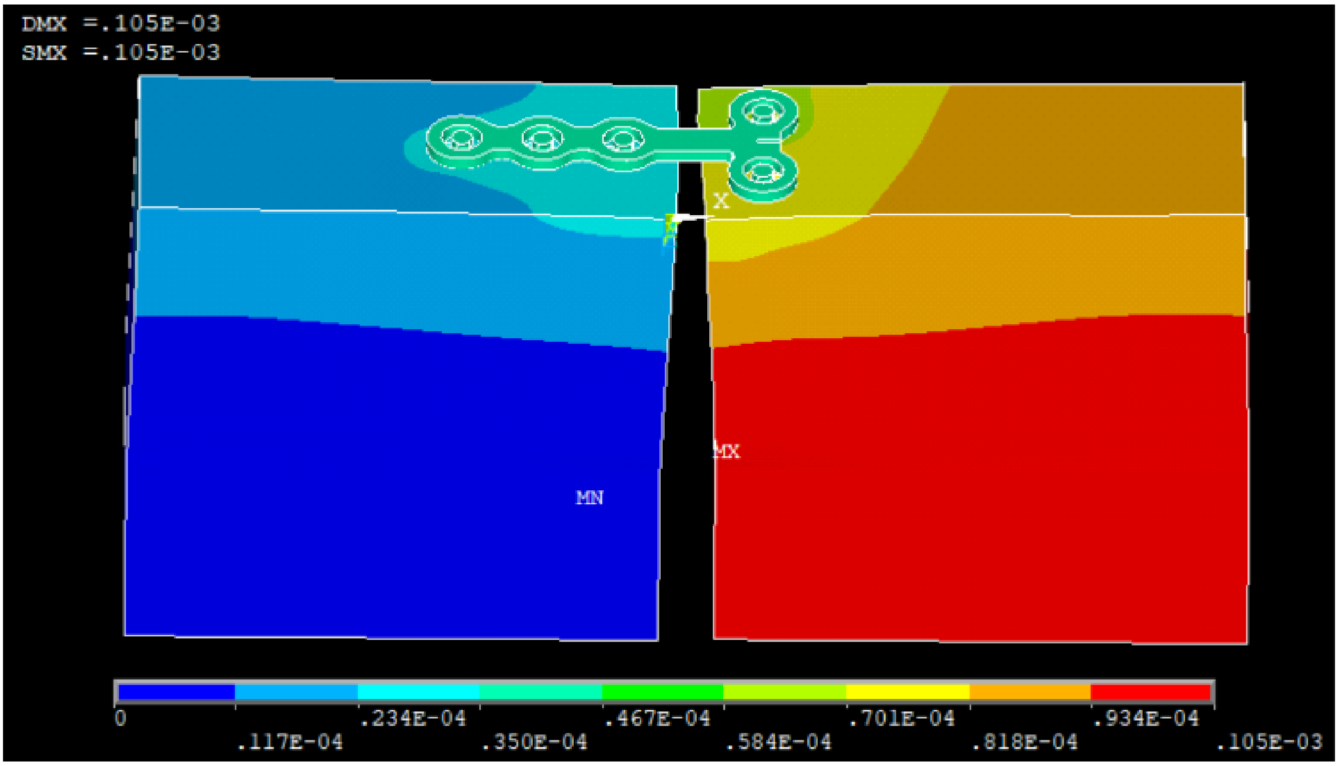

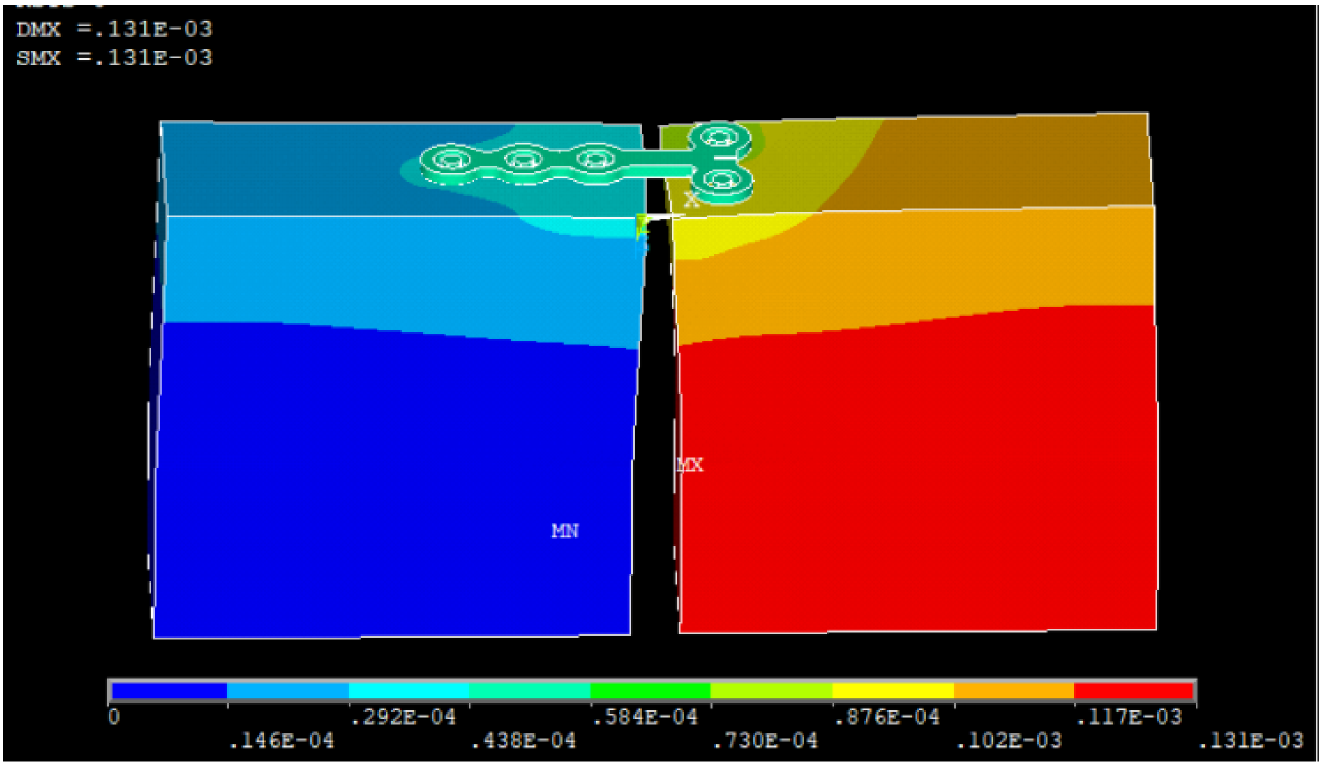

Figure 107: Prototype 8. In the image above, the deformation of the specimen is shown for a force of 80 N, while in the image below, the deformation is shown for a force of 100 N.

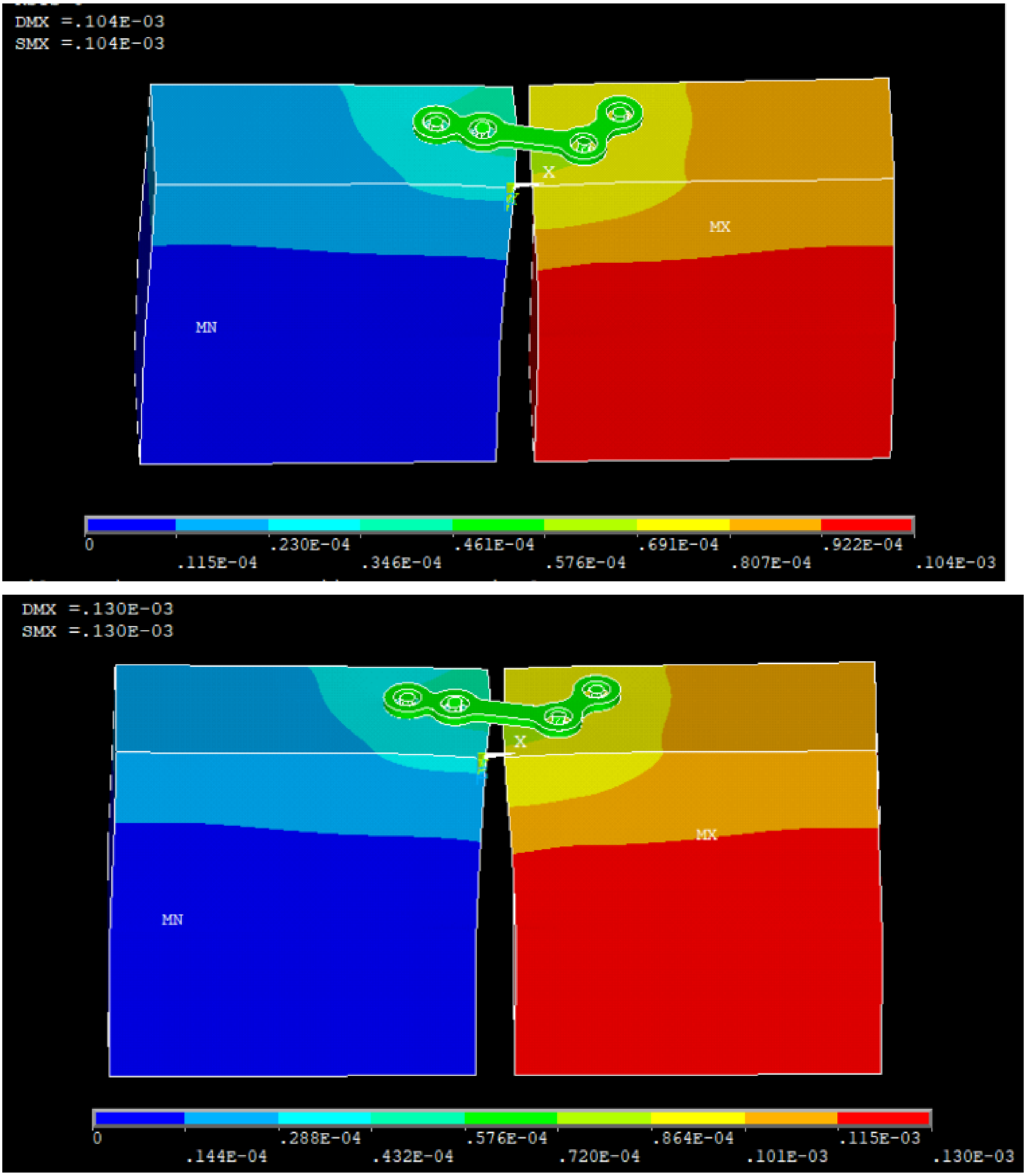

Figure 108: Prototype 9. In the image above, the deformation of the specimen is shown for a force of 80 N, while in the image below, the deformation is shown for a force of 100 N.

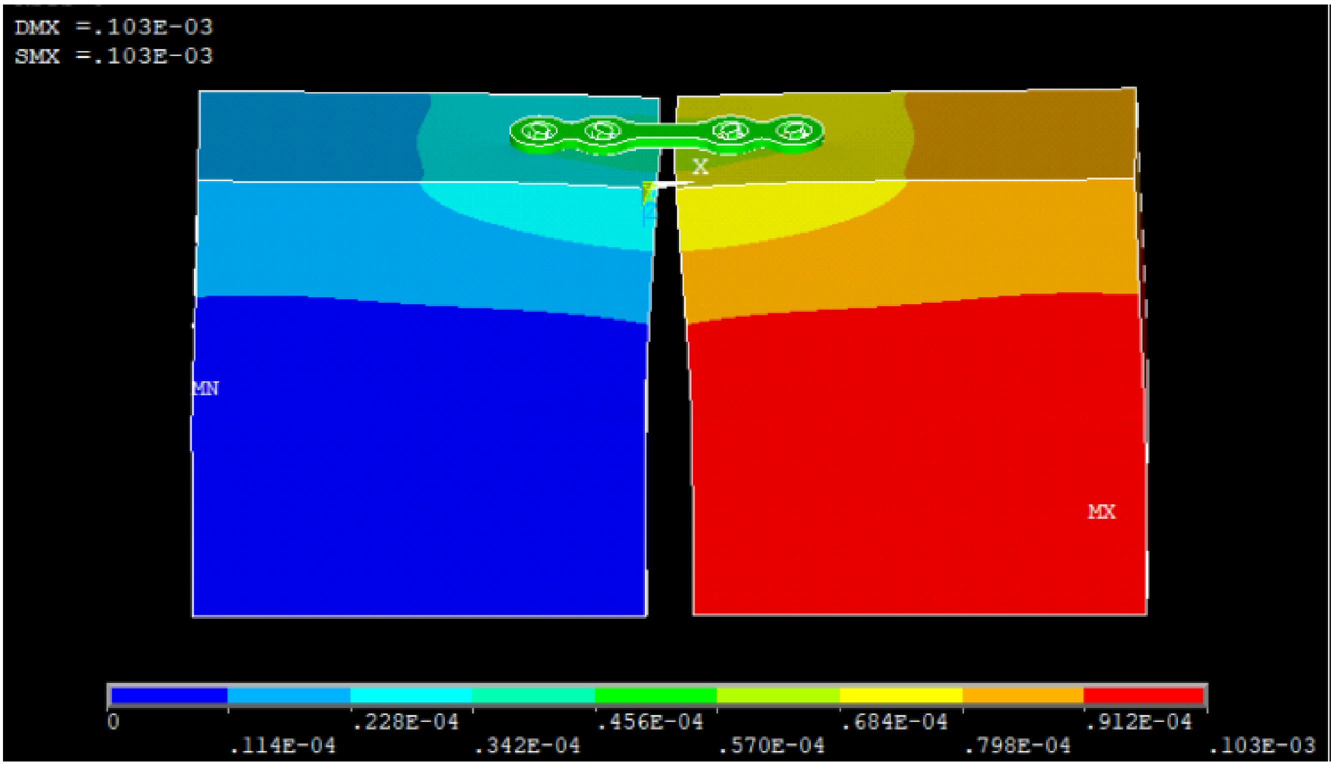

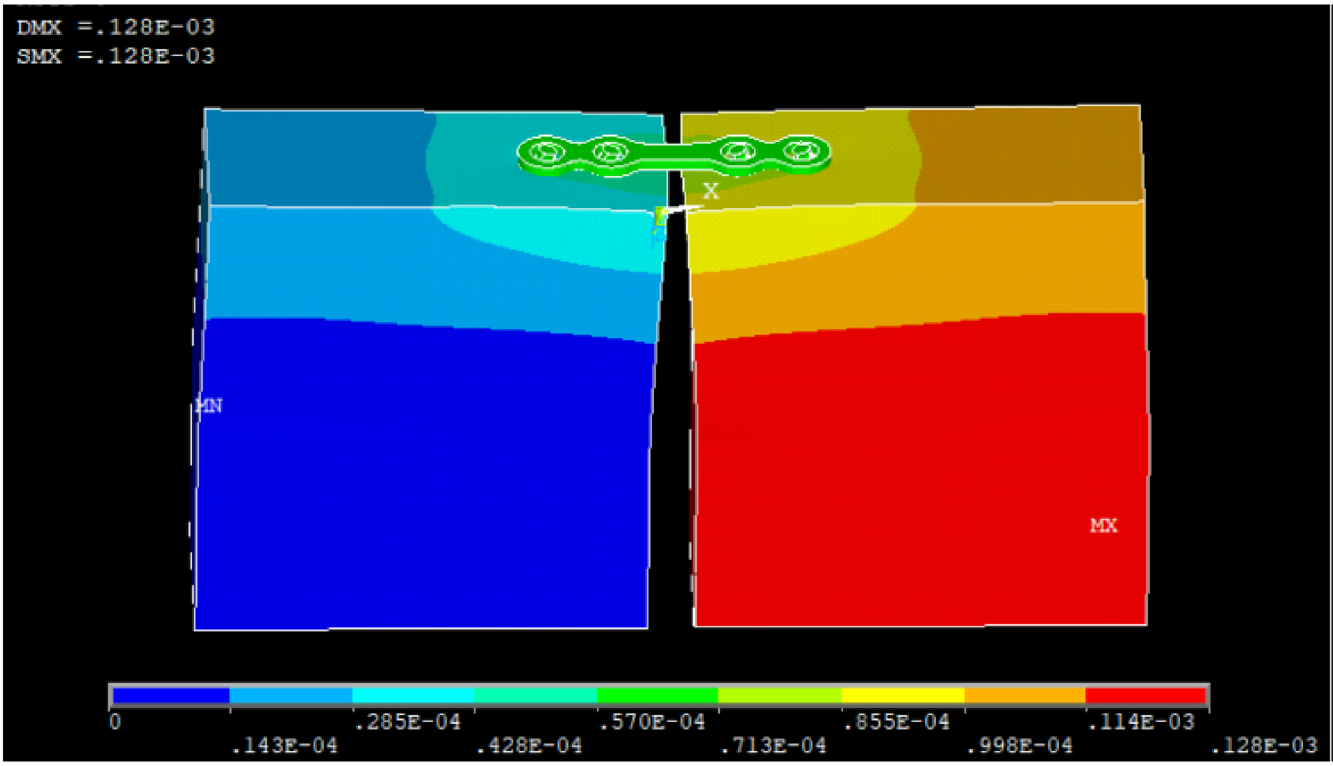

Figure 109: Prototype 10. In the image above, the deformation of the specimen is shown for a force of 80 N, while in the image below, the deformation is shown for a force of 100 N.

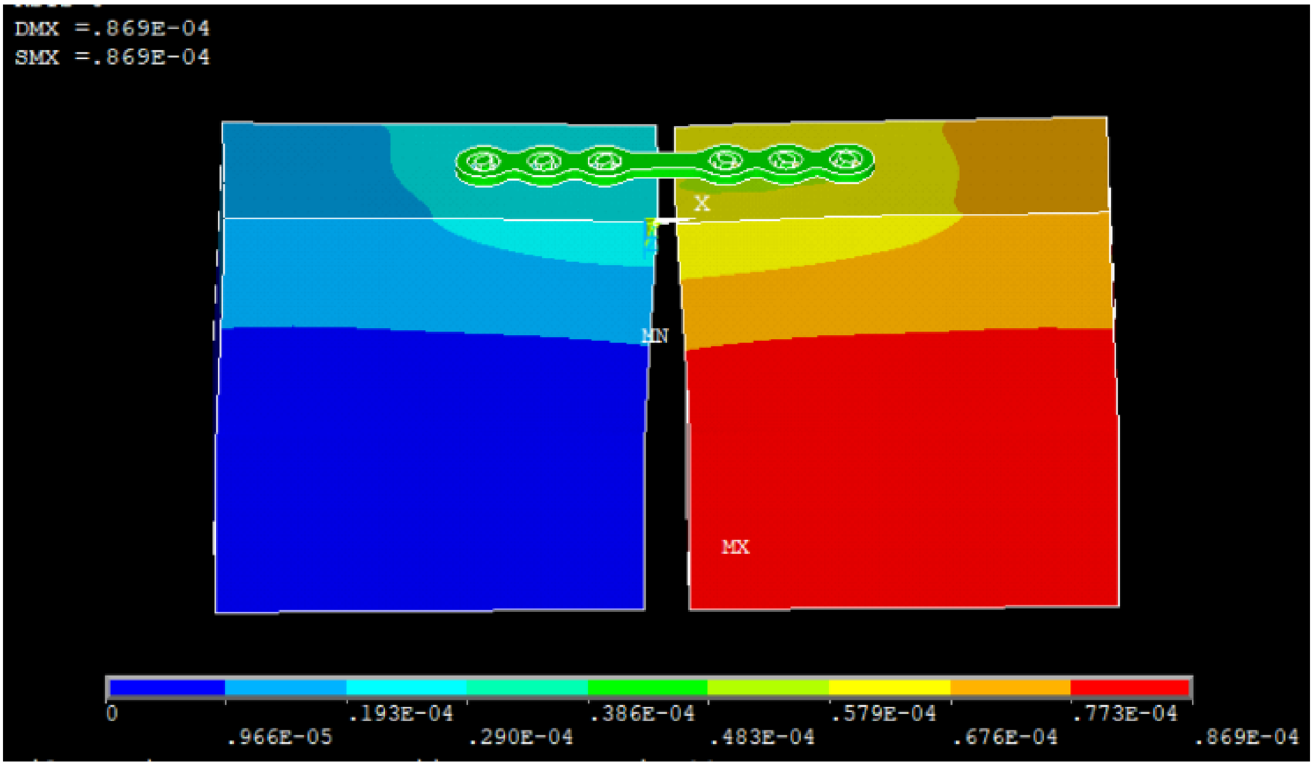

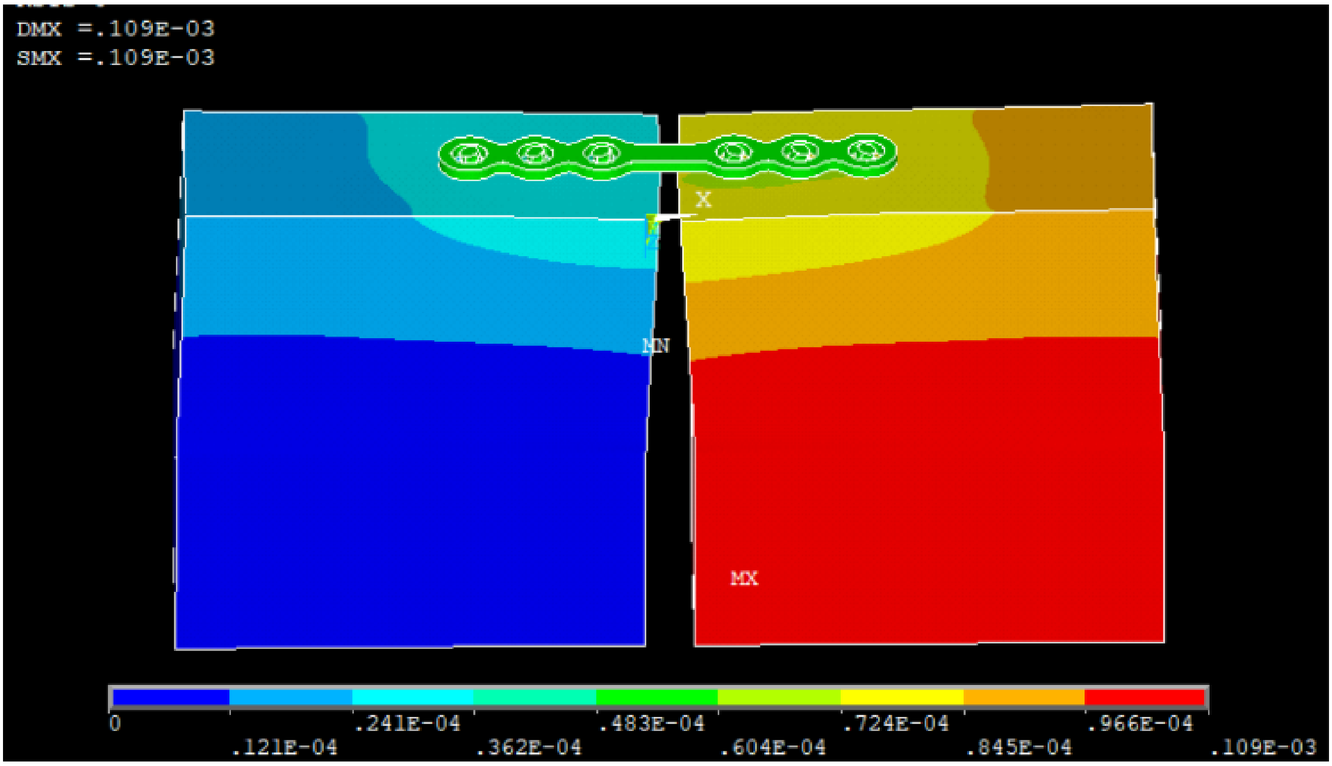

Figure 110: Prototype 11. In the image above, the deformation of the specimen is shown for a force of 80 N, while in the image below, the deformation is shown for a force of 100 N.

For each prototype, two tensile analyses were conducted using different force values to obtain the Force-Displacement curve associated with the test. In *Tables 15, 16, and 17*, we can see a summary of the displacement data calculated numerically and the corresponding stiffness values calculated based on these displacements for each of the 11 endoprosthesis prototypes along each of the three directions: x, y, and z.

In this tables, the first column indicates the number of the considered prototype, the second column shows the maximum deformation corresponding to a force of 80 N, the third column presents the maximum deformation corresponding to a force of 100 N, and finally, the fourth column displays the stiffness value calculated from the force-displacement graph of each prototype using the forces of 80 N and 100 N along with their associated deformations. The deformation is expressed in millimeters (mm), while the stiffness is measured in kilonewtons per millimeter (N/mm).

PROTOTYPE NUMBER	X1 [mm]	X2 [mm]	STIFFNESS [N/mm]
1	6,39E-02	7,99E-02	1250
2	5,07E-02	6,34E-02	1574,8
3	6,51E-02	8,14E-02	1227
4	5,28E-02	6,60E-02	1515,5
5	1,15E-01	1,44E-01	689,66
6	1,24E-01	1,55E-01	645,16
7	1,07E-01	1,34E-01	740,74
8	1,05E-01	1,31E-01	769,23
9	1,04E-01	1,30E-01	769,23
10	1,03E-01	1,28E-01	800
11	8,69E-02	1,09E-01	904,98

Table 15: In this table, we can see a summary of the displacement data calculated from the static tension analysis along the x-axis and the stiffness values for each of the endoprosthesis prototypes.

PROTOTYPE NUMBER	Y1 [mm]	Y2 [mm]	STIFFNESS [N/mm]
1	5,41E-03	7,26E-03	10811
2	3,53E-03	4,41E-03	22727
3	4,40E-03	5,49E-03	18349
4	2,64E-03	3,31E-03	29851
5	9,80E-03	1,23E-02	8163,3
6	1,72E-02	2,15E-02	4651,2
7	1,31E-02	1,64E-02	6079
8	9,90E-03	1,24E-02	8097,2
9	1,25E-02	1,56E-02	6389,8
10	7,90E-03	9,86E-03	10204
11	6,08E-03	7,61E-03	13072

Table 16: In this table, we can see a summary of the displacement data calculated from the static tension analysis along the x-axis and the stiffness values for each of the endoprosthesis prototypes.

PROTOTYPE NUMBER	Z1 [mm]	Z2 [mm]	STIFFNESS [N/mm]
1	1,63E-02	2,04E-02	4890
2	1,42E-02	1,77E-02	5633,8
3	1,77E-02	2,26E-02	40568
4	1,52E-02	1,90E-02	5249,3
5	2,37E-02	2,98E-02	3327,8
6	2,68E-02	3,61E-02	2141,3
7	2,26E-02	2,82E-02	3546,1
8	2,35E-02	2,94E-02	3389,8
9	2,45E-02	3,07E-02	3220,6
10	2,51E-02	3,14E-02	3174,6
11	2,15E-02	2,68E-02	3731,3

Table 17: In this table, we can see a summary of the displacement data calculated from the static tension analysis along the x-axis and the stiffness values for each of the endoprosthesis prototypes.

In *Table 18*, the summarized data of the maximum Von Mises stress for each prototype is presented. Specifically, the first column indicates the specimen number, the second column reports the maximum von Mises stress within the bone-like material specimen, the third column shows the maximum von Mises stress for the screws, and the fourth column presents the maximum von Mises stress for the prosthetic plate. The von Mises stress values are expressed in MPa. The appendix includes figures illustrating the von Mises stress distribution for each model and each of the three components.

PROTOTYPE NUMBER	VON MISES STRESS BONE [MPa]	VON MISES STRESS SCREWS [MPa]	VON MISES STRESS PLATE [MPa]
1	1,86	95,6	23,3
2	1,83	64,3	25,3
3	2,36	94,3	17,6
4	1,93	55,6	20,5
5	9,43	159	23,8
6	8,41	223	59,3
7	5,89	214	61,2
8	5,61	207	42,1
9	6,01	157	59,7
10	4,68	161	25,4
11	5,03	117	26

Table 18: In this table, we can see a summary of the Von Mises stress data calculated from the static tension analysis for each of the endoprosthesis prototypes.

DISCUSSION OF MODEL 2 RESULTS

As we can see from the results of the numerical tensile test for Model 2, the deformed region corresponds to the bone volumes in contact with the prosthesis. This is due to the choice of constraints applied to this model.

Specifically, the lower part of the bone specimen volumes for both blocks of the model was constrained in such a way that all nodes in that region moved in unison. In one of the volumes, the nodes were fully fixed, resulting in zero displacement, while in the other volume, all degrees of freedom of the nodes were equalized, ensuring identical displacement for all these nodes.

As shown in the tables, the stiffness values along the x-axis for this model are in the order of hundreds of Newtons. This value is influenced by both the stiffness of the prosthesis and that of the bone specimen. In particular, the tables indicate that the stiffness calculated along all three axes is higher for the first four prototypes compared to the others. This is consistent with the fact that the first four prototypes have a greater thickness, measuring 2 mm, while the remaining ones have a thickness of 1.3 mm. It also aligns with the fact that the elastic modulus of the plate in these first four prototypes is higher than that of the others, as Grade 5 titanium is stiffer than Grade 4 titanium, which is used for the remaining prototypes.

Since some prototypes have similar shapes, we can analyze how the stiffness of the model varies with changes in material and geometric dimensions. Regarding the stiffness along the x-axis, the axis along which the traction occurs, it can be observed that:

- Prototypes 1 and 5 have similar geometries, both featuring four screws equidistant from each other and positioned perpendicularly to the plate. The main differences between them lie in their dimensions and the materials used. Prototype 1 is thicker and made of Grade 5 titanium, while Prototype 5 is made of Grade 4 titanium and is thinner. The tables show that Prototype 1 has higher stiffness values compared to Prototype 5, which aligns with the fact that Grade 5 titanium has a higher elastic modulus. Therefore, given the same shape, it is expected that Prototype 1 exhibits greater stiffness.

- Prototypes 3 and 10 have similar geometries, both featuring four screws inclined at 15 degrees toward the end of the prosthesis. Prototype 3 is thicker and made of Grade 5 titanium, whereas Prototype 10 is made of Grade 4 titanium and is thinner. The tables show that Prototype 3 has higher stiffness values compared to Prototype 10, which is consistent with the fact that Grade 5 titanium has a higher elastic modulus. Thus, given the same shape, it is expected that Prototype 3 will exhibit greater stiffness.

- Prototypes 4 and 11 have similar geometries, both featuring six screws inclined at 15 degrees toward the centre of the prosthesis. Prototype 4 is thicker and made of Grade 5 titanium, while Prototype 11 is made of Grade 4 titanium and is thinner. The tables indicate that Prototype 4 has higher stiffness values compared to Prototype 11, which aligns with the fact that Grade 5 titanium has a higher elastic modulus. Therefore, given the same shape, it is expected that Prototype 4 will exhibit greater stiffness.

- Prototypes 1, 3, 5, and 10 all feature four screws but with different inclinations. Comparing Prototypes 1 and 3, both made of the same material but with different screw inclinations, we can see that their stiffness values are very similar. This suggests that, for this material and thickness, the screw inclination does not seem to affect the overall stiffness of the prototype. Conversely, when comparing Prototypes 5 and 10, also made of the same material but with different screw inclinations, we observe that Prototype 10 has higher stiffness than Prototype 5. This indicates that, for this material and thickness, the screw inclination does influence the overall stiffness of the prototype, making it stiffer.

- Prototypes 6 and 9 have the same material and plate geometry. However, while Prototype 6 has all screws positioned perpendicularly to the plate, Prototype 9 has two inclined screws and two perpendicular screws. The tables show that Prototype 6 has lower stiffness compared to Prototype 9, confirming that, in this case as well, the screw inclination increases the overall stiffness of the specimen compared to the one with all screws perpendicular to the plate.

- Prototypes 2 and 4 are made of the same material and both feature six screws. The main difference between them is the screw inclination: in Prototype 2, all screws are perpendicular, whereas in Prototype 4, they are all inclined. Additionally, there is a slight difference in the plate geometry: in Prototype 2, the screws are equidistant from each other, while in Prototype 4, there is a central zone with screws concentrated at the extremities. From the table, it can be seen that prototype 2 has a slightly higher stiffness than prototype 4.

- Prototypes 6 and 7 both feature four screws positioned perpendicularly to the plate and have similar shapes. In particular, Prototype 6 has an L-shape, but instead of a 90-degree angle between the two arms, it has an angle of 118.25 degrees. The tables show a difference in the stiffness of these two specimens, with Prototype 7 being stiffer than Prototype 6.

- Prototypes 1 and 2 are made of the same material and have similar geometries, with the difference that prototype 2 has 6 screws, while prototype 1 has only 4. From the tables, we can see that the stiffness of prototype 2 is greater than that of prototype 1, indicating that as the number of screws increases, the prototype becomes stiffer.

Therefore, we can observe that for this model, in the first four specimens—those made of Grade 5 titanium—the difference in stiffness appears to be proportional only to the number of screws and not to their inclination. Conversely, for the specimens made of Grade 4 titanium, the difference in stiffness is proportional to the number of screws and is also influenced by screw inclination. In models with the same number of screws, those with inclined screws exhibited higher stiffness.

Regarding the stiffness along the y-axis, from the tables we can observe that:

- Prototypes 6, 7, and 9 exhibit the lowest stiffness among all prototypes, with values below tens of kN/mm. From this data, we can deduce that their L-shaped geometry significantly influences the stiffness along this axis. They are the only ones with this type of geometry, whereas all the remaining specimens have a geometry that develops exclusively along the x-axis.

- Specimens 2 and 4, which share the same geometry and are made of the same material but differ in screw inclination, show a difference in stiffness. Specifically, specimen 4, which has screws inclined at 15 degrees toward the center of the plate, exhibits greater stiffness compared to specimen 2, which has screws perpendicular to the plate.

- For specimens with the same number and inclination of screws but made of different materials, we can observe that their stiffness aligns with the material properties of the plate. That is, specimens made of grade 5 titanium are stiffer than those made of grade 4 titanium. Indeed, specimen 3 is stiffer than specimen 10, as is specimen 4 compared to specimen 11.

Finally, examining stiffness along the z-axis in detail, we can observe that the first four specimens exhibit greater stiffness compared to the others. Between the two groups of prostheses, mini and micro, there is a difference, but within each group, the stiffness values are relatively similar to one another.

From the numerical analysis, in addition to the deformation of the specimen, the distribution of von Mises stresses was also obtained. From the numerical analysis results, as shown in the figures in the appendix, the maximum von Mises stresses for each prototype, whose values are reported in *Table 18*, are located as follows: in the bone-like material, at the interface with the screws; in the screws, also at the contact area with the bone; and in the plate, at its central region. As observed from the table data, the screws experience the highest stresses, while the bone-like material is subjected to lower stresses, in agreement with its deformability.

Specifically, the yield stress of grade 5 titanium, used for the plates of the first four specimens and for all screws, is 795 MPa; the yield stress of grade 4 titanium, used for the plates of specimens 5 to 11, is 485 MPa; and the yield stress of the bone-like material is 48 MPa. The stress values reported in the table are significantly lower than the yield stresses because the numerical analyses were conducted in the elastic regime, and the applied forces were chosen based on the experimental test, being relatively low and far from the failure loads of the specimens. These forces correspond to the elastic behavior of the specimens.

From *Table 18*, it is evident that the prototypes exhibiting the highest stress values are those made of grade 4 titanium. The effect of the number of screws in the plate and their inclination can be analyzed through the following prototypes:

- Prototypes 1 and 5 have similar geometries, both featuring four equidistant screws, all perpendicular to the plate. The difference lies in their dimensions and materials: Prototype 1 is made of grade 5 titanium and is thicker, whereas Prototype 5 is made of grade 4 titanium and is thinner. From the tables, it can be observed that the plates exhibit similar stress distributions and comparable maximum stress values. However, both the screws and the bone-like specimen in Prototype 1 experience lower maximum stresses compared to Prototype 5.

- Prototypes 3 and 10 have similar geometries, both featuring four screws inclined at 15 degrees toward the prosthesis end. Prototype 3 is made of grade 5 titanium and is thicker, while Prototype 10 is made of grade 4 titanium and is thinner. The tables indicate that Prototype 10 exhibits higher maximum stresses for each component compared to Prototype 3.

- Prototypes 4 and 11 share similar geometries, each incorporating six screws inclined at 15 degrees toward the prosthesis center. Prototype 4 is made of grade 5 titanium and is thicker, whereas Prototype 11 is made of grade 4 titanium and is thinner. The tables reveal that Prototype 11 has higher maximum stresses in all components compared to Prototype 4.

- Prototypes 6 and 9 have the same plate material and geometry. However, in Prototype 6, all screws are perpendicular to the plate, whereas in Prototype 9, two screws are inclined, and two remain perpendicular. The tables indicate that the plates exhibit similar stress distributions and maximum stress values, but both the screws and the bone-like specimen in Prototype 9 experience lower maximum stresses compared to Prototype 6. In this model, screw inclination significantly affects stress values.

- Prototypes 6 and 7 both feature four screws positioned perpendicularly to the plate and have similar shapes. However, Prototype 6 has an L-shaped structure with an angle of 118.25 degrees between its two arms, rather than a 90-degree angle as in Prototype 7. The tables show that maximum stresses in the bone-like specimen and screws are higher in Prototype 6 than in Prototype 7, while the plate experiences higher stresses in Prototype 7 than in Prototype 6.

- Prototypes 1 and 2 are made of the same material and have similar geometries, with the difference that Prototype 2 has six screws, whereas Prototype 1 has only four. The tables indicate that the stresses in the bone-like specimen and the plate are similar, whereas the maximum stresses in the screws differ, with Prototype 2 experiencing lower stresses in the screws compared to Prototype 1.

MODEL 2 TENSILE AND ROTATIONAL ANALYSIS

In this section, we will see how the numerical tensile analyses were conducted, where rotation was also considered, for those specimens that experienced both rotation and tension during the experimental tensile test. Below, we outline all the steps followed to perform this analysis.

Once the geometry created in SolidWorks was imported into Ansys, the following steps were performed to conduct the tensile test on Model 2 of all prototypes:

1) The materials for the plate and screws were assigned, specifically the elastic modulus and Poisson's ratio corresponding to the materials used in their construction. For prototypes 2, mini endoprostheses, the plate material is Grade 5 titanium, while for prototypes 8 and 11, micro endoprostheses, the material is Grade 4 titanium. Additionally, the material for the screws were assigned, their material is grade 5 titanium. The material for the bone-like volume was also assigned, whose elastic modulus was calculated by taking a weighted average of the elastic moduli of the two materials that composed the bone specimen, namely 50 PCF and 15 PCF, which have elastic moduli of 1.469 GPa and 173 MPa, respectively. The material properties used in the analysis are listed in *Table 19* below.

ELEMENT	MATERIAL	ELASTIC MODULUS [GPa]	POISSON'S RATIO
PLATE MINI	Grade 5 Titanium	110	0,33
PLATE MICRO	Grade 4 Titanium	105	0,34
SCREW	Grade 5 Titanium	110	0,33
BONE	weighted average PCF	3,94E-01	0,3

Table 19: This table lists the two materials used for the construction of the prosthetic model plates: Grade 4 titanium and Grade 5 titanium -depending on the prototype, one material or the other was used as previously indicated. The material of the screw and the material for the bone-like volume.

2) A mesh was created for the volumes using the SOLID185 tetrahedron element with a free structure. The mesh size used for the analysis of this model was selected based on the results obtained from the sensitivity studies, which are described in the following chapters. A mesh size of 0.5 mm was employed for the prototype number 2, whereas a mesh size of 0.65 mm was used for the remaining ones.

3) The contacts between the plate and screws were modeled as rigid contact, meaning all degrees of freedom for the nodes in the hole area were matched with those of the nodes in the screw area that passed through the hole. This approach aims to replicate the behavior observed in the experimental tests, specifically the pivoting housing of the screw that connects the plate to the screw.

4) The contact between the screws and the bone section into which they are threaded was represented by merging the nodes of the two contacting surfaces, namely the surface of the screw and the bone surface into which the screw is inserted.

5) Finally, the loads and constraints were applied. One of the two bone-like material volumes was constrained with a fixed support to simulate the experimental test, where a bone sample was placed inside a holding clamp that held it in place. Specifically, the holding clamp used in the experimental test did not contain the entire volume of the sample, but only a part of it; the sample was inserted into the fixture for only 2.5 cm. To precisely replicate this, the fixed support was applied only to the last 2.5 cm of the bone-like material volume. This constraint involved selecting all the nodes of this volume and imposing a displacement of zero along the x, y, and z axes. For the other volume, to simulate the experimental test in which the second volume was placed in a different holding clamp and pulled, all the nodes of the last 2.5 cm of the volume were selected, and their degrees of freedom along the x-axis were constrained to be equal using the CP command, ensuring that they moved together, just as in the experimental test. The desired force was then applied to this set of nodes.

6) Finally, the rotational effect observed during the experimental tests must be simulated. Due to the choice of the SOLID185 element, which does not include rotational degrees of freedom around the three axes, it was not possible to directly apply a pure moment to the nodes of the tensile-tested bone specimen volume. To simulate the rotation, the following approach was adopted: the nodes of the two lateral faces of the tensile-loaded bone specimen were selected, the degrees of freedom along the z-axis for each of the two faces were constrained to be equal using the CP command, and two forces of equal magnitude, opposite in direction, and equal to the applied tensile force were imposed along the z-axis on each lateral face.

Figure 111 below provides an example of how the constraints and loads were applied, as previously described.

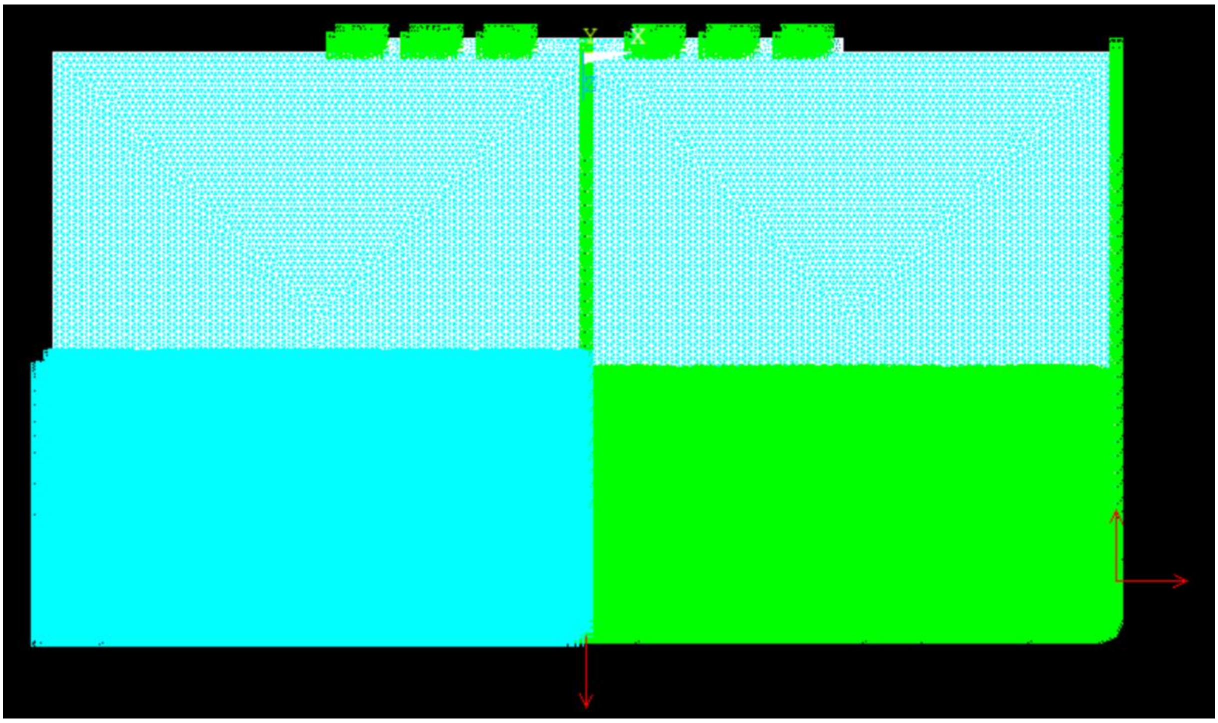

Figure 111: In the figure, the constraints applied to Model 2 of prototype 11 are shown. The fixed constraints are indicated in light blue, the degrees of freedom constraints are shown in green, and the applied forces are depicted in red.

The forces selected for the static analysis of this specimen, later used to derive the force-displacement graph, were chosen based on the results of the experimental test. During the experimental test, it was observed that the specimen exhibited an initial phase of elastic deformation before undergoing plastic deformation, during which the force-deformation curve followed a linear trend. Therefore, the forces used in our numerical analysis were selected within the elastic deformation range of the specimen.

As a result, the force values chosen to represent the linear elastic behavior of the prosthesis prototypes were 80 N and 100 N.

Once all these steps were completed, the tensile test solution was launched. Finally, using the post-processor, it was possible to display the results of the test, where both the initial and the deformed geometries are shown. The deformation along each individual axis can also be observed. In the following images, we can observe the deformation of the prosthesis prototypes along the x-axis, which is the axis along which the tensile test is performed. This deformation is shown for both force values chosen as the applied load, which were then used to calculate the model's stiffness.

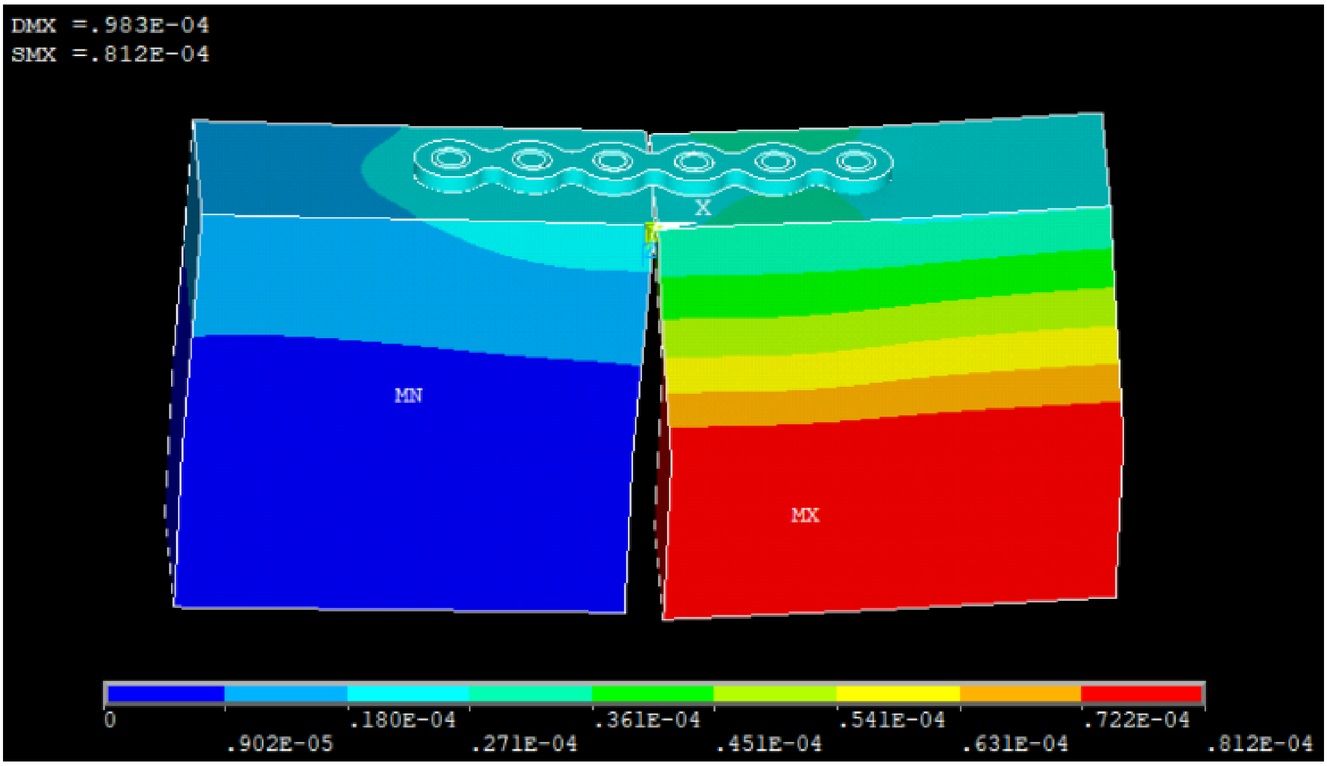

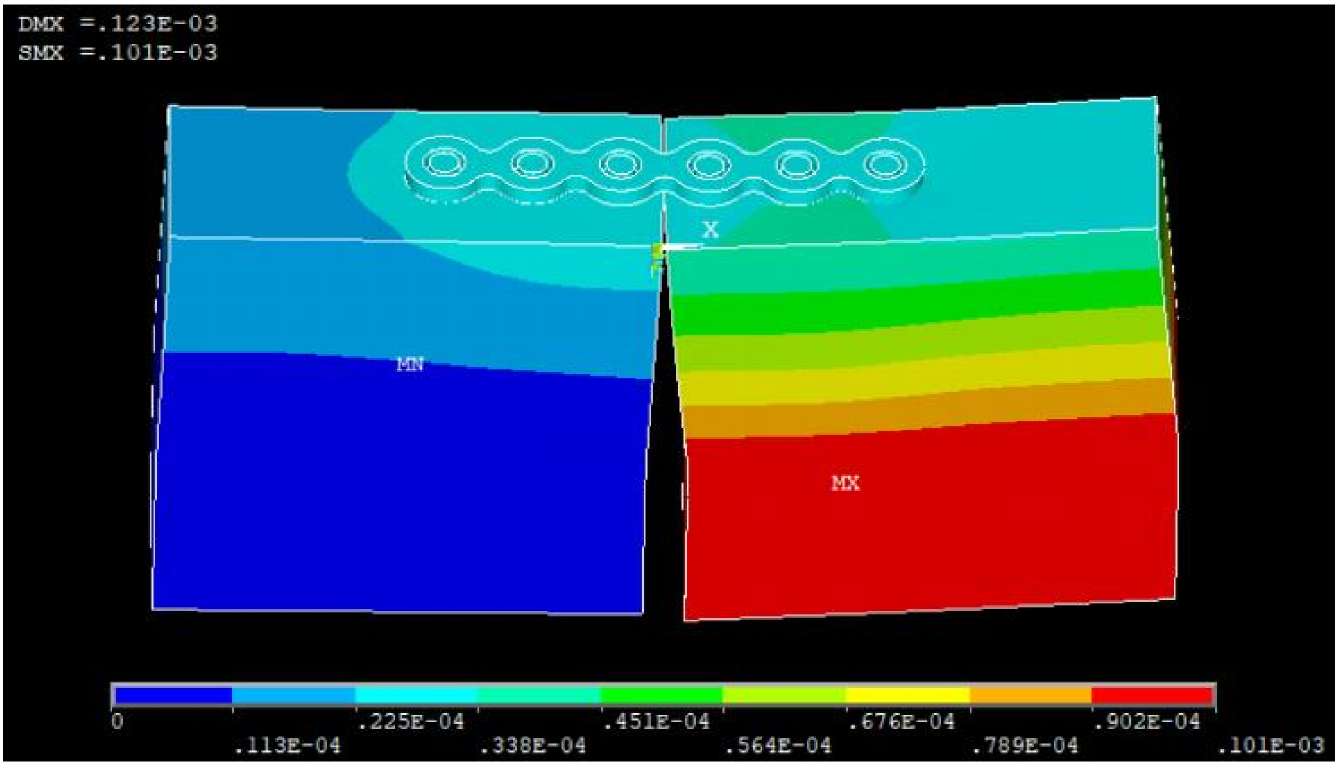

Figure 112: Prototype 2. In the image above, the deformation of the specimen is shown for a force of 80 N, while in the image below, the deformation is shown for a force of 100 N.

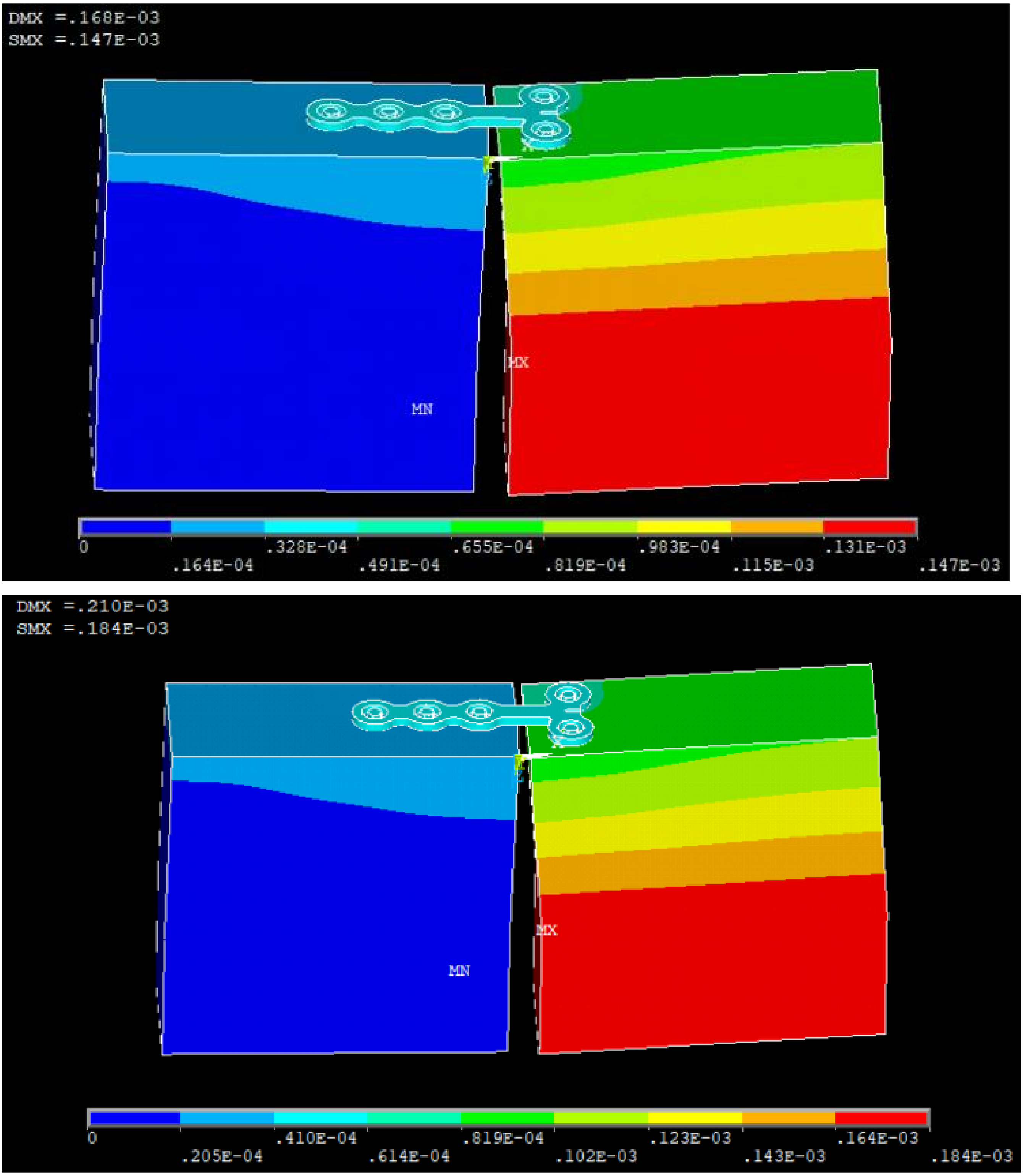

Figure 113: Prototype 8. In the image above, the deformation of the specimen is shown for a force of 80 N, while in the image below, the deformation is shown for a force of 100 N.

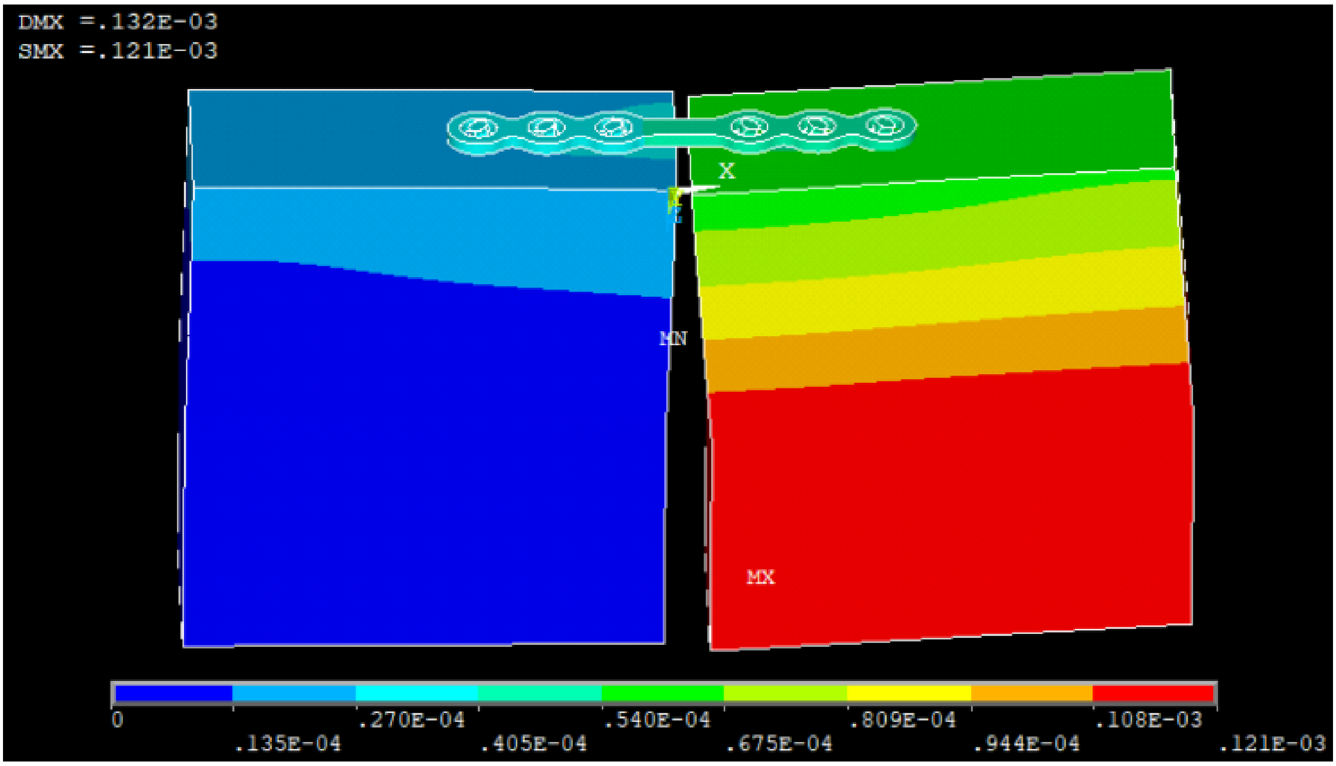

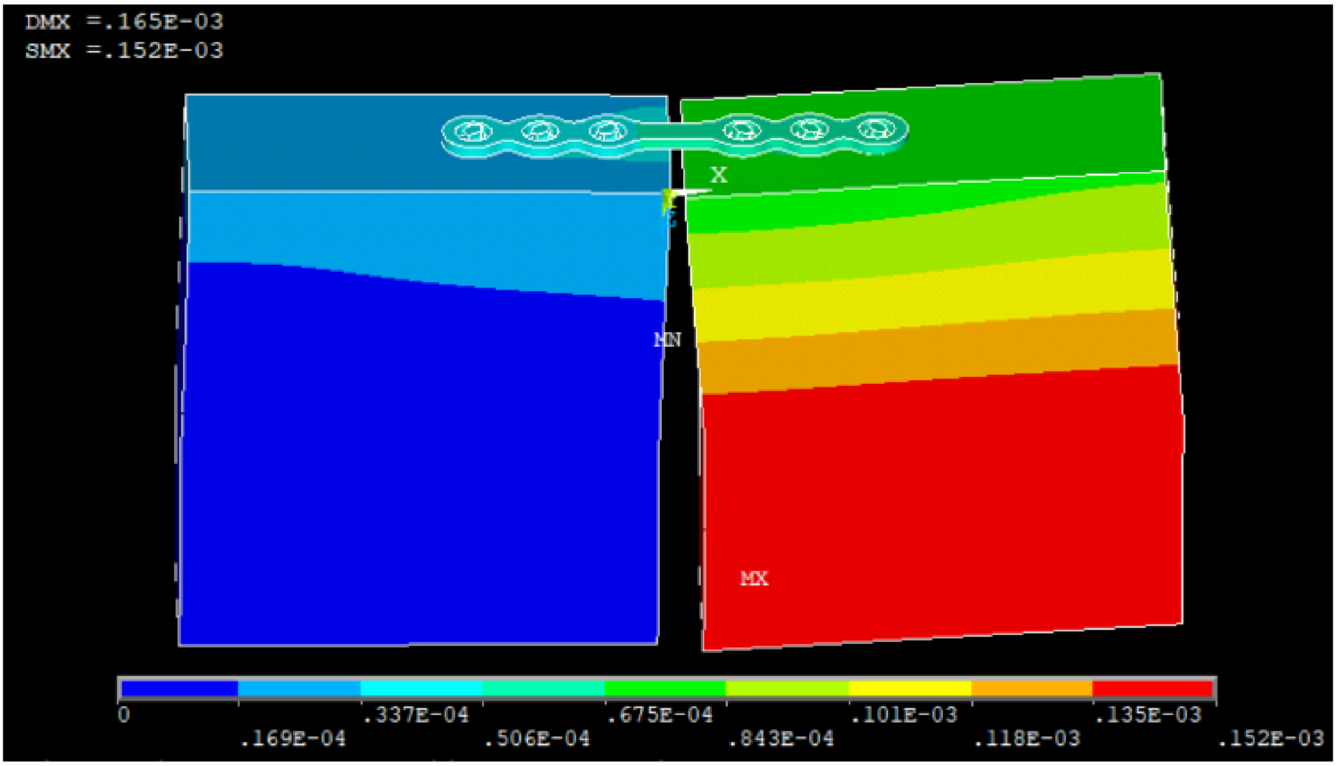

Figure 114: Prototype 11. In the image above, the deformation of the specimen is shown for a force of 80 N, while in the image below, the deformation is shown for a force of 100 N.

For each prototype, two tensile analyses were conducted using different force values to obtain the Force-Displacement curve associated with the test. In *Tables 20, 21, and 22*, we can see a summary of the displacement data calculated numerically and the corresponding stiffness values calculated based on these displacements for each of the 11 endoprosthesis prototypes along each of the three directions: x, y, and z.

In this tables, the first column indicates the number of the considered prototype, the second column shows the maximum deformation corresponding to a force of 80 N, the third column presents the maximum deformation corresponding to a force of 100 N, and finally, the fourth column displays the stiffness value calculated from the force-displacement graph of each prototype using the forces of 80 N and 100 N along with their associated deformations. The deformation is expressed in millimeters (mm), while the stiffness is measured in kilonewtons per millimeter (N/mm).

PROTOTYPE NUMBER	X1 [mm]	X2 [mm]	STIFFNESS [N/mm]
2	8,12E-02	1,01E-01	1010,1
8	1,47E-01	1,84E-01	540,54
11	1,21E-01	1,52E-01	645,16

Table 20: In this table, we can see a summary of the displacement data calculated from the static tension and rotational analysis along the x-axis and the stiffness values for each of the three endoprosthesis prototypes.

PROTOTYPE NUMBER	Y1 [mm]	Y2 [mm]	STIFFNESS [N/mm]
2	4,72E-03	5,89E-03	17094
8	1,12E-02	1,40E-02	7142,9
11	7,12E-03	8,90E-03	11236

Table 21: In this table, we can see a summary of the displacement data calculated from the static tension and rotational analysis along the y-axis and the stiffness values for each of the three endoprosthesis prototypes.

PROTOTYPE NUMBER	Z1 [mm]	Z2 [mm]	STIFFNESS [N/mm]
2	7,17E-02	8,97E-02	1111,1
8	9,81E-02	1,23E-01	816,33
11	7,68E-02	9,60E-02	1041,7

Table 22: In this table, we can see a summary of the displacement data calculated from the static tension and rotational analysis along the z-axis and the stiffness values for each of the three endoprosthesis prototypes.

In *Table 23*, the data representing the maximum von Mises stress for each of the three considered prototypes, subjected to a tensile force of 100 N, are summarized. Specifically, the first column indicates the specimen number, the second column reports the maximum von Mises stress within the bone-like material specimen, the third column shows the maximum von Mises stress for the screws, and the fourth column presents the maximum von Mises stress for the prosthetic plate. The von Mises stress values are expressed in MPa. The appendix includes figures illustrating the von Mises stress distribution for each model and each of the three components.

PROTOTYPE NUMBER	VON MISES STRESS BONE [MPa]	VON MISES STRESS SCREWS [MPa]	VON MISES STRESS PLATE [MPa]
2	2,09	102	75,2
8	5,49	228	41,5
11	5,18	134	41,1

Table 23: In this table, we can see a summary of the Von Mises stress data calculated from the static tension and rotational analysis for each of the three endoprosthesis prototypes.

CHAPTER 3: EXPERIMENTAL TEST

In this chapter, we will describe the tensile tests performed in the laboratory for each of the 11 supplied specimens. We will explain how the specimens to be tested were obtained and how the tensile tests were conducted. Finally, we will present the results obtained during these tests.

The first step involved screwing the prostheses onto the bone-like material specimens to simulate the fixation of a fracture, as this is the primary purpose of the studied prostheses. Each prosthesis was fixed to two blocks of bone-like material, with one-half of the prosthesis screwed into one volume and the other half into another, ensuring that the two bone-like material specimens were kept as close together as possible.

The screws were inserted at specific angles, as not all specimens had screws placed perpendicularly to the plate; for some, the screws were inclined at specific angles, specifically:

- Prototypes 1, 2, 5, 6, 7, and 8 had screws inserted perpendicularly to the plate.
- Prototypes 4 and 11 had screws inserted at a 15-degree inclination relative to the vertical axis, oriented toward the center of the prosthesis.
- Prototypes 3 and 10 also had screws inserted at a 15-degree inclination relative to the vertical axis, but in the opposite direction, meaning they were inclined outward from the prosthesis.
- Prototype 9 had two screws inserted perpendicularly to the plate, while the other two were inclined at 15 degrees, one toward the right and the other toward the left.

Figure 115 shows the prosthesis prototypes screwed onto the bone-like material blocks.

Figure 115: This is a picture of all eleven prostheses used in this analysis.

SET-UP PREPARATION

Once the prosthesis-bone complex was assembled, the tensile test setup was prepared. This test involves holding one end of the specimen fixed while applying a force to the other end, pulling the specimen to separate its two ends.

The tensile testing machine used in this study required modifications to the standard holding clamps to allow axial load application to the specimen, as the tensile force was intended to act axially on the bone-like material. This modification necessitated a sufficiently large holding clamp to accommodate the specimen.

For this purpose, parallelepiped-shaped clamps with a hollowed interior were used, allowing the bone-like specimen to fit inside. These clamps were adjustable in width, enabling them to be tightened securely around the specimen to ensure a firm grip during testing.

The machine utilized two vertically aligned clamps: the upper clamp held the first volume fixed, while the lower clamp applied the tensile load by pulling the second volume downward. Each of the two clamps contained one of the bone-like material specimens to which the prosthesis was attached. The specimens were positioned in the clamps so that the section in contact with the prosthesis remained outside the clamp. Specifically, the last 2.5 cm of the bone-like material specimen extended inside the gripping system.

An additional precaution during the setup was aligning the lower edge of the upper clamp with the lower edge of the upper bone-like volume. Similarly, for the lower clamp, its upper edge was aligned with the upper edge of the lower bone-like specimen.

For prototype number 1, the previously described setup was adopted. However, during testing, it was observed that the volume of bone-like material inside the clamp was not sufficiently stable and tended to rotate within the holding clamp.

For prototype number 2, to address the rotation issue encountered in the test of prototype number 1, two additional bone-like material blocks were inserted to fully occupy the height of the clamp. Specifically, for the upper clamp, the additional block was placed above the specimen, while for the lower clamp, it was positioned below the specimen. Despite this modification, rotation still occurred during the tensile test.

For prototype number 3, the same setup as the previous model was used, but with the addition of a rubber disc between the bone-like specimen and the clamp. However, tensile testing revealed that this modification was not effective in preventing rotation.

For prototype number 4, the setup used for prototype number 1 was reinstated, but with the addition of a metal disc between the bone-like specimen and the clamp. This configuration was found to be optimal, and it was subsequently used for all remaining specimens.

The described setups are illustrated in *Figures 116 and 117*:

Figure 116: In this figure, we can see the experimental setup for the traction test. From right to left, the setups are shown in the following order: prototype 1, prototype 2, prototype 3.

Figure 117: In this figure, we can see the experimental setup for the traction test for prototype 4, which was then adopted for all remaining prosthesis prototypes.

Once our system was positioned within the machine's grasping, the parameters for the test simulation were set as follows:

- The initial displacement, corresponding to the specimen's starting position in the machine, was set to zero.
- An initial tensile load of 50 N was applied to preload the system, thereby associating an initial force with the imposed displacement and stabilizing the system within the testing machine.
- A tensile speed of 5 mm/min was imposed.

RESULTS

During the tensile test, displacement was measured, and force-displacement graphs were generated for each of the 11 specimens, where for each measured displacement, the corresponding force value was associated. The resulting graphs are shown in the following *Figures*, where all obtained data is presented.

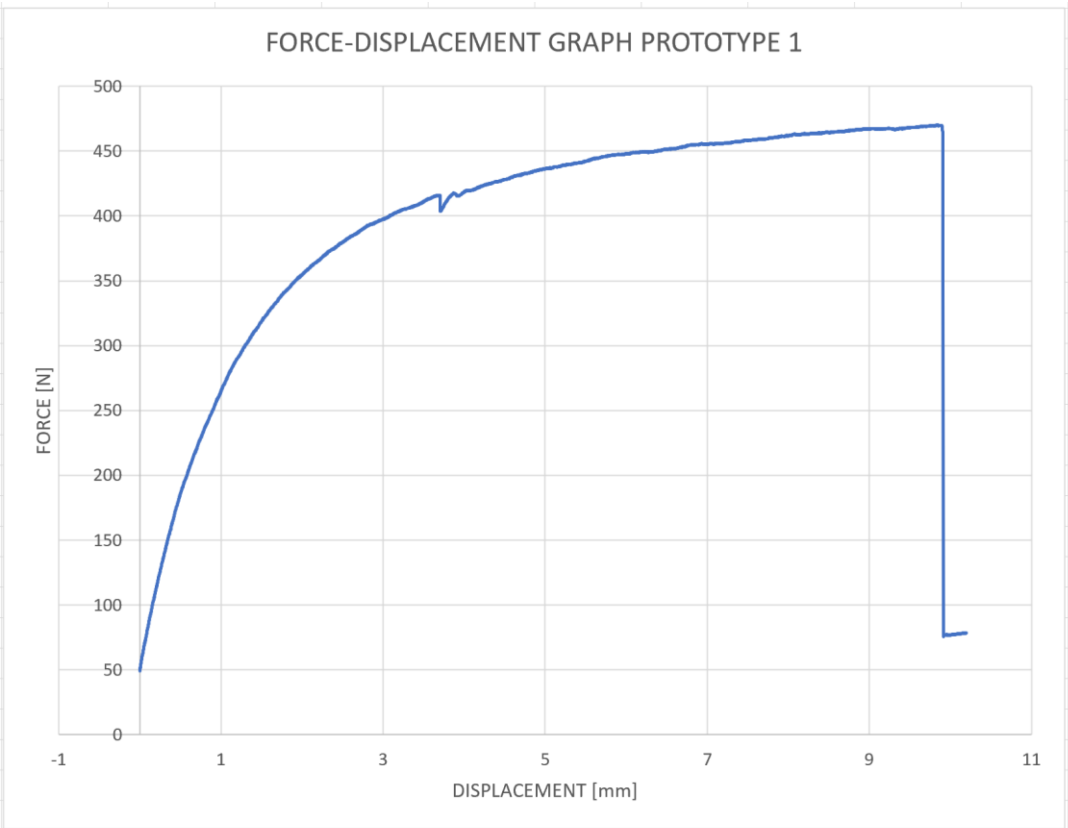

Figure 118: In this image, we can see the force-displacement graph obtained from the tensile test performed in the laboratory for Prototype 1.

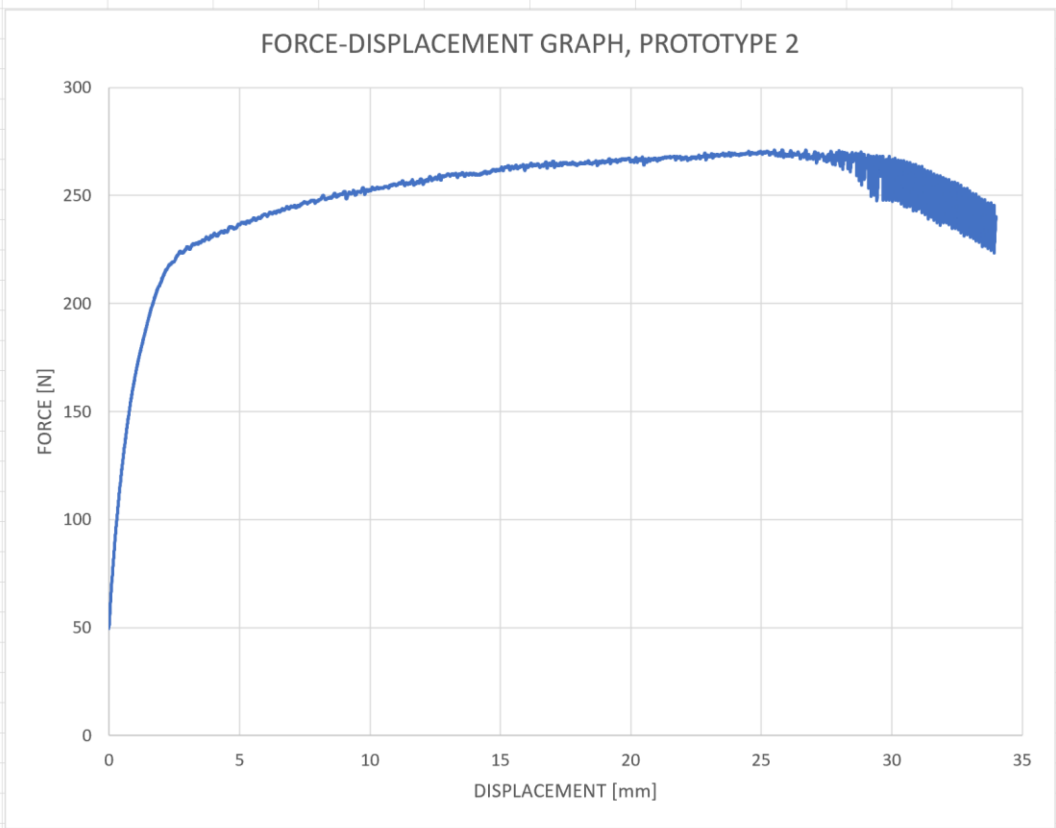

Figure 119: In this image, we can see the force-displacement graph obtained from the tensile test performed in the laboratory for Prototype 2.

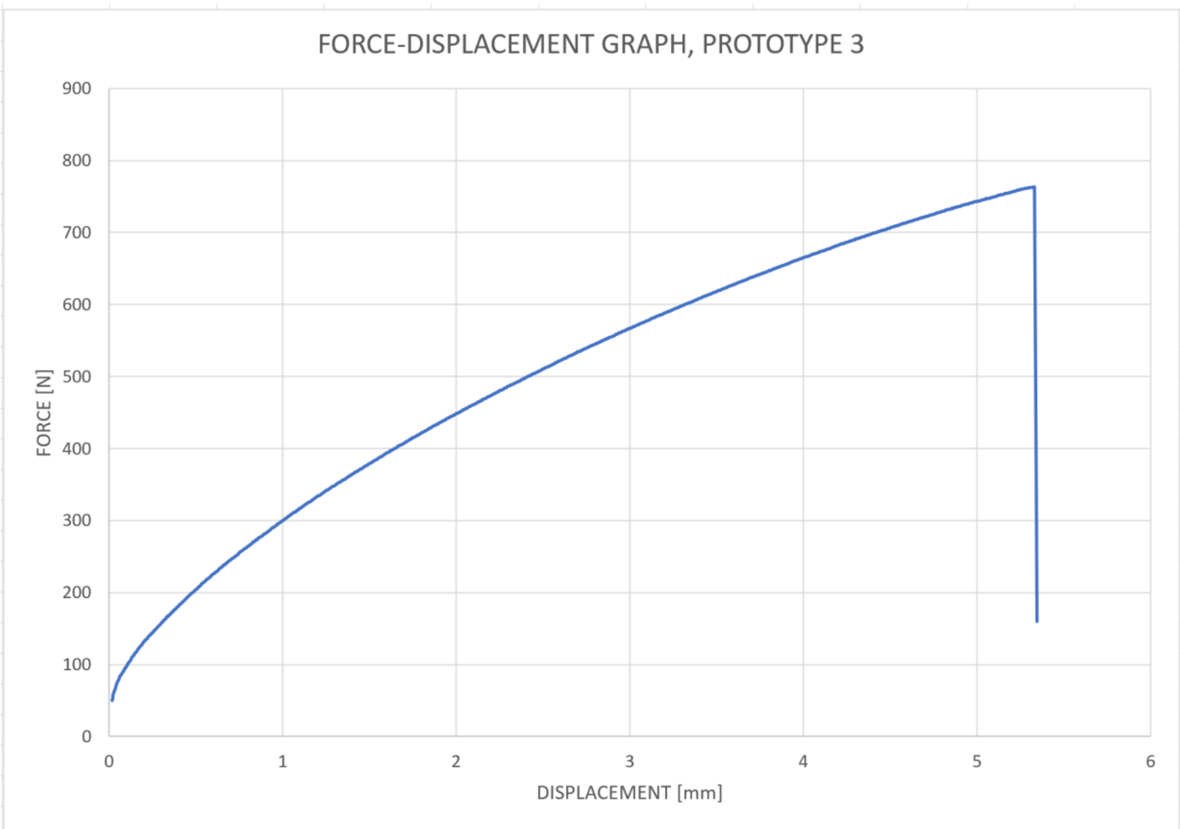

Figure 120: In this image, we can see the force-displacement graph obtained from the tensile test performed in the laboratory for Prototype 3.

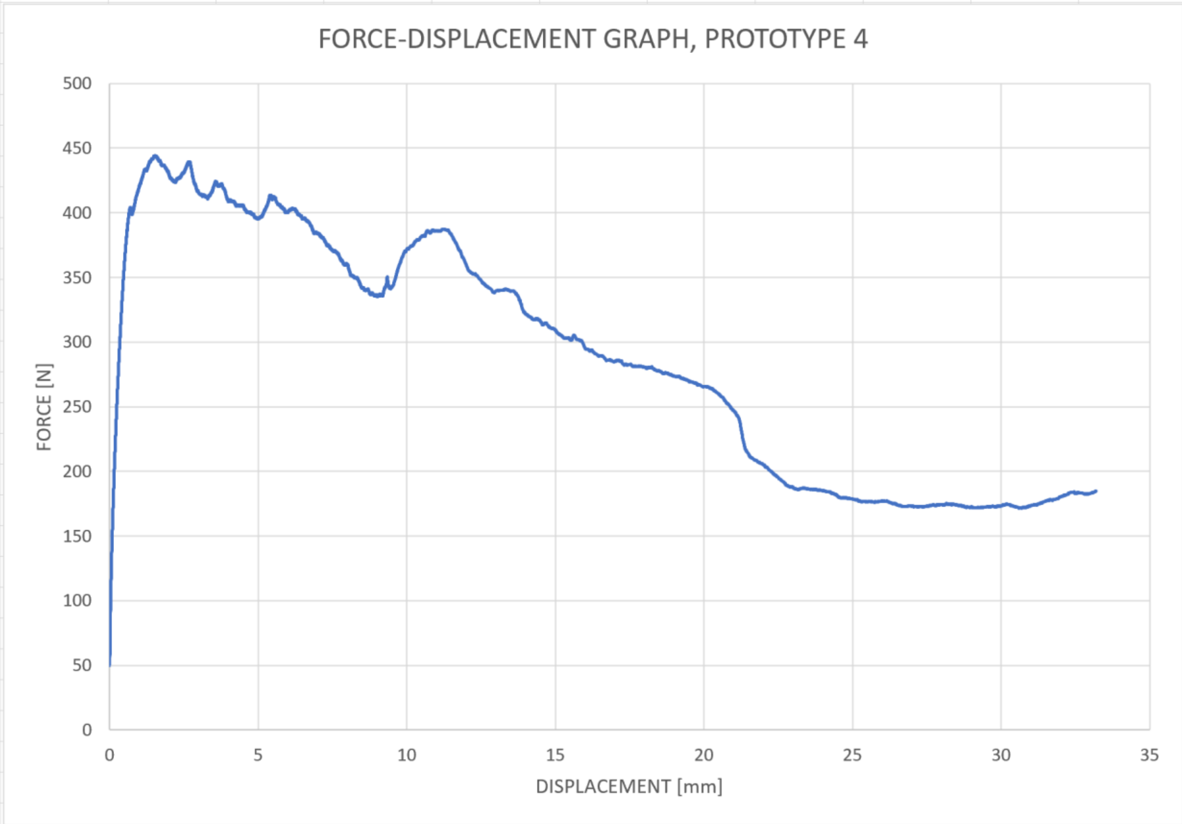

Figure 121: In this image, we can see the force-displacement graph obtained from the tensile test performed in the laboratory for Prototype 4.

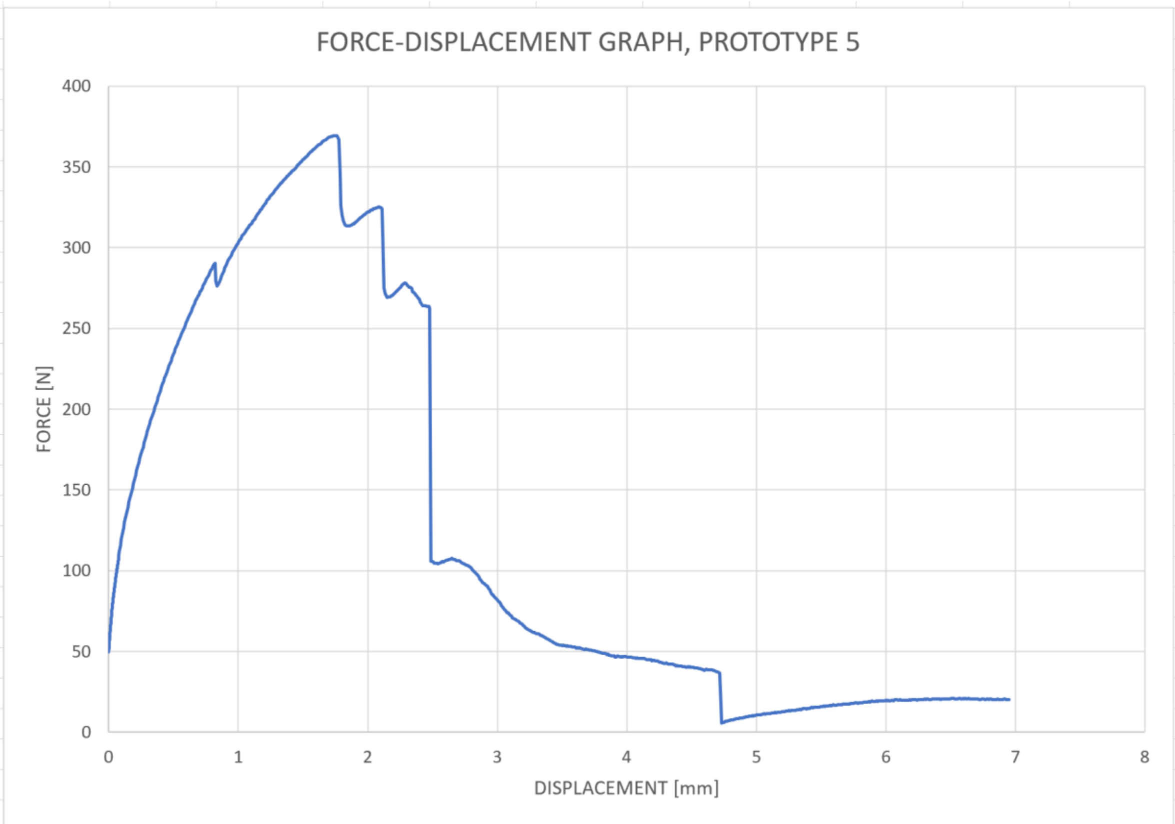

Figure 122: In this image, we can see the force-displacement graph obtained from the tensile test performed in the laboratory for Prototype 5.

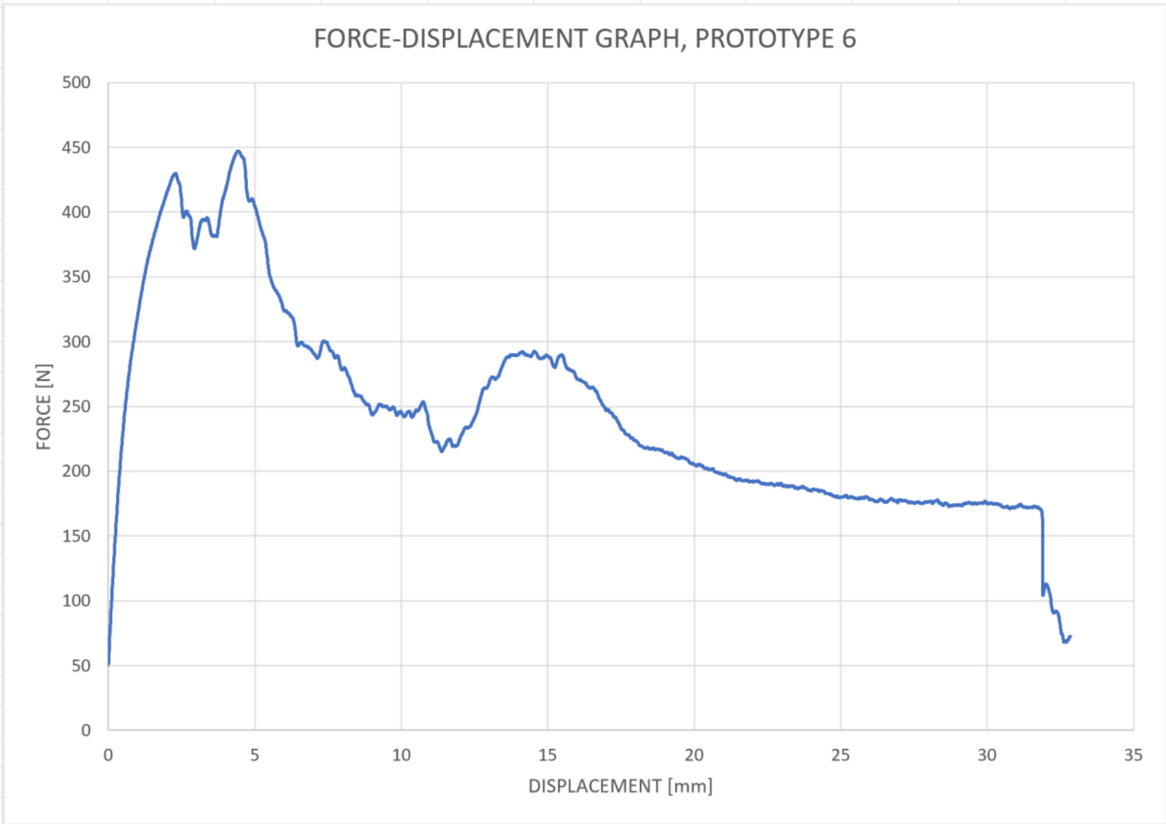

Figure 123: In this image, we can see the force-displacement graph obtained from the tensile test performed in the laboratory for Prototype 6.

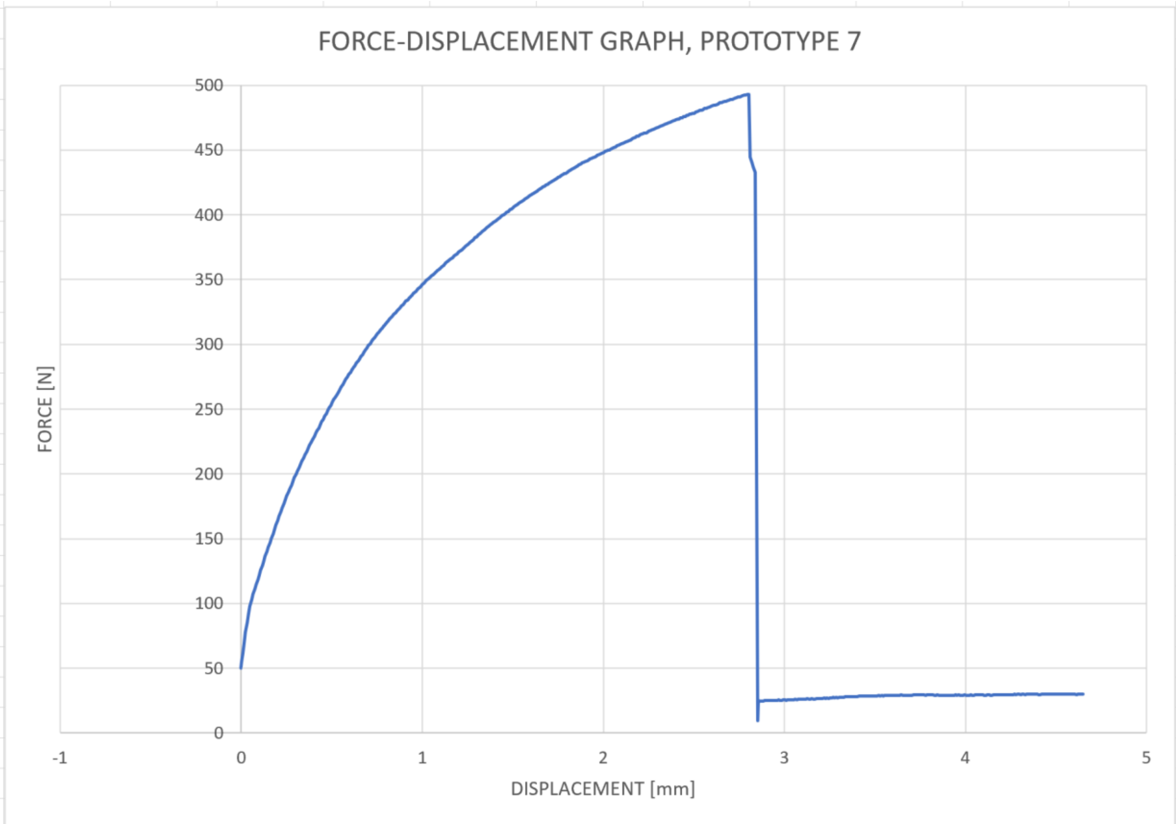

Figure 124: In this image, we can see the force-displacement graph obtained from the tensile test performed in the laboratory for Prototype 7.

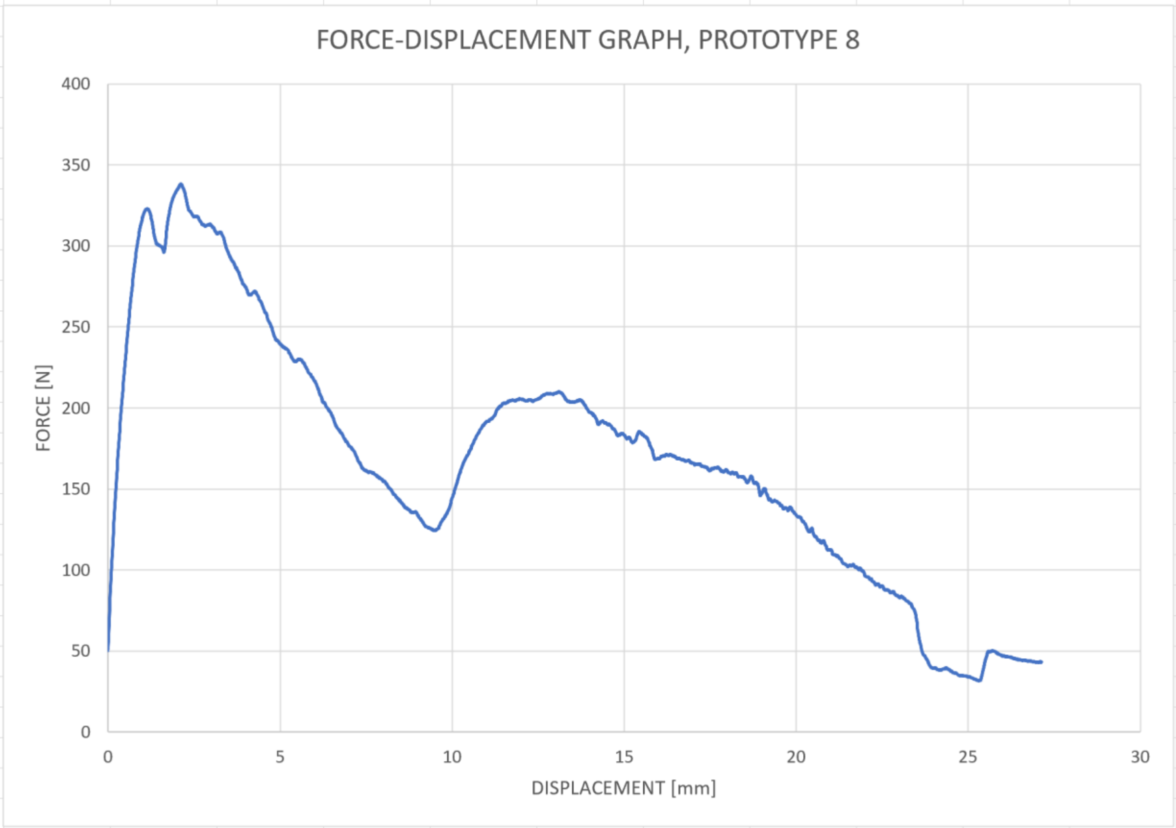

Figure 125: In this image, we can see the force-displacement graph obtained from the tensile test performed in the laboratory for Prototype 8.

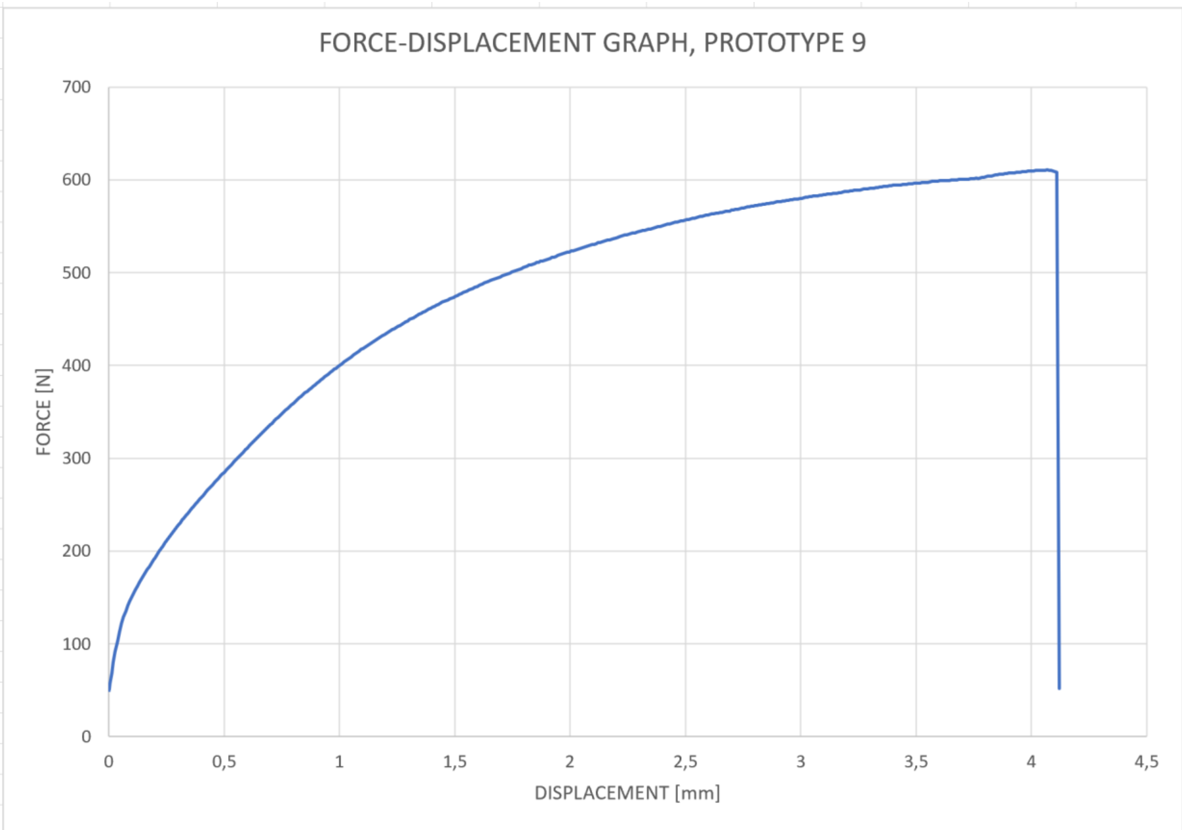

Figure 126: In this image, we can see the force-displacement graph obtained from the tensile test performed in the laboratory for Prototype 9.

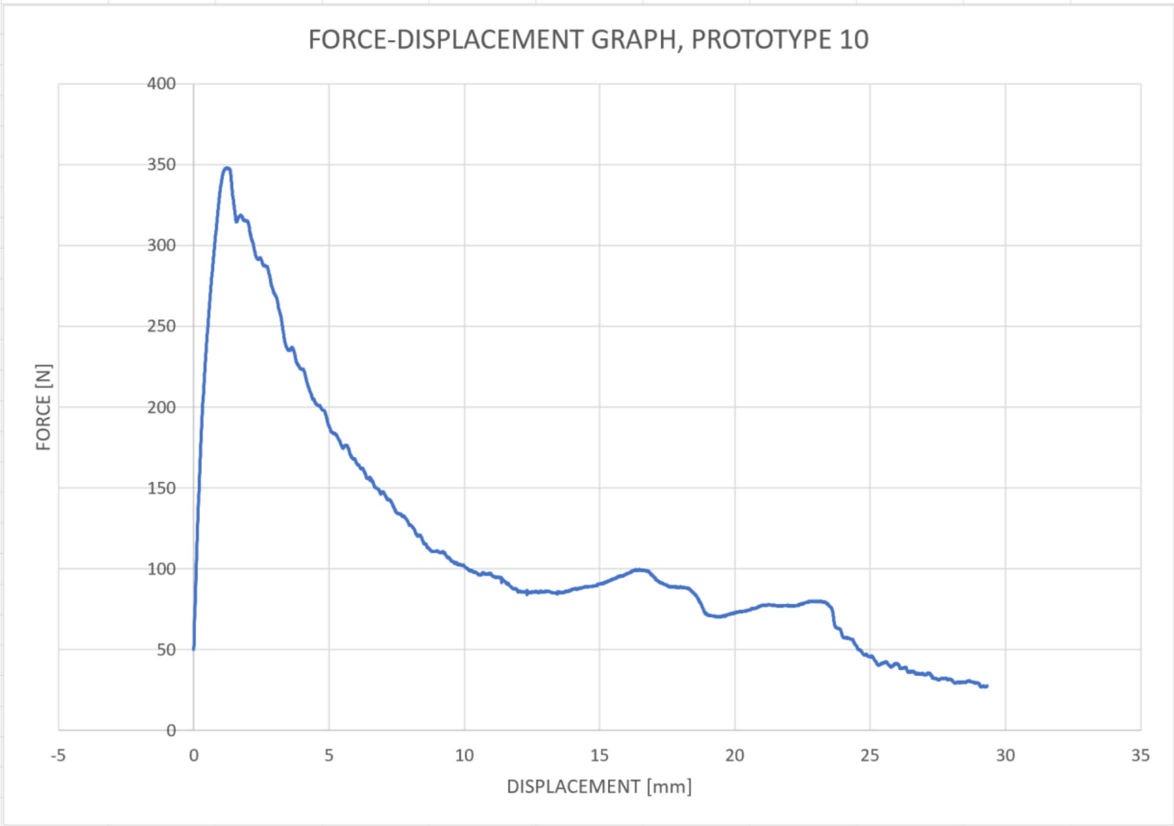

Figure 127: In this image, we can see the force-displacement graph obtained from the tensile test performed in the laboratory for Prototype 10.

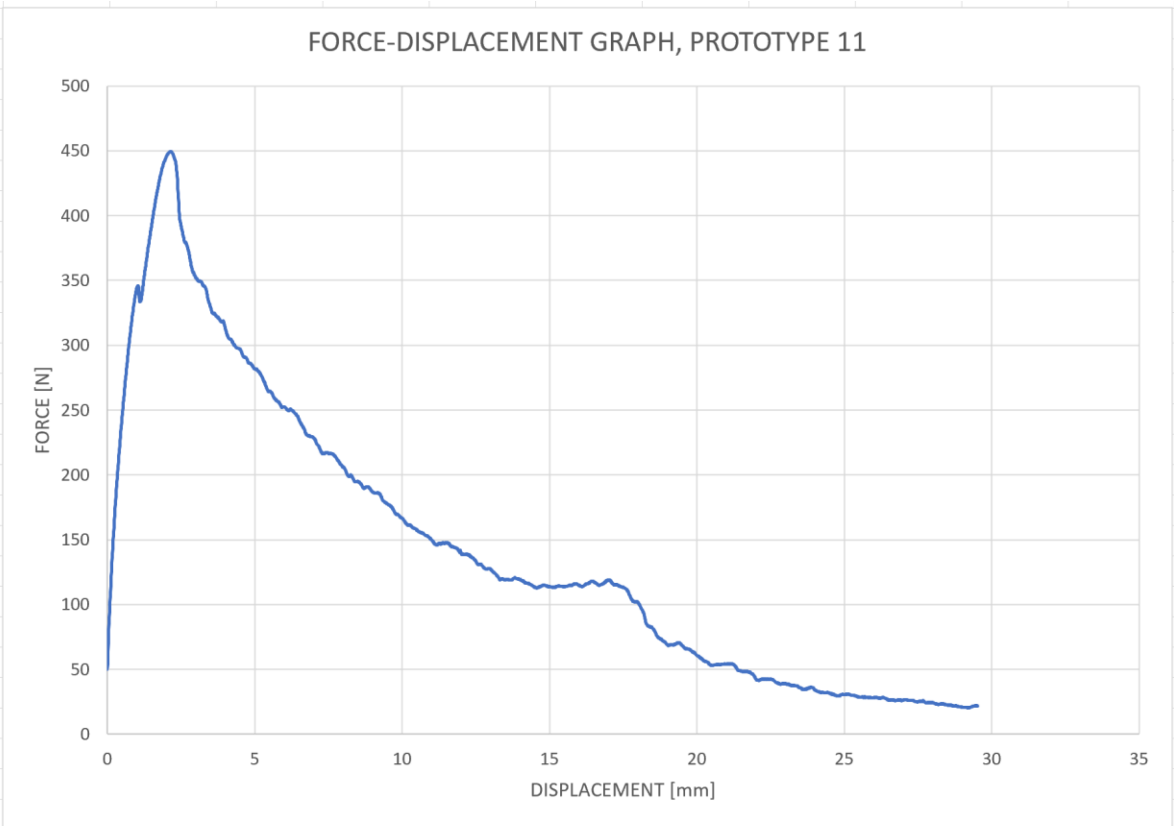

Figure 128: In this image, we can see the force-displacement graph obtained from the tensile test performed in the laboratory for Prototype 11.

The most relevant part of these graphs is the initial section, where all specimens exhibit linear elastic behavior, undergoing elastic deformation. This is the portion that can be reproduced in numerical simulations. For each prototype, the stiffness of these linear segments was determined based on displacement and associated force data and is tabulated in *Table 24* below. In the tables, the first column indicates the number of the considered prototype, the second column shows the maximum deformation corresponding to a force of 80 N, the third column presents the maximum deformation corresponding to a force of 100 N, and finally, the fourth column displays the stiffness value calculated from the experimental force-displacement graph of each prototype using the forces of 80 N and 100 N along with their associated deformations.

PROTOTYPE NUMBER	X1 [mm]	X2 [mm]	STIFFNESS [N/mm]
1	8,76E-02	1,53E-01	300,52
2	1,60E-01	3,00E-01	145,31
3	5,85E-02	1,05E-01	416,57
4	1,96E-02	3,49E-02	1347,8
5	3,16E-02	6,38E-02	639,68
6	6,40E-02	1,17E-01	424,64
7	2,35E-02	5,74E-02	737,16
8	5,08E-02	1,02E-01	445,23
9	2,16E-03	1,75E-01	744,5
10	4,95E-02	9,16E-02	527,47
11	4,50E-02	8,75E-02	504,94

Table 24: The stiffness values of each prototype in the initial segment of the force-displacement curve are shown, specifically in the region where they behave elastically.

Below, we present the appearance of the specimen at the end of the experimental tensile test, facilitating the interpretation of the force-displacement graphs. This allows us to analyze, for specimens that fractured, the exact location of the failure, while for the others, how the prosthesis deformed.

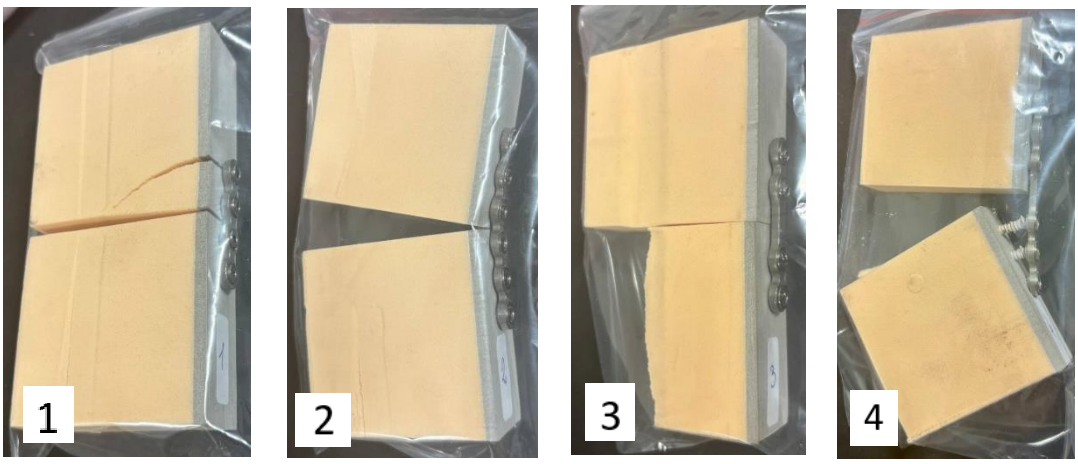

Figure 129: The following image shows the results of the experimental tensile tests, displaying photographs of the specimens after testing. The sequence starts in the right corner with Prototype 1 and follows the numerical order to the left corner with Prototype 4.

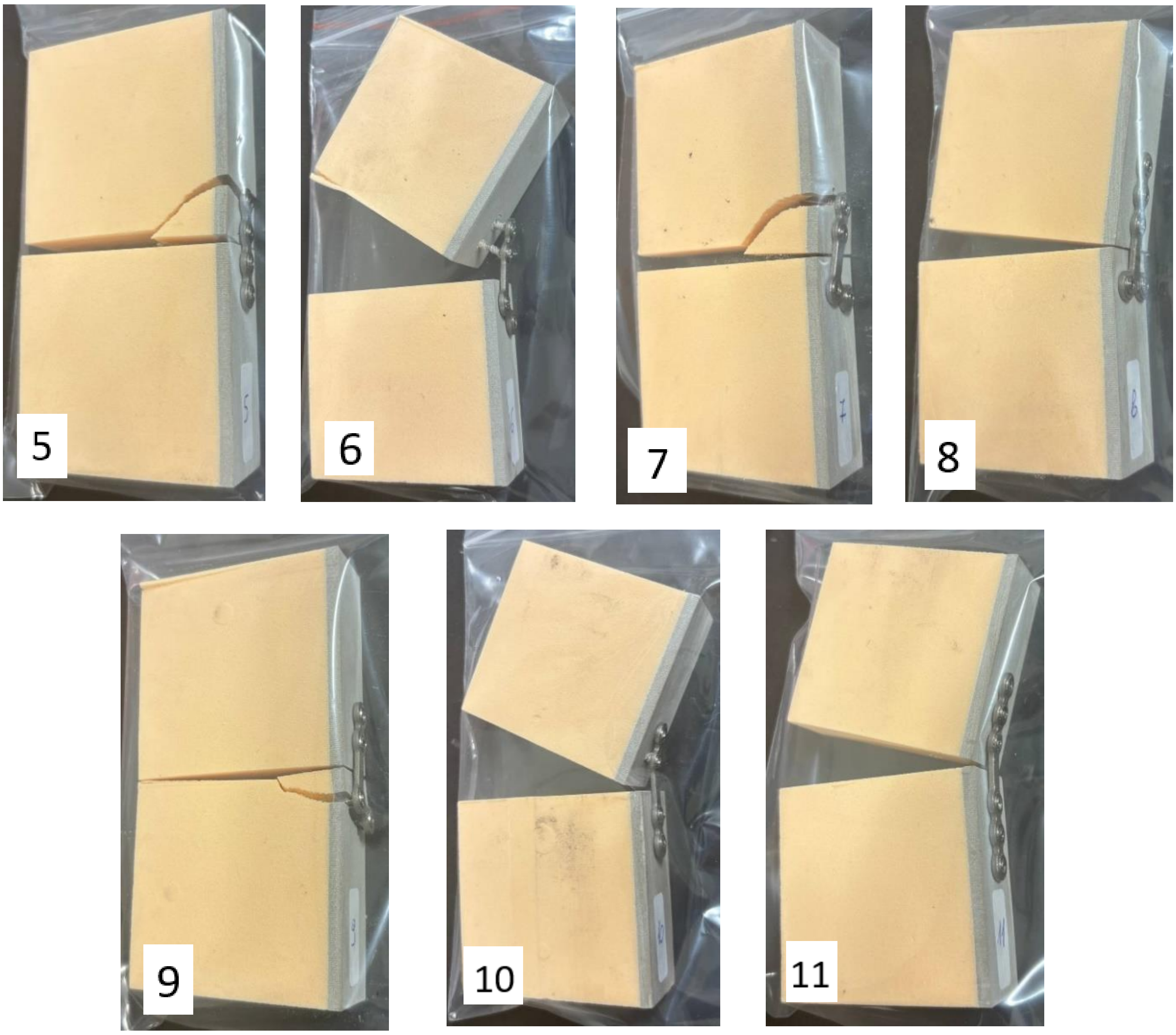

Figure 130: The following image shows the results of the experimental tensile tests, displaying photographs of the specimens after testing. The sequence starts in the upper right corner with Prototype 5 and follows the numerical order down to the lower left corner with Prototype 11.

DISCUSSION OF EXPERIMENTAL TEST

The force-displacement graphs presented above contain the data collected during the laboratory tensile test performed on all prosthesis prototypes screwed into two bone-like material blocks. Let us now analyze the significance of these data in detail.

- Specimen 1: Failure occurred when the applied force reached 469 N, with a deformation of 9.88 mm. Specifically, the failure took place at the uppermost screw of the bone specimen that was held fixed. During the tensile test, the bone-like material block being pulled experienced slight rotation, whereas the fixed block remained stable within the holding clamp.

- Specimen 2: No failure occurred, as seen in the graph. Instead, the prosthesis deformed at the center of its length. This was due to both rotation and sliding of both bone-like material blocks during the test.

- Specimen 3: Failure occurred at 763 N, with a deformation of 5.33 mm. The failure took place in the bone-like material far from the prosthesis and screws, specifically at the point where the tensile specimen started contacting the holding clamp. During the test, the pulled bone-like material block experienced slight rotation, whereas the fixed block remained stable in the holding clamp.

- Specimen 4: No failure occurred, as indicated in the graph. Instead, detachment of the two upper screws from the pulled volume was observed. The pulled bone-like material block underwent both rotation and sliding, while the fixed block remained stable within the holding clamp.

- Specimen 5: Failure occurred at 369 N, with a deformation of 1.74 mm. Specifically, it happened at the uppermost screw of the fixed bone specimen. During the tensile test, both bone-like material blocks remained stable within the holding clamps.

- Specimen 6: No failure occurred, as seen in the graph. However, detachment of the lowest screw in the fixed volume was observed. During the test, the fixed bone-like material block experienced both rotation and sliding, whereas the pulled block remained stable in the holding clamp.

- Specimen 7: Failure occurred at 492 N, with a deformation of 2.79 mm. Specifically, the failure took place at the lowest screw of the pulled bone specimen. During the tensile test, both bone-like material blocks remained stable within the holding clamps.

- Specimen 8: No failure occurred, as shown in the graph. Instead, the prosthesis deformed at its central length. This was due to both rotation and sliding of the pulled bone-like material block during the test.

- Specimen 9: Failure occurred at 610 N, with a deformation of 4.06 mm. Specifically, failure took place at the two screws in the pulled bone specimen. During the tensile test, both bone-like material blocks remained stable within the holding clamps.

- Specimen 10: No failure occurred, as indicated in the graph. However, detachment of the lowest screw in the fixed volume was observed. During the test, the fixed bone-like material block experienced both rotation and sliding, whereas the pulled block remained stable in the holding clamp.

- Specimen 11: No failure occurred, as seen in the graph. Instead, the prosthesis deformed at its central length. This was due to both rotation and sliding of the stable bone specimen during the test.

Thus, not all specimens failed. Only specimens 1, 3, 5, 7, and 9 underwent failure, as shown both in the graphs and in Figure 167. The failure occurred in the bone-like material, as it is the material with the lowest elastic modulus and is more brittle, while the prosthesis and screws, which are more rigid and have a higher elastic modulus, did not fail. Among the failed specimens, specimen 3 does not provide relevant insights into the effect of the prosthesis fixation on bone. This is because its failure occurred in the bone volume within the holding clamp, rather than in the bone region in contact with the prosthesis, which is the focus of this study. For all other specimens, the bone volume did not fail. Instead, deformation of the prosthesis was observed in specimens 2, 8, and 11, while detachment of some screws occurred in specimens 4, 6, and 10**.**

By analyzing the stiffness of the specimens tabulated in *Table 24*, we can observe the following:

- Prototypes 1 and 5 have similar geometries; both contain four screws, evenly spaced and perpendicular to the plate. The difference lies in their dimensions and materials. Prototype 1 is thicker and made of Grade 5 titanium, while Prototype 5 is made of Grade 4 titanium and is thinner. From the table, we see that Prototype 5 exhibits higher stiffness values compared to Prototype 1. This contradicts expectations since Grade 5 titanium has a higher elastic modulus; for the same shape, Prototype 1 should have greater stiffness. This discrepancy might be due to differences in the experimental setup. Specifically, unlike Prototype 1, Prototype 5 had metal discs between the bone-like specimen and the edge of the holding clamps, which may have influenced its stiffness.

- Prototypes 3 and 10 also share a similar geometry, with four screws inclined at 15 degrees towards the prosthesis end. Prototype 3 is thicker and made of Grade 5 titanium, while Prototype 10 is made of Grade 4 titanium and is thinner. According to the table, Prototype 10 exhibits higher stiffness values than Prototype 3, which contradicts expectations. Since Grade 5 titanium has a higher elastic modulus, Prototype 3 should have greater stiffness if the shape remains the same. Again, this discrepancy could be due to differences in experimental setup—unlike Prototype 3, Prototype 10 had metal discs between the bone-like specimen and the holding clamps, which may have affected its stiffness.

- Prototypes 4 and 11 have similar geometries, both containing six screws inclined at 15 degrees toward the prosthesis center. Prototype 4 is thicker and made of Grade 5 titanium, while Prototype 11 is made of Grade 4 titanium and is thinner. The table indicates that Prototype 4 has higher stiffness values than Prototype 11, which aligns with expectations since Grade 5 titanium has a higher elastic modulus. In this case, unlike previous examples, the experimental setup was identical for both prototypes.

- Prototypes 1, 3, 5, and 10 all have four screws but with different inclinations. For Prototypes 1 and 3, both made of the same material but with different screw angles, the stiffness values appear similar. However, Prototype 3 has slightly higher stiffness than Prototype 1, suggesting that screw inclination affects stiffness. Similarly, for Prototypes 5 and 10, also made of the same material but with different screw inclinations, Prototype 5 exhibits greater stiffness than Prototype 10, reinforcing the idea that screw inclination influences overall stiffness. However, due to the rotational effects observed during testing, it is uncertain whether screw inclination consistently increases stiffness. In one case, it increases stiffness, while in another, it has the opposite effect.

- Prototypes 6 and 9 are made of the same material and share the same plate geometry. However, Prototype 6 has all screws perpendicular to the plate, while Prototype 9 has two inclined screws and two perpendicular screws. The table shows that Prototype 6 has significantly lower stiffness than Prototype 9, meaning that, in this case, screw inclination increases overall stiffness. It should be noted, however, that Prototype 9 remained stable during testing, whereas Prototype 6 experienced both sliding and rotation.

- Prototypes 2 and 4 are made of the same material and contain six screws each. The main difference is screw inclination: in Prototype 2, all screws are perpendicular, whereas in Prototype 4, all screws are inclined. Additionally, their plate geometries differ slightly—Prototype 2 has evenly spaced screws, while Prototype 4 has a central gap with screws concentrated at the ends. According to the table, Prototype 4 has significantly higher stiffness than Prototype 2, but this difference cannot be attributed solely to screw inclination. The experimental setup was different for these specimens; unlike Prototype 2, Prototype 4 had metal discs between the bone-like material and the holding clamps.

- Prototypes 6 and 7 both have four screws positioned perpendicular to the plate and share similar shapes. Specifically, Prototype 6 has an L-shaped design, but instead of a 90-degree angle between the arms, it has a 118.25-degree angle. The table shows that Prototype 7 is stiffer than Prototype 6. This effect can be attributed to both the prosthesis plate shape and the fact that Prototype 7 remained stable during testing, whereas Prototype 6 underwent both sliding and rotation.

CHAPTER 4: DISCUSSION

COMPARISON OF NUMERICAL AND EXPERIMENTAL DATA

In this chapter, we will compare the results obtained from the numerical simulations performed on the FEM model of the various prosthesis prototypes with the results obtained from the experimental tests conducted in the laboratory.

The comparison will be carried out only for Prototype Model 2, as Prototype Model 1 was an excessive approximation of the general specimen and produced stiffness values that could not be compared with the actual stiffness, being excessively high. The order of magnitude of the numerical stiffness is in kN/mm, while the order of magnitude for the experimental stiffness is in N/mm. This discrepancy is due to the excessive simplicity of Model 1 compared to the real model and the constraints that were imposed. The main reason for the excessive stiffness lies in the fact that the screws in this model were considered cylinders with infinite stiffness, while in reality, they have a stiffness of 110 GPa. Furthermore, in this numerical analysis, the deformation of the plate is calculated, whereas in the laboratory, the deformation of the model as a whole was measured.

We will now analyze in detail the comparison between the stiffness of Prototype Model 2 and the actual stiffness.

For Model 2 of each prototype, two tensile analyses were conducted using different force values to obtain the Force-Displacement curve associated with the analysis. Using this graph, the stiffness of the prototype was calculated and compared with the stiffness determined from experimental data to evaluate the accuracy of this model. This comparison can be made because, in the experimental tests, the specimen exhibits a linear elastic behavior in the initial phase of the tensile test. This behavior is the same as that simulated in the numerical analysis performed on the FEM model of the specimens.

In *Table 25* below, we can see the comparison for each of the 11 prosthesis prototypes between the stiffness calculated from the numerical analyses ("Model 2 stiffness") and the stiffness obtained from the experimental test data ("experimental stiffness"), along with the relative percentage error between the experimental stiffness and the corresponding numerical stiffness.

PROTOTYPE NUMBER	NUMERICAL STIFNESS [MPa]	EXPERIMENTAL STIFFNESS [MPa]	ERROR %
1	1250	300,52	315,9
2	1574,8	145,31	983,8
3	1227	416,57	194,5
4	1515,5	1347,8	12,4
5	689,66	639,68	7,8
6	645,16	424,64	51,9
7	740,74	737,16	0,5
8	769,23	445,23	72,8
9	769,23	744,5	3,3
10	800	527,47	51,7
11	904,98	504,94	79,2

Table 25: For each of the 11 prototypes, the comparison between the experimental stiffness and the actual stiffness along the x-axis can be observed.

As we can see from the data in *Table 25*, the stiffness values calculated using Model 2 for all 11 prototypes are comparable to the experimental stiffness values, as they share the same order of magnitude, namely N/mm. Specifically, the stiffness calculated from numerical analyses is generally higher than the experimentally measured stiffness. This occurs because the FEM model, by discretizing the volume, has fewer degrees of freedom than the real model (which has an infinite number of degrees of freedom), making the finite element model stiffer than the actual specimen.

If we analyze the data in more detail, we can observe that the first three specimens exhibit significantly high errors, exceeding 100%. This is because the experimental setup varied from test to test for these first three specimens, leading to excessive sliding and rotation during the trials. These effects influenced the stiffness of the specimen, making it more deformable.

As discussed in the previous chapter, not all specimens experienced failure, and not all underwent a pure tensile test—some were affected by rotation or sliding.

In particular, for prototypes 1, 3, 5, 7, and 9, a tensile test was successfully conducted in the laboratory without encountering sliding or rotation. For these specimens—except for the first two, where the setup was not yet finalized—the numerical stiffness values are similar to the experimental ones, with errors below 10%, although the FEM model still predicts slightly higher stiffness due to volume discretization. These specimens are highlighted in the following table:

PROTOTYPE NUMBER	NUMERICAL STIFNESS [MPa]	EXPERIMENTAL STIFFNESS [MPa]	ERROR %
1	1250	300,52	315,9
3	1227	416,57	194,5
5	689,66	639,68	7,8
7	740,74	737,16	0,5
9	769,23	744,5	3,3

Table 26: This table presents the comparison between numerical and experimental stiffness values for the specimens that did not experience rotation or sliding during the experimental test, namely specimens 1, 3, 5, 7, and 9.

These prototypes, which during the experimental laboratory test were subjected only to tensile forces and were not influenced by rotation or sliding, all resulted in specimen failure. Except for prototype number 3, whose failure occurred in the bone specimen at the point of contact with the edge of the holding clamp, the other prototypes fractured in areas of interest, as the failures occurred in the bone specimen at the points of contact with the prosthesis screws.

Next, we will analyze the distribution of Von Mises stresses obtained from the numerical models and compare them with the failure locations of the specimens. The failure points observed during the experimental tests coincide with the points where the maximum Von Mises stress occurred during the numerical analyses, as can be seen in the figures provided in the appendix.

Regarding prototype number 1, during the experimental tests, the failure point was observed at the level of the outermost screw in the bone specimen that was held fixed. From the stress distribution obtained from the numerical analysis, it was observed that the highest stress concentrations occurred precisely in the contact area between the screw and the bone, with the maximum peak located at the two screws at the extremities of the prosthesis.

Similarly, for prototype number 5, during the experimental tests, the fixed bone specimen failed at the level of the outermost screw of the prosthesis. From the stress distribution obtained from the numerical analysis, it was observed that the highest stresses occurred in the contact area between the screw and the bone, with the maximum peak located at the two screws at the extremities of the prosthesis.

For prototype number 7, failure during the experimental tests occurred at the outermost screw of the longer arm of the L-shaped prototype. From the stress distribution obtained from the numerical analysis, it was observed that the highest stress concentrations were located precisely in the contact area between the screw and the bone, with the maximum peak at the screw that, during the experimental test, caused the failure of the bone specimen.

Finally, prototype number 9 failed during the experimental tests, with failure occurring in the bone specimen at the screws on the short side of the L-shaped prototype. From the stress distribution obtained from the numerical analysis, it was observed that the highest stresses were located precisely in the contact area between the screw and the bone, with the screws on the short side of the L-shape being the most subjected to stress.

For prototypes 2, 8, and 11, however, rotation of one of the two bone-like material specimens occurred during the tensile test. To enable a realistic comparison between numerical and experimental stiffness values, a numerical tensile test was conducted for these specimens, incorporating the imposed rotation of the bone-like material specimen being pulled (using specific constraints). To better visualize the effect of rotation on specimen stiffness, the following data have been compared: stiffness calculated from numerical data for the pure tensile test ("numerical tensile stiffness"), stiffness obtained from experimental data ("experimental stiffness") and stiffness calculated from numerical data for the tensile test with rotation ("numerical tensile & rotational stiffness"). For both numerical stiffness values (pure tensile and tensile with rotation), the percentage error relative to the experimental stiffness was calculated.

The results are summarized in the following *table 27*, where: in the first column, there is the number of the considered prototype; in the second column, there is the stiffness value obtained from the numerical analyses considering pure tension; in the third column, there is the stiffness value derived from the force-deformation graph of the experimental test; in the fourth column, there is the percentage error of the numerical stiffness under pure tension compared to the experimental stiffness; in the fifth column, there is the stiffness value obtained from the numerical analyses considering both the specimen's rotation and tension; and finally, in the last column, there is the percentage error of the numerical stiffness for the tension-rotation analysis compared to the experimental stiffness.

PROTOTYPE NUMBER	NUMERICAL TENSILE STIFFNESS [Mpa]	EXPERIMENTAL STIFFNESS [MPa]	ERROR %	NUMERICAL TENSILE & ROTATIONAL STIFNESS [MPa]	ERROR %
2	1574,8	145,31	983,8	1010,1	595,1
8	769,23	445,23	72,8	540,54	21,4
11	904,98	504,94	79,2	645,16	27,8

*Table 27**:** This table presents the comparison between numerical (pure tensile and tensile with rotation) and experimental stiffness values for specimens 2, 8, and 11.*

As shown in *Table 27*, the error relative to the experimental stiffness decreases significantly when the specimen's rotation is also considered in the numerical analysis. The error decreases from over 70% when only tensile forces are considered to below 30% when rotation is also taken into account. This occurs because the numerical stiffness decreases when rotation is included in the analysis. Moreover, the error remains significant since, in addition to the effect of rotation, these specimens also experienced slight slippage during the experimental test, which was not considered in the numerical analysis. Except for Prototype 2, as previously mentioned, since its experimental setup was not identical to the others and caused excessive slippage, resulting in a very low experimental stiffness value.

For the remaining prototypes, namely numbers 4, 6, and 10, a direct comparison between numerical and experimental stiffness values is not feasible. During the experimental test, these prototypes exhibited excessive sliding in addition to rotation. Furthermore, these specimens experienced screw detachment from the bone, an effect not considered in this study. Indeed, as seen in *Table 25,* these prototypes show high errors between numerical and experimental stiffness values, on the order of 100%.

SENSITIVITY ANALYSIS OF NUMERICAL MODELS

Before performing the numerical tensile analyses for Models 1 and 2, a sensitivity analysis of the model was conducted to determine the optimal mesh size for the discretization of the volume in our FEM model of the prostheses. This step was necessary because the discretization of the total model volume for numerical analyses introduces a certain discretization error, which affects the accuracy of the results. Therefore, the objective was to identify a mesh size that minimizes these discretization errors while maintaining a reasonable computational cost for the simulation.

The goal of this process was to achieve model convergence, meaning that further refinement of the mesh would no longer produce significant variations in the results. To accomplish this sensitivity analysis, different mesh sizes were tested while keeping all other model parameters constant, specifically the elastic modulus and Poisson's ratio of the various materials. In particular, the mesh size was progressively reduced, ensuring that each successive mesh was nested within the previous one (i.e., each mesh contained the nodes of the preceding mesh), allowing for a direct comparison of results.

This analysis was performed for both Model 1 and Model 2, and the corresponding results are presented below.

MODEL 1

For the sensitivity analysis of Model 1, the initial mesh size was set equal to the thickness of the plate and was progressively halved to ensure that each subsequent mesh was nested within the previous one. The mesh sizes used for the mini endoprostheses were: 2 mm, 1 mm, 0.5 mm, and 0.25 mm, while those used for the micro endoprostheses were: 1.3 mm, 0.65 mm, and 0.325 mm.

The elastic moduli of the plate and screws were kept constant. For the mini endoprostheses, these values were 110 GPa and 110 × 10^3 GPa, respectively, with a Poisson's ratio of 0.33 for both. For the micro endoprostheses, the elastic moduli were 105 GPa and 110 × 10^3 GPa, with a Poisson's ratio of 0.34 and 0.33.

The tables below present the results of the sensitivity analysis for selected prototypes: prototype 1 and 2 (for the mini endoprostheses) and prototypes 5, 7, and 11 (for the micro endoprostheses). In the tables, the data are summarized as follows: the first column indicates the reference axis along which the deformation was considered; the second column shows the mesh size expressed in mm; the third column presents the maximum deformation corresponding to the applied force of 80 N; the fourth column shows the maximum deformation corresponding to the applied force of 100 N; the sixth column indicates the stiffness calculated from the force-deformation graph using the forces of 80 N and 100 N with their respective deformation values; and finally, the last column reports the error between the stiffness of the considered mesh and that of the previous mesh. The deformations are given in mm, while the stiffness values are in kN/mm.

PROTOTYPE 1					
	MESH [mm]	X1 [mm]	X2 [mm]	STIFFNESS [kN/mm]	ERROR %
ALONG X	2	1,14E-03	1,42E-03	71,429	
	1	1,21E-03	1,51E-03	66,667	7,14
	0,5	1,25E-03	1,57E-03	62,5	6,67
	0,25	1,27E-03	1,59E-03	62,5	0,00
	MESH [mm]	Y1 [mm]	Y2 [mm]	STIFFNESS [kN/mm]	ERROR %
ALONG Y	2	1,19E-04	1,48E-04	675,676	
	1	1,07E-04	1,34E-04	746,269	10,45
	0,5	1,07E-04	1,33E-04	772,201	3,47
	0,25	1,09E-04	1,36E-04	735,294	4,78
	MESH [mm]	Z1 [mm]	Z2 [mm]	STIFFNESS [kN/mm]	ERROR %
ALONG Z	2	8,28E-05	1,03E-04	970,874	
	1	7,13E-05	8,92E-05	1000	3,00
	0,5	8,23E-05	1,03E-04	970,874	2,91
	0,25	8,84E-05	1,11E-04	904,977	6,79

Table 28: The table presents the displacement values along the three axes and the corresponding stiffness values calculated for each selected mesh size of Prototype 1. The last column shows the error in the stiffness calculation between each mesh and the subsequent one.

PROTOTYPE 2					
	MESH [mm]	X1 [mm]	X2 [mm]	STIFFNESS [kN/mm]	ERROR %
ALONG X	2	1,95E-03	2,43E-03	41,667	
	1	2,03E-03	2,54E-03	39,216	6,25
	0,5	2,14E-03	2,68E-03	37,037	5,88
	0,25	2,17E-03	2,71E-03	37,037	0,00
	MESH [mm]	Y1 [mm]	Y2 [mm]	STIFFNESS [kN/mm]	ERROR %
ALONG Y	2	1,21E-04	1,51E-04	662,252	
	1	1,10E-04	1,37E-04	729,927	10,22
	0,5	1,06E-04	1,32E-04	760,456	4,18
	0,25	1,09E-04	1,12E-04	6000	689,00
	MESH [mm]	Z1 [mm]	Z2 [mm]	STIFFNESS [kN/mm]	ERROR %
ALONG Z	2	1,08E-04	1,35E-04	743,494	
	1	7,23E-05	9,03E-05	1000	34,50
	0,5	9,06E-05	1,13E-04	884,956	11,50
	0,25	8,97E-05	1,36E-04	432,9	51,08

Table 29: The table presents the displacement values along the three axes and the corresponding stiffness values calculated for each selected mesh size of Prototype 2. The last column shows the error in the stiffness calculation between each mesh and the subsequent one.

PROTOTYPE 5					
	MESH [mm]	X1 [mm]	X2 [mm]	STIFFNESS [kN/mm]	ERROR %
ALONG X	1,3	1,48E-03	1,85E-03	54,054	
	0,65	1,55E-03	1,94E-03	51,282	5,13
	0,325	1,59E-03	1,99E-03	50	2,50
	MESH [mm]	Y1 [mm]	Y2 [mm]	STIFFNESS [kN/mm]	ERROR %
ALONG Y	1,3	1,78E-04	2,23E-04	445,434	
	0,65	1,72E-04	2,15E-04	460,829	3,46
	0,325	1,66E-04	2,07E-04	4,88E+02	5,85
	MESH [mm]	Z1 [mm]	Z2 [mm]	STIFFNESS [kN/mm]	ERROR %
ALONG Z	1,3	1,21E-04	1,51E-04	666,667	
	0,65	8,45E-05	1,06E-04	943,396	41,51
	0,325	9,36E-05	1,17E-04	854,701	9,40

Table 30: The table presents the displacement values along the three axes and the corresponding stiffness values calculated for each selected mesh size of Prototype 5. The last column shows the error in the stiffness calculation between each mesh and the subsequent one.

PROTOTYPE 7					
	MESH [mm]	X1 [mm]	X2 [mm]	STIFFNESS [kN/mm]	ERROR %
ALONG X	1,3	3,95E-03	4,93E-03	20,408	
	0,65	4,11E-03	5,14E-03	19,417	4,86
	0,325	4,17E-03	5,22E-03	19,048	1,90
	MESH [mm]	Y1 [mm]	Y2 [mm]	STIFFNESS [kN/mm]	ERROR %
ALONG Y	1,3	8,02E-04	1,00E-03	100	
	0,65	8,67E-04	1,08E-03	92,593	7,41
	0,325	8,79E-04	1,10E-03	90,909	1,82
	MESH [mm]	Z1 [mm]	Z2 [mm]	STIFFNESS [kN/mm]	ERROR %
ALONG Z	1,3	1,74E-04	2,18E-04	458,716	
	0,65	1,40E-04	1,75E-04	573,066	24,93
	0,325	1,52E-04	1,90E-04	526,316	8,16

Table 31: The table presents the displacement values along the three axes and the corresponding stiffness values calculated for each selected mesh size of Prototype 7. The last column shows the error in the stiffness calculation between each mesh and the subsequent one.

PROTOTYPE 11					
	MESH [mm]	X1 [mm]	X2 [mm]	STIFFNESS [kN/mm]	ERROR %
ALONG X	1,3	3,73E-03	4,66E-03	21,505	
	0,65	3,85E-03	4,81E-03	20,833	3,12
	0,325	3,90E-03	4,88E-03	20,408	2,04
	MESH [mm]	Y1 [mm]	Y2 [mm]	STIFFNESS [kN/mm]	ERROR %
ALONG Y	1,3	2,01E-04	2,52E-04	393,701	
	0,65	2,00E-04	2,49E-04	408,998	3,89
	0,325	1,99E-04	2,49E-04	399,202	2,40
	MESH [mm]	Z1 [mm]	Z2 [mm]	STIFFNESS [kN/mm]	ERROR %
ALONG Z	1,3	1,43E-04	1,78E-04	563,38	
	0,65	9,48E-05	1,18E-04	847,458	50,42
	0,325	9,21E-05	1,15E-04	869,565	2,61

Table 32: The table presents the displacement values along the three axes and the corresponding stiffness values calculated for each selected mesh size of Prototype 11. The last column shows the error in the stiffness calculation between each mesh and the subsequent one.

The results obtained from this sensitivity analysis show that convergence is reached, minimizing the discretization error, for mesh sizes of 0.25 mm for the mini endoprostheses, and for mesh sizes of 0.325 mm for the micro endoprostheses. For the tensile tests of all models, a mesh size of 0.25 mm was used for all the mini endoprostheses and 0.35 mm for all the micro endoprostheses, as these provided the best compromise between error reduction and computational cost.

MODEL 2

For the sensitivity test of Model 2, the mesh size was initially set to the height of the plate's thickness, progressively halving the value so that the meshes were self-contained. Therefore, the mesh values used for the mini-implants were: 2 mm, 1 mm, and 0.5 mm. The meshes used for the micro implants were: 1.3 mm, and 0.65 mm. Smaller meshes were not considered due to computational resource limitations.

The elastic moduli of the screws, bone specimens, and plate were kept constant, respectively, 110 GPa, 395.6 MPa, and for mini-implants 110 GPa, while for micro-implants, it was 105 GPa. Their Poisson's ratios were respectively 0.33, 0.30, and 0.33 for mini-implants, 0.33, 0.30, and 0.34 for micro implants.

In the tables, the data are summarized as follows: the first column indicates the reference axis along which the deformation was considered; the second column shows the mesh size expressed in mm; the third column presents the maximum deformation corresponding to the applied force of 80 N; the fourth column shows the maximum deformation corresponding to the applied force of 100 N; the sixth column indicates the stiffness calculated from the force-deformation graph using the forces of 80 N and 100 N with their respective deformation values; and finally, the last column reports the error between the stiffness of the considered mesh and that of the previous mesh. The deformations are given in mm, while the stiffness values are in N/mm.

PTOTOTYPE 1					
ALONG X	MESH [mm]	X1 [mm]	X2[mm]	STIFFNESS [N/mm]	ERROR %
	2	5,84E-02	7,30E-02	1369,9	
	1	5,23E-02	6,54E-02	1526,7	10,27
	0,5	4,75E-02	5,94E-02	1680,7	9,16
ALONG Y	MESH [mm]	Y1 [mm]	Y2[mm]	STIFFNESS [N/mm]	ERROR %
	2	4,37E-03	5,47E-03	18182	
	1	4,53E-03	5,67E-03	17544	3,64
	0,5	4,00E-03	5,01E-03	19802	11,40
ALONG Z	MESH [mm]	Z1 [mm]	Z2[mm]	STIFFNESS [N/mm]	ERROR %
	2	1,28E-02	1,60E-02	6172,8	
	1	1,21E-02	1,52E-02	6578,9	6,17
	0,5	1,20E-02	1,50E-02	6666,7	1,32

Table 33: The table presents for prototype 1 the displacement values obtained from the numerical tests along the axes, the respective associated stiffness values, the convergence error, the stiffness value calculated from the experimental tests, and the error of the numerical result compared to the experimental value.

PTOTOTYPE 2					
	MESH [mm]	X1 [mm]	X2[mm]	STIFFNESS [N/mm]	ERROR %
ALONG X	2	3,64E-02	4,54E-02	2222,2	
	1	3,76E-02	4,70E-02	2127,7	4,44
	0,5	3,77E-02	4,71E-02	2127,7	0,00
	MESH [mm]	Y1 [mm]	Y2[mm]	STIFFNESS [N/mm]	ERROR %
ALONG Y	2	2,56E-03	3,20E-03	31250	
	1	2,70E-03	3,38E-03	29412	6,25
	0,5	2,62E-03	3,26E-03	31250	5,88
	MESH [mm]	Z1 [mm]	Z2[mm]	STIFFNESS [N/mm]	ERROR %
ALONG Z	2	1,01E-02	1,26E-02	7936,5	
	1	1,04E-02	1,30E-02	7692,3	3,17
	0,5	1,05E-02	1,31E-02	7633,6	0,77

Table 34: The table presents for prototype 2 the displacement values obtained from the numerical tests along the axes, the respective associated stiffness values, the convergence error, the stiffness value calculated from the experimental tests, and the error of the numerical result compared to the experimental value.

PTOTOTYPE 3					
	MESH [mm]	X1 [mm]	X2[mm]	STIFFNESS [N/mm]	ERROR %
ALONG X	2	5,16E-02	6,45E-02	1550,4	
	1	5,17E-02	6,46E-02	1550,4	0,00
	0,5	4,86E-02	6,08E-02	1639,3	5,42
	MESH [mm]	Y1 [mm]	Y2[mm]	STIFFNESS [N/mm]	ERROR %
ALONG Y	2	3,14E-03	3,92E-03	25641	
	1	4,42E-03	5,52E-03	18182	41,02
	0,5	3,29E-03	4,11E-03	24390	25,45
	MESH [mm]	Z1 [mm]	Z2[mm]	STIFFNESS [N/mm]	ERROR %
ALONG Z	2	1,31E-02	1,64E-02	6079	
	1	1,52E-02	1,91E-02	5235,6	16,11
	0,5	1,34E-02	1,67E-02	6024,1	13,09

Table 35: The table presents for prototype 3 the displacement values obtained from the numerical tests along the axes, the respective associated stiffness values, the convergence error, the stiffness value calculated from the experimental tests, and the error of the numerical result compared to the experimental value.

PTOTOTYPE 4					
	MESH [mm]	X1 [mm]	X2[mm]	STIFFNESS [N/mm]	ERROR %
ALONG X	2	4,26E-02	5,32E-02	1886,8	
	1	3,65E-02	4,57E-02	2173,9	13,21
	0,5	3,94E-02	4,93E-02	2020,2	7,61
	MESH [mm]	Y1 [mm]	Y2[mm]	STIFFNESS [N/mm]	ERROR %
ALONG Y	2	2,23E-03	2,78E-03	36364	
	1	2,27E-03	2,70E-03	46512	21,82
	0,5	1,94E-03	2,42E-03	41580	11,86
	MESH [mm]	Z1 [mm]	Z2[mm]	STIFFNESS [N/mm]	ERROR %
ALONG Z	2	1,09E-02	1,36E-02	7352,9	
	1	1,05E-02	1,31E-02	7575,8	2,94
	0,5	1,12E-02	1,40E-02	7194,2	5,30

Table 36: The table presents for prototype 4 the displacement values obtained from the numerical tests along the axes, the respective associated stiffness values, the convergence error, the stiffness value calculated from the experimental tests, and the error of the numerical result compared to the experimental value.

PROTOTYPE 5					
	MESH [mm]	X1 [mm]	X2[mm]	STIFFNESS [N/mm]	ERROR %
ALONG X	1,3	6,28E-02	7,85E-02	1273,9	
	0,65	8,51E-02	1,06E-01	956,94	33,12
	MESH [mm]	Y1 [mm]	Y2[mm]	STIFFNESS [N/mm]	ERROR %
ALONG Y	1,3	5,83E-03	7,28E-03	13793	
	0,65	7,11E-03	8,89E-03	11236	22,76
	MESH [mm]	Z1 [mm]	Z2[mm]	STIFFNESS [N/mm]	ERROR %
ALONG Z	1,3	1,52E-02	1,90E-02	5277	
	0,65	1,72E-02	2,15E-02	4640,4	13,72

Table 37: The table presents for prototype 5 the displacement values obtained from the numerical tests along the axes, the respective associated stiffness values, the convergence error, the stiffness value calculated from the experimental tests, and the error of the numerical result compared to the experimental value.

PROTOTYPE 6					
	MESH [mm]	X1 [mm]	X2[mm]	STIFFNESS [N/mm]	ERROR %
ALONG X	1,3	6,14E-02	7,67E-02	1307,2	
	0,65	9,27E-02	1,16E-01	858,37	52,29
	MESH [mm]	Y1 [mm]	Y2[mm]	STIFFNESS [N/mm]	ERROR %
ALONG Y	1,3	8,14E-03	1,02E-02	9852,2	
	0,65	1,27E-02	1,59E-02	6309,1	56,16
	MESH [mm]	Z1 [mm]	Z2[mm]	STIFFNESS [N/mm]	ERROR %
ALONG Z	1,3	1,73E-02	2,16E-02	4728,1	
	0,65	1,93E-02	2,41E-02	4158	13,71

Table 38: The table presents for prototype 6 the displacement values obtained from the numerical tests along the axes, the respective associated stiffness values, the convergence error, the stiffness value calculated from the experimental tests, and the error of the numerical result compared to the experimental value.

PROTOTYPE 7					
	MESH [mm]	X1 [mm]	X2[mm]	STIFFNESS [N/mm]	ERROR %
ALONG X	1,3	6,36E-02	7,94E-02	1265,8	
	0,65	8,11E-02	1,01E-01	1005	25,95
	MESH [mm]	Y1 [mm]	Y2[mm]	STIFFNESS [N/mm]	ERROR %
ALONG Y	1,3	8,89E-03	1,11E-02	9049,8	
	0,65	1,07E-02	1,34E-02	7434,9	21,72
	MESH [mm]	Z1 [mm]	Z2[mm]	STIFFNESS [N/mm]	ERROR %
ALONG Z	1,3	1,75E-02	2,19E-02	4524,9	
	0,65	1,64E-02	2,05E-02	4830,9	6,33

Table 39: The table presents for prototype 7 the displacement values obtained from the numerical tests along the axes, the respective associated stiffness values, the convergence error, the stiffness value calculated from the experimental tests, and the error of the numerical result compared to the experimental value.

PROTOTYPE 8					
	MESH [mm]	X1 [mm]	X2[mm]	STIFFNESS [N/mm]	ERROR %
ALONG X	1,3	5,68E-02	7,10E-02	1408,5	
	0,65	8,02E-02	1,00E-01	1010,1	39,44
	MESH [mm]	Y1 [mm]	Y2[mm]	STIFFNESS [N/mm]	ERROR %
ALONG Y	1,3	5,52E-03	6,90E-03	14493	
	0,65	7,56E-03	9,44E-03	10638	36,24
	MESH [mm]	Z1 [mm]	Z2[mm]	STIFFNESS [N/mm]	ERROR %
ALONG Z	1,3	1,79E-02	2,24E-02	4424,8	
	0,65	1,72E-02	2,15E-02	4640,4	4,65

Table 40: The table presents for prototype 8 the displacement values obtained from the numerical tests along the axes, the respective associated stiffness values, the convergence error, the stiffness value calculated from the experimental tests, and the error of the numerical result compared to the experimental value.

PROTOTYPE 9					
	MESH [mm]	X1 [mm]	X2[mm]	STIFFNESS [N/mm]	ERROR %
ALONG X	1,3	6,46E-02	8,08E-02	1234,6	
	0,65	7,82E-02	9,78E-02	1020,4	20,99
	MESH [mm]	Y1 [mm]	Y2[mm]	STIFFNESS [N/mm]	ERROR %
ALONG Y	1,3	8,73E-03	1,09E-02	9132,4	
	0,65	1,01E-02	1,26E-02	8000	14,16
	MESH [mm]	Z1 [mm]	Z2[mm]	STIFFNESS [N/mm]	ERROR %
ALONG Z	1,3	1,72E-02	2,15E-02	4683,8	
	0,65	1,78E-02	2,22E-02	4555,8	2,81

Table 41: The table presents for prototype 9 the displacement values obtained from the numerical tests along the axes, the respective associated stiffness values, the convergence error, the stiffness value calculated from the experimental tests, and the error of the numerical result compared to the experimental value.

PROTOTYPE 10					
	MESH [mm]	X1 [mm]	X2[mm]	STIFFNESS [N/mm]	ERROR %
ALONG X	1,3	6,62E-02	8,27E-02	1212,1	
	0,65	7,20E-02	9,00E-02	1111,1	9,09
	MESH [mm]	Y1 [mm]	Y2[mm]	STIFFNESS [N/mm]	ERROR %
ALONG Y	1,3	5,32E-03	6,65E-03	15038	
	0,65	5,47E-03	6,83E-03	14706	2,26
	MESH [mm]	Z1 [mm]	Z2[mm]	STIFFNESS [N/mm]	ERROR %
ALONG Z	1,3	1,73E-02	2,15E-02	4662	
	0,65	1,71E-02	2,13E-02	4694,8	0,70

Table 42: The table presents for prototype 10 the displacement values obtained from the numerical tests along the axes, the respective associated stiffness values, the convergence error, the stiffness value calculated from the experimental tests, and the error of the numerical result compared to the experimental value.

PROTOTYPE 11					
	MESH [mm]	X1 [mm]	X2[mm]	STIFFNESS [N/mm]	ERROR %
ALONG X	1,3	5,35E-02	6,68E-02	1503,8	
	0,65	6,48E-02	8,10E-02	1234,6	21,80
	MESH [mm]	Y1 [mm]	Y2[mm]	STIFFNESS [N/mm]	ERROR %
ALONG Y	1,3	3,38E-03	4,23E-03	23529	
	0,65	4,46E-03	5,58E-03	17857	31,76
	MESH [mm]	Z1 [mm]	Z2[mm]	STIFFNESS [N/mm]	ERROR %
ALONG Z	1,3	1,31E-02	1,64E-02	6079	
	0,65	1,54E-02	1,94E-02	5063,3	20,06

Table 43: The table presents for prototype 11 the displacement values obtained from the numerical tests along the axes, the respective associated stiffness values, the convergence error, the stiffness value calculated from the experimental tests, and the error of the numerical result compared to the experimental value.

For this model, we can see that all the prototypes belonging to the micro-prosthesis group, i.e., prototypes 5 to 11, achieve convergence. However, the convergence error is still significant, and better computational resources would be needed to perform analyses with smaller meshes and achieve better convergence. On the other hand, for the prototypes belonging to the mini-prosthesis group, i.e., prototypes 1 to 4, it can be seen that convergence is not achieved only by prototype 3, while the other prototypes do achieve it. However, even for these prototypes, better computational resources would be required to perform analyses with smaller meshes and achieve better convergence.

Once the optimal mesh size was found to achieve convergence of the finite element model, another sensitivity analysis was performed, where the elastic modulus of the bone-like material was varied to make the model as close to reality as possible. Since the bone-like material specimen was made of two different materials, an overall elastic modulus for the entire volume of the specimen was calculated by performing a weighted average between the elastic moduli of the two materials used in the bone-like specimen.

This sensitivity analysis was conducted for two specimens, prototype numbers 5 and 7, and the data are summarized in *Table 44* and *Table 45*. The data are summarized in the following way: the first column indicates the value of the elastic modulus of the bone-like material specimen (in MPa), the second column shows the maximum deformation along the x-axis corresponding to the applied force of 80 N (in mm), the third column shows the maximum deformation along the x-axis corresponding to the applied force of 100 N (in mm), the fourth column shows the stiffness calculated from the force-deformation graph using the forces of 80 N and 100 N with their respective deformation values (in N/mm), the fifth column shows the experimental stiffness obtained from the force-deformation graph derived from the laboratory test (in N/mm), and finally, the last column shows the percentage error between the numerically obtained stiffness and the experimentally obtained stiffness.

ELASTIC MODULUS [Mpa]	X1 [mm]	X2 [mm]	NUMERICAL STIFNESS [N/mm]	SPERIMENTAL STIFNESS [N/mm]	ERROR %
561,6	8,51E-02	1,06E-01	956,94	639,68	49,60
432,2	1,06E-01	1,33E-01	740,74	639,68	15,80
406,3	1,12E-01	1,40E-01	714,29	639,68	11,66
393,5	1,15E-01	1,44E-01	689,66	639,68	7,81

Table 44: The table presents for prototype 5 the value of the elastic modulus, the displacement values obtained from the numerical tests along the x-axis, the respective associated stiffness values, the stiffness value calculated from the experimental tests, and the error of the numerical result compared to the experimental value.

ELASTIC MODULUS [Mpa]	X1 [mm]	X2 [mm]	NUMERICAL STIFNESS [N/mm]	SPERIMENTAL STIFNESS [N/mm]	ERROR %
561,6	8,11E-02	1,01E-01	1005	737,16	36,33
432,2	9,96E-02	1,24E-01	819,67	737,16	11,19
406,3	1,05E-01	1,31E-01	769,23	737,16	4,35
393,5	1,07E-01	1,34E-01	740,74	737,16	0,49

Table 45: The table presents for prototype 5 the value of the elastic modulus, the displacement values obtained from the numerical tests along the x-axis, the respective associated stiffness values, the stiffness value calculated from the experimental tests, and the error of the numerical result compared to the experimental value.

As we can see from the data in the tables, the best value for the elastic modulus is 393.5 MPa.

CONCLUSION

After an introductory chapter that provides a detailed analysis of the state of the art regarding canine endoprostheses designed to replace a missing part of the radius bone in a dog's forelimb—due to a specific bone tumor, osteosarcoma—and after examining the biomechanics of canine gait in Chapter 1, the core of this thesis is introduced.

In Chapter 2, numerical simulations were conducted and analyzed. Starting with 11 prototype canine endoprostheses, used for fracture fixation, the models of the prosthetic components—plate and screws—were designed using the CAD software SolidWorks. Initially, a simplified model representing only the prosthesis, including the plate and screws (Model 1), was created. Subsequently, a second model of the prosthesis fixed to the bone (Model 2) was developed, where the bone was modeled based on the prototype provided for experimental testing. A static structural analysis was performed on both models using ANSYS APDL, subjecting them to a pure tensile load, and the corresponding force-deformation graph was obtained. The force values applied in these tests were derived from experimental data. During tensile testing, the prostheses initially exhibited elastic behavior before undergoing plastic deformation. The forces used in the numerical simulations to generate the force-deformation graph correspond to the elastic behavior region observed in the experimental tests.

Chapter 3 provides a detailed analysis of the experimental tests. After describing the setup of the tensile tests conducted using a dedicated testing machine, the force-displacement graphs obtained from these experiments were analyzed. For each model, the respective graph was generated, and the meaning of the obtained results was explained. Special attention was given to both the elastic behavior of the model and the forces that led to failure, highlighting the fracture point of the prosthesis-bone assembly (where applicable) or the point of plastic deformation of the prosthesis.

Finally, in Chapter 4, sensitivity analyses were conducted for both Model 1 and Model 2**.** For Model 1, five samples were chosen for the sensitivity analysis, while for Model 2, the analysis was performed for each individual model. The purpose of the sensitivity analysis is to evaluate the numerical error caused by the discretization of the geometry volume. Specifically, it assesses how the model's stiffness changes as the mesh size varies. The goal was to select the optimal mesh value to then compare it with the experimental data. For Model 2, a second sensitivity analysis was conducted to determine the optimal value of the elastic modulus for the bone-like material specimen. In this analysis, the best mesh, identified in the previous sensitivity study, was used, and the elastic modulus of the bone was varied to achieve convergence with the experimentally obtained stiffness value.

Finally, the results obtained from numerical simulations were compared with the results of the experimental tests to validate the numerical model used. The comparison showed that for those prototypes that did not undergo slipping or rotation during the tensile test in the laboratory, the numerical stiffness was comparable to the experimental stiffness. For the prototypes that experienced rotation of the specimen during the tensile test, another FEM model was created to obtain a better comparison. In this new model, in addition to the tensile force, a rotation of the bone specimen being tested was also applied, and it was observed that the stiffness of the prototype calculated with this new model was much closer to the experimental stiffness compared to the numerical stiffness calculated using only the tensile test. Finally, for the prototypes that underwent slipping and thread stripping of the screw during the laboratory tests, the numerical stiffness was much higher than the experimental stiffness, because slipping and thread stripping drastically reduce the stiffness of the specimen.

Regarding future work, the design of this model could be improved by incorporating a rocker washer, which was not included in this study, to achieve a more realistic interaction between the screws and the plate. Additionally, future studies could conduct numerical simulations using finer mesh sizes, which were not feasible due to the limitations of the available computational resources. Finally, the model could also be employed to analyze forces not considered in this study, such as compressive, bending, and torsional forces.

REFERENCES

[1] TUMORS OF THE SKELETAL SYSTEM *William S. Dernell, Nicole P. Ehrhart, Rodney C. Straw, and David M. Vail* 2012

[2] DOG BREEDS AND CONFORMATIONS PREDISPODES TO OSTEOSARCOMA IN THE UK: A VETCOMPASS STUDY *Dan G. O'Neill, Grace L. Edmund, Jade Urquhart-Gilmore, David B. Church, Lynda Rutherford, Matthew J. Smalley, Dave C. Brodbelt* 2023

[3] DEMOGRAPHIC CHAR- ACTERISTICS, SITE AND PHYLOGENETIC DISTRIBUTION OF DOGS WITH APPENDICULAR OSTEOSARCOMA: 744 DOGS (2000–2015) *Tuohy JL, Shaevitz MH, Garrett LD, Ruple A, Selmic LE* 2019

[4] CANINE AXIAL SKELETAL OSTEOSARCOMA A RETROSPECTIVE STUDY OF 116 CASES (1986–1989) *Heyman SJ, Diefenderfer DL, Goldschmidt MH et al.*, 1992.

[5] CANINE OSTEOSARCOMA: 1462 CASES REVIEWED TO UNCOVER PATTERNS OF HEIGHT, WEIGHT, BREED, SEX, AGE AND SITE INVOLVEMENT *Kistler KR,* 1981.

[6] THE ANIMAL-DEPENDENT RISK FACTORS IN CANINE OSTEOSARCOMAS *Sapierzynski R, Czopowicz M* 2017

[7] OCCURRENCE OF THE MOST COMMON TUMOUR DIAGNOSES AND INFLUENCE OF AGE, BREED, BODY SIZE, SEX AND NEUTERING STATUS ON TUMOUR DEVELOPMENT *Gruntzig K, Graf R, Boo G, Guscetti F, Hassig M, Axhausen KW, et al.* 2016

[8] CHARACTERIZATION OF THE BIOLOGICAL BEHAVIOUR OF APPENDICULAR OSTEOSARCOMA IN ROTTWEILERS AND A COMPARISON WITH OTHER BREEDS: A REVIEW OF 258 DOGS *McNeill CJ, Overley B, Shofer FS, Kent MS, Clifford CA, Samluk M, et al.* 2007

[9] WHAT DO WE KNOW ABOUT CANINE OSTEOSARCOMA TREATMENT? – REVIEW *M. Szewczyk & R. Lechowski & K. Zabielska* 2015

[10] OUTCOME AND PROGNOSIS FOR CANINE APPENDICULAR OSTEOSARCOMA TREATED WITH STEREOTACTIC BODY RADIATION THERAPY IN 123 DOGS *Tiffany Wormhoudt Martin, Lynn Griffin, James Custis, Stewart D. Ryan, Mary Lafferty, Mary-Keara Boss, Daniel Regan, Sangeeta Rao, Del Leary, Stephen J. Withrow, Susan M. LaRue* 2020

[11] RADIATION-INDUCED CHANGES TO BONE COMPOSITION EXTEND BEYOND PERIOSTEAL *BONE Gurjit S. Mandaira , Megan E. Oestb , Kenneth A. Mannb , Michael D. Morrisc , Timothy A. Damronb , David H. Kohn* 2020

[12] CARBOPLATIN VERSUS ALTERNATING CARBOPLATIN AND DOXORUBICIN FOR THE ADJUVANT TREATMENT OF CANINE APPENDICULAR OSTEOSARCOMA: A RANDOMIZED, PHASE III TRIAL. Skorupski KA, Uhl JM, Szivek A, Allstadt Frazier SD, Rebhun RB, Rodriguez CO 2016

[13] STEREOTACTIC RADIO-SURGERY FOR TREATMENT OF OSTEOSARCOMAS INVOLVING THE DISTAL PORTIONS OF THE LIMBS IN DOGS *Farese JP, Milner R, Thompson MS et al*, 2004.

[14] HIGH-DOSE SAMARIUM-153 ETHYLENE DIAMINE TETRAMETHYLENE PHOSPHONATE: LOW TOXICITY OF SKELETAL IRRADIATION IN PATIENTS WITH OSTEOSARCOMA AND BONE METASTASES *Anderson PM, Wiseman GA, Dispenzieri A et al*, 2002

[15] OSTEOGENIC SARCOMA AND CISPLATIN CHEMOTHERAPY IN DOGS: 16 CASES (1986–1989) *Kraegel SA, Madewell BR, Simonson E, Gregory CR* 1991

[16] AMPUTATION AND CISPLATIN FOR TREATMENT OF CANINE OSTEOSARCOMA *Straw RC, Withrow SJ, Richter SL et al,* 1991

[17] USE OF SINGLE-AGENT CARBOPLATIN AS ADJUVANT OR NEOADJUVANT THERAPY IN CONJUNCTION WITH AMPUTATION FOR APPENDICULAR OSTEOSARCOMA IN DOGS *Phillips B, Powers BE, Dernell WS et al,* 2009

[18] RESULTS OF SURGERY AND DOXORUBICIN CHEMOTHERAPY IN DOGS WITH OSTEOSARCOMA *Berg J, Weinstein MJ, Springfield DS et al,* 1995

[19] HYPERTHERMIC ISOLATED REGIONAL PERFUSION WITH CISPLATIN IN THE LOCAL TREATMENT OF SPONTANEOUS CANINE OSTEOSARCOMA: ASSESSMENT OF SHORT-TERM EFFECTS *Van Ginkel RJ, Hoekstra HJ, Meutstege FJ et al*, 1995.

[20] INTERCALARY BONE GRAFTS FOR JOINT AND LIMB PRESERVATION IN 17 DOGS WITH HIGH GRADE MALIGNANT TUMORS OF THE DIAPHYSIS *Liptak JM, Dernell WS, Straw RC et al*, 2004

[21] BONE ALLOGRAFTS AND ADJUVANT CISPLATIN FOR THE TREATMENT OF CANINE APPENDICULAR OSTEOSARCOMA IN 18 DOGS *Morello E, Buracco P, Martano M et al*, 2001.

[22] CORTICAL ALLOGRAFT AND ENDOPROSTHESIS FOR LIMB-SPARING SURGERY IN DOGS WITH DISTAL RADIAL OSTEOSARCOMA: A PROSPECTIVE CLINICAL COMPARISON OF TWO DIFFERENT LIMB-SPARING TECHNIQUES *Julius M. Liptak, William S. Dernell, Nicole Ehrhart, Mary H. Lafferty, Gabrielle J. Monteith, Stephen J. Withrow* 2006

[23] LONG-TERM OUTCOME OF DOGS TREATED WITH ULNAR ROLLOVER TRANSPOSITION FOR LIMB-SPARING OF DISTAL RADIAL OSTEOSARCOMA: 27 LIMBS IN 26 DOGS *Bernard Seguin, Matthew D. O'Donnell, Peter J. Walsh, Laura E. Selmic* 2017

[24] DEVELOPMENT AND EXPERIMENTAL EVALUATION OF A NOVEL, PATIENT SPECIFIC IMPLANT FOR LIMB SPARING SURGERY *Timothy Joseph Horn* 2014

[25] LONGITUDINAL BONE TRANSPORT FOR TREATMENT OF PRIMARY BONE TUMORS IN DOGS: TECHNIQUE DESCRIPTION AND OUTCOME IN 9 DOGS *Ehrhart N*, 2005.

[26] BONE TRANSPORT OSTEOGENESIS FOR LIMB SALVAGE FOLLOWING RESECTION OF PRIMARY BONE TUMORS: EXPERIENCE WITH 6 CASES (1991–1996*) Tommassini M, Ehrhart N, Ferretti A et al,* 2000.

[27] USE OF AN IPSILATERAL VASCULARIZED ULNAR TRANSPOSITION AUTOGRAFT FOR LIMB-SPARING SURGERY OF THE DISTAL RADIUS IN DOGS: AN ANATOMIC AND CLINICAL STUDY *Bernard Seguin, Peter J. Walsh, David R. Mason, Erik R. Wisner, Jessica L. Parmenter, William S. Dernell* 2003

[28] OUTCOMES OF LIMB-SPARING SURGERY USING TWO GENERATIONS OF METAL ENDOPROSTHESIS IN 45 DOGS WITH DISTAL RADIAL OSTEOSARCOMA. A VETERINARY SOCIETY OF SURGICAL ONCOLOGY RETROSPECTIVE STUDY *Katherine E. Mitchell1 , Sarah E. Boston2 , Marvin Kung3 , Sarah Dry4 , Rod C. Straw3 , Nicole P. Ehrhart5 , and Stewart D. Ryan* 2016

[29] CLINICAL OUTCOMES OF PATIENT-SPECIFIC POROUS TITANIUM ENDOPROSTHESES IN DOGS WITH TUMORS OF THE MANDIBLE, RADIUS, OR TIBIA: 12 CASES (2013–2016) *Jonathan P. Bray, Andrew Kersley, Warwick Downing, Katherine R. Crosse, Andrew J. Worth, Arthur K. House, Guy Yates, Alastair R. Coomer, Ian W. M. Brown* 2017

[30] PERSONALIZED 3D-PRINTED ENDOPROSTHESES FOR LIMB SPARING IN DOGS: MODELING AND IN VITRO TESTING *Anatolie Timercan, Vladimir Brailovski, Yvan Petit, Bertrand Lussier, Bernard Séguin* 2019

[31] LIMB-SPARING IN DOGS USING PATIENT-SPECIFIC, THREE-DIMENSIONAL-PRINTED ENDOPROSTHESIS FOR DISTAL RADIAL OSTEOSARCOMA: A PILOT STUDY *Bernard Séguin, Chris Pinard, Bertrand Lussier, Deanna William, Lynn Griffin, Brendan Podell, Sebastian Mejia, Anatolie Timercan, Yvan Petit, Vladimir Brailovski* 2020

[32] DEVELOPMENT OF A NOVEL ENDOPROSTHESIS FOR CANINE LIMB-SPARING USING A FINITE ELEMENT APROACH *James S.P., Santoni B.G., Heyliger P.R.* 2010

[33] IN VITRO FORCE MAPPING OF NORMAL CANINE HUMERORADIAL AND HUMEROULNAR *Joints Mason, D.R.*, et al., 2005

[34] CANINE ANATOMY A SYSTEMIC STUDY. 4TH ED. *Adams, D.R.,* 2004

[35] DETAILED ANATOMY OF THE ANTEBRACHIOCARPAL JOINT IN DOGS *Mikic, Z.D., G. Ercegan, And T. Somer*, 1992

[36] MILLER'S ANATOMY OF THE DOG *Evans, H.E. And M.E. Miller,. 3rd Ed*. 1993

[37] MAGNETIC RESONANCE IMAGING OF NORMAL CANINE CARPAL LIGAMENTS *Nordberg, C.C. And K.A. Johnson,* 1999

[38] COMPUTED TOMOGRAPHY AND MORPHOMETRY OF THE CARPAL CANAL IN THE DOG *Turan, E. And H. Erden,* 2003

[39] ARTHROSCOPY OF THE ANTEBRACHIOCARPAL JOINT IN DOGS *Warnock, J.J. And B.S. Beale. J* 2004.

[40] REVIEW OF KINEMATIC ANALYSIS IN DOGS *Gabriella S. Sandberg, Bryan T. Torres, Steven C. Budsberg*, 2020

[41] KINETIC AND KINEMATIC GAIT ANALYSIS IN DOGS *Ron M. McLaughlin*, 2001

[42] RECENT DEVELOPMENTS IN CANINE LOCOMOTOR ANALYSIS: A REVIEW *Robert L. Gillette, T. Craig Angl* 2008

[43] RELIABILITY OF GROUND REACTION FORCES MEASURED ON A TREADMILL SYSTEM IN HEALTHY DOGS *Barbara A. Bockstahler, Monika Skalicky, Christian Peham, Marion Muller, Dragan Lorinson* 2007

[44] COMPARISON OF THE TROTTING GAITS OF LABRADOR RETRIEVERS AND GREYHOUNDS *Bertram, J.E., Lee, D.V., Case, H.N., Todhunter, R.J.,* 2000

[45] TWO-DIMENSIONAL LINK-SEGMENT MODEL OF THE FORELIMB OF DOGS AT A WALK *Cheri Nielsen, Susan M. Stover, Kurt S. Schulz, Mont Hubbard, David A. Hawkins*, 2003

[46] KINEMATIC GAIT ANALYSES IN HEALTHY GOLDEN RETRIEVERS *Gabriela C.A. Silva , Mariana Trés Cardoso, Thais P. Gaiad, Marina P. Brolio, Vanessa C. Oliveira, Antonio Assis Neto, Daniele S. Martins and Carlos E. Ambrósio* 2014

APPENDIX

In the following figures, the results of the tensile analysis for Model 1 related to Von Mises stresses are presented. For each prototype, the stress distribution in the specimen can be observed during both tensile tests performed, first with an applied force of 80 N and then with a force of 100 N. The numerical results shown in the figures are expressed in Pascals (Pa).

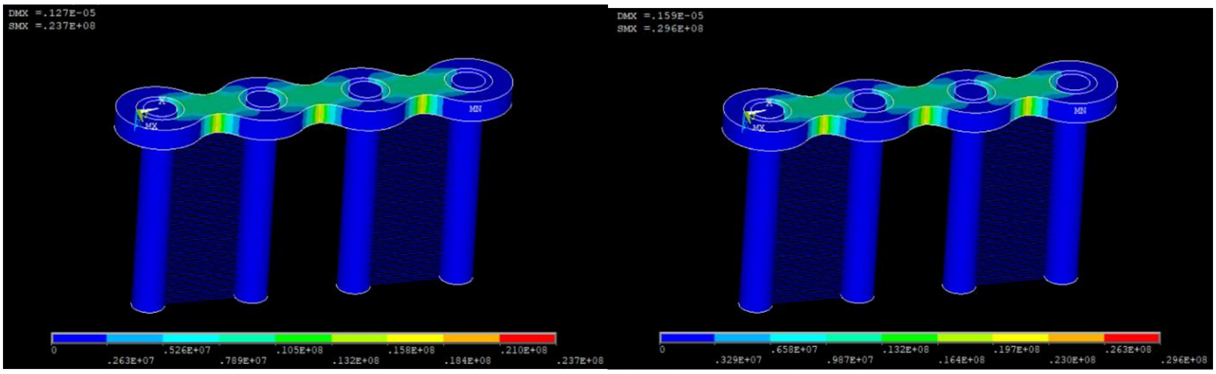

Figure 131: Prototype 1. In this image, the Von Mises stresses resulting from the tensile analysis with a force of 80 N are shown on the right, while on the left, the stresses after the tensile analysis with a force of 100 N are displayed.

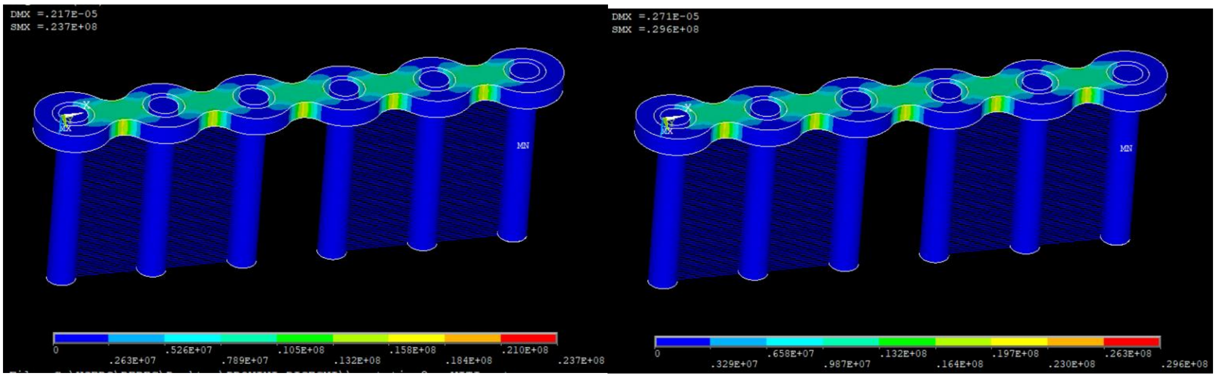

Figure 132: Prototype 2. In this image, the Von Mises stresses resulting from the tensile analysis with a force of 80 N are shown on the right, while on the left, the stresses after the tensile analysis with a force of 100 N are displayed.

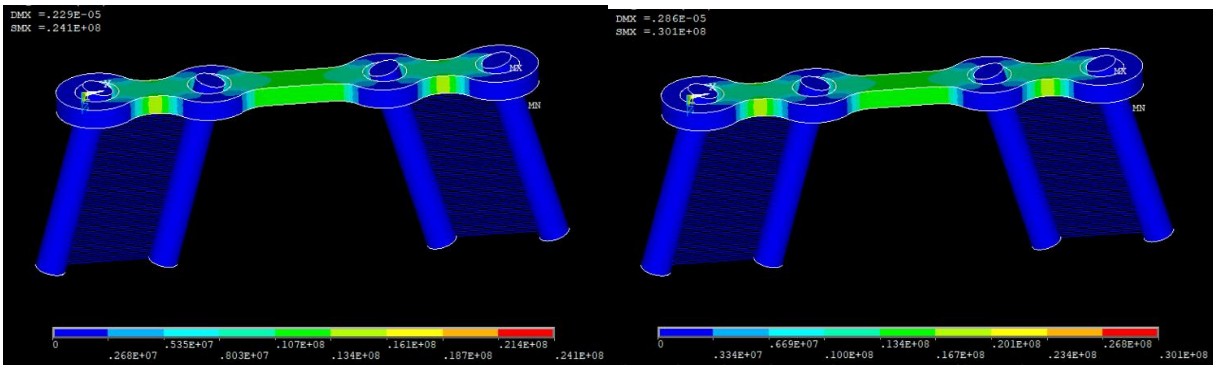

Figure 133: Prototype 3. In this image, the Von Mises stresses resulting from the tensile analysis with a force of 80 N are shown on the right, while on the left, the stresses after the tensile analysis with a force of 100 N are displayed.

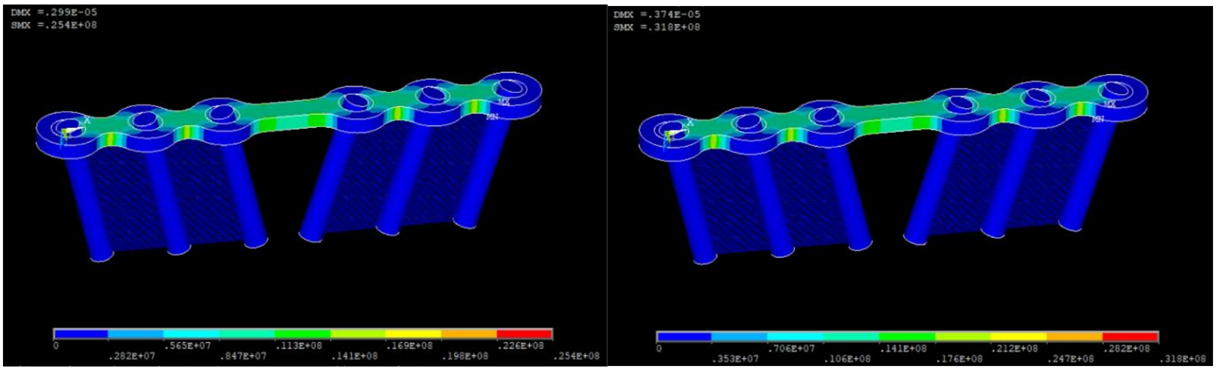

Figure 134: Prototype 4. In this image, the Von Mises stresses resulting from the tensile analysis with a force of 80 N are shown on the right, while on the left, the stresses after the tensile analysis with a force of 100 N are displayed.

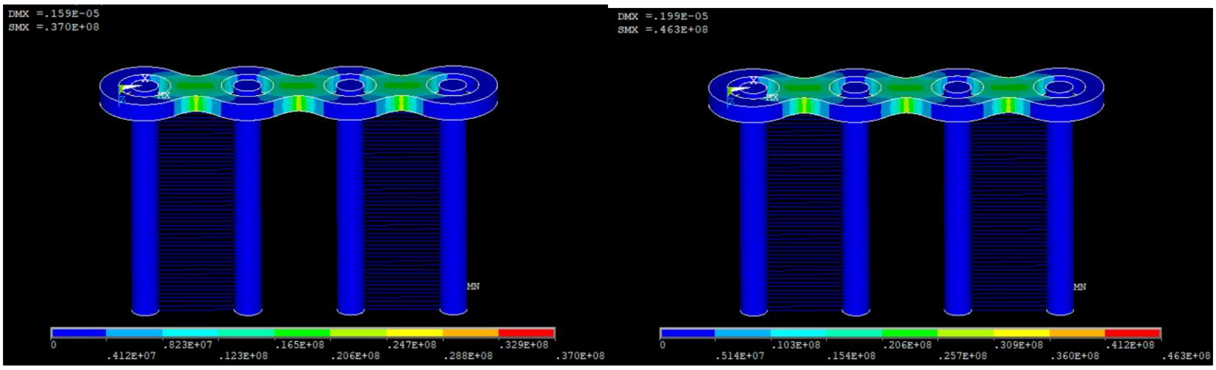

Figure 135: Prototype 5. In this image, the Von Mises stresses resulting from the tensile analysis with a force of 80 N are shown on the right, while on the left, the stresses after the tensile analysis with a force of 100 N are displayed.

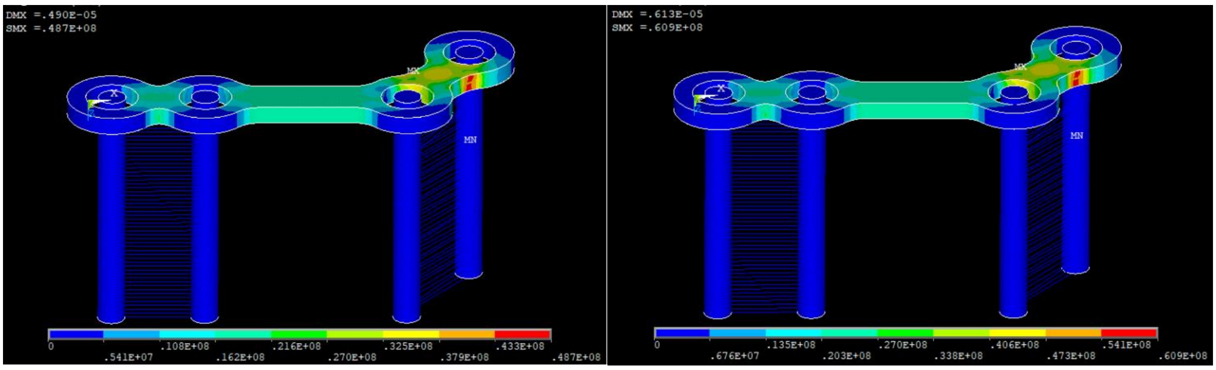

Figure 136: Prototype 6. In this image, the Von Mises stresses resulting from the tensile analysis with a force of 80 N are shown on the right, while on the left, the stresses after the tensile analysis with a force of 100 N are displayed.

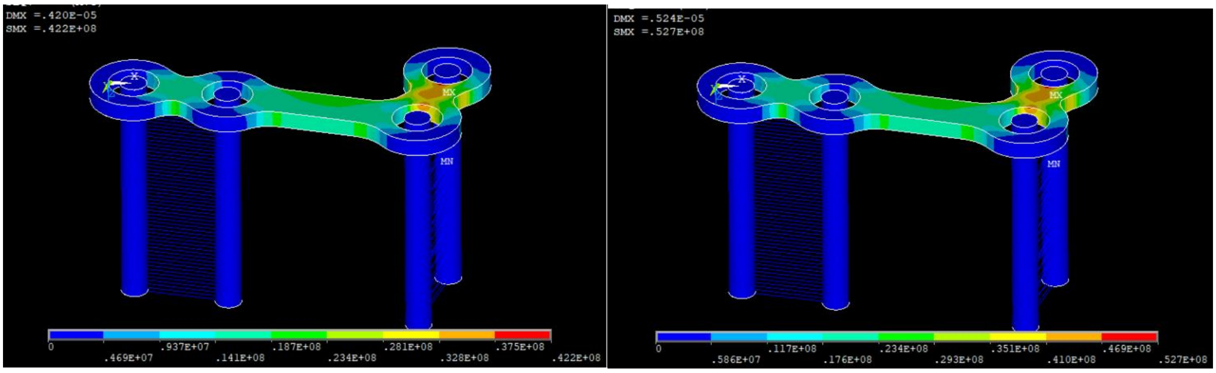

Figure 137: Prototype 7. In this image, the Von Mises stresses resulting from the tensile analysis with a force of 80 N are shown on the right, while on the left, the stresses after the tensile analysis with a force of 100 N are displayed.

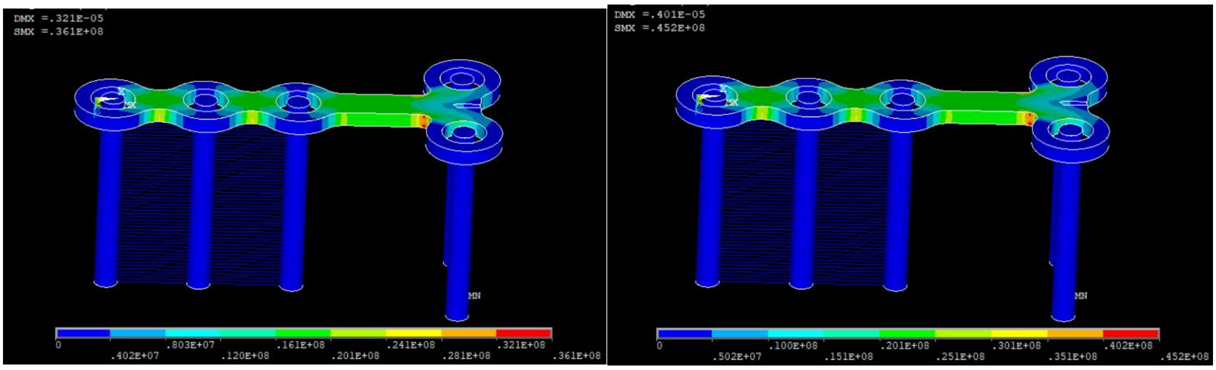

Figure 138: Prototype 8. In this image, the Von Mises stresses resulting from the tensile analysis with a force of 80 N are shown on the right, while on the left, the stresses after the tensile analysis with a force of 100 N are displayed.

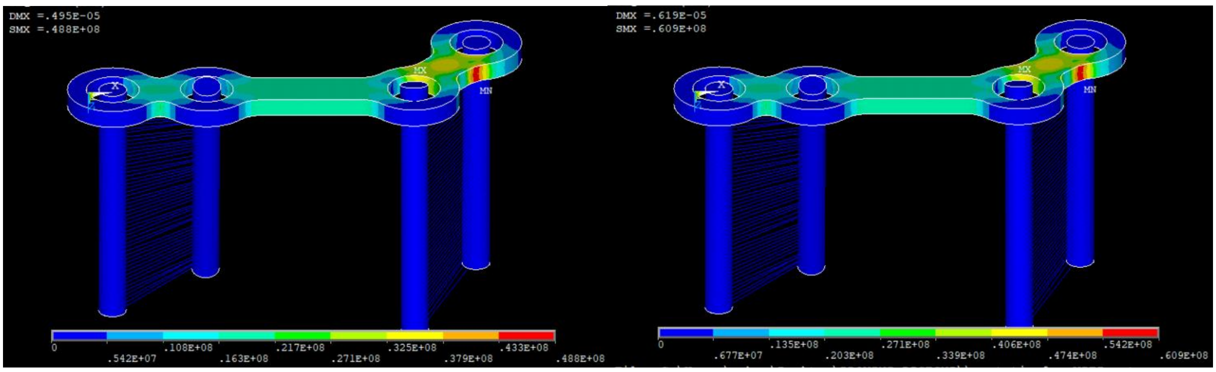

Figure 139: Prototype 9. In this image, the Von Mises stresses resulting from the tensile analysis with a force of 80 N are shown on the right, while on the left, the stresses after the tensile analysis with a force of 100 N are displayed.

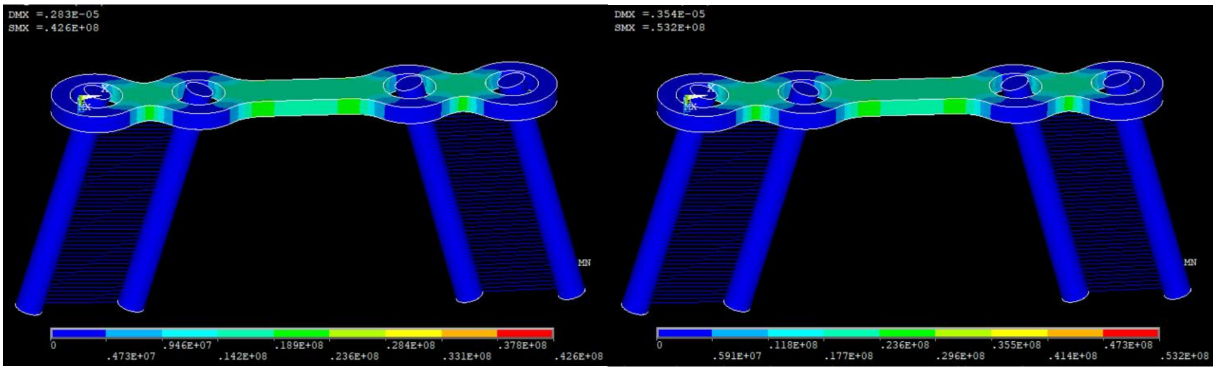

Figure 140: Prototype 10. In this image, the Von Mises stresses resulting from the tensile analysis with a force of 80 N are shown on the right, while on the left, the stresses after the tensile analysis with a force of 100 N are displayed.

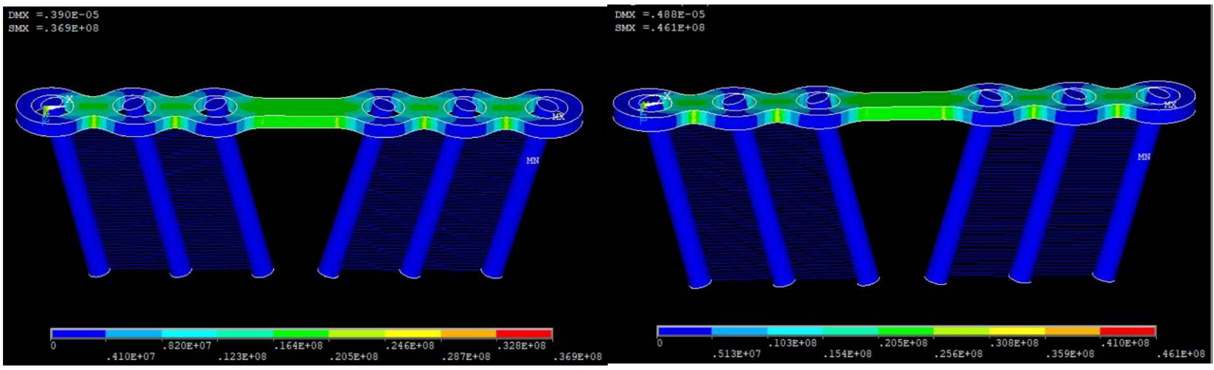

Figure 141: Prototype 11. In this image, the Von Mises stresses resulting from the tensile analysis with a force of 80 N are shown on the right, while on the left, the stresses after the tensile analysis with a force of 100 N are displayed.

In the following figures, the results of the tensile analysis for Model 2 related to Von Mises stresses are presented. For each prototype, the stress distribution in the specimen as a whole and its components can be observed for the tensile test performed with a force of 100 N. The numerical results shown in the figures are expressed in Pascals (Pa).

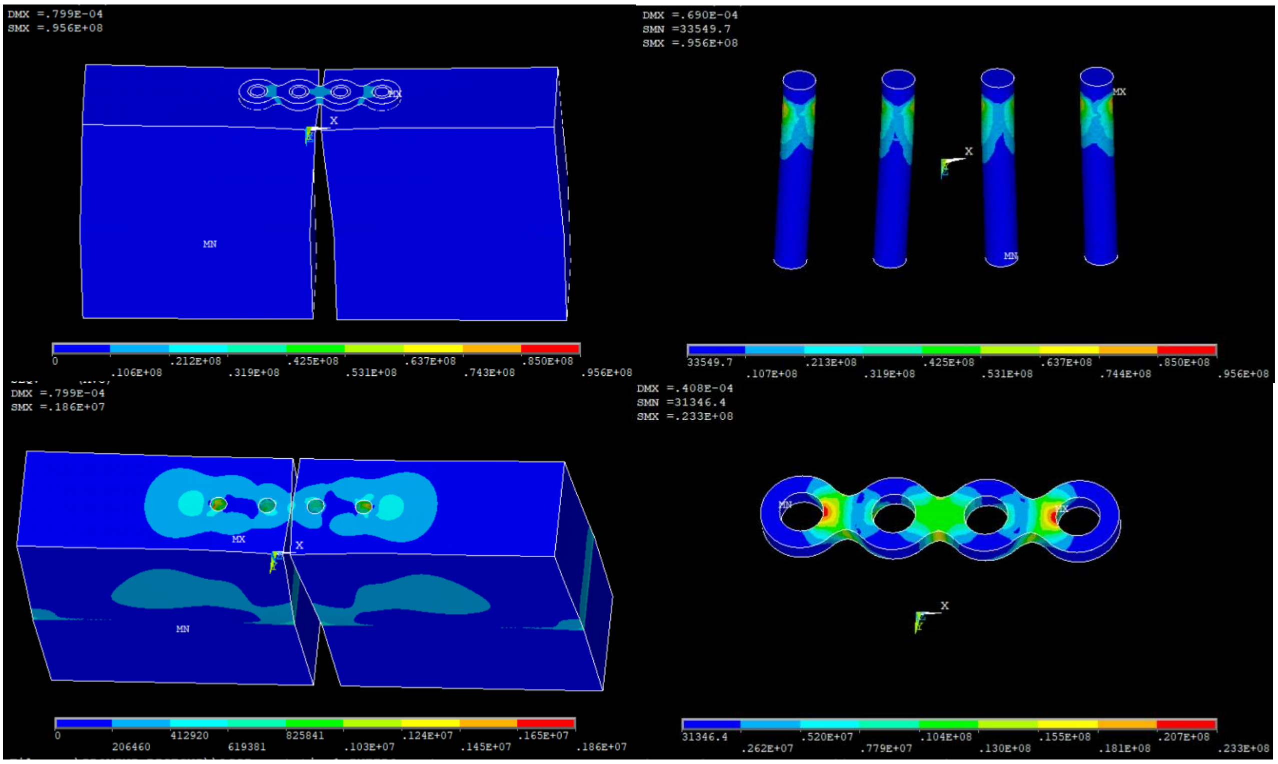

Figure 142: Prototype 1. In this image, the Von Mises stresses resulting from the tensile analysis of the entire specimen are shown in the upper right, while in the upper left, the Von Mises stresses developing along the screws are displayed. The lower right part shows the stresses along the bone specimen, and finally, the lower left part presents the stresses along the prosthetic plate.

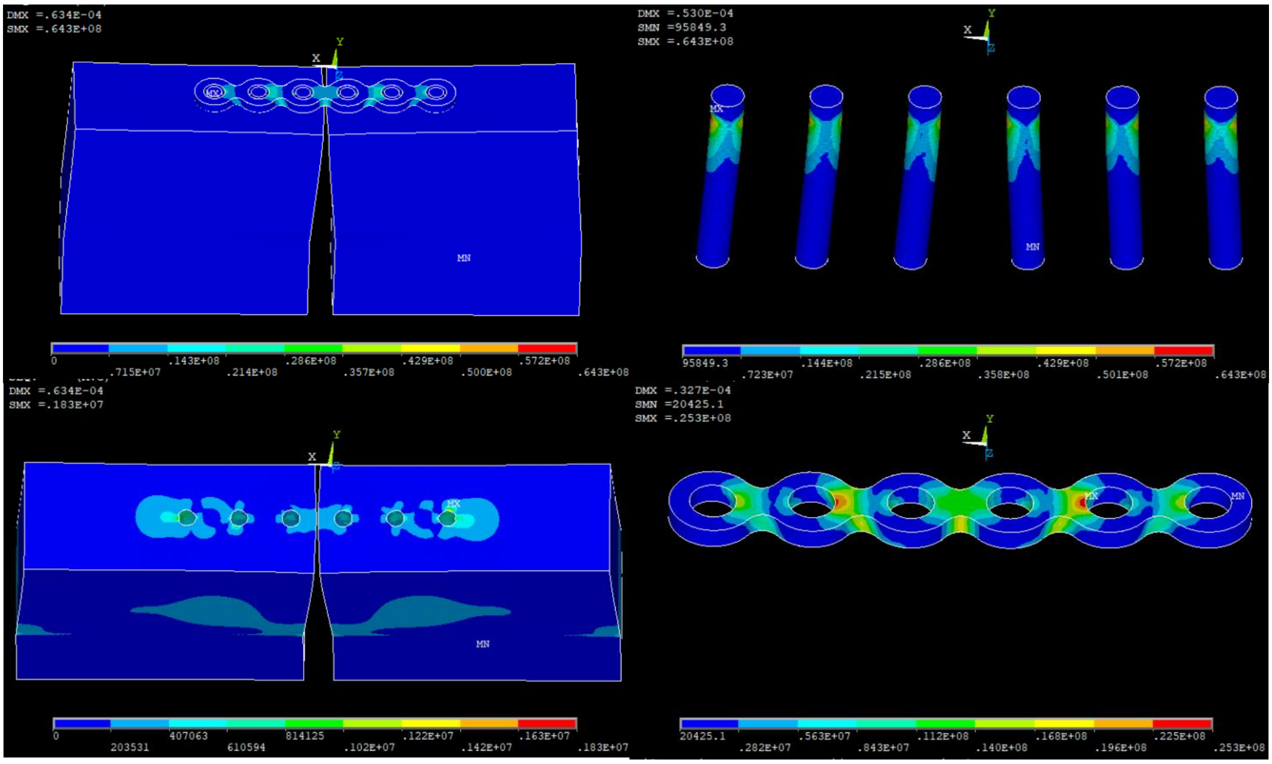

Figure 143: Prototype 2. In this image, the Von Mises stresses resulting from the tensile analysis of the entire specimen are shown in the upper right, while in the upper left, the Von Mises stresses developing along the screws are displayed. The lower right part shows the stresses along the bone specimen, and finally, the lower left part presents the stresses along the prosthetic plate.

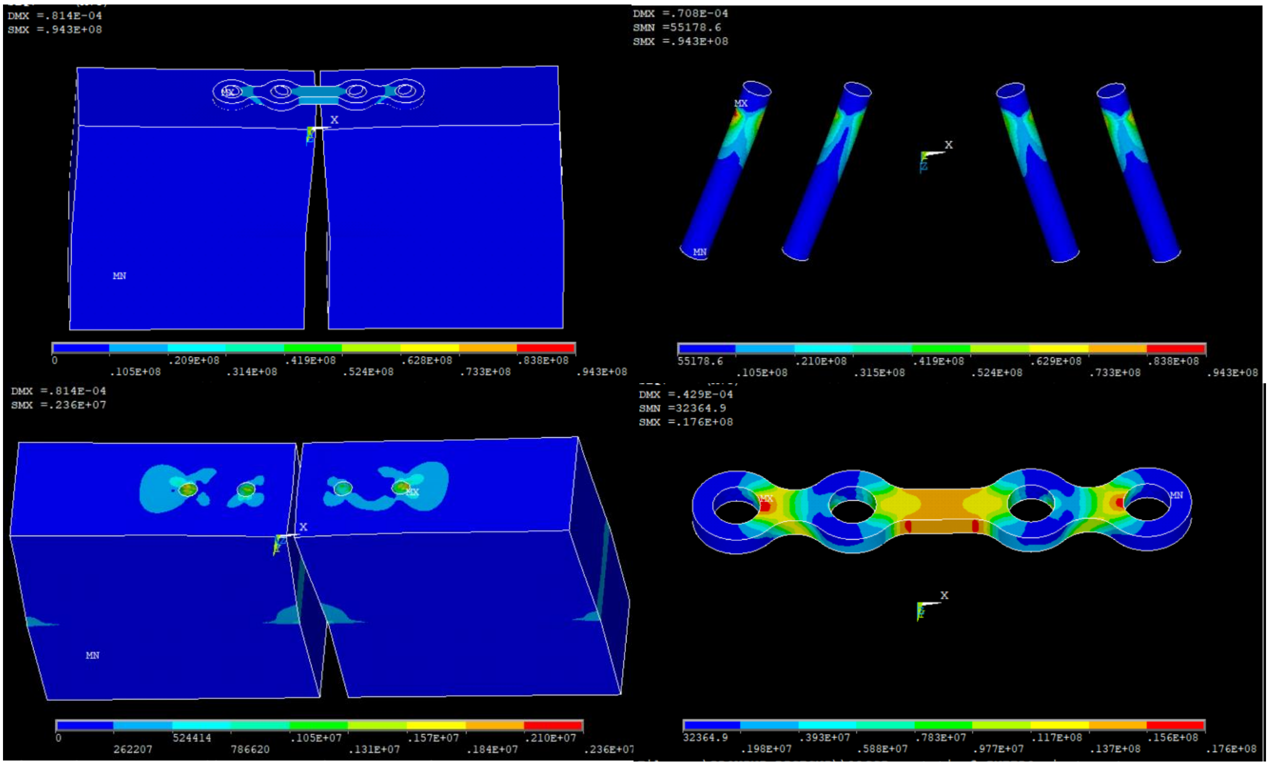

Figure 144: Prototype 3. In this image, the Von Mises stresses resulting from the tensile analysis of the entire specimen are shown in the upper right, while in the upper left, the Von Mises stresses developing along the screws are displayed. The lower right part shows the stresses along the bone specimen, and finally, the lower left part presents the stresses along the prosthetic plate.

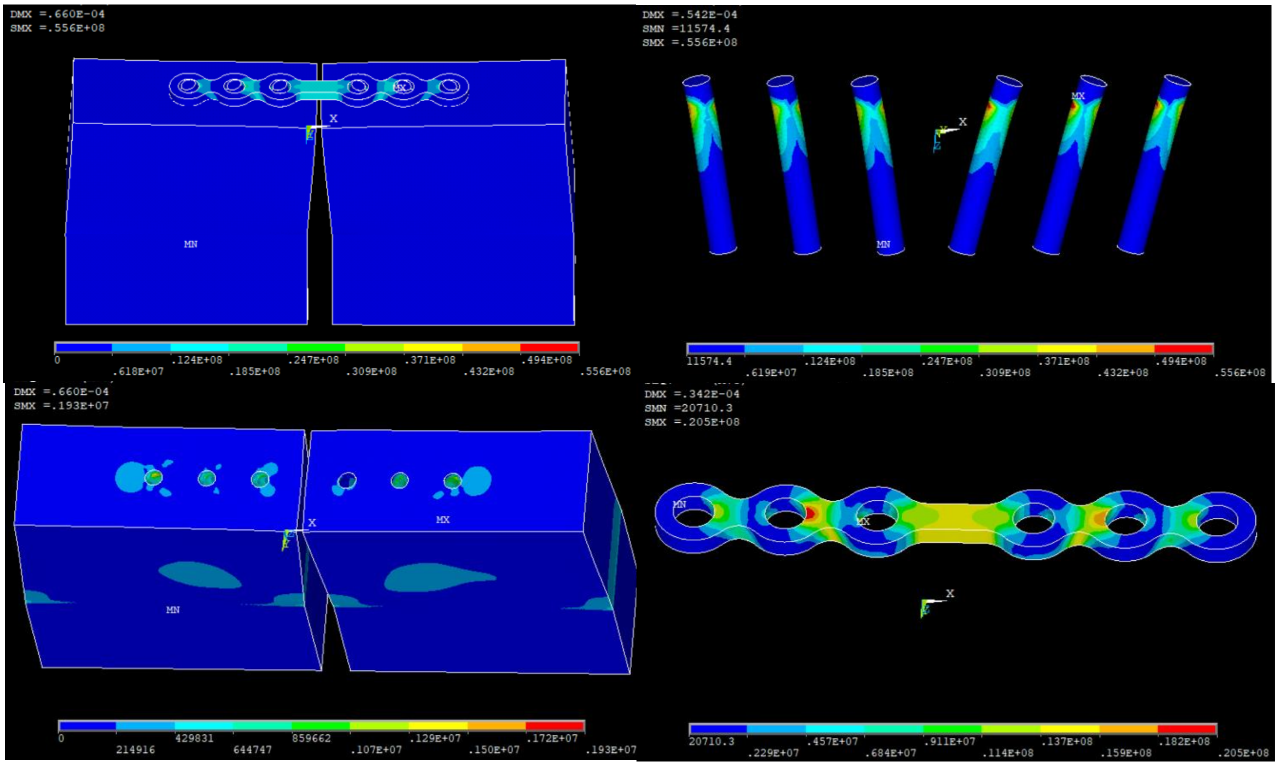

Figure 145: Prototype 4. In this image, the Von Mises stresses resulting from the tensile analysis of the entire specimen are shown in the upper right, while in the upper left, the Von Mises stresses developing along the screws are displayed. The lower right part shows the stresses along the bone specimen, and finally, the lower left part presents the stresses along the prosthetic plate.

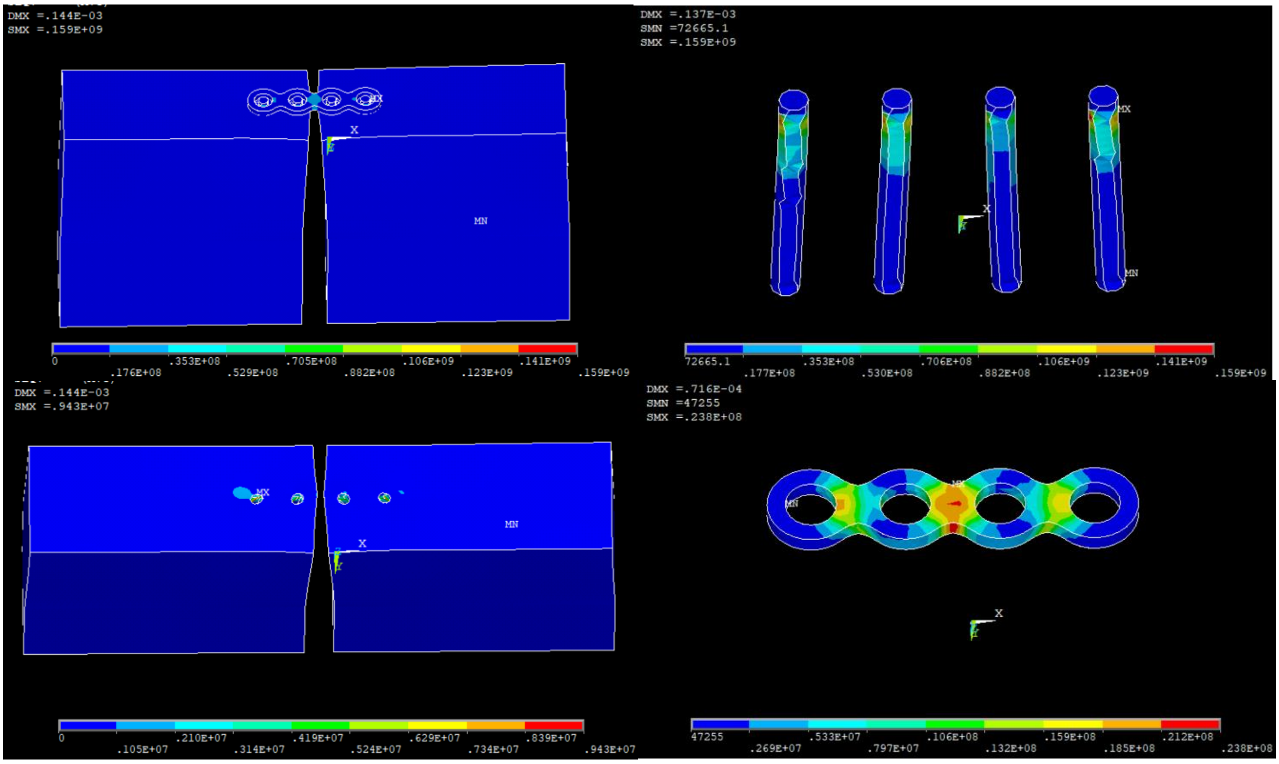

Figure 146: Prototype 5. In this image, the Von Mises stresses resulting from the tensile analysis of the entire specimen are shown in the upper right, while in the upper left, the Von Mises stresses developing along the screws are displayed. The lower right part shows the stresses along the bone specimen, and finally, the lower left part presents the stresses along the prosthetic plate.

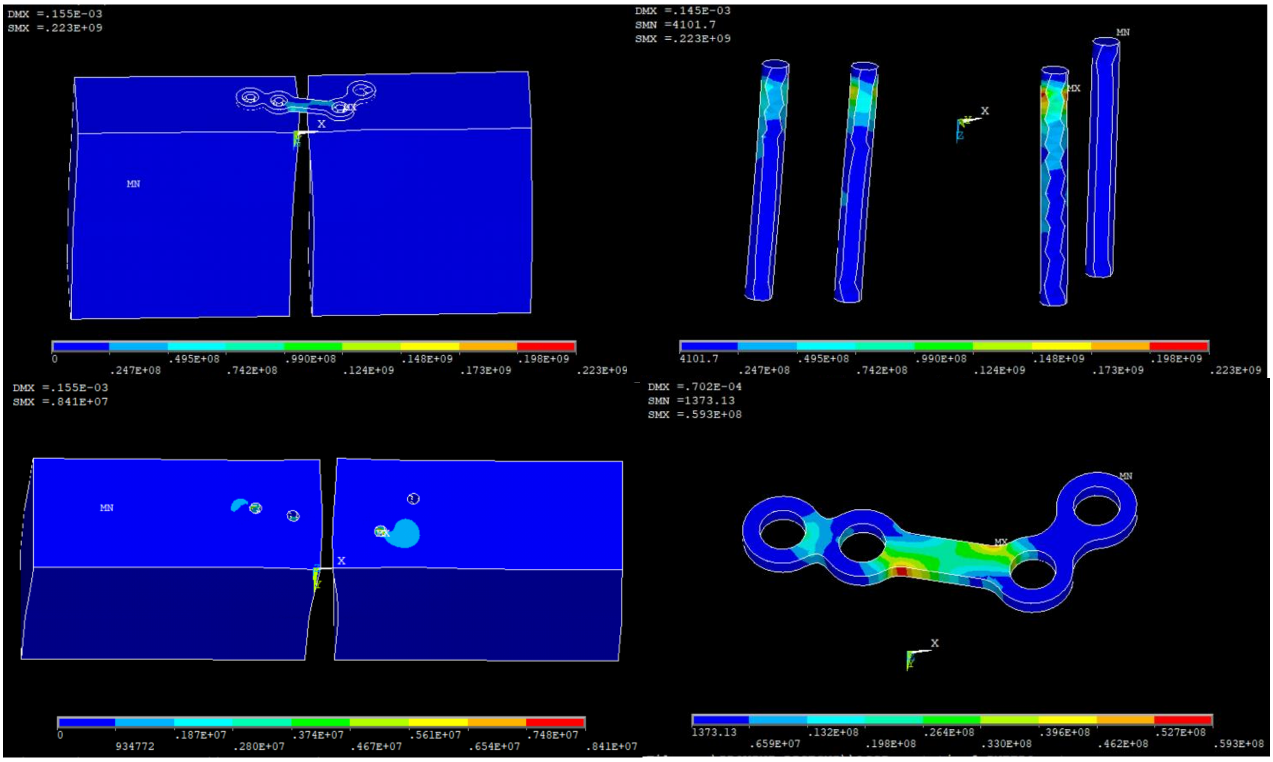

Figure 147: Prototype 6. In this image, the Von Mises stresses resulting from the tensile analysis of the entire specimen are shown in the upper right, while in the upper left, the Von Mises stresses developing along the screws are displayed. The lower right part shows the stresses along the bone specimen, and finally, the lower left part presents the stresses along the prosthetic plate.

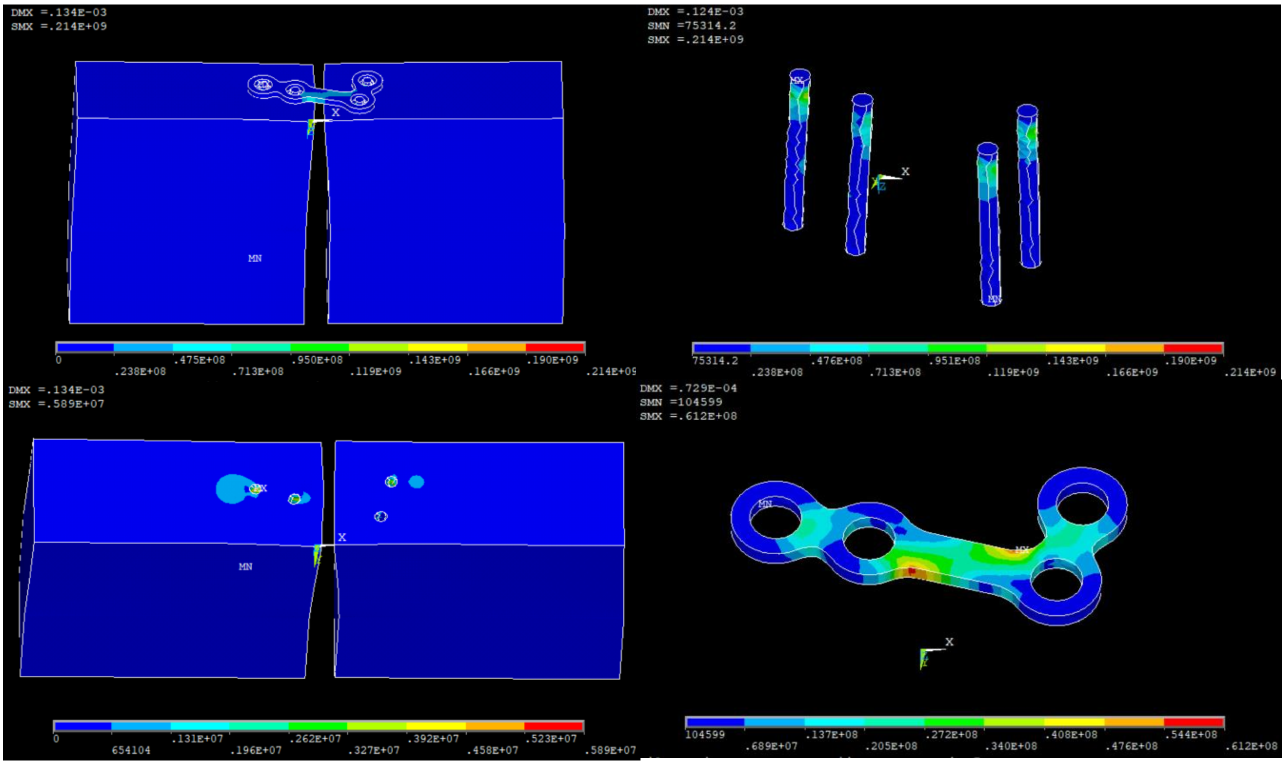

Figure 148: Prototype 7. In this image, the Von Mises stresses resulting from the tensile analysis of the entire specimen are shown in the upper right, while in the upper left, the Von Mises stresses developing along the screws are displayed. The lower right part shows the stresses along the bone specimen, and finally, the lower left part presents the stresses along the prosthetic plate.

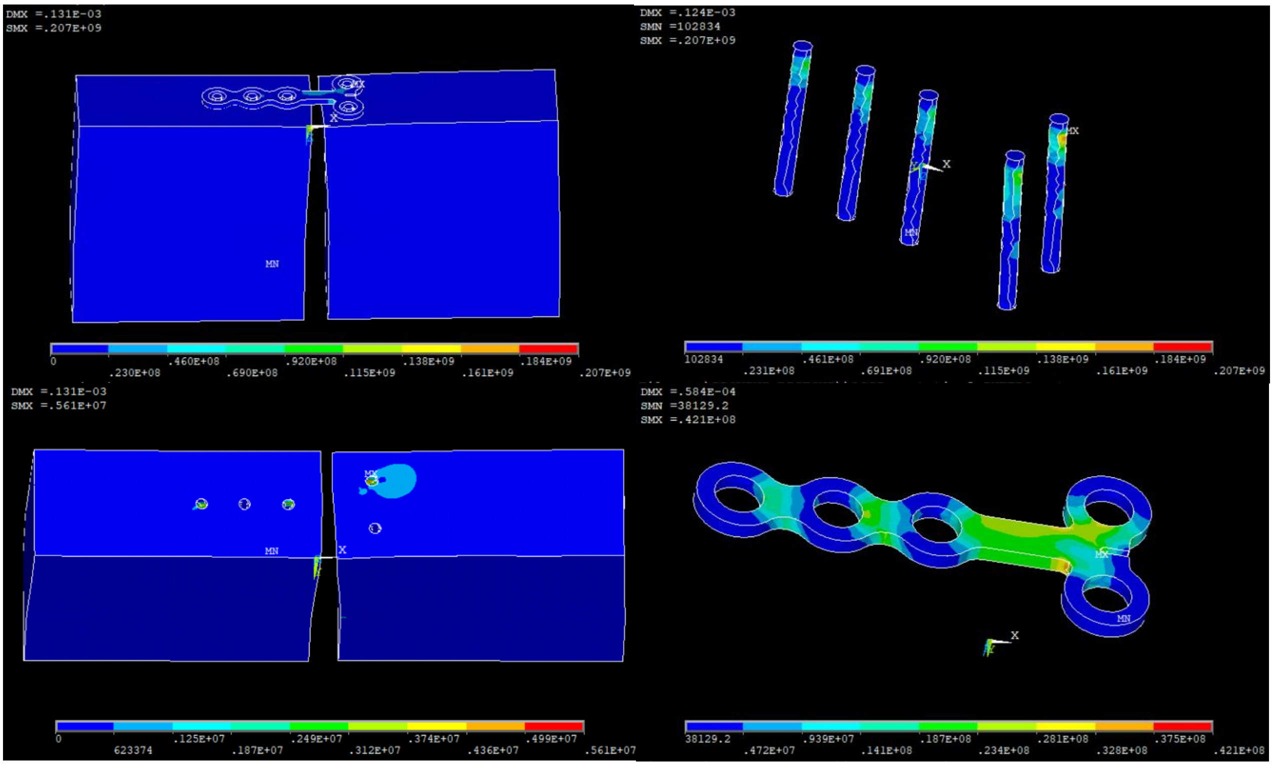

Figure 149: Prototype 8. In this image, the Von Mises stresses resulting from the tensile analysis of the entire specimen are shown in the upper right, while in the upper left, the Von Mises stresses developing along the screws are displayed. The lower right part shows the stresses along the bone specimen, and finally, the lower left part presents the stresses along the prosthetic plate.

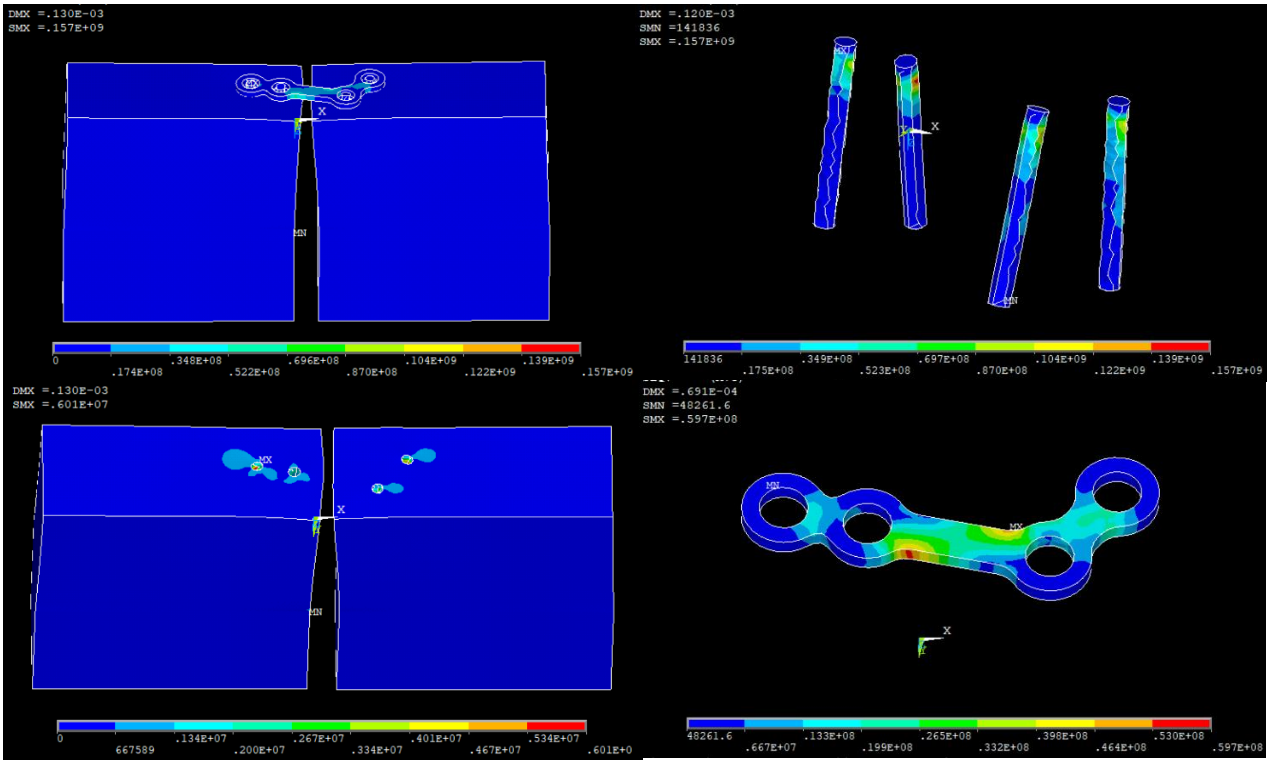

Figure 150: Prototype 9. In this image, the Von Mises stresses resulting from the tensile analysis of the entire specimen are shown in the upper right, while in the upper left, the Von Mises stresses developing along the screws are displayed. The lower right part shows the stresses along the bone specimen, and finally, the lower left part presents the stresses along the prosthetic plate.

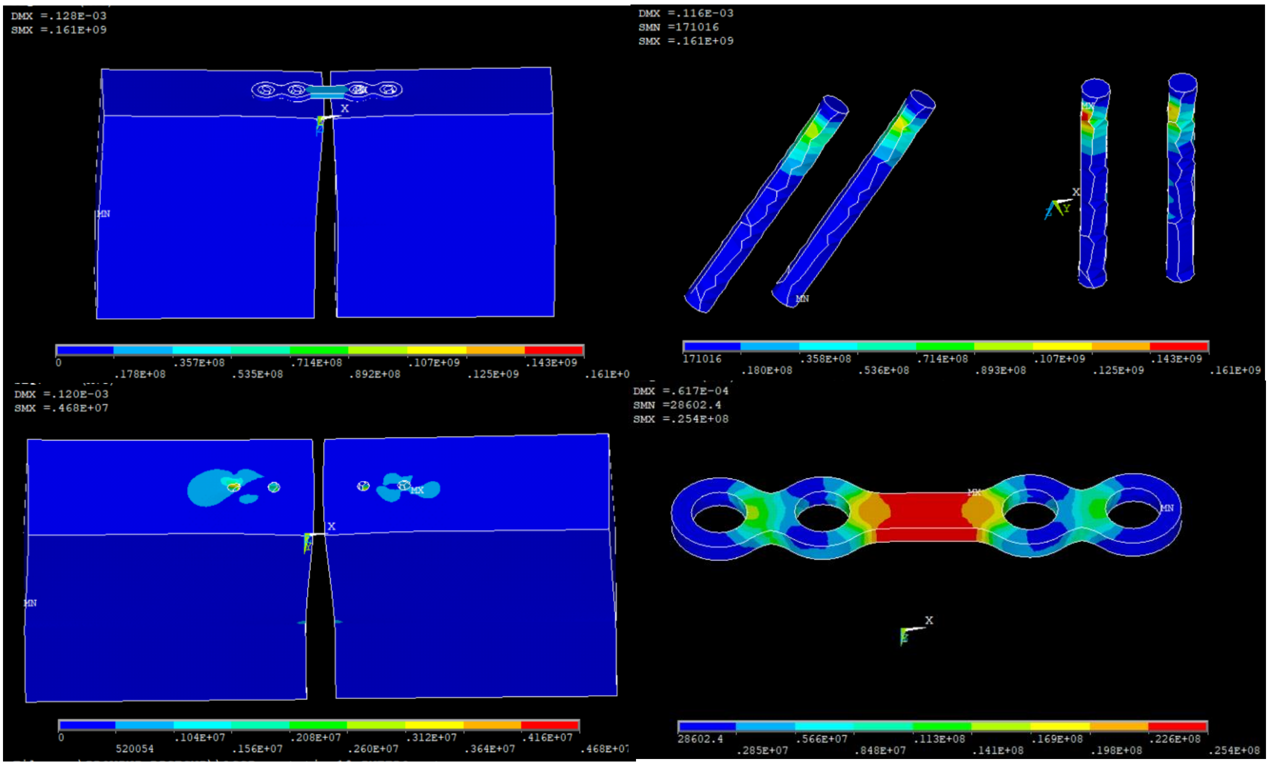

Figure 151: Prototype 10. In this image, the Von Mises stresses resulting from the tensile analysis of the entire specimen are shown in the upper right, while in the upper left, the Von Mises stresses developing along the screws are displayed. The lower right part shows the stresses along the bone specimen, and finally, the lower left part presents the stresses along the prosthetic plate.

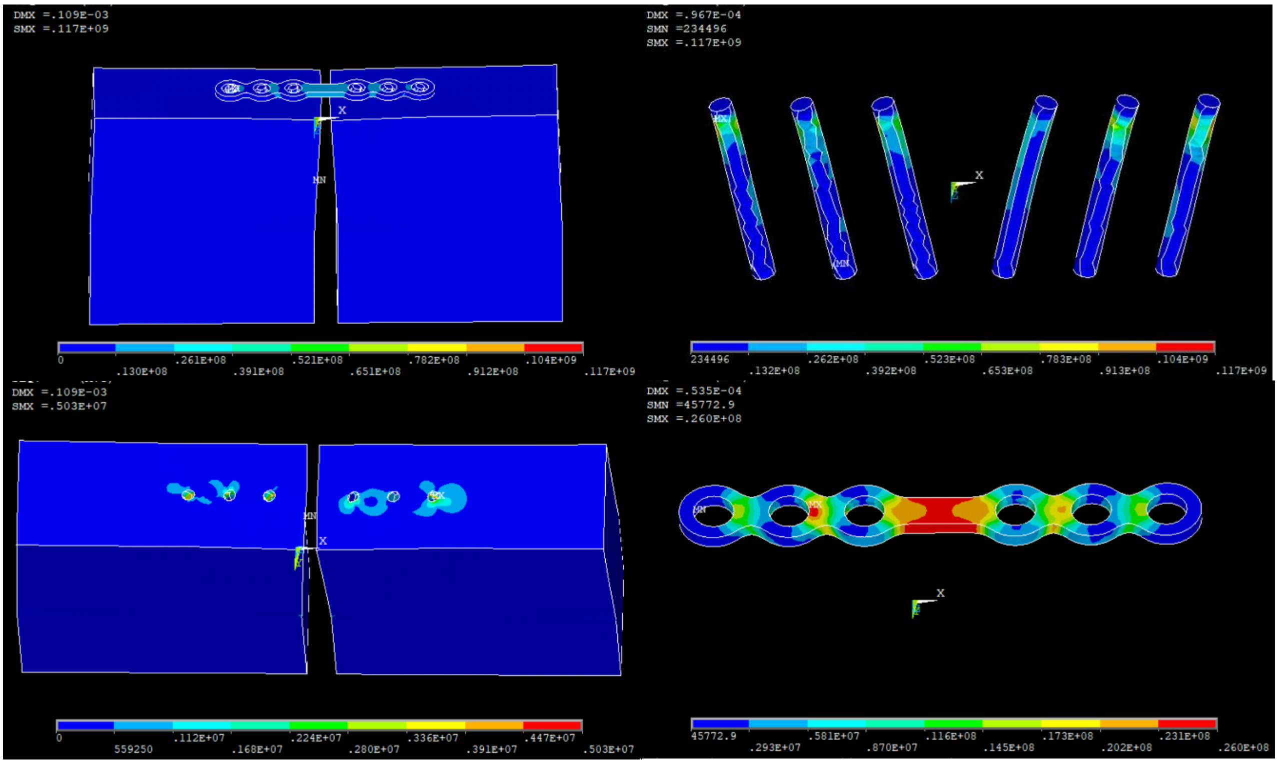

Figure 152: Prototype 11. In this image, the Von Mises stresses resulting from the tensile analysis of the entire specimen are shown in the upper right, while in the upper left, the Von Mises stresses developing along the screws are displayed. The lower right part shows the stresses along the bone specimen, and finally, the lower left part presents the stresses along the prosthetic plate.

In the following figures, the results of the tensile analysis, including the rotation of the bone specimen, for Model 2 related to Von Mises stresses are presented. For each of the three prototypes, the stress distribution in the specimen as a whole and its components can be observed for the tensile test performed with a force of 100 N. The numerical results shown in the figures are expressed in Pascals (Pa).

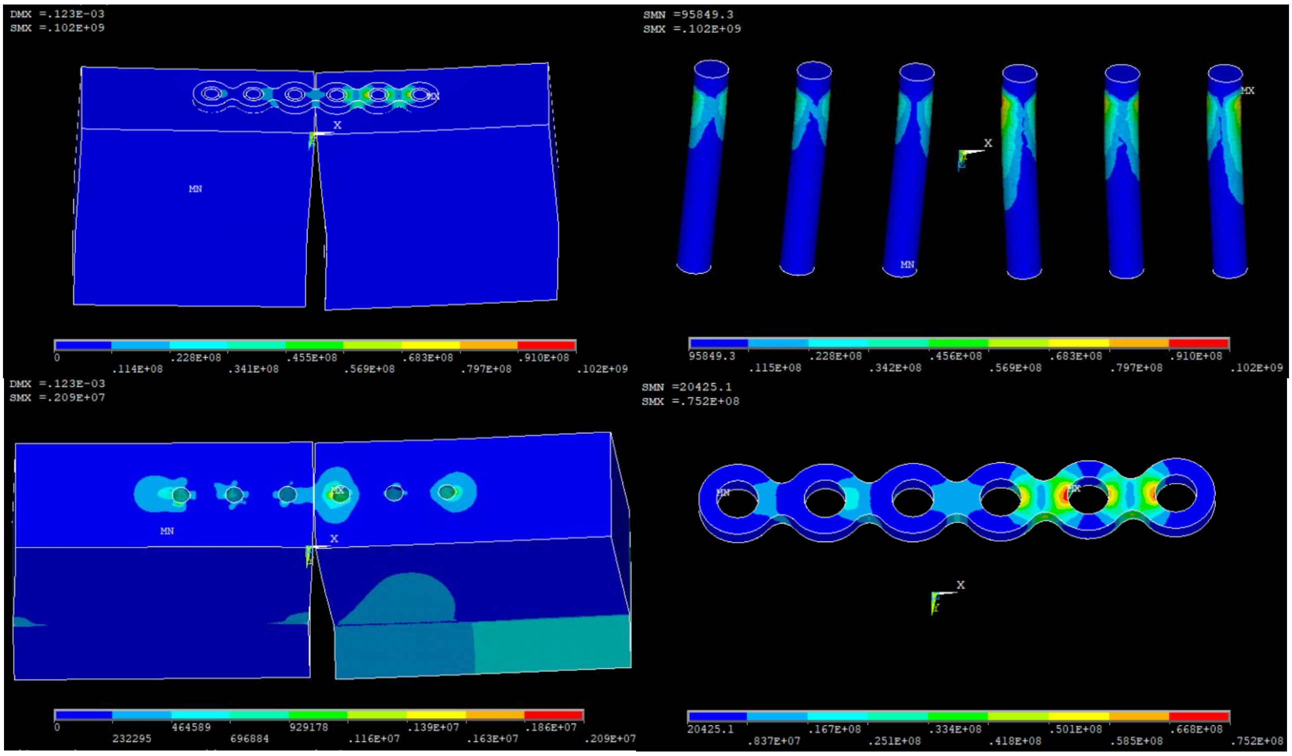

Figura 153: Prototype 2. In this image, the Von Mises stresses resulting from the numerical analysis of the entire specimen are shown in the upper right. In the upper left, the Von Mises stresses developing along the screws are displayed, while the lower right part shows the stresses along the bone specimen. Finally, the lower left part presents the stresses along the prosthetic plate.

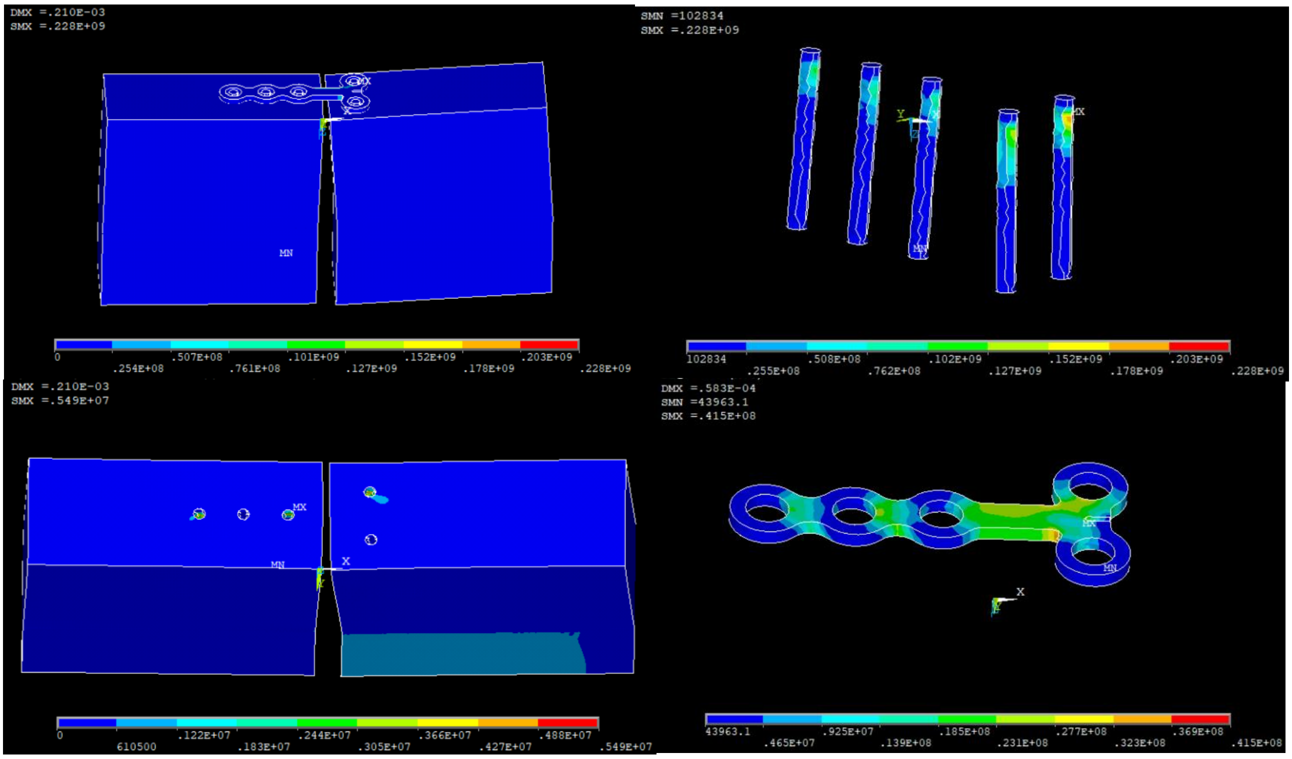

Figure 154: Prototype 8. In this image, the Von Mises stresses resulting from the numerical analysis of the entire specimen are shown in the upper right. In the upper left, the Von Mises stresses developing along the screws are displayed, while the lower right part shows the stresses along the bone specimen. Finally, the lower left part presents the stresses along the prosthetic plate.

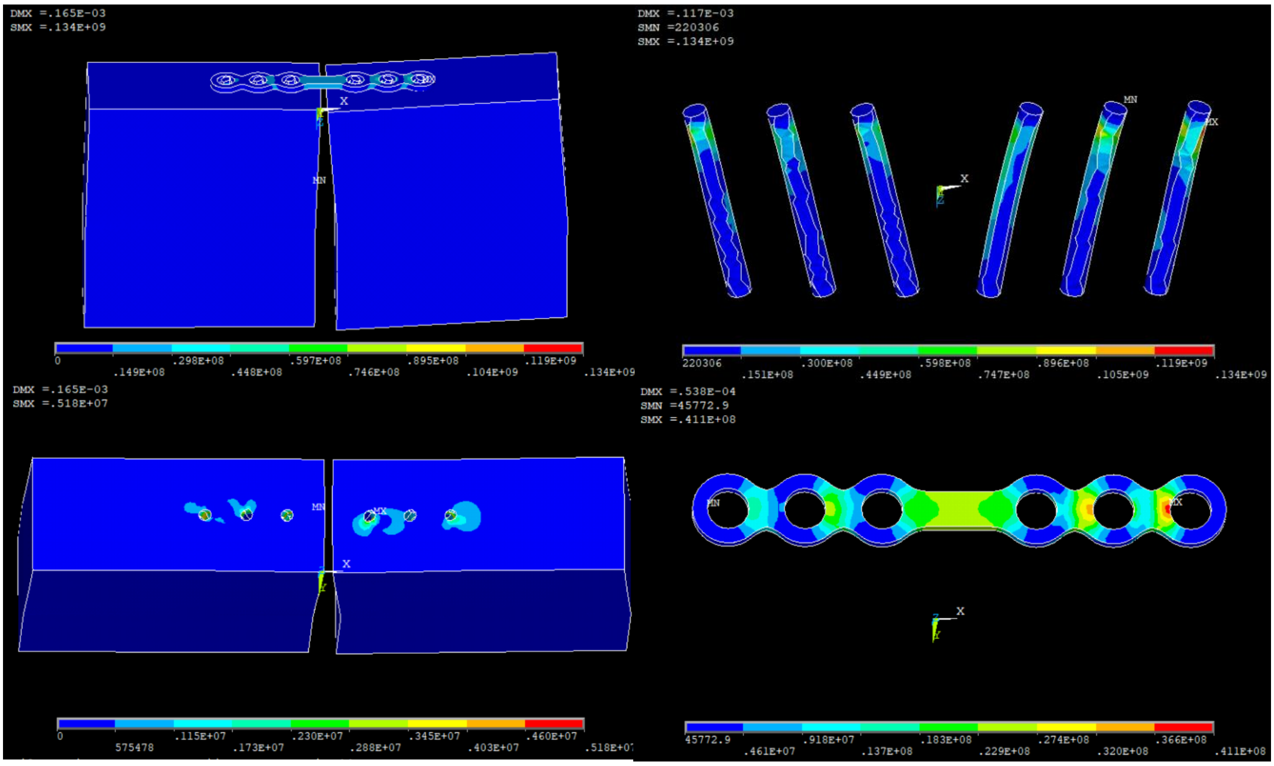

Figure 155: Prototype 11. In this image, the Von Mises stresses resulting from the numerical analysis of the entire specimen are shown in the upper right. In the upper left, the Von Mises stresses developing along the screws are displayed, while the lower right part shows the stresses along the bone specimen. Finally, the lower left part presents the stresses along the prosthetic plate.